



**Michigan  
Technological  
University**

Michigan Technological University  
**Digital Commons @ Michigan Tech**

---

Dissertations, Master's Theses and Master's Reports

---

2020

## Detection and thermal stabilization of virus based on surface properties

Xue Mi

*Michigan Technological University, xmi@mtu.edu*


Copyright 2020 Xue Mi

---

### Recommended Citation

Mi, Xue, "Detection and thermal stabilization of virus based on surface properties", Open Access Dissertation, Michigan Technological University, 2020.  
<https://doi.org/10.37099/mtu.dc.etr/1020>

Follow this and additional works at: <https://digitalcommons.mtu.edu/etr>

 Part of the [Biochemical and Biomolecular Engineering Commons](#)

DETECTION AND THERMAL STABILIZATION OF VIRUS BASED ON SURFACE  
PROPERTIES

By  
Xue Mi

A DISSERTATION

Submitted in partial fulfillment of the requirements for the degree of

DOCTOR OF PHILOSOPHY

In Chemical Engineering

MICHIGAN TECHNOLOGICAL UNIVERSITY

2020

© 2020 Xue Mi

This dissertation has been approved in partial fulfillment of the requirements for the Degree of DOCTOR OF PHILOSOPHY in Chemical Engineering.

Department of Chemical Engineering

Dissertation Advisor: *Dr. Caryn Heldt*

Committee Member: *Dr. Adrienne Minerick*

Committee Member: *Dr. Lei Pan*

Committee Member: *Dr. Marina Tanasova*

Department Chair: *Dr. Pradeep K. Agrawal*

# Table of Contents

List of Figures .....	vii
List of Tables .....	xii
Preface.....	xiii
Acknowledgements.....	xiv
Abstract.....	xv
1 Introduction and overview .....	1
1.1 Introduction .....	2
1.2 Overview .....	3
1.3 Reference.....	5
2 Literature review .....	7
2.1 General overview of viral diseases and viruses.....	8
2.1.1 Viral diseases outbreak .....	8
2.1.2 Viral structure and families.....	9
2.2 Virus characterization.....	11
2.2.1 Virus surface properties .....	11
2.2.1.1 Hydrophobicity .....	12
2.2.1.2 Surface charge and isoelectric point (pI) .....	13
2.2.2 Traditional virus surface characterization methods .....	14
2.2.2.1 Hydrophobic interaction chromatography (HIC).....	14
2.2.2.2 Aqueous two-phase system (ATPS) partitioning method	16
2.2.2.3 Zeta potential .....	17
2.2.2.4 Isoelectric focusing (IEF) .....	21
2.2.3 Novel surface characterization: chemical force microscopy (CFM) 22	
2.2.3.1 Fundamental principles of atomic force microscope	
(AFM) 23	
2.2.3.2 Force measurement (approach curve vs. withdraw curve)	
25	
2.3 Virus detection .....	30
2.3.1 Past and current virus detection methods.....	30
2.3.1.1 Transmission electron microscopy (TEM) .....	30
2.3.1.2 Immunoassays.....	31
2.3.1.3 Polymerase chain reaction .....	33
2.3.1.4 In vitro cell culture assays.....	34
2.3.2 Gold nanoparticles (AuNPs) in virus detection .....	36

	2.3.2.1	AuNPs properties .....	36
	2.3.2.2	Detection of specific viruses using AuNPs.....	37
2.4		Virus thermal stability .....	42
	2.4.1	Viral based vaccines .....	42
	2.4.2	Cold chain and cold storage problem.....	42
	2.4.3	Conventional vaccine formulation to stabilize viral vaccines .....	44
	2.4.4	Novel formulations to enhance the thermal stability of virus by complex coacervation.....	46
2.5		References .....	51
3		Virus surface chemistry characterization.....	64
	3.1	Introduction .....	65
	3.2	Experimental section .....	66
	3.2.1	Materials .....	66
	3.2.2	Virus purification .....	67
	3.2.3	Virus samples and control surfaces preparation .....	67
	3.2.4	AFM probe modification .....	67
	3.2.5	AFM imaging, force measurement and analysis.....	68
	3.3	Results and discussion.....	68
	3.3.1	Virus and virus surrogate immobilization.....	69
	3.3.2	AFM probe modification .....	72
	3.3.3	Virus surface probing by CFM .....	75
	3.4	Conclusions .....	77
	3.5	References .....	78
4		Virus isoelectric point determination.....	82
	4.1	Introduction .....	83
	4.2	Experimental section .....	85
	4.2.1	Materials. ....	85
	4.2.2	Buffers.....	85
	4.2.3	Virus production, purification, and titration. ....	85
	4.2.4	Virus samples and control surfaces preparation. ....	86
	4.2.5	AFM probe functionalization.....	86
	4.2.6	AFM imaging, force measurement, and analysis.....	87
	4.2.7	Zeta potential measurement. ....	87
	4.2.8	ATPS measurement. ....	87
	4.2.9	Theoretical calculation of virus surface potential and pI.....	88
	4.3	Results and discussion.....	88
	4.3.1	Surface and probe preparations.....	88
	4.3.2	Virus pI using CFM. ....	91

	4.3.3	Comparison to theoretically calculated virus pI and surface potential.	
		94	
	4.4	Conclusions .....	96
	4.5	References .....	97
5		Virus detection by mannitol-induced gold nanoparticle aggregation .....	101
	5.1	Introduction .....	102
	5.2	Experimental section .....	104
	5.2.1	Materials .....	104
	5.2.2	Virus titration and purification.....	104
	5.2.3	Synthesis and characterization of AuNPs.....	104
	5.2.4	Coating and characterization of virus-AuNPs complexes .....	105
	5.2.5	Proof-of-concept tests .....	106
	5.2.6	Statistical analysis.....	106
	5.3	Results and discussion.....	107
	5.3.1	Rationale of virus detection method .....	107
	5.3.2	Synthesis and characterization of AuNPs .....	108
	5.3.3	Concentration dependence .....	109
	5.3.4	Application: virus detection in protein solution matrix .....	112
	5.3.5	Application: evaluation of surface contamination .....	113
	5.3.6	Nonspecific virus detection.....	114
	5.4	Conclusions .....	115
	5.5	References .....	116
6		Stabilization of viruses through complex coacervation.....	121
	6.1	Introduction .....	122
	6.2	Materials and Methods .....	124
	6.2.1	Materials .....	124
	6.2.2	Virus production, purification and titration .....	125
	6.2.3	Formation of virus complex coacervates .....	125
	6.2.4	Virus complex coacervates characterization and quantification.....	125
	6.2.5	Virus thermal stability study.....	126
	6.3	Results and Discussion.....	127
	6.3.1	Virus coacervates characterization .....	127
	6.3.2	Encapsulation of virus as a function of coacervate charge stoichiometry .....	128
	6.3.3	Thermal stability of encapsulated virus vs. free virus .....	131
	6.4	Conclusions .....	134
	6.5	References .....	135

7	Conclusion and future work.....	139
7.1	Conclusions .....	140
7.2	Future work .....	142
7.3	References .....	144
A	Supplementary information .....	145
A.1	Virus isoelectric point determination .....	145
A.2	Virus detection by mannitol-induced gold nanoparticle aggregation .....	151
A.3	Stabilization of viruses through complex coacervation .....	155
B	Copyright permission documentation.....	159
B.1	Figure 2.1 permission .....	159
B.2	Figure 2.2 permission .....	160
B.3	Figure 2.4 permission .....	161
B.4	Figure 2.5 permission .....	162
B.5	Figure 2.6 permission .....	164
B.6	Figure 2.7 permission .....	165
B.7	Figure 2.8 permission .....	167
B.8	Figure 2.9 permission .....	168
B.9	Figure 2.10 permission .....	168
B.10	Figure 2.11 permission .....	168
B.11	Figure 2.12 permission .....	169
B.12	Figure 2.13 permission .....	171
B.13	Figure 2.14 permission .....	172
B.14	Figure 2.15 permission .....	173
B.15	Figure 2.16 permission .....	174

## List of Figures

<b>Figure 2.1</b> Hydrophobic/hydrophilic residues on a PPV surface protein. Reprinted from [32] with permission. ....	12
<b>Figure 2.2</b> Arrangement of functional groups on a viral surface protein. Reprinted [37] from with permission. ....	13
<b>Figure 2.3</b> Hydrophobic interaction chromatography.....	15
<b>Figure 2.4</b> Electrical double layer and zeta potential. Reprinted [58] from with permission. ....	18
<b>Figure 2.5</b> Components of a typical atomic force microscope. Reprinted from [83] with permission. ....	24
<b>Figure 2.6</b> AFM imaging. (A) Schematic illustration of the lateral dimension of scanned samples affected by the shape and size of AFM tip, and (B) adenovirus before and after repeated loading of 100 pN force 61 times, reprinted from [88] with permission. ....	25
<b>Figure 2.7</b> AFM force curves. (A) Approach and withdraw curves four regions, zero force region I, non-contact approach region II, contact region III, and non-contact withdraw region IV, and (B) conversion of F-Z curve to F-D curve. Reprinted from [90] with permission. ....	26
<b>Figure 2.8</b> CFM characterization of surface properties (A) Characterizing <i>S. cerevisiae</i> cell surface charges recorded in 1 mM KNO <sub>3</sub> solutions of varying pH between the surface of yeast cell and a carboxyl group modified probe. Reprinted from [95] with permission. (B) Characterizing <i>Aspergillus fumigatus</i> surface hydrophobic and hydrophilic regions recorded in acetate buffer between the surface of pathogen and a methyl group modified probe. Reprinted from [82] with permission. ....	28
<b>Figure 2.9</b> TEM images of uranyl acetate negative stained AAV2. (A) Full AAV particle, and (B) empty AAV particle. Reprinted from [99] with permission.....	30
<b>Figure 2.10</b> Immunoassays. (A) Indirect sandwich ELISA: 1) a capture antibody coated on the bottom of a plate well; 2) any viral antigen present in the analyte binds to capture antibody; 3) detection antibody is added, and binds to virus; 4) enzyme-labeled secondary antibody is added and binds to detection antibody; 5) substrate is added, results in a detectable color change converted by the enzyme. (B) Europium nanoparticles labeled monoclonal antibodies conjugate-linked fluorescent immunochromatography strip test for influenza A virus (H1N1). Reprinted from [105] with permission.....	32



<b>Figure 2.11</b> Overview of a Polymerase Chain Reaction Cycle. Reprinted from [107] with permission. ....	33
<b>Figure 2.12</b> In vitro cell culture assays. (A) Plaque formation of adenoviruses serotype 41 with crystal violet stain, reprinted from [113] with permission, (B) CPE effect of PK-13 cells infected by PPV, and (C) MTT assay of PK-13 cells infected by PPV, courtesy of Pratik U. Joshi, Michigan Technological University, Houghton, MI.....	35
<b>Figure 2.13</b> Characterization of isolated AuNPs (A) UV-Vis absorption spectrum, (B) DLS particle size, (C) TEM image, compared with (D) UV-Vis absorption spectrum, (E) DLS particle size, (F) TEM image of aggregated AuNPs in 100 mM NaCl. The insets show the real color of isolated and aggregated AuNPs. Reprinted from [119] with permission. ....	37
<b>Figure 2.14</b> Virus and protein stability with osmolyte. Reprinted from [148] with permission. ....	41
<b>Figure 2.15</b> Cold chain. (A) A typical flow of cold chain, reprinted from [161] with permission. (B) A vaccine vial monitor (VVM) to indicate the cumulative heat exposure of vaccine, reprinted from [162] with permission. ....	43
<b>Figure 2.16</b> Complex coacervation. (A) Scheme of complex coacervation of cationic polymer chitosan and anionic polymer hyaluronic acid (HA) in 0.1 M sodium acetate solution. Reprinted from [178] and [179] with permission. (B) Schematic representation of a typical phase diagram to define the phase boundaries as a function of salt concentration vs. polymer concentration for a given stoichiometry, pH, and temperature. Different colors represent different polymer chain lengths. Reprinted from [173] with permission. (C) BSA encapsulation via complex coacervation. Reprinted from [190] with permission. ....	48
<b>Figure 3.1</b> Overview of AFM probe surface modification and virus attachment on a gold surface. (A) AFM probes were functionalized with either a hydrophobic methyl group, a negatively charged carboxyl acid group, or a positively charged quaternary amine group. (B) Virus particles were immobilized with NHS/EDC chemistry. (Virus image was created in BioRender) .....	69
<b>Figure 3.2</b> Topographic images and corresponding height analysis of virus surrogate NH <sub>2</sub> -functionalized silica NPs with different ratios of COOH and CH <sub>3</sub> -capped thiol linkers and controls. Silica NPs were imaged after immobilization with (A) 9:1, (B) 1:1, and (C) 1:9 COOH to CH <sub>3</sub> ratios. Control surfaces were (D) methyl-modified surface, (E) bare gold surface, and (F) NHS-EDC surface. ....	71
<b>Figure 3.3</b> Topographic images and corresponding height analysis of virus. (A) PPV covalently bound to gold, (B) BVDV covalently bound to gold, (C) PPV deposited on gold, and (D) BVDV deposited on gold. ....	72

<b>Figure 3.4</b> Probe functionalization confirmation. Adhesion histograms and representative force-distance curves (retraction only) of positive control surface with a CH <sub>3</sub> -terminated, COOH-terminated, or a NR <sub>4</sub> <sup>+</sup> -terminated probe. (A) CH <sub>3</sub> -terminated probe with a CH <sub>3</sub> -modified surface, (B) COO <sup>-</sup> -terminated probe with a primary amine-modified silica NPs, and (C) NR <sub>4</sub> <sup>+</sup> -terminated probe with a COOH-modified surface. (A) Measured in PBS buffer at pH 7.2, and (B&C) measured in 20 mM phosphate buffers at pH 7.0. Multiple (n= 500) F-D curves were recorded over 500 nm × 500 nm areas.....	74
<b>Figure 3.5</b> Adhesion histograms and representative force-distance curves (retraction only) of virus with a CH <sub>3</sub> -terminated, COO <sup>-</sup> -terminated, or a NR <sub>4</sub> <sup>+</sup> -terminated probe, recorded in PBS at pH 7.2 (for hydrophobicity measurement) or 20 mM phosphate buffers at pH 7.0 (for surface charge measurement). Multiple (n= 500) F-D curves were recorded over 500 nm × 500 nm areas. (Virus images were created in BioRender) .....	76
<b>Figure 4.1</b> Overview of AFM probe functionalization and virus immobilization on a gold surface. (A) AFM probes were functionalized with either a negatively charged carboxyl acid group or a positively charged quaternary amine group and (B) virus particles were immobilized with NHS/EDC chemistry. ....	89
<b>Figure 4.2</b> Topographic image and corresponding height analysis of viruses and controls. (A) PPV, (B) BVDV, (C) NH <sub>2</sub> -functionalized silica NPs, and (D) carboxylic acid-modified surface.....	90
<b>Figure 4.3</b> Adhesion histograms and representative <i>F-D</i> curves (retraction part) of PPV with a COO <sup>-</sup> -terminated probe (A) or a NR <sub>4</sub> <sup>+</sup> -terminated probe (B), recorded in 20 mM citrate or phosphate buffers of varying pH. Multiple (n= 500) <i>F-D</i> curves were recorded over 500 nm × 500 nm areas. ....	92
<b>Figure 4.4</b> PPV pI determination using a variety of methods. (A) CFM with the COO <sup>-</sup> probe, (B) CFM with the NR <sub>4</sub> <sup>+</sup> probe, (C) zeta potential, and (D) ATPS. The CFM data were fit to a sigmoidal curve. Error bars are the standard deviation of three separate experiments. * <i>p</i> <0.01 using Student's <i>t</i> -test. ....	93
<b>Figure 4.5</b> BVDV pI determination using two methods. (A) CFM with the COO <sup>-</sup> probe, (B) CFM with the NR <sub>4</sub> <sup>+</sup> probe, and (C) zeta potential. The CFM data were fit to a sigmoidal curve. Error bars are the standard deviation of three separate experiments. * <i>p</i> <0.01 and <sup>+</sup> <i>p</i> <0.05 using Student's <i>t</i> -test. ....	94
<b>Figure 5.1</b> The outcome of AuNPs aggregation detection of virus. ....	107
<b>Figure 5.2</b> Characterization of synthesized and coated AuNPs. (A) TEM image of the AuNPs, the inset image showing the color of synthesized AuNPs, (B) zeta potential, (C) UV-Vis absorption spectrum, (D) hydrodynamic diameter. ....	109

**Figure 5.3** Concentration dependence for detection of PPV versus control BSA & thyroglobulin. (A&D&G) Size profile of PPV, BSA or thyroglobulin coated AuNPs as a function of concentrations before and after 1 M mannitol addition as measured by DLS. (B&E&H) Size profile of PPV, BSA or thyroglobulin coated AuNPs as a function of concentrations after 1 M NaCl addition as measured by DLS. (C&F&I) Change in AuNPs aggregation size for PPV, BSA or thyroglobulin after 1 M mannitol addition. Solid markers represent PPV, open markers represent BSA and thyroglobulin. All data points are the average of three separate tests and error bars represent the standard deviation. Concentrations are plotted as a log scale. TEM images of (J) 8 log PPV, (K) 8 log PPV-coated AuNPs and (L) 8 log PPV-coated AuNPs with 1 M mannitol. \*p <0.05 for virus compared to BSA and thyroglobulin controls. ....110

**Figure 5.4** Detection of virus in a protein solution matrix. (A) The average size of PPV-coated AuNPs in different concentrations of BSA before and after 1 M mannitol addition and measured by DLS. (B) The change in the size of PPV-coated AuNPs in different concentrations of BSA after 1 M mannitol addition. Solid symbols represent PPV and open symbols represent BSA only. All data points are the average of three separate tests and error bars represent the standard deviation. .113

**Figure 5.5** Swab sampling to detect contamination of PPV on a surface. (A) The process of swab sampling, (B) Size aggregation measured by DLS for swabbed PPV versus control swabbed BSA. Swabbed PPV is  $106.9 \pm 100.2$  MTT<sub>50</sub>/mL as measured by the MTT assay and  $10^{7.4}$  MTT<sub>50</sub>/mL as measured by the PPV-AuNPs aggregation assay in 1 M mannitol. All data points are the average of three separate tests and error bars represent the standard deviation. ....114

**Figure 5.6** Concentration dependence for detection of BVDV. (A) Size profile of BVDV coated AuNPs as a function of concentrations before and after 1 M mannitol addition as measured by DLS. (B) Size profile of BVDV coated AuNPs as a function of concentrations after 1 M NaCl addition as measured by DLS. (C) Change in AuNPs aggregation size for BVDV after 1 M mannitol addition. All data points are the average of three separate tests and error bars represent the standard deviation. \*p <0.05 for virus compared to BSA and thyroglobulin controls in **Figure 5.3**. ....115

**Figure 6.1** Optical micrographs of virus encapsulation within coacervate droplets. (A&B&C) PPV coacervates, and (D&E&F) BVDV coacervates. (A&D) Brightfield micrograph of virus coacervate droplets, (B&E) fluorescent image of NHS-Rhodamine tagged virus, and (C&F) overlay of the brightfield and fluorescent images. ....128

**Figure 6.2** Turbidity of encapsulated virus. (A) PPV coacervates, and (B) BVDV coacervates. All data points are the average of three separate tests and error bars represent the standard deviation.....129

**Figure 6.3** Live virus titration. (A&B&C) Encapsulated PPV, and (D&E) encapsulated BVDV. (A&D) 4 log<sub>10</sub> (MTT<sub>50</sub>/mL), (B&E) 5 log<sub>10</sub> (MTT<sub>50</sub>/mL), and (C) 6 log<sub>10</sub> (MTT<sub>50</sub>/mL). All data points are the average of three separate tests and error bars represent the standard deviation.....130

**Figure 6.4** Partition coefficient. (A&B&C) Encapsulated PPV, and (D&E) encapsulated BVDV. (A&D) 4 log<sub>10</sub> (MTT<sub>50</sub>/mL), (B&E) 5 log<sub>10</sub> (MTT<sub>50</sub>/mL), and (C) 6 log<sub>10</sub> (MTT<sub>50</sub>/mL). All data points are the average of three separate tests and error bars represent the standard deviation.....131

**Figure 6.5** Thermal stability of free and encapsulated virus. (A) PPV, and (B) BVDV. All data points are the average of three separate tests and error bars represent the standard deviation. ....132

## List of Tables

<b>Table 2.1</b> Viral families related to human infections [16-18] .....	10
<b>Table 2.2</b> The electrostatic properties of viruses by different characterization methods..	20
<b>Table 2.3</b> Virus detection using AuNPs .....	39
<b>Table 2.4</b> FDA-approved viral vaccines types, formulation, and thermal stability [164, 169, 170] .....	46
<b>Table 3.1</b> Adhesion force at different AFM probe functionalization conditions. ....	73
<b>Table 3.2</b> Model virus properties. ....	75
<b>Table 3.3</b> Mean force measured during CFM at a pH of 7.2 for the methyl probe and 7.0 for the charged probes.....	76
<b>Table 4.1</b> Model virus properties. ....	91
<b>Table 4.2</b> Computational electrostatic surface properties of the model virus vs. CFM-determined pI. ....	95
<b>Table 6.1</b> Model virus properties. ....	127

## Preface

Chapter 3 is about single-particle chemical force microscopy to characterize virus surface chemistry (CFM). Under the supervision of my advisor Dr. Caryn Heldt, I performed all of the experimental work, collected and analyzed all the data, drew all the figures, and wrote the chapter. This chapter is in preparation for submission as a peer-reviewed methods paper.

Chapter 4 is about virus isoelectric point determination using single-particle CFM. The majority of the experiments, data collection and analysis, figures design, and writing of the paper were performed by me. The aqueous two-phase system (ATPS) cross-partitioning in Figure 4.4D to determine the isoelectric point of porcine parvovirus (PPV) is a collaboration work by Emily K. Bromley, Pratik U. Joshi, and myself. Emily prepared the ATPS samples, and I performed the MTT assay to titrate it. Pratik proposed how to analyze the data and helped in the writing about the ATPS. Dr. Heldt guided me on how to analyze the data and write the paper. Dr. Fei Long guided me on how to perform the AFM and helped me solve the technical problems of the AFM instrument when I collected the raw data. Jessica Brassard supported the artwork of virus icons in Figure 4.1. This chapter has been submitted to *Langmuir* and is currently under revision.

Chapter 5 is on mannitol-induced gold nanoparticle (AuNPs) aggregation for the ligand-free detection of viral particles. It was a collaborative research project with Dr. James Chen Yong Kah and Dr. Eugenia Li Ling Yeo from National University of Singapore and my group members Elizabeth M. Lucier and Dylan G. Turperinen. Elizabeth helped run the DLS measurement for PPV-coated AuNPs in Figure 5.3 and performed the experiments for bovine viral diarrhea virus BVDV-coated AuNPs in Figure 5.6, Dylan analyzed the BVDV data in Figure 5.6, and Eugenia trained me how to synthesize and coat the AuNPs. I performed the majority of the experiments, analyzed the data, created the figures, and wrote the paper under the supervision of my advisor Dr. Heldt. Jessica Brassard supported the artwork of icons in Figure 5.1. This chapter has been published in the peer-review journal *Analyst*.

Chapter 6 is about the stabilization of viruses: a stepping stone toward thermostable vaccines. It was a collaborative research project with Dr. Sarah L. Perry and Whitney C. Blocher McTigue from University of Massachusetts Amherst and my group members Pratik U. Joshi and Mallory K. Bunker. Whitney trained me on how to form coacervates and helped process the combined fluorescent and brightfield microscopic images in Figure 6.1. Pratik helped obtain the fluorescent and brightfield images of virus coacervates in Figure 6.1 and help me titrate half of the PPV coacervates samples at different ratios of polypeptides by MTT assay in Figure 6.3. Mallory helped me form half of the PPV and BVDV coacervates samples in Figure 6.2 & 6.3 MTT. I have done the rest of the experimental work, analyzed the data, designed the figures, and wrote the chapter, based on the suggestions and corrections of Dr. Heldt, along with comments from Dr. Perry and Whitney Blocker McTigue. This chapter is in preparation for submission to a peer-review journal paper.

## Acknowledgements

First and foremost, I would like to express my deepest gratitude to my advisor, Dr. Caryn Heldt, for her constant encouragement, patient mentoring, and generous support throughout my entire graduate school studies. Her creative mind, critical thinking, and great passion for science deeply influenced and inspired me to overcome the difficulties I met in my research. I'm very grateful to Dr. Heldt for giving me the opportunity to join her lab, funding me generously, and all of her help with my professional and personal development. I want to thank the Department of Chemical Engineering of Michigan Tech, NSF (CAREER-1451959 and 1159425), Portage Health Foundation, and the James and Lorna Mack Chair in Bioengineering for funding.

I would like to thank Dr. Adrienne Minerick, Dr. Lei Pan, and Dr. Marina Tanasova for serving as my committee members and providing insightful feedback. I also want to thank Dr. Minerick for the use of her instruments, her lab space, and her professional advice and support on my career. I also thank Dr. Xiaohu Xia for serving as my proposal committee member. I am grateful to Dr. Fei Long for the training and the help on the AFM instrument, Dr. Chito Kendrick for his assistance and instruction in the Microfabrication Facility, Dr. Pinaki Mukherjee and Owen Mills for assistance with TEM imaging. I also thank Dr. Ong, Dr. Agrawal, Dr. Morrison, and Dr. Co for their kind encouragement and support. I also appreciate Taana and Alexis in Chemical Engineering for being so nice to me.

I want to express my thanks to all my labmates for their support, assistance, and friendship, especially Pratik, Dylan, Ellie, Emily, and Mallory, who helped me with experiments for my publications. Besides, my sincere gratitude to Dr. Kah and Dr. Yeo from National University of Singapore for collaboration on virus detection project and to Dr. Perry and Whitney from University of Massachusetts Amherst for collaborative research on virus thermal stability study.

Finally, I would like to thank my best friends, Lisha, Hua, Huanhuan, Jinxiang and Hongze, you guys were always there, when I was lonely or frustrated. I would like to express my deepest thanks to my mother Lihui Su and my father Yongzheng Mi for their unconditional love and support throughout my life. Their love and support was truly the reason why I was able to endure and finish my Ph.D. study.

## Abstract

Viral diseases take the lives of millions of people each year. The most effective methods to prevent viral disease outbreak are viral detection to reduce contact with viral pathogens and vaccines to prevent disease. To reduce the costs of the detection of viruses and improve vaccine formulation, we explored viral surface properties. The properties we have focused on are viral hydrophobicity and surface charge using chemical force microscopy (CFM). CFM is a single-particle technique that measures the adhesion force of a functionalized atomic force microscopy (AFM) probe, and in this study, a virus covalently bound to a surface. The non-enveloped porcine parvovirus (PPV) and enveloped bovine viral diarrhea virus (BVDV) were used to demonstrate the use of CFM for viral particles with different surface properties.

The high hydrophobicity of PPV and BVDV by CFM was used for a ligand-free, non-specific virus detection method that relies on the interaction of virus with osmolytes. It was previously found that the osmolyte mannitol can preferentially aggregate viruses while leaving proteins in solution. The virus was incubated with gold nanoparticles (AuNPs), and aggregation of the virus-AuNP complex with mannitol was detected by dynamic light scattering (DLS).

The isoelectric point (pI) of PPV and BVDV by CFM was used for a vaccine formulation strategy of virus particle encapsulation by polymers that relies on electrostatic interactions of the virus with polypeptides. The random screen of different ratios of polyelectrolytes to encapsulate viruses could be reduced by knowing the virus pIs. An encapsulated non-enveloped PPV is thermally stabilized, demonstrating that this method is promising for formulating thermostable vaccines.

We have developed a unique detection method and can improve vaccine formulation that would reduce the impact of viral diseases worldwide, based on the viral surface properties.



# 1 Introduction and overview

## 1.1 Introduction

Viruses are nanoscale-sized infectious agents [1], which cause many diseases such as influenza, smallpox, acquired immunodeficiency syndrome (AIDS), severe acute respiratory syndrome (SARS), and Ebola. In the age of modern medicine, viral diseases continue to take the lives of millions of people each year around the world [2], resulting in significant human, social, and economic losses. The most effective methods to prevent viral disease outbreak are viral detection to reduce contact with viral pathogens and vaccines to prevent disease.

Traditional virus detection methods, such as enzyme-linked immunosorbent assay (ELISA) [3], lateral flow immunoassay [4], and polymerase chain reaction (PCR) [5], require ligands that bind to either viral capsid proteins or viral nucleic acids. Ligands are typically antibodies or oligonucleotides, and are expensive, have limited chemical stability, and can only detect one specific type of virus at a time. There are ligand-free detection methods, such as transmission electron microscopy (TEM) [6], and in-vitro cell culture assays [7], but both are time-consuming, labor-intensive, and expensive. The high cost of traditional virus detection methods limits their accessibility in low resources countries.

Low resource countries also have lower vaccination rates due to the need for being transported and stored at cold temperatures [8]. If temperatures are not maintained, the vaccine may lose its potency and could no longer be effective in fighting disease. This is called the cold storage problem [8]. Finding a way to stabilize a virus thermally, so a vaccine does not need to be transported and stored in cold temperatures, is important to the health and safety of many people.

To benefit the public health and safety, a ligand-free, general virus detection method using gold nanoparticles (AuNPs) aggregation, and the use of polyelectrolyte dense phases to stabilize viruses thermally was explored. However, to design a new, inexpensive virus detection method and to reduce the need to screen different ratios of polyelectrolytes randomly, we have chosen to explore viral surface properties first.

The properties we have focused on are the hydrophobic and electrostatic surface properties of viruses, which determine the viral mobility and colloidal behavior in a liquid medium [9-12]. The viral surface characteristics need to be thoroughly understood for better manipulating of virus interactions with AuNPs and polyelectrolytes. Common methods for characterizing the surface properties of viruses are hydrophobic interaction chromatography (HIC) [13-14], aqueous two-phase system (ATPS) cross-partitioning [15], zeta potential [16], and isoelectric focusing (IEF) [17]. However, they are bulk measurements and limited by the purity of virus samples [18, 19] and solution conditions [15, 16, 20]. Moreover, except for IEF, these methods require a large amount of purified virus samples, of which the cost is high. Thus, an inexpensive, robust, reliable, and single-particle technique chemical force microscopy (CFM) [21] was chosen to characterize viral surface properties.

## 1.2 Overview

The dissertation begins with an introduction of this research stated here as chapter 1. Chapter 2 contains a literature review on why this research is needed and the principal background of the research. We discuss the limitations of traditional virus surface characterization methods and show the promise of the single-particle method CFM to characterize viral surface properties. Also, we discuss the disadvantages of the past and current virus detection methods and show the advantage of using AuNPs to detect the virus. Towards the end of this chapter, we talk about the cold storage problem of conventional formulation and discuss novel vaccine formulation strategies to stabilize viral vaccines thermally.

In Chapter 3, we demonstrate how we developed the single-particle method CFM to characterize virus surface characteristics, focusing on the hydrophobicity and surface charge, which determine the viral mobility and control the viral colloidal behavior during adsorption. CFM allows the characterization of viral capsid surface chemistry in known solution conditions with small amounts of virus samples. This single-particle method requires the functionalization of an atomic force microscopy (AFM) probe and the covalent bonding of the virus to a surface. Conditions were explored during each of these processes to understand the key variables for the measurement of virus adhesion to functionalized AFM probes. A non-enveloped porcine parvovirus (PPV), and an enveloped bovine viral diarrhea virus (BVDV) were used to demonstrate the use of CFM for viral particles with different surface properties. CFM with an AFM probe terminated with hydrophobic methyl groups was used to study the surface hydrophobicity of a virus. An AFM probe terminated with either negatively charged carboxyl acids or with positively charged quaternary amines was used to study the surface charge of the virus. With the method appearing to be robust, we used CFM for further virus electrostatic properties measurement.

In Chapter 4, we used CFM to determine the isoelectric point (pI) of two viruses PPV and BVDV. Traditional determination of virus pI has focused on the bulk characterization of a viral solution. However, virus capsids are extremely heterogeneous, and a single-particle method may give more information on the range of surface charge observed across a population. We have validated the CFM by determining the pI of PPV to be 4.8-5.1, which has a known pI value of 5.0 in the literature and to predict the unknown pI of BVDV to be 4.3-4.5. Bulk measurements, zeta potential, and aqueous two-phase systems (ATPS) cross-partitioning methods were also used to validate the new CFM method for virus pI. Most methods were in good agreement. CFM can detect the surface charge of viral capsids at a single-particle level and enable the comparison of surface charge between different types of viruses.

In Chapter 5, the biochemical surface properties of viruses were exploited for ligand-free, nonspecific virus detection. The detection depends on the interaction of the virus with the osmolyte mannitol. Osmolytes are naturally occurring molecules that have a high affinity for water. By binding water, the highly hydrophobic virus is partially dehydrated, which causes aggregation. It has been found that the osmolyte mannitol can preferentially aggregate virus while leaving proteins in solution. This led to the

development of a ligand-free detection of virus using AuNP aggregation. A non-enveloped PPV was incubated with AuNPs, and aggregation of the PPV-AuNP complex with mannitol was detected by DLS. The lowest detectable concentration of PPV was statistically determined to be  $10^6$  MTT<sub>50</sub>/mL, which is lower than standard antibody assays. PPV was also detected when swabbed from a dry surface and in the presence of a protein solution matrix. The enveloped BVDV was also detected using the mannitol-induced aggregation of BVDV-coated AuNPs. The lowest detectable concentration of BVDV was statistically determined to be  $10^4$  MTT<sub>50</sub>/mL. This demonstrates that gold nanoparticle aggregation can detect viruses without the use of specific ligands.

Chapter 6 explores the use of polyelectrolyte dense phases to thermally stabilize the virus. We have developed a method of encapsulation of virus particles in polymers that relies on the electrostatic interaction of viruses with polypeptides. Encapsulating virus particles in polypeptides is a potential solution to the cold storage problem. When oppositely charged polypeptides are in solution, the electrostatic interactions of the polypeptides create a dense phase liquid called a complex coacervate. Two viruses, PPV and BVDV, were explored to form the virus complex coacervates. The amount of charged polypeptides corresponded to the difference in the pI of the two viruses. The PPV and BVDV coacervates at each maximum extraction condition were used to explore the effect of complex coacervates on the stability of viruses against high temperatures. The encapsulated non-enveloped PPV is thermally stabilized. Coacervates could help prevent the cold storage problem seen not only in developing countries but is also a very real problem here in rural parts of America.

Chapter 7 reviews the major findings from this research and discusses the future directions of the research.

### 1.3 Reference

1. Payne, S., *Viruses: from understanding to investigation*. 2017: Academic Press.
2. Ritchie, H. and M. Roser. *Causes of Death*. Our World in Data [cited 2019 September 30]; Available from: <https://ourworldindata.org/causes-of-death>.
3. Lai, S.C., et al., *Development of an Enzyme-Linked Immunosorbent Assay for Rapid Detection of Dengue Virus (DENV) NS1 and Differentiation of DENV Serotypes during Early Infection*. Journal of Clinical Microbiology, 2019. **57**(7).
4. Yu, S.T., et al., *Clinical evaluation of rapid fluorescent diagnostic immunochromatographic test for influenza A virus (H1N1)*. Scientific Reports, 2018. **8**.
5. Nanda, S., et al., *Universal virus detection by degenerate-oligonucleotide primed polymerase chain reaction of purified viral nucleic acids*. Journal of Virological Methods, 2008. **152**(1-2): p. 18-24.
6. Nagler, F. and G. Rake, *The use of the electron microscope in diagnosis of variola, vaccinia, and varicella*. Journal of bacteriology, 1948. **55**(1): p. 45.
7. Santa Maria, F., et al., *Inactivation of Zika virus in platelet components using amotosalen and ultraviolet A illumination*. Transfusion, 2017. **57**(8): p. 2016-2025.
8. Comes, T., K.B. Sandvik, and B. Van de Walle, *Cold chains, interrupted: The use of technology and information for decisions that keep humanitarian vaccines cool*. Journal of Humanitarian Logistics and Supply Chain Management, 2018. **8**(1): p. 49-69.
9. van Voorthuizen, E.M., N.J. Ashbolt, and A.I. Schafer, *Role of hydrophobic and electrostatic interactions for initial enteric virus retention by MF membranes*. Journal of Membrane Science, 2001. **194**(1): p. 69-79.
10. Dika, C., et al., *Isoelectric point is an inadequate descriptor of MS2, Phi X 174 and PRD1 phages adhesion on abiotic surfaces*. Journal of Colloid and Interface Science, 2015. **446**: p. 327-334.
11. Meder, F., et al., *The role of surface functionalization of colloidal alumina particles on their controlled interactions with viruses*. Biomaterials, 2013. **34**(17): p. 4203-4213.
12. Brown, M.R., et al., *Defining the Mechanistic Binding of Viral Particles to a Multi-modal Anion Exchange Resin*. Biotechnology Progress, 2018. **34**(4): p. 1019-1026.
13. Johnson, S.A., et al., *The step-wise framework to design a chromatography-based hydrophobicity assay for viral particles*. Journal of Chromatography B-Analytical Technologies in the Biomedical and Life Sciences, 2017. **1061**: p. 430-437.
14. Shields, P.A. and S.R. Farrah, *Characterization of virus adsorption by using DEAE-sepharose and octyl-sepharose*. Applied and Environmental Microbiology, 2002. **68**(8): p. 3965-3968.
15. Miörner, H., P. Albertsson, and G. Kronvall, *Isoelectric points and surface hydrophobicity of Gram-positive cocci as determined by cross-partition and*

- hydrophobic affinity partition in aqueous two-phase systems*. Infection and immunity, 1982. **36**(1): p. 227-234.
16. Samandoulgou, I., I. Fliss, and J. Jean, *Zeta Potential and Aggregation of Virus-Like Particle of Human Norovirus and Feline Calicivirus Under Different Physicochemical Conditions*. Food and Environmental Virology, 2015. **7**(3): p. 249-260.
  17. Braun, M., et al., *A simple method to estimate the isoelectric point of modified Tomato bushy stunt virus (TBSV) particles*. Electrophoresis, 2017. **38**(21): p. 2771-2776.
  18. Shi, H. and V.V. Tarabara, *Charge, size distribution and hydrophobicity of viruses: Effect of propagation and purification methods*. Journal of Virological Methods, 2018. **256**: p. 123-132.
  19. Dika, C., et al., *Impact of the virus purification protocol on aggregation and electrokinetics of MS2 phages and corresponding virus-like particles*. Physical Chemistry Chemical Physics, 2013. **15**(15): p. 5691-5700.
  20. Aronino, R., et al., *Removal of viruses from surface water and secondary effluents by sand filtration*. Water Res, 2009. **43**(1): p. 87-96.
  21. Noy, A., D.V. Vezenov, and C.M. Lieber, *Chemical force microscopy*. Annual Review of Materials Science, 1997. **27**(1): p. 381-421.

## **2 Literature review**

## 2.1 General overview of viral diseases and viruses

### 2.1.1 Viral diseases outbreak

Viruses are small “obligate parasites”, typically range from 20-400 nm in size [1], relying on a living host for production [2]. Viruses are known to cause human disease, including influenza, hepatitis, smallpox, measles, severe acute respiratory syndrome (SARS), and acquired immune deficiency syndrome (AIDS). Viral diseases can seriously or mortally damage human organs, including lungs, liver, intestines, central nervous system, and immune system. Viruses are responsible for 10–15% of human cancers [3] and are responsible for killing millions of people in the world each year [4]. Viral infectious disease outbreak is one of the greatest threats to public health in the twenty-first century [5].

For example, the 2014–2016 Ebola outbreak in West Africa caused more than 28,616 suspected cases and 11,310 deaths [6]. It was the largest and most severe Ebola outbreak ever recorded since the virus was first discovered in 1976 [7]. The second-worst ever Ebola outbreak in the Democratic Republic of the Congo (DRC) from August 2018 is still ongoing [8]. As of September 2019, more than 3,000 people have been infected with Ebola, and over 2,000 people have died [8]. Ebola virus disease (EVD) has symptoms of fever, body pains, vomiting and diarrhea, and sometimes bleeding inside and outside the body, from 2 to 21 days after infection with the Ebola virus [9]. Currently, there is no licensed vaccine or cure for EVD. However, an experimental recombinant vesicular stomatitis virus–Zaire Ebola virus (rVSV-ZEBOV) vaccine has been used to protect over 90,000 people under a compassionate use protocol in ongoing DRC Ebola outbreak and showed a high level of protection against EVD (97.5% vaccine efficacy) [10]. Also, two investigational treatment monoclonal antibodies, mAb114 and REGN-EB3, showed a significant improvement in the survival rate for Ebola patients during the ongoing DRC outbreak [11]. The spread of Ebola could also be reduced by early virus detection.

Moreover, the global measles outbreak also hit the U.S. and has become a national focus. Measles is caused by a Measles morbillivirus in the paramyxovirus family [12]. It is highly contagious and can spread through direct contact with infected people and through the air. People infected with the measles can show symptoms of high fever, cough, runny nose, red and watery eyes, Koplik spots, and a measles rash [13]. Measles can be very dangerous, especially for children under five years old. From January 1 to September 26, 2019, a total of 1,243 cases of measles have been confirmed in 31 states of the U.S., most of the outbreaks were in New York, Michigan and Washington State in unvaccinated communities [14]. The measles outbreak could be prevented with the available safe, cost-effective measles, mumps, and rubella (MMR) vaccine [13]. According to the World Health Organization (WHO), measles vaccination prevented an estimated 21.1 million deaths worldwide from 2000 to 2017 [15].

Viral infectious diseases can still cause significant mortality, morbidity, and economic burdens for people today. The most effective methods to prevent viral disease outbreak are vaccines to prevent disease and to detect viruses to reduce contact with viral



pathogens. A full understanding of the viral particles plays a crucial role in the design of viral vaccines and virus detection technologies.

### **2.1.2 Viral structure and families**

Virus structures are designed for effective replication within the host organism. Viruses contain genetic material (either a DNA or RNA genome) and are surrounded by protective protein coats. The viral genome can be single-stranded (ss) or double-stranded (ds), linear or circular in shape, and a thousand to a million base pairs in size [1, 2]. The protein coat is called a capsid and is encoded by the viral genome [1, 2]. The viral capsid is made up of multiple copies of identical protein subunits. There are two major patterns of viral capsid: helical symmetry and icosahedral symmetry [1, 2]. Some virus families possess an additional lipid bilayer covering, into which viral glycoproteins are inserted, known as enveloped viruses [1, 2]. The viral envelopes are derived from host cell membranes. Other virus families that do not contain a lipid bilayer carrying viral glycoproteins, called non-enveloped or naked viruses [1, 2].

Both the enveloped and non-enveloped viruses from different viral families can cause human infectious disease, as shown in **Table 2.1** [16-18]. One basic unit of viral taxonomy is the virus family. All viruses in the same family share similar characteristics, such as genome type, presence or absence of an envelope, approximate size, etc. The vaccine development against a viral disease is based on the virus properties, but for each virus in the same viral family, the vaccine approach could be different due to the distinct transmission route and tropism.

**Table 2.1** Viral families related to human infections [16-18]

<b>Viral family</b>	<b>Virus</b>	<b>Structure</b>	<b>Genome</b>	<b>Disease</b>	<b>Licensed vaccine</b>
Adenoviridae	Adenovirus 4&7	Non-enveloped	dsDNA	Respiratory Disease	Live-attenuated
Bunyaviridae	Hantaan virus	Enveloped	ssRNA	Hemorrhagic fever	
Calciviridae	Norwalk virus	Non-enveloped	ssRNA	Gastroenteritis	
Coronaviridae	SARS coronavirus	Enveloped	ssRNA	SARS	
Filoviridae	Ebola virus	Enveloped	ssRNA	EVD	
Flaviviridae	Yellow fever virus; Dengue virus	Enveloped	ssRNA	Yellow fever; Dengue fever Hepatitis, primary hepatocellular carcinoma	Live-attenuated
Hepadnaviridae	Hepatitis B virus (HBV)	Enveloped	dsDNA		Subunit
Hepeviridae	Hepatitis E virus (HEV)	Non-enveloped	ssRNA	Hepatitis	Subunit (China)
Herpesviridae	Herpes simplex virus (HSV) -1&2; Varicella zoster virus (VZV)	Enveloped	dsDNA	Oral & genital sores; Chickenpox	Live-attenuated (for VZV)
Orthomyxoviridae	Influenza A&B virus	Enveloped	ssRNA	Flu	Live-attenuated, inactivated, subunit
Papovaviridae	Human papillomavirus (HPV) 6, 11, 16, 18, 31, 33, 45, 52, & 58	Non-enveloped	dsDNA	Cervical cancers, genital warts	Subunit
Paramyxoviridae	Measles virus; Mumps virus	Enveloped	ssRNA	Measles; Mumps	Live-attenuated
Parvoviridae	Human parvovirus B19	Non-enveloped	ssDNA	Erythema infectiosum, aplastic anemia	
Picornaviridae	Poliovirus; Hepatitis A virus (HAV)	Non-enveloped	ssRNA	Poliomyelitis; Hepatitis	Inactivated
Poxviridae	Variola virus	Enveloped	dsDNA	Smallpox	Live-attenuated
Reoviridae	Rotavirus	Non-enveloped	dsRNA	Diarrheal disease (in children)	Live-attenuated
Retroviridae	HIV type 1	Enveloped	ssRNA	AIDS	
Rhabdoviridae	Rabies virus	Enveloped	ssRNA	Rabies	Inactivated
Togaviridae	Rubella virus	Enveloped	ssRNA	Rubella	Live-attenuated

## 2.2 Virus characterization

### 2.2.1 Virus surface properties

Viruses contain a capsid, which is a shell made up of 20 standard amino acids and is packed with the viral genome [2]. There are many characteristic features of viruses, such as morphology, structure, surface roughness, and mechanical properties such as intrinsic elasticity, stiffness, brittleness, and resistance to material fatigue. Two of the most important properties are the hydrophobic and electrostatic surface properties of viruses, since the viral mobility and colloidal behavior in liquid medium are mainly governed by electrostatics and the hydrophobic effects [19-25]. The electrostatic forces belong to long-range interactions. The sign and magnitude of the forces are controlled by surface charges of viruses and target surfaces, and solution conditions such as pH, ionic strengths, etc. Hydrophobic interactions occurred at shorter separation distances and could play a major role when electrostatic interactions are the weakest. For example, high concentrations of salt solutions could screen virus surface charges.

In biotechnology manufacture, the processes can be separated into upstream processes and downstream processes. The upstream process is the first phase of bioprocess, focusing on biological materials inoculated and grown in cell culture to generate certain types of biological pharmaceutical products. The downstream process focuses on recovering, concentrating, and purifying the upstream bioproducts to meet quality requirements. The downstream unit operations such as hydrophobic interaction chromatography (HIC), and ion-exchange chromatography (IEC), are commonly used to remove virus contaminations in therapeutic products such as antibodies or other therapeutic proteins to ensure the safety of these biological pharmaceutical products by mammalian cells. Also, these unit operations are commonly used for purifying viral-based products as vaccines or gene therapy vectors. In either case, the viral surface properties, mainly surface hydrophobicity and charge play a crucial role in these highly selective, easy to scale-up, and interaction-based chromatography techniques in downstream bioprocessing operations [23, 24, 26-31]. To design the optimal parameters, such as pH, salt concentrations, and resin charge and hydrophobicity in chromatography operations, a detailed understanding of viral electrostatic and hydrophobic surface properties will benefit for either viral clearance in therapeutic products or maximum virus recovery in vaccine or gene therapy products.

In addition, with an advanced understanding of viral surface characteristics, the interactions of viruses with other molecules like osmolytes or polypeptides could be manipulated to target the viral particles specifically, to improve virus detection and vaccine formulation. Since virus detections to reduce contact with viral pathogens and vaccines to prevent disease are the most effective methods to prevent viral disease outbreak, public health could be likely improved with research on viral surface properties. The goal of this research is to save lives clinically and to reduce outbreaks of viral diseases.

### 2.2.1.1 Hydrophobicity

One important surface characteristic dominating virus interactions with other target substrates is the higher hydrophobicity of viruses as compared to many other biomolecules [32, 33]. The hydrophobic effect will minimize the area of contact between hydrophobic regions on the viruses and water molecules. The surface hydrophobicity of the virus mainly originates from nonpolar surface amino acids, which make up either the viral capsid protein or glycoproteins in the viral envelope. Among the 20 standard amino acids, aliphatic, and aromatic amino acids contribute to the heterogeneous hydrophobic patches on the viral surface [34]. The distribution of hydrophobic and hydrophilic residues on the PPV major capsid protein VP2 is shown in **Figure 2.1** [32]. The landscape of the hydrophobic residues determines the net surface hydrophobicity of the virus and governs its adsorption to other hydrophobic surfaces.

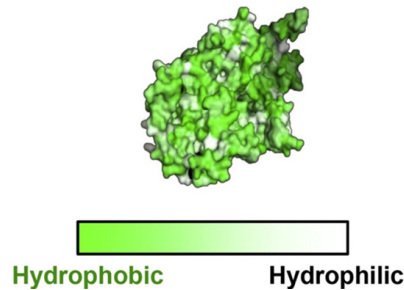


**Figure 2.1** Hydrophobic/hydrophilic residues on a PPV surface protein. Reprinted from [32] with permission.

In a study of MS-2 virus retention by microfiltration (MF) membranes, it was found that negatively charged virus can be absorbed to negatively charged polyvinylidene fluoride (PVDF) membranes in a 10-20 mM citrate-phosphate buffer at pH 7.0 [19]. It indicated that hydrophobic interaction played a major role in the virus-filter adsorption. Furthermore, the virus retention almost doubled with the addition of sodium chloride (NaCl) and calcium chloride (CaCl<sub>2</sub>) as compared to the no salt solution [19], likely due to increased hydrophobic interactions by salt ions. The salt ions can bind water molecules, reduce virus surface solvation, and expose the hydrophobic regions of virus and filter to facilitate virus-filter hydrophobic adsorption. If electrostatic interactions dominated, then the same charges would repel and impede adsorption, and the addition of salt would interrupt electrostatic interactions and reduce virus retention. Also, the difference of adhesion of three bacteriophages MS2, PRD1, and ΦX174 between a positively charged quaternary amine-modified membrane and a negatively charged sulfonic acid-modified membrane followed the relative hydrophobicity order ΦX174 < MS2 < PRD1 at high ionic strengths 100 mM sodium nitrate (NaNO<sub>3</sub>) solution, rather than surface charge densities order ΦX174 < PRD1 < MS2 [20]. It also indicated that the viral surface hydrophobicity dominated the interactions with charged membranes when electrostatic interactions are the weakest. Understanding virus surface hydrophobicity would provide insight into virus adsorption [25], purification [30], and virus detection [35], thus reducing experiments required.

### 2.2.1.2 Surface charge and isoelectric point (pI)

Another key surface property that governs colloidal behavior in the virus adsorption process is the surface charge, which is pH-dependent in polar media. One such measure of the viral surface charge is the isoelectric point (pI), which corresponds to the pH where the net charge on the whole viral particle is zero [36]. The surface charge of the virus mainly originates from the ionizable polar side chains of its surface amino acids, which make up for the viral capsid protein or glycoproteins of the viral envelope. Among the 20 standard amino acids, lysine, arginine, and histidine contribute to the protonated amine groups on the viral surface, while aspartic acid (or aspartate) and glutamic acid (or glutamate) contribute to the deprotonated carboxyl groups on the viral surface [34]. The excess of protonated or deprotonated functional groups of the charged amino acids highly contributes to the net surface charge of viruses, shown in **Figure 2.2** [37]. When environmental liquid pH is lower than the viral pI, the protonated functional groups are in excess, and the virus surface carries a net positive charge. At environmental liquid pH higher than the pI, the deprotonated functional groups are in excess, and the virus surface carries a net negative charge. In each case, viruses with the same charges repel each other. At the viral pI, the deprotonated carboxyl groups balance out the protonated amino groups, and the virus surface is charge neutral. The viral particles tend to form aggregates at their pI due to the repulsive interaction between viruses is the smallest [38].

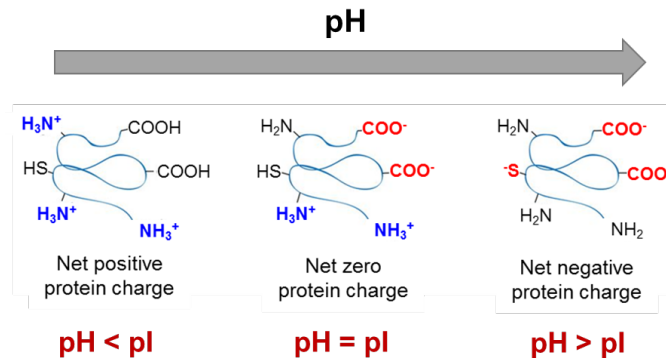


**Figure 2.2** Arrangement of functional groups on a viral surface protein. Reprinted [37] from with permission.

The surface charges of viral capsid proteins at a certain pH based on the dissociation constants of charged amino acids can be used for calculation of the virus pI using the Henderson-Hasselbalch equation [39]. However, current theoretical calculations of virus pI are commonly based on the whole amino acid sequence of the viral surface capsid proteins or glycoproteins. However, this approach does not consider protein folding. Only the surface amino acids actually contribute to the experimental pI, whereas all amino acids, even ones that are buried, contribute to the calculated pI. In addition, theoretical calculations do not consider the effects of chemical modifications (e.g., amino acids phosphorylated or acetylated) [40] or the effects of other structural components like viral enveloped lipid bilayer [41] on the electrostatic surface properties of viruses.

Viruses are rather complex systems, and their surface electrostatic properties need to be verified by experimental methods.

Knowing the surface charge and pI of a virus is very important, but there are limited data on the viral pI values [36]. The pI of a virus can be used to evaluate the electrostatic interaction between the virus and solid phase charged groups to predict the likelihood of virus attachment to a charged surface [23, 26-28]. The pI can also be used to create virus removal filters based on electrostatic adsorption [42, 43] and to eliminate empty virus capsids that lack nucleic acids during packaging from full virus particles by anion exchange chromatography for gene therapy purification [44]. Moreover, pI can be used to design complex coacervates, which are formed due to electrostatic interactions [45].

The relative contributions of hydrophobic and electrostatic forces to viral mobility and colloidal behavior in the liquid medium and their dependences on the viral surface properties are poorly understood. Thus, there is a need to explore general methods to characterize viral surface characteristics for better manipulation of virus interactions.

## **2.2.2 Traditional virus surface characterization methods**

There is no universal method to quantify the hydrophobicity of viruses. A direct comparison of the net surface hydrophobicity of different viruses could hardly be found in the literature [32, 33, 46, 47]. In addition, the majority of pIs of viruses measured experimentally in the literature are from 3.5-7 [36], viruses with very basic pI do not exist; however, the measured pI values of viruses for the same virus species by different characterization methods can vary widely. Various characterization methods have been employed to determine the surface characteristics of viruses, including HIC, aqueous two-phase system (ATPS) cross-partitioning, zeta potential, and isoelectric focusing (IEF).

### **2.2.2.1 Hydrophobic interaction chromatography (HIC)**

A HIC method has been established to measure the relative hydrophobicity of viral particles. HIC is based on the hydrophobic interactions between the target viral particles and hydrophobic ligands on the stationary phase of the chromatography column [32, 33]. Kosmotropic salt ions in the Hofmeister series have higher polarity and stronger binding to water molecules. As is shown in **Figure 2.3**, at high salt concentration, kosmotropic salt ions can facilitate the hydrophobic interactions between the hydrophobic patches on the viral surfaces and hydrophobic ligands on the stationary phase by excluding water molecules from the virus and ligand surfaces [48]. As a result, a virus–hydrophobic ligand complex is formed. The complex will be separated by disrupting the hydrophobic interactions that occur when the concentrations of kosmotropic salt in solution are lowered. At high concentrations of salt, the kosmotropic ions bind the water molecules, reducing viral particle solvation and increasing the hydrophobic interactions between biomolecules and chromatography ligands. By lowering the salt concentration, water molecules will be released from the kosmotropic ions, and the viral particles will be rehydrated and eluted from the hydrophobic bindings. With a linear or step gradient

that reduces the salt concentrations, hydrophilic proteins can be eluted first at high salt concentrations, while hydrophobic viral particles will be eluted later at lower salt concentrations. This simple high-salt HIC method can be performed on either high-performance liquid chromatography (HPLC) or fast protein liquid chromatography (FPLC) systems.

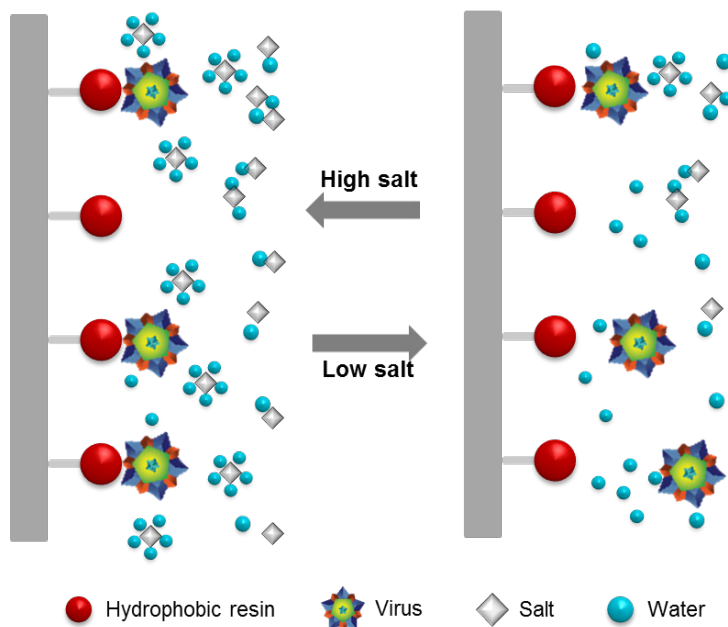


**Figure 2.3** Hydrophobic interaction chromatography.

To quantify the relative hydrophobicity, either retention time or elution salt concentration can be normalized in a simple 0-1 relative hydrophobicity scale. HIC has been used to characterize the surface hydrophobic properties of three different bacteriophages and four mammalian viruses [33]. By designating the highest concentration of salt eluted protein RNase as reference 0, relative hydrophobicity values could be used to indicate and compare the net hydrophobicity of viruses [33, 46]. A HIC with a Tosoh Phenyl 750M resin on an FPLC by a step gradient of 0.8 M sodium citrate at pH 8.0 was able to rank the relative hydrophobicity of viruses from low to high:  $\Phi$ X174 phage < PP7 phage < Minute virus of mice (MVM) < PR772 phage = Reovirus-3 < Xenotropic murine leukemia virus (XMuLV)  $\leq$  Pseudorabies virus [33]. In addition, the peak spreading in the elution of viruses reflected some heterogeneity in their hydrophobicity profiles. The HIC with a Tosoh Phenyl 5PW resin on an HPLC by a step gradient of 0.5 M sodium citrate at pH 8.0 was also used to compare the hydrophobicity of an infectious MVM and a non-infectious MVM virus-like particle (MVM-VLP), with the same control protein RNase as reference 0. The VLP is a non-infectious, multi-proteins structured molecule that resembles the authentic virus, maintaining the same surface characteristics and conformation and can be self-assembled by recombinant expression of the viral capsid protein. The relative hydrophobicity values were 0.28 and

0.35 for MVM and MVM-VLP, respectively, showing that MVM-VLP is more hydrophobic than the MVM [46].

In addition, an adsorption glass column using Octyl Sepharose-4 fast flow resin in an adsorbing solution (10 mM imidazole and 4 M NaCl) at pH 7 was used to characterize the viral surface hydrophobicity by eluting the viral particles by decreasing the NaCl concentrations [47]. The elution rates of viruses were determined by plotting the cumulative eluted percentage of adsorbed viruses as a function of solution ionic strengths to compare the hydrophobicity of different viruses [47]. Viruses that eluted the fastest had the lowest surface hydrophobicity, while for the viruses that eluted the slowest was the most hydrophobic. The rank of measured viral hydrophobicity from hydrophobicity of viruses from low to high are  $\Phi$ X174 phage < coxsackievirus B4 (CB4) < echovirus 1 (E1) < CB 5 < E4 < poliovirus 1 (P1) < CB3 < T7 phage < T3 phage < f2 phage < E5 < MS2 phage [47]. The same method was also used to characterize the surface hydrophobicity of bacteriophages by another research group, showed that MS2 and T4 are hydrophobic viruses while  $\Phi$ X 174 is more hydrophilic [22], which is consistent with the previously published result [47].

HIC is a simple and reliable method to characterize the hydrophobicity of non-destructive viral particles, and the eluted fractions allow for distinguishing the infectious versus non-infectious viral particles by further virus detection techniques. However, it requires the same protein reference or same chromatography column resins to quantify the relative hydrophobicity values and to compare the hydrophobicity degree of different viruses. Moreover, viruses won't elute off of HIC sometimes due to the high hydrophobicity [32], and chromatography takes a lot of samples.

#### *2.2.2.2 Aqueous two-phase system (ATPS) partitioning method*

A biomolecule partitioning method using ATPS can also be used to measure the surface hydrophobicity and pI. ATPSs are formed by mixing water-soluble polymers or a water-soluble polymer and a salt beyond a critical concentration resulting in two immiscible aqueous phases [49]. ATPS polymer-polymer (e.g polyethylene glycol (PEG)-dextran) [50] or aqueous polymer-salt (e.g PEG-citrate) [51, 52] can be used to preferentially partition biomolecules. This method has been extensively used for separation and purification of biomolecules [51-55], but a few studies characterize the surface properties of biomolecules [49, 50]. Unlike other methods requiring expensive equipment and chemicals and complex procedures, this method is simple and inexpensive. The main driving forces for biomolecules interactions between the two phases are hydrophobic and electrostatic interactions, so the surface properties could be characterized by evaluating the partition behavior [52].

An ATPS partitioning method containing PEG-dextran was reported to characterize the surface hydrophobicity and isoelectric point of various groups of streptococci and staphylococci bacteria [50]. To increase the selectivity of polymers, hydrophobic and charged groups were covalently bound to the PEG polymer. The relative surface hydrophobicity was determined by comparing the partitioning of bacteria in the systems comprising PEG, PEG palmitate (P-PEG), or PEG stearate (St-PEG) [50]. Palmitate and stearate addition to PEG differentiated the degree of hydrophobicity of the



PEG-rich phase. The higher the surface hydrophobicity of bacteria, the higher the hydrophobic affinity of bacteria towards the PEG-rich phase. A relative surface hydrophobicity affinity index was determined to be streptococci group A > streptococci group C&G > staphylococci [50]. In a similar study, the partitioning of bacteria in the system containing positively charged trimethylamino PEG (PEG-TMA) was compared to the system containing negatively charged PEG sulfonate (PEG-S) at different pH [50]. The study demonstrated that the attractive forces of the bacteria towards the PEG-rich phase containing PEG-TMA gradually increased with pH above pI; thus, the partitioning increased in the PEG-rich phase. On the contrary, the repulsive forces between bacteria and the PEG-rich phase containing PEG-S increased with the pH, thus diminishing the partitioning of bacteria in the PEG-rich phase. The pH at which the partitioning trend in PEG-TMA intersected with the PEG-S trend was determined to be the pI of bacteria [50].

Though this method can hardly compare the relative hydrophobicity defined by different ATPS systems, the pI of biomolecules should not be affected by different combinations of ATPS composition. Also, a cross-partition using the same PEG-dextran system but with two different salt compositions sodium sulfate ( $\text{Na}_2\text{SO}_4$ ) and NaCl was used to determine the pI of four different proteins serum albumin, hemoglobin, transferrin, papain [56]. The partition coefficient, which was defined as the protein absorbance at the top phase to that at the bottom phase, was plotted against different solution pH. The cross-point of the two curves of different salt compositions was used to determine the pI values of proteins. Proteins which carried a more negative charge had higher partition coefficients in  $\text{Na}_2\text{SO}_4$  than in NaCl [56]. This ATPS cross-partition method showed its promise for determining the pI of viral particles, but it is an indirect and not a common method for characterizing viral surface chemistry. The high concentrations of salt and polymer in ATPS could produce a big osmotic shock to the viral particles that might lead to structural deformations of the viral particles [57]. Thus, this method has been used less commonly.

### 2.2.2.3 Zeta potential

When a charged viral particle is in a polar liquid, an electrical double layer forms around the particle. As shown in **Figure 2.4** [58], the inner layer is referred to a “Stern layer”, which contains a rigid layer of counter-ions attached to the charged particle, and the outer layer is referred to as a “diffuse layer”, which is a loose outer layer of free ions in liquid attracted to the Stern layer. When the charged viral particle moves in the liquid, an effective boundary exists between the ions in the diffuse layer that move together with the virus and ions that remain with the bulk liquid, known as the “slipping plane”. Zeta potential is the electric potential from the “slipping plane” relative to a point in the bulk fluid far away from the particle.

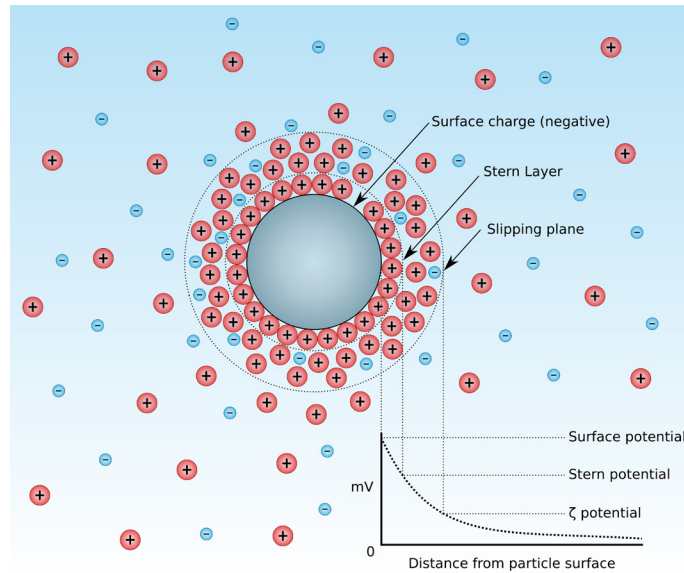


**Figure 2.4** Electrical double layer and zeta potential. Reprinted [58] from with permission.

Zeta potential, a measure of surface charges of virus particles, can be assessed through the electrophoretic mobility of particles, which is defined by the ratio of the drift velocity of particles and the applied electric field [59]. Zeta potential is typically measured by either microelectrophoresis [60] or electrophoretic light scattering (ELS) [61]. Microelectrophoresis involves the placement of a virus suspension in a known ionic strength buffer into an electrophoresis cell, which is subjected to an electric field. The time it takes for viral particles to move over a given distance in the constant electric field is monitored by fluorescent microscopy [60]. The drift velocity could be used to calculate the electrophoretic mobility by **Equation 2.1** [59]. Although it is a reliable method to measure the electrophoretic mobility and can further estimate the zeta potential, it is too labor-intensive and time-consuming to track individual viral particles over time.

$$\mu_e = \frac{v_d}{E} \quad (2.1),$$

where  $\mu_e$  is the electrophoretic mobility,  $v_d$  is the drift velocity, and  $E$  is the electric field strength.

To overcome these disadvantages, the rapid and simple method of ELS can measure the electrophoretic mobility. ELS has a continuous oscillation of the poles of an electrical field applied by electrodes to oscillate charged biomolecules. This oscillation leads to the scattered light intensity fluctuation proportional to the electrophoretic mobility of the particles. The fluctuation of scattered light intensity is detected as a frequency shift on the spectrum by a photodetector and further converted into the magnitude of the drift velocity of particles. Then electrophoretic mobility could also be measured by **Equation 2.1**.

Zeta potential could be further calculated from the electrophoretic mobility measured either by microelectrophoresis or ELS by the Henry equation [62], as shown in **Equation 2.2**.

$$z = \frac{3\mu_e\eta}{2\varepsilon f(k\cdot\alpha)} \quad (2.2),$$

Where  $z$  is the zeta potential,  $\eta$  is the viscosity of the medium,  $\mu_e$  is the electrophoretic mobility,  $\varepsilon$  is the dielectric constant of the medium, and  $f(k\cdot\alpha)=1.5$  known as the Smoluchowski approximation [63], valid for large macromolecules, like viral particles, in polar media, when the ratio of particle radius ( $\alpha$ ) to thickness of double electric layer ( $1/k$ ) is very large.

Both electrophoretic mobility ( $\mu_e$ ) and zeta potential as a function of pH can be used to characterize the viral surface charge and determine the pI of the virus at which either the  $\mu_e$  or zeta potential is zero [22, 61, 64, 65]. The characterized electrostatic properties of viruses are shown in **Table 2.2**.

The  $\mu_e$  can be used to characterize the viral surface charge and estimate the pI of the virus, and it is affected by solution ionic strengths [20]. To compare the absolute value of the  $\mu_e$ , the surface charges of viruses from low density to high density are  $\Phi X174 < PRD1 < MS2$  [20]. They all carried a negative charge at the neutral pH. The pI values of an MS2 bacteriophage was further determined to be  $\sim 3.5$  [65]. The absolute value of the  $\mu_e$  decreased when increasing the salt concentration at a fixed pH [65]. It was due to the salt screening effect of particle charges by more ions present in the solution. The  $\mu_e$  measurement should be conducted in a rather low ionic strength of buffer solutions to maximize the electrical double layer. Besides, the  $\mu_e$  profiles as a function of solution ionic strengths for MS2 phage and its VLPs are different when determined by different virus purification methods [66]. The residual impurities existed in the tested virus solutions can either become the charged target for measurement, or the impurities can bind to viral particles surface. Furthermore, different virus propagation methods have been shown to affect the  $\mu_e$  of MS2 phage [64]. Negative  $\mu_e$  over the entire pH range resulted in no measured pI on agar propagation [64]. It might due to the purification incompletely eliminated the agar impurities like agaropectin.

**Table 2.2** The electrostatic properties of viruses by different characterization methods

Characterization principle	Target	Electrostatic property	Method conditions	Reference
Electrophoretic mobility ( $\mu_e$ )	$\Phi$ X174 phage	$\mu_e$ -1.6 to -1 ( $10^{-8} \text{ m}^2 \text{ V}^{-1} \text{ s}^{-1}$ )	1-100 mM sodium nitrate (NaNO <sub>3</sub> ) solutions at pH 7	[20]
	PRD1 phage	$\mu_e$ -1.8 to -1 ( $10^{-8} \text{ m}^2 \text{ V}^{-1} \text{ s}^{-1}$ )		
	MS2 phage	$\mu_e$ -3.5 to -1 ( $10^{-8} \text{ m}^2 \text{ V}^{-1} \text{ s}^{-1}$ )		
	MS2 phage	pI ~3.5	1-100 mM NaNO <sub>3</sub> solutions at various pH	[65]
	MS2 phage	$\mu_e$ profile varies with different purification methods	1-100 mM NaNO <sub>3</sub> solutions at pH 7, different virus purification methods	[66]
	MS2 VLP			
	MS2 phage	pI ~3.6 (broth); Negative $\mu_e$ , pI N/A (agar)	1 mM NaCl solution at various pH, different virus propagation methods (broth or agar)	[64]
Zeta potential	Norovirus GI.1 VLP	pI 4.25	20 mM citrate phosphate buffer at various pH	[61]
	Norovirus GII.4 VLP	pI 4.16		
	Feline calicivirus VLP	pI 3.9		
	T4 phage	pI 2 (7.7 mM KCl solution)	0.002, 2.6, and 7.7 mM potassium chloride (KCl) solutions at various pH	[22]
	$\Phi$ X 174 phage	pI 2-2.6 at 0.002-7.7 mM KCl solution		
Isoelectric focusing (IEF)	Tomato Bushy Stunt Virus (TBSV)	pI 4.1	Agarose gel-based strip	[67]
	TBSV (CP-6XD)	pI 3.2		
	TBSV (CP-4XCys)	pI 5.0		
	TBSV (CP-4XHis)	pI 8.2		
	TBSV (CP-Au)	pI 8.5		
	Full rat parvovirus	pI 5.8-6.2	Agarose gel-based strip	[44]
	Empty rat parvovirus	pI 6.3		
	Norovirus Funabashi VLP	pI 5.9	Solution-based capillary	[68]
	Norovirus Norwalk VLP	pI 5.9		
	Norovirus Seto VLP	pI 6.0		
	Norovirus Hawaii VLP	pI 6.0		
Norovirus Kashiwa VLP	pI 5.5			
Norovirus Narita VLP	pI 6.9			
Chromatofocusing	MVM	pI 5.99	[46]	

MVM-VLP	pI 5.81	Nonporous ethylvinylbenzene/divinyl benzene (EVB-DVB) copolymer resin grafted with carboxylic acid with an HPLC	
$\phi$ X174 phage	pI 6.7-7.0	Nonporous EVB-DVB copolymer resin grafted with tertiary amine	[69]

Zeta potential has also been shown to estimate the pI values of viruses. The measured pI values of norovirus and feline calicivirus VLPs match with the aggregation behavior near their pIs detected by DLS [61]. However, zeta potential measurements can also be affected by the solution ionic strengths. Zeta potential as a function of pH curves for T4 and  $\Phi$ X 174 bacteriophage varied at different ionic strengths of solutions [22].

Both  $\mu_e$  and zeta potential characterize the viral electrostatic properties. However, the measured results could be affected by the ionic strengths of solutions [22, 65], different virus propagation [64], and purification methods [64, 66]. The  $\mu_e$  and zeta potential measured by either microelectrophoresis or ELS also require a large amount of highly purified and concentrated virus solutions, which are typically very expensive.

#### 2.2.2.4 Isoelectric focusing (IEF)

To overcome the limitations of  $\mu_e$  and zeta potential, a small-scale of electrophoretic technique, isoelectric focusing (IEF), has also commonly been used to determine the viral pI. IEF is an electrophoretic technique based on the separation of zwitterionic molecules, such as viral particles and proteins, according to their pIs [70]. A virus sample is introduced into an immobilized pH gradient under the influence of an electric field. The pH gradient increases from the anode (positively charged electrode) to cathode (negatively charged electrode). The viral particle will carry either a positive charge if in a pH region below its pI or a negative charge if in a pH region above its pI and can migrate according to their surface charge towards the oppositely charged electrode in the stable pH gradient. The overall charge of the viral particle will decrease until it reaches the pH position that corresponds to its pI when it carries a net zero charge. Since viral particles will not be electrically attracted to either electrode, the migration stops, and the viral particles are focused into narrow bands, indicating their pI values [71]. The bands can be visualized by silver staining. IEF can be performed in a variety of formats, gel-based strip IEF and solution-based capillary IEF are the most commonly used to determine the pI of a virus [67, 68, 70]. The pI of viruses determined by IEF can be found in **Table 2.4**.

An agarose gel-based strip IEF was used to predict the movement of wild type TBSV and its derivatives in host plants by measuring corresponding viral pI values [67]. The same gel system was used to determine the pI of full and empty rat parvovirus particles, and the difference of pI was further used to purify full viral particles from its empty particles by a weak DEAE anion exchange chromatography [44]. In addition, a capillary IEF was used to determine the pIs of noroviruses VLPs to be 5.5-6.9, which can

be further used for virus detection with whole column imaging techniques [68]. However, the detected pIs are not consistent with the pIs of norovirus VLPs by zeta potential, which is 4.16-4.25 [61]. It might be due to the IEF measure both the internal and external amino acids, while the zeta potential only measured the external surface charge.

IEF has been shown to be a simple and inexpensive method to determine the virus pI and need only a small amount of virus samples. However, this method typically requires long and complicated experimental steps and has difficulty characterizing more hydrophobic viruses due to low solubility inhibiting their migration [67, 68, 72].

To overcome the difficulty of characterizing hydrophobic viruses, an IEF on the ion-exchange column technique known as chromatofocusing has been developed to determine the pI of viruses. The results can be found in **Table 2.2**. Instead of using the applied electric field, chromatofocusing uses a retained, self-generated pH gradient by running buffers with chromatography. The chromatographic technique, chromatofocusing, can be used to determine the pI of virus based on elution pH and retention time [69]. The pH at which viruses eluted from the column at several runs of ionic strengths was used to calculate the true pI of the virus [69] by an established multiple charge state (MCS) mathematical model [69, 73]. Chromatofocusing using a weak cation-exchange determined the pI of an MVM and an MVM-VLP [46]. In addition, chromatofocusing using a weak anion-exchange column estimated the pI of a bacteriophage  $\phi$ X174 [69].

HIC, ATPS cross-partitioning, zeta potential, and IEF are used for characterizing the surface properties of viruses. However, they are bulk measurements and limited by the purity of the virus samples [64, 66] and solution conditions [22, 50, 61]. Impurities either from virus propagation or purification in virus solutions can affect the surface characterization by two possible approaches. First, the measured result could depend on the impurities rather than the viral particles if the virus concentrations are too low while impurities are in relatively high concentration [36]. Second, the measured result could be the alternated viral surface properties if impurities are in low concentration but can bind to or shield the viral surface [36]. In addition, except for IEF, these methods require a large volume of purified virus samples, of which the cost is high. IEF does not need a high volume of virus samples, but it has difficulty characterizing more hydrophobic viruses with low solubility. Besides, silver staining or a fluorescent label needs to add to the high concentration of the virus sample. Moreover, all of these methods cannot distinguish individual viral particles with different properties from the average viral particle population. Thus, there is a need to explore an inexpensive, robust, reliable, and single-particle technique to characterize viral surface properties.

### **2.2.3 Novel surface characterization: chemical force microscopy (CFM)**

A novel surface characterization method, chemical force microscopy (CFM) [74], which uses an atomic force microscope (AFM), can be used for single-particle viral surface characteristics. AFM is an imaging tool with a sub-nanometer resolution, which uses a probe to scan a sample surface to get the surface topography. The AFM probe is a microcantilever with a very tiny tip mounted at one end. Functionalization of the AFM probe tip with well-defined functional groups enables AFM to measure molecular

interactions between a modified AFM tip and a sample, as CFM. CFM can provide information on the chemical natures of the measured samples.

CFM has many advantages for the virus surface characterization over traditional surface characterization methods. One significant advantage of CFM over other microscopic methods, such as electron microscopy and scanning tunnel microscopy, is that the study can be performed in physiological aqueous solutions without disturbing the natural state of the virus [75], avoiding complex samples preparations like staining [76] and coating with conductive material [77], as required for electron microscopy. In addition, the CFM can precisely target the virus particles over other impurities [78], which lays the foundation for a single-particle measurement. Moreover, CFM requires low amounts of biological samples [79], which can overcome the disadvantages of bulk characterization methods, which consume large amounts of purified viruses. Other advantages of CFM include high spatial resolution of a few nanometers [80], sensitive force resolving capacity of a few piconewtons [81], and simultaneous force probing and biochemical sites locating features [82].

### *2.2.3.1 Fundamental principles of atomic force microscope (AFM)*

An AFM consists of a mounted cantilever with a tiny tip at its free end, a laser beam from a diode directed to the back of the mounted cantilever, a quadrant photodiode detector measuring the reflected beam, a piezoelectric translator sample stage, an electronic feedback loop by a controller, and a computer with software processing the signals to images or force curves, as shown in **Figure 2.5** [83]. An AFM operates by scanning an AFM tip over a sample and measuring the deflection of the cantilever due to the tip interacting with the samples [84]. A sample is fixed on a flat piezoelectric translator stage which controls the sample movement along with horizontal (x-y) and vertical (z) directions during scanning [84, 85]. A laser beam impinges on the backside of the cantilever and is reflected to a photodiode detector [84, 85]. The detector amplifies the deflection of the cantilever. The z displacement at each scanned (x,y) point is recorded and plotted, yielding a three-dimensional topographic image [84, 85].

To obtain topographic images, the AFM can operate in two basic modes, contact and tapping mode [80, 84]. In contact mode, an AFM cantilever is brought into gentle contact with the sample surface. The normal force between the tip and sample is dependent on the tip-sample distance and keeps constant during the image scanning [84]. When an AFM tip passes over a point (x,y), which has an increased height, the tip-sample distance is reduced, and so the tip-sample force is increased. The increased force will result in an upward deflection of AFM cantilever and is detected by the photodiode detector. It will trigger the feedback system to restore the pre-set force by controlling the piezoelectric stage to move the sample away from the probe along the z-direction. The z displacement equals the height of that point (x,y), and the height of each point on the sample within a scanned area will be determined to form a topographic image. The imaging mode is very simple and favorite for a flat rigid surface in liquid, but not ideal for soft biological samples, like viruses, due to relative high lateral forces that would easily damage the samples [80].

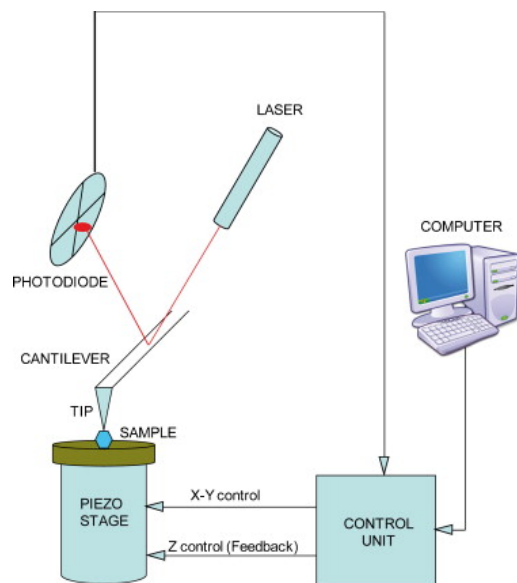


**Figure 2.5** Components of a typical atomic force microscope. Reprinted from [83] with permission.

To reduce the dragging forces due to the lateral sample movement and minimize the biological sample damage, the alternative tapping mode is more appropriate for imaging viruses. Instead of continuously touching the sample surface, the AFM cantilever oscillates near its resonance frequency across the samples. The amplitude of the oscillation is set to be constant [84]. When a tip scans a point  $(x,y)$ , which has an increased height, the amplitude will decrease, and the feedback loop will restore the pre-set amplitude by moving the piezoelectric sample stage to record the height [80].

In AFM topographic images, height information can reflect the true size of the sample, but not a lateral dimension. When a tip scans a sample, and only one side of the tip touches the sample, the cantilever begins to deflect before the tip apex actually reach the sample. Similarly, the other side of the tip still contacts the sample, and the cantilever bends even after the tip apex has passed the sample. As is shown in **Figure 2.6A** [80], the measured lateral dimension is larger than the actual lateral size of the sample. Thus, the sharper the tip, the greater lateral resolution could be achieved. Besides, an AFM cantilever with low stiffness might be ideal in contact mode to minimize the damage for the samples, while a cantilever with high spring constant is preferred in tapping mode to reduce the instabilities and noise.



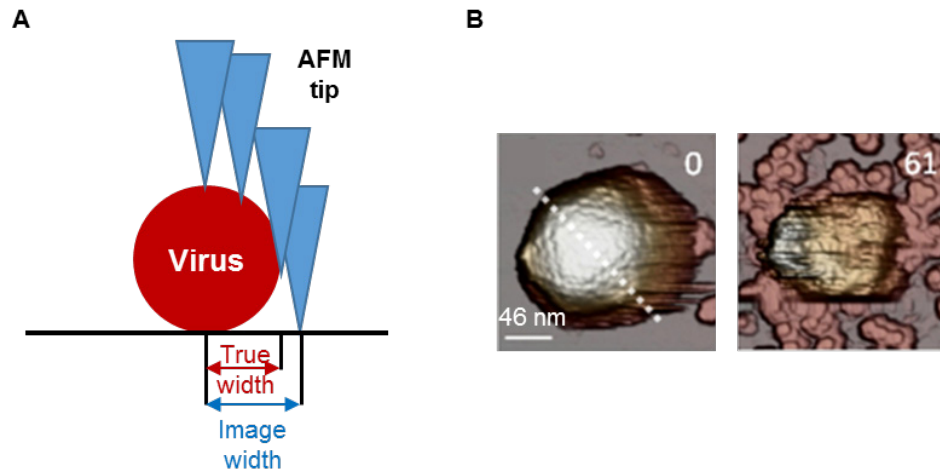


**Figure 2.6** AFM imaging. (A) Schematic illustration of the lateral dimension of scanned samples affected by the shape and size of AFM tip, and (B) adenovirus before and after repeated loading of 100 pN force 61 times, reprinted from [88] with permission.

As an imaging tool, AFM has been extensively used to study the morphologies of biomolecules ranging from the sub-nanometer-scaled proteins [86] to micron-sized living cells in liquid close to its physiological conditions [87]. One major use of AFM is to visualize single viruses and their structural components [80] and dynamic structural changes [88]. As shown in **Figure 2.6B** [88], an intact icosahedral symmetric viral capsid structure of adenovirus and the details of repeating protein subunits (capsomers) on the virus could be seen in the left, while in the right, the disruption of adenovirus capsid and release of the viral genome due to stress is observed by the real-time AFM topographic images. The images of structure changes could help further identify the mechanical properties of viruses.

### 2.2.3.2 Force measurement (approach curve vs. withdraw curve)

AFM is not only a high-resolution image tool to provide virus structure information, but also an excellent characterization method for mechanical properties and surface chemistry of viruses due to its force measurements functions. The interactions between the tip and sample can be measured by the deflection of the AFM cantilever as a function of sample z displacement during the AFM tip approach and withdrawal cycle [89]. A typical force curve is shown in **Figure 2.7A** [90]. Approach and withdraw curves can be roughly divided into four regions [90]. Region I, when an AFM tip is far from a sample, no interactive force can be observed between the tip and the sample. With closer distances (region II), the AFM probe will be pulled into contact with the sample by van der Waals attraction forces. The jump-to-contact occurs when the gradient of the interactive force exceeds the spring constant of the cantilever. After contact with the sample (region III), the AFM cantilever will have a positive deflection due to the repulsive interaction between the tip and sample. This is the region on the approach curve where the elastic properties of the sample can be measured. The tip will approach the

sample until a pre-set force threshold is reached. Afterward, the AFM tip will change direction and move away from the sample, and the AFM cantilever will have a negative deflection due to adhesion. Region IV, when the cantilever restoring force exceeds the adhesion between the AFM tip and sample, jump-off-contact occurs. If the AFM tip has been modified with chemical functional groups, then the chemical interaction formed during contact with the sample will bend the cantilever during withdraw more than its initial deflection during the approach. The finite force required to pull the AFM probe off the surface of the specimen is the interested adhesive force by CFM. Region IV on the withdraw curve is where the surface chemistry of the sample can be measured. After jump-off the sample, the tip returns to the initial zero force region I.

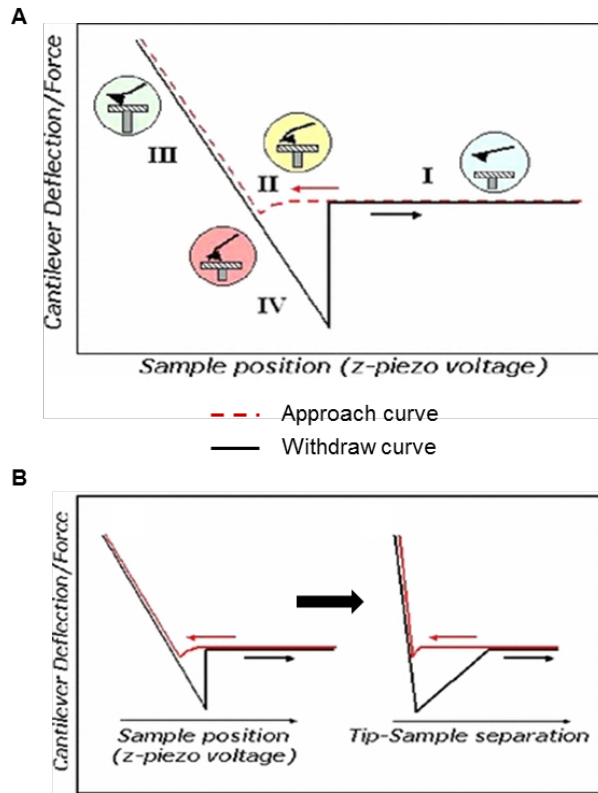


**Figure 2.7** AFM force curves. (A) Approach and withdraw curves four regions, zero force region I, non-contact approach region II, contact region III, and non-contact withdraw region IV, and (B) conversion of F-Z curve to F-D curve. Reprinted from [90] with permission.

The forces between the AFM tip and samples can be measured by the deflection of the AFM cantilever during the sample approach and withdrawal [89]. The deflection can be converted into force using Hooke's law, shown in **Equation 2.3** [91].

$$F = -k_c d \quad (2.3),$$

Where  $F$  is the force,  $k_c$  is the spring constant of AFM cantilever, and  $d$  is the cantilever deflection.

The AFM directly measures the cantilever deflection as a function of sample z-piezo displacement, and the actual tip-sample distance or separation is given by **Equation 2.4** [91].

$$D = Z - d \quad (2.4),$$

Where  $D$  is the actual tip-sample distance or separation,  $Z$  is the distance between the sample surface and the rest position of the cantilever.

Therefore, a raw force-z displacement curve will be converted to a force-distance (F-D) curve, as shown in **Figure 2.7B** [90]. Commercial AFM cantilever spring constants can range from 0.01 to 100 N/m, enabling the force sensitivity down to 10 pN [90].

The majority of force studies on viruses are performed by nanoindentation [78, 92-94] using the approach curve. Nanoindentation is achieved by pushing the viral particles, so the cantilever will bend and result in an approach curve, to study the mechanical response of viral particles. After tip contact with the viral particle, the particle will progressively indent by increasing the z-displacement, resulting in a repulsive force bending the cantilever, and an almost linear approach curve on the soft viral surface. The approach curve reflects the stiffness and intrinsic elasticity of the viral particle [83]. When the indentation depth exceeds its elastic limit, the viral particle will break and result in an irregular approach curve with an upward slope. The rupture force of viral particles could be determined to indicate structural strengths, as opposed to brittleness [83]. In addition, the resistance of viral particles to material fatigue could be determined by the number of indentations withstanding the controlled low-force approach before structure damages occur [83].

The withdraw curve during the force measurements on virus particles can provide information on virus surface properties using CFM. In theory, CFM can measure molecular interactions from strong covalent bonds (~100 nN) to weak van der Waals force [74] (~1 pN), which is a suitable option for measurement of the hydrophobic or electrostatic interactions between virus particles and modified AFM tips with corresponding chemistries. CFM enables one to characterize virus surface properties at a single-particle level with less consumption of samples [79].

By modifying the AFM tip with a chemical functional group, CFM has been reported to study the surface charges of a single *S. cerevisiae* cell with a carboxyl acid (COOH) functionalized AFM probe [95]. The surface charges of the microbial cell are explored by the adhesion force at different solution pH from 3 to 10, as shown in **Figure 2.8A** [95]. Different force curves observed with the same chemical group functionalized probe and cell surface at different pH liquid environments could be due to a change of ionization state of the carboxyl groups modified AFM probe and single *S. cerevisiae* cell surface. No adhesion observed at pH greater than 6 is likely due to the electrostatic repulsion between the negatively charged carboxyl terminated probe and the negatively charged single *S. cerevisiae* cell. Whereas, the adhesion force observed at pH less than 5 is likely because of the positively charged cell surface attracting the negatively charged COO- terminated probe. In addition, CFM has been reported to study the surface hydrophobicity on microbial pathogen *Aspergillus fumigatus* with a hydrophobic methyl (CH<sub>3</sub>) group modified AFM probe, as shown in **Figure 2.8B** [82]. A CFM adhesion map was recorded simultaneously with the topographic image, which allows accurately locating the hydrophobic R region and hydrophilic P region on the pathogen surface. The

difference of surface hydrophobicity between the R and P region was also confirmed with the F-D curve, showing the R region had strong adhesion with the hydrophobic CH<sub>3</sub> probe, while no adhesion for P region.

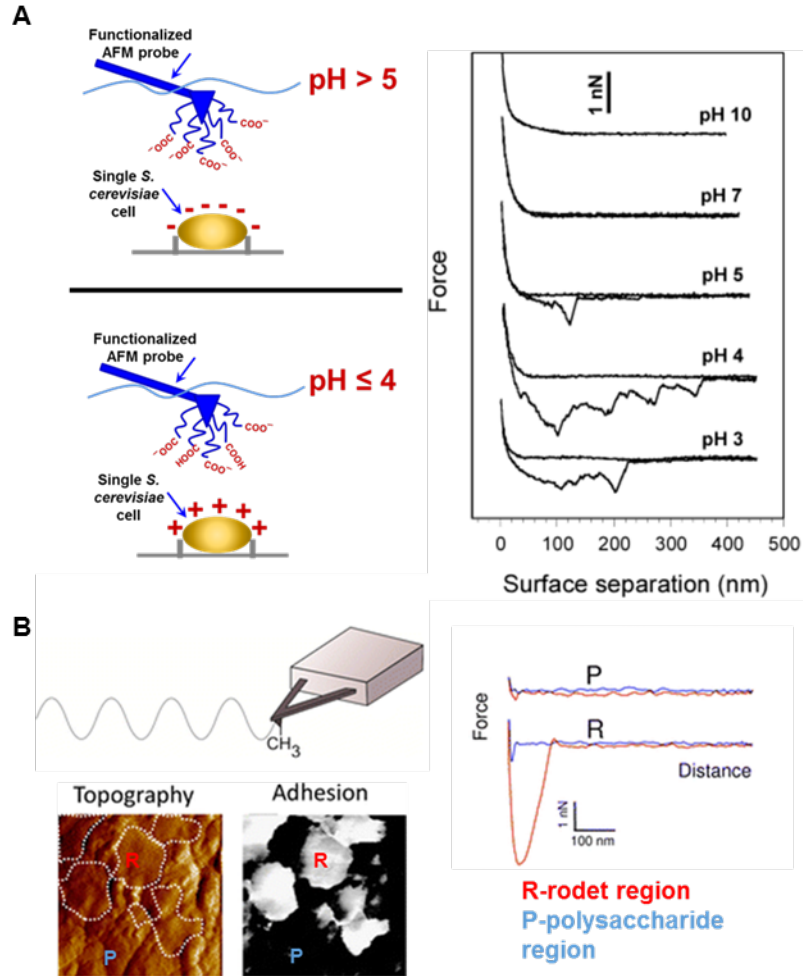


**Figure 2.8** CFM characterization of surface properties (A) Characterizing *S. cerevisiae* cell surface charges recorded in 1 mM KNO<sub>3</sub> solutions of varying pH between the surface of yeast cell and a carboxyl group modified probe. Reprinted from [95] with permission. (B) Characterizing *Aspergillus fumigatus* surface hydrophobic and hydrophilic regions recorded in acetate buffer between the surface of pathogen and a methyl group modified probe. Reprinted from [82] with permission.

Alternatively, the AFM probe could be modified with target biomolecules to interact with a chemical functional group modified substrate. CFM has been reported to explore the surface charge and to measure the pI values of various proteins bovine serum albumin (BSA), fibrinogen, myoglobin, and ribonuclease A to be 4.5-5.0, 5.5-6.0, 6.5-7.0, and 9.5-10, respectively [79]. In this research, they modify the AFM with each protein and use the modified probe to pull forces on two positively charged substrate at various solution pH. The inflection point on the curve of adhesion forces as a function of

solution pH was used to denote the pI of the corresponding protein. Besides, a fungal pathogen cell modified AFM probe has been used to explore the surface hydrophobicity of different fungus. An AFM probe either modified with a wild-type *Candida glabrata* or a mutant strain with epa6 surface protein deletion to pull force on a hydrophobic CH<sub>3</sub> group modified substrate in solution [96]. From the adhesion force histograms from recording 100-400 F-D curves, they found 30-50 nN for the wild-type strain, almost zero adhesion for the mutant strain, and concluded that strong hydrophobicity of wild-type *Candida glabrata* cells was mainly due to its surface epa6 proteins [96].

CFM is suitable to study the surface chemical interactions of soft biological molecules, showing its potential for application in viral particles. Virus particles are easy to find in the AFM but hard to measure if they are on the tip. Therefore, CFM with the AFM probe terminated with a chemical functional group and viral particles on a surface was used in my research on characterizing virus surface properties. In this approach, CFM can detect the surface chemistry of viral capsids at a single particle level. This way has the potential to determine the heterogeneity of a virus population and the effect of virus purification on that population.

More details of the CFM method, including AFM probe modifications, sample immobilization, and measurements of virus surface properties, can be found in **Chapter 3**. Virus surface properties can be used to manipulate viruses and play a key role in virus interactions with other targets, but there is very limited information in the literature on viral surface properties. With a thorough understanding of virus surface chemistry characterized by the single-particle technique CFM, virus detection, and thermal stability could be significantly improved to target viral particles specifically.

## 2.3 Virus detection

### 2.3.1 Past and current virus detection methods

#### 2.3.1.1 Transmission electron microscopy (TEM)

Transmission electron microscopy (TEM) can visualize a 2-dimensional internal and external viral structure. It was a predominant method for virus detection due to its magnifying power (5,000,000×) [97] to reveal structures inside viruses for identification. The virus sample preparation typically required a staining procedure with heavy metals salts (such as uranyl acetate or phosphotungstic acid) [76] to increase the contrast of viral particles against its background.

The use of TEM for viral detections contributed to the discovery of many types of viruses such as adenovirus, enterovirus, paramyxovirus, and reovirus isolated from cell cultures inoculated with clinical viral samples [98]. In addition, the TEM works as a characterization tool to confirm the presence of viruses visually since it can reveal internal virus morphological information, such as the presence or absence of an envelope, nuclear acid, spike, capsid symmetry type, size, and shape. An example of TEM to identify empty adeno-associated virus (AAV) capsids, which lack genome during packaging, from full AAV capsid, is shown in **Figure 2.9** [99]. Full AAV particles are impermeable to the heavy salt uranyl acetate, as shown in **Figure 2.9A**, while empty AAV particles lack DNA exhibiting a ring-like morphology, as shown in **Figure 2.9B**. AAV particles are observed as 25 nm spheres by TEM.

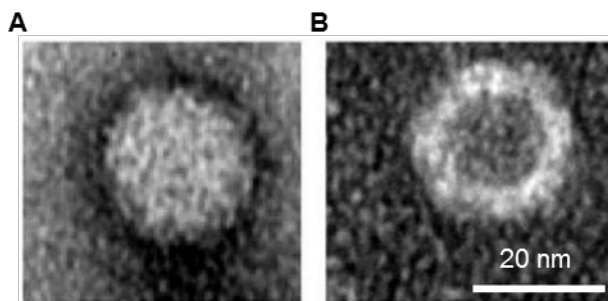


**Figure 2.9** TEM images of uranyl acetate negative stained AAV2. (A) Full AAV particle, and (B) empty AAV particle. Reprinted from [99] with permission.

Currently, TEM has rarely been used as a direct virus detection tool in clinical diagnosis due to its poor detection sensitivity, typically required a high concentration of particles, with a minimum of  $10^6$  particles/mL [76]. Besides, it is impossible for the screening of a lot of samples as in a viral disease outbreak, due to the high cost of TEM maintenance and the sample preparation and virus location on the TEM grids is time-consuming. Also, it cannot identify the viral particle as infectious or not, though it can identify the presence of nuclear acid. Therefore, the use of TEM for direct virus detection has gradually declined since the 1990s [100] due to two major developments: the

invention of immunoassays, such as enzyme-linked immunosorbent assay (ELISA) and the discovery of molecular detection techniques such as polymerase chain reaction (PCR). Meanwhile, to differentiate between infectious and noninfectious virus particles and quantify the infectious virus particles, cell-based in vitro assays have been developed.

### 2.3.1.2 Immunoassays

Currently, immunoassays remain the standard method to detect the presence and concentration of virus particles, which rely on the principle of an antibody to recognize and bind a specific viral antigen. An antigen is any substance, such as viruses or bacteria that can stimulate an immune response. An antibody is a large, Y-shaped protein immunoglobulin that is produced by human B lymphocytes to help eliminate an antigen found in the body [101]. Antibodies produced immediately after viral invasion can also be an indicator in viral disease diagnosis; thus, immunoassays can either detect the presence of specific viral antigen or the corresponding antibody produced by the immune system. Immunoassays use detectable labels, typically chemically-linked or conjugated to antibodies or antigens to detect the presence of corresponding antigens or antibodies. The detectable labels could be radioactive isotopes [102], fluorescent substances [101], luminescent molecules [103], or enzymes that produce a color change [104]. Thus, immunoassays have developed into a variety of formats.

Enzyme-linked immunosorbent assay (ELISA) is the most widely used immunoassay for virus detection. ELISA is based on an enzyme-labeled antibody capable of detecting a viral antigen fixed to a solid plate surface. The virus is detected by measuring the product of a substrate and the conjugated enzyme (such as horseradish peroxidase or alkaline phosphatase), change the color of a substrate as the typical emission signal [104]. ELISA can be performed in a variety of ways; one common approach is an indirect sandwich ELISA, as shown in **Figure 2.10A**. The quantity of bounded viral particles is proportional to the intensity of colorimetric change. ELISA is also a very sensitive virus detection method but requires numerous washing steps and costly assumption of antibodies, and has a risk of the false-positive result by the cross-reactivity of the used antibodies.

Lateral flow immunoassay is a one-step modified enzyme immunoassay for the rapid, simple, low-cost detection for the presence or absence of a target analyte in a liquid sample matrix. It is based on an antibody binding the antigen specifically in the sample and is shown in **Figure 2.10B** [105]. It is similar to ELISA except the line is visualized with colloidal gold and not an enzyme, and the capture antibodies are immobilized in the test and control lines as the antigen sample flow through the system. The antigen-antibody complex will be captured at the test line by the primary antibody. Also, the excess labeled antibody will be captured at the control line by the secondary antibody. The excess liquid sample will move to the absorption pad, which maintains the flow rate of the sample over the membrane and stops the backflow. The intensity of color at the test line reflects the amount of target antigen and can be seen by the naked eyes or measured with an optical reader. The color at the control line indicates that a strip functions properly as a valid test. The most typical application is for medical diagnostics as a point-of-care device, such as a rapid strep test of bacterial throat infection, and a

home pregnancy test. The lateral flow immunoassay with gold nanoparticles as a direct coloring or fluorescent signal makes this assay easy and quick to perform, but it has a low sensitivity and accuracy, allowing for false positive/negative results.

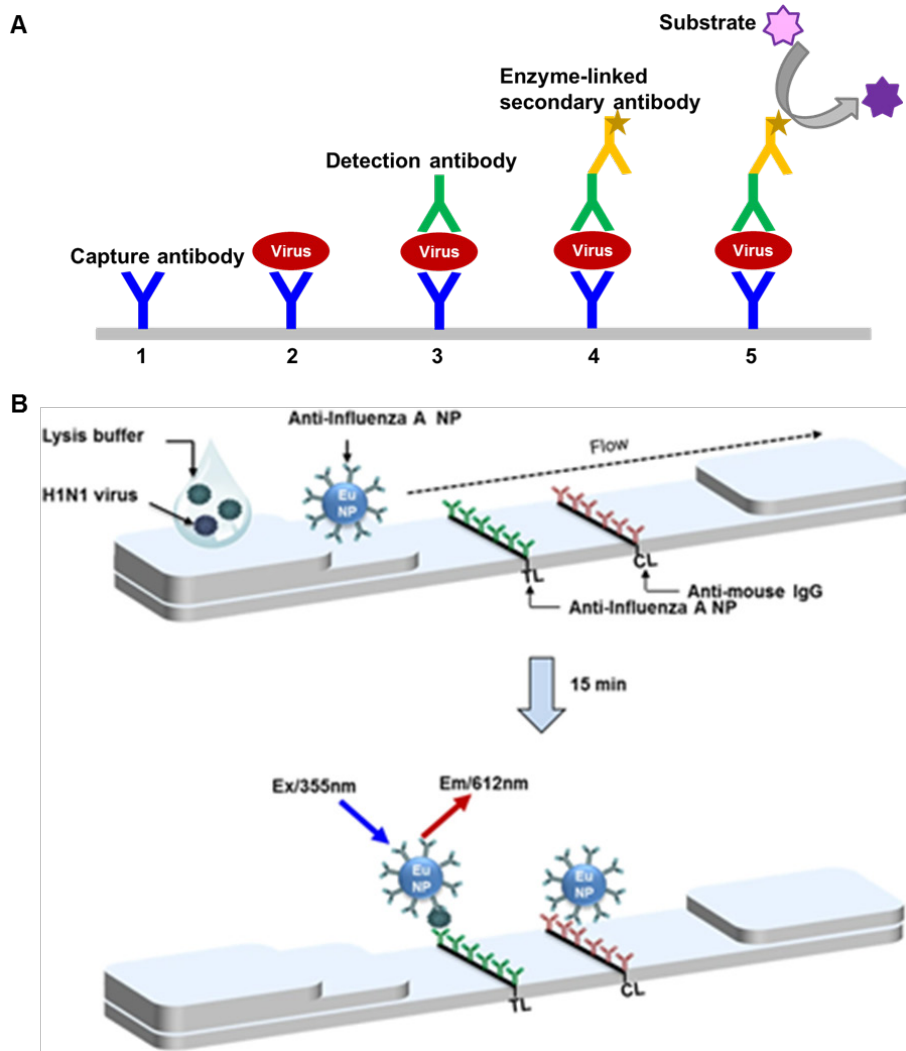


**Figure 2.10** Immunoassays. (A) Indirect sandwich ELISA: 1) a capture antibody coated on the bottom of a plate well; 2) any viral antigen present in the analyte binds to capture antibody; 3) detection antibody is added, and binds to virus; 4) enzyme-labeled secondary antibody is added and binds to detection antibody; 5) substrate is added, results in a detectable color change converted by the enzyme. (B) Europium nanoparticles labeled monoclonal antibodies conjugate-linked fluorescent immunochromatography strip test for influenza A virus (H1N1). Reprinted from [105] with permission.

As immunoassays mainly rely on labeled antibodies to recognize the viral antigen for virus detection, and this method required numerous washing steps and costly antibodies. In some circumstances, the antibodies might have cross-reactivity resulting in false-positive/negative results and low assay sensitivity. To overcome these drawbacks,



measuring the nucleic acids instead of the outer capsid proteins is another way to detect viruses.

### 2.3.1.3 Polymerase chain reaction

Polymerase chain reaction (PCR) is a more sensitive and rapid specific virus molecular detection technique, compared with immunoassays. The PCR technique is used to amplify viral DNA sequences from clinical samples. The amplification is done in cycles using four nucleotides, a thermostable DNA polymerase (e.g., *Taq* polymerase and *Pfu* polymerase), and primers [106]. Four basic nucleotides are the basic unit of DNA molecules. DNA primers are short nucleotide sequences functioning as a starting point for DNA synthesis. DNA polymerase is an enzyme that synthesizes DNA from nucleotides. A typical PCR cycle includes thermal denature of the target DNA sample, primer annealing, and primer extension by the DNA polymerase, as shown in **Figure 2.11** [107].

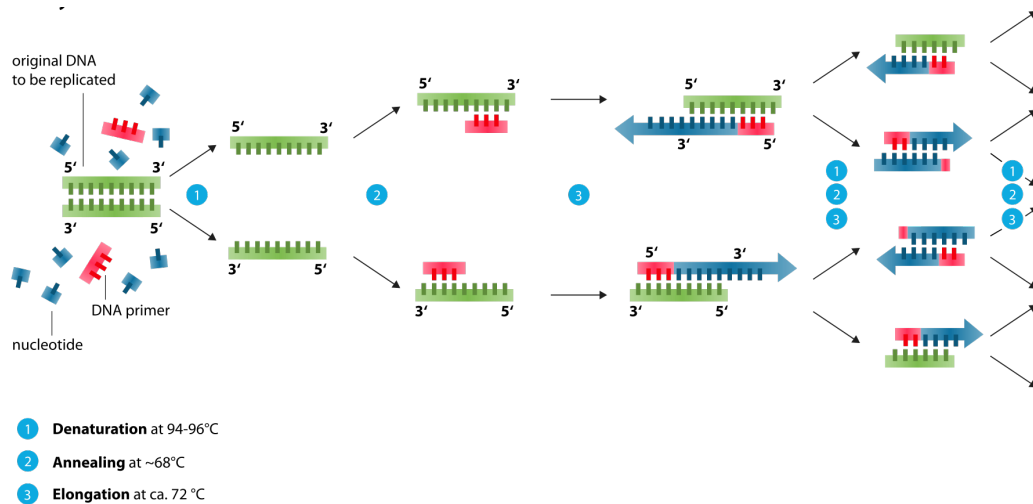


**Figure 2.11** Overview of a Polymerase Chain Reaction Cycle. Reprinted from [107] with permission.

The PCR cycle is performed by an automated thermal cycler machine and results in an exponential amplification of the target DNA sample by repeating the cycles. This cycle is repeated approximately 25–35 times, depending on the input DNA. The amplified product can then be stained with a chemical dye such as ethidium bromide or contains the pre-labeled DNA primers with fluorescent dyes (fluorophores), and is analyzed by standard agarose or polyacrylamide gel electrophoresis [106]. The standard PCR can only detect specific DNA, and it typically takes several days to get the analyzed result by gel electrophoresis. It is a qualitative method to detect the presence or absence of the virus.

To overcome the limitations of standard PCR techniques, many variants have been developed. The two most important developments are reverse transcription-PCR

(RT-PCR) and real-time PCR (quantitative PCR, qPCR). RT-PCR allows the detection and amplification of viral RNA sequences. The RNA is reverse transcribed into complementary DNA (cDNA), which is then amplified by the standard PCR procedure. Typically, it can serve as the first step in qPCR. qPCR, in contrast to conventional PCR, analyzes the result at its end, quantifies DNA throughout the reactions in a quick time (1-4 hours). qPCR uses fluorescence to measure the real-time accumulation of amplified DNA. The amplified DNA is typically hydrated with a TaqMan probe, of which one end is a fluorescent reporter, and the other end is a quencher, then releases the fluorescent reporter away from the quencher [108]. Thus, the amount of fluorescence released during amplification is directly proportional to the amount of amplified DNA and can be measured in real-time. It also quantifies RNA as RT-qPCR.

The (RT-)qPCR is a very sensitive technique that allows the rapid detection of viral nucleic acid and is considered a reference method for detecting donated blood for transfusion-transmitted viruses ( HIV-1 and HCV) [109]. However, it requires the known sequence information of virus to design virus-specific primer and is effective for low target numbers.

Next-Generation Sequencing (NGS) can allow the detecting of novel viruses without knowing genome sequence information. It can detect a broad range of viruses, has a higher sample throughput, needs a shorter turnaround time, and is very effective in the tracking of viral disease outbreak such as influenza [110] and Ebola [111]. The data processing of NGS requires specialized personnel and expensive equipment and is complex. However, the price is reduced every year.

#### *2.3.1.4 In vitro cell culture assays*

In-vitro cell culture assays can detect a broad range of viruses and are very sensitive for detecting infectious viral particles. There are several cell-based infectivity assays that have been extensively used for measuring the concentration of infectious virus by inoculating the virus samples with indicator cells.

Plaque assay is a reliable method to determine the titers of many different viruses [112]. Virus samples are serially diluted, and aliquots of each dilution are used to infect monolayer of susceptible cells grown on a nutrient semi-solid medium such as agar gel or carboxymethyl cellulose. An infectious virus infects a cell, replicates, then causes cell lysis, which releases virions to infect adjacent cells. The gel restricts the spread of the infectious virions. Eventually, one infectious virus particle produces a circular area of infected cells called a plaque, which can be observed by a light microscope or even by the naked eye if large enough. The living cells are often stained by a dye crystal violet to increase the contrast between the plaque and background, showing clear plaques on a dark background, as shown in **Figure 2.12A** [113]. The formation of plaque typically requires 5-14 days. Results of plaque assays are generally counted manually and reported as a plaque-forming unit (PFU) per unit volume (mL). To perform the plaque assay, the viruses must cause host cell lysis and need to be diluted so that the plaques can be individually seen. Therefore, many dilutions of virus samples have to be initially guessed and tested.

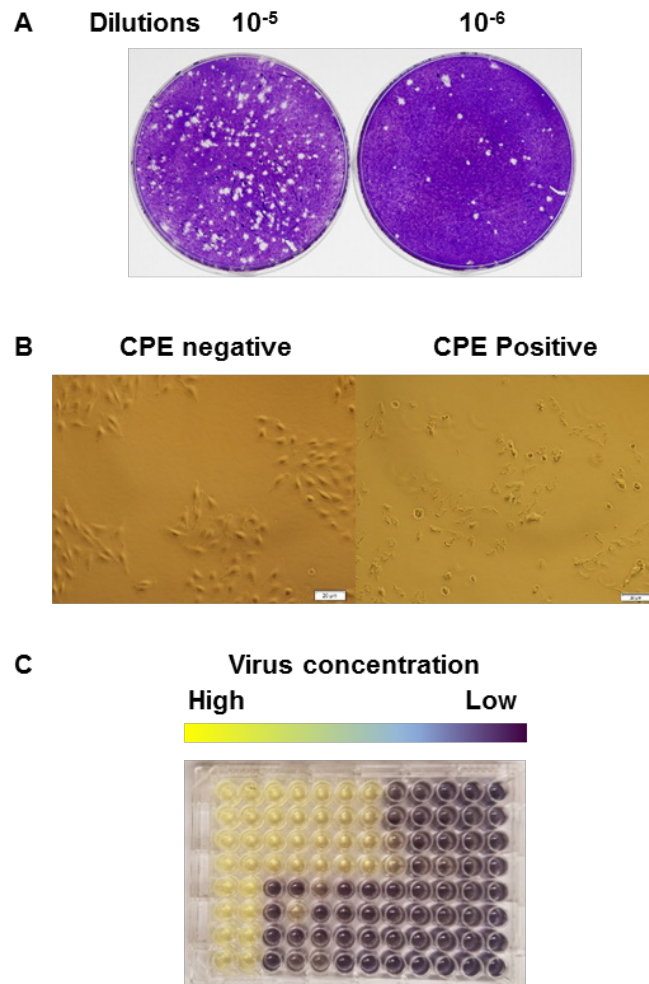


**Figure 2.12** In vitro cell culture assays. (A) Plaque formation of adenoviruses serotype 41 with crystal violet stain, reprinted from [113] with permission, (B) CPE effect of PK-13 cells infected by PPV, and (C) MTT assay of PK-13 cells infected by PPV, courtesy of Pratik U. Joshi, Michigan Technological University, Houghton, MI

As some viruses cannot form plaques, a 50% tissue culture infectious dose (TCID<sub>50</sub>) infectivity assay was developed as an alternative virus titration method. TCID<sub>50</sub> infectivity assay can detect the presence of an infectious virus in a sample based on the observation of cell morphology change, such as cell monolayer destruction, swelling and clumping, focal degeneration, rounding of the infected cell, cell fusion forming syncytia, and the appearance of nuclear or cytoplasmic inclusion bodies [114]. These morphological changes in host cells caused by viral infection are called the cytopathic effect (CPE). A CPE of cell destruction is shown in **Figure 2.12B**. Like the plaque assay, serial dilutions of the virus is used to infect monolayer of host cells. Typically after 7-14 days of post-inoculation, the infected cells are observed under a light microscope and scored manually as CPE positive or negative. The scored results are used to

mathematically calculate a virus titer as TCID<sub>50</sub> per unit volume (mL), which denotes CPE occurring in 50% of the inoculated cells [115].

Both the plaque assay and TCID<sub>50</sub> infectivity assay need staff with extensive training and experienced eyes; also, the result readouts are low-throughput. An MTT assay was developed to be a more efficient and objective virus titration method. The MTT assay is a colorimetric virus titration assay based on the determination of cell viability rather than cell cytopathology. Like the plaque and TCID<sub>50</sub> infectivity assay, virus samples are serially diluted and added into the indicator cell monolayers. After 5-10 days of incubation of the indicator cells with the virus, a tetrazolium MTT salt is added to the infected cells. The reduction of the yellow MTT agent by mitochondrial reductase within the metabolically viable cells forms insoluble purple formazan crystals [116]. The crystals are solubilized later to form a purple-colored solution. The color intensity, which is proportional to the number of alive cells remaining, can be read by a spectrophotometer. For the high dilution of virus, where no cells survive, it will show the original yellow color of the MTT agent. **Figure 2.12C** shows the MTT result of PPV infected porcine kidney-13 (PK-13) cells in a 96-well plate. The virus dilution that kills 50% of the control host cells is determined to be the virus titer MTT<sub>50</sub> per unit volume (mL) [117].

In-vitro cell culture assays have been a “golden standard” for virus detection in the laboratory for decades, and it is a sensitive method to detect very low amounts of infectious virus particles due to the virus propagation in the infected host cells. It can also be used for screening of large numbers of virus samples. However, these assays typically require a long post-inoculation time 1-2 weeks for the detection of CPE or cell viability. Furthermore, false-positive results may occur since some cells could have morphological changes due to chemical components in the tested virus samples.

In all, past and current virus methods have many drawbacks, such as low throughput, intensive labor, special and expensive equipment, chemicals, and consumables requirements. Therefore, nanotechnology is being developed to overcome the limitations of current methods for wider application of virus detection to benefit public health.

## **2.3.2 Gold nanoparticles (AuNPs) in virus detection**

### *2.3.2.1 AuNPs properties*

The unique optical properties of gold nanoparticles (AuNPs) originate from their surface plasmon resonance (SPR) that is affected by both the particle size and the inter-particle distance. The electric field of the penetrated incident light can cause the free surface conduction AuNPs electrons to polarize and oscillate, and resonance is achieved only when their frequency is approximately the same [118]. The resulted plasmon oscillation is distributed over the whole AuNPs volume, so the SPR of AuNPs is called localized surface plasmon resonance (LSPR) [118]. The LSPR wavelength of AuNPs is dependent on the size of individual AuNPs and the inter-particle separations of the AuNPs. The intensity of the light that is passing through the AuNPs can be measured by ultraviolet-visible (UV-Vis) absorption spectroscopy. A red-shift and peak broadening of

the UV-Vis absorption spectrum occurs with AuNPs aggregates. It may also involve a color change from red to dark blue or gray based on the gold nanoparticle aggregation extent and concentration. In addition to their LSPR absorption, light scattering is another key optical property of AuNPs. The scattered light intensity from AuNPs as a function of time can be measured by dynamic light scattering (DLS) to determine the hydrodynamic size of AuNPs. The typical characterization of AuNPs aggregation by UV-Vis, DLS, and TEM is shown in **Figure 2.13** [119].

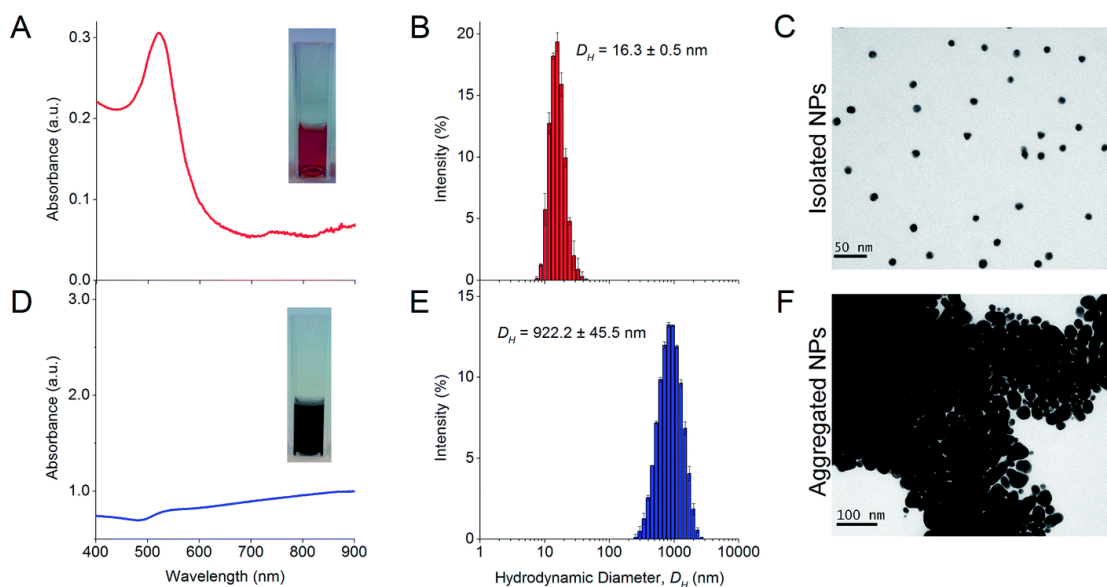


**Figure 2.13** Characterization of isolated AuNPs (A) UV-Vis absorption spectrum, (B) DLS particle size, (C) TEM image, compared with (D) UV-Vis absorption spectrum, (E) DLS particle size, (F) TEM image of aggregated AuNPs in 100 mM NaCl. The insets show the real color of isolated and aggregated AuNPs. Reprinted from [119] with permission.

### 2.3.2.2 Detection of specific viruses using AuNPs

Recent studies have tried to harness the unique properties of AuNPs to develop various rapid, sensitive, simple virus detection methods. A summary of recent studies of detection of human viruses using AuNPs is found in **Table 2.3**. The AuNPs detection signals commonly are measured by UV-Vis absorption spectroscopy, DLS, surface-enhanced Raman spectroscopy (SERS), color change, and enhanced or quenched fluorescent emission. Both the nucleic acids and capsid proteins of the virus can be used as biochemical detection targets. The design and principle of the detection methods could be dramatically different, but the similarity is that these AuNPs detection methods typically involve using antibodies for capturing virus capsid proteins or using complementary oligonucleotides for detecting virus nucleic acids. Once the virus is captured, nanoparticle aggregation is induced to identify the difference between a sample with and without virus. The antibodies and oligonucleotides are very expensive, have limited chemical stability, and can only detect one specific type of virus at a time.

Thus, a ligand-free, general AuNPs virus detection is preferred. Two examples of ligand-free detection have been shown for the Influenza B virus [120] and HPV-16 L1 VLP [121] and can be found in **Table 2.3**. For Influenza B, the detection is based on the specific binding capacity of sialic acid to the enveloped protein hemagglutinin; for the HPV-16 L1 VLP, the detection is based on the presence of the virus that inhibits the AuNPs aggregated by salt. Other biomolecules like proteins could also prevent the salt induced-aggregation if the concentration is high enough [119]. However, neither of the above mechanism could be developed for a general virus detection method. The most common principle for the virus detection summarized in **Table 2.3** is colorimetric UV-Vis. However, this type of detection is not sensitive to lower degrees of aggregation and not suitable for the analysis of colored samples. Light scattering-based assays typically have a better limit of detection than UV-Vis; examples include HBV surface antigen [122, 123] and HIV-1 U5 cDNA [124]. In addition, the smaller the AuNPs size, the better limit of detection that could be achieved. Based on review of current AuNPs aggregation methods for virus detection, a small sized gold sphere by DLS could be promising for exploring the ligand-free general virus detection method.

Virus particles can aggregate in a variety of solution conditions through the manipulation of pH and salt concentration. Viruses tend to form aggregates close to their pI, where the net charge of the virus surface is neutral, and the repulsive electrostatic forces on the virus surfaces are the lowest. MS2,  $\Phi$ X174, and PRD1 bacteriophage particles formed aggregates when the pH was lowered from 7 to near their pI of 4 [20]. Viruses show different degrees of aggregation depending on salt types and concentration. A NaCl solution ranging from 0.5-4 M reversibly aggregated the hepatitis B surface antigen (HBsAg) virus-like particles (VLPs) into oligomeric particles, while 1-2 M ammonium sulfate irreversibly aggregated the VLPs [125].

**Table 2.3** Virus detection using AuNPs

Target	AuNPs shape and size	Conjugated ligand	Detection principle	Limit of detection	Assay time	Reference
HBV surface antigen	50-100 nm citrate sphere	Antibody	DLS	0.005 IU/mL	1 h	[123]
HBV surface antigen	20-40 nm basic fuchsin goldflower	Antibody	SERS	0.01 IU/mL	~1 h	[126]
HBV surface antigen	68×30 nm CTAB rod	Antibody	Colorimetric UV-Vis	0.01 IU/mL	-	[122]
HBV DNA	CTAB rod	DNA probe	Fluorometric	15 pM	~1 h	[127]
HBV DNA	8-15 nm citrate sphere	DNA probe	Colorimetric UV-Vis	0.36 pM	75 min	[128]
HBV DNA	10 nm citrate sphere	DNA probe	Scanometric detection of silver stain	1 fM	1.5 h	[129]
HCV RNA	20 nm citrate sphere	RNA-specific oligonucleotide	Colorimetric UV-Vis	4.57 IU/mL	~30 min	[130]
HCV gene	8-15 nm citrate sphere	DNA probe	Colorimetric UV-Vis	0.36 pM	75 min	[128]
HCV gene	10-15 nm citrate sphere	hairpin DNA probe	Electrocatalytic	~1 pM	60 min	[131]
HCV RNA	15 nm citrate sphere	None (but induced by primer)	Colorimetric UV-Vis	~10 IU/mL	110 min	[132]
HIV-1 U5 cDNA	16-30 nm CTAB sphere	DNA-specific oligonucleotide	Colorimetric UV-Vis; DLS	0.1 nM; 10 pM	30 min	[124]
HIV-1 cDNA	3 nm graphene decorated imidazole termini sphere	DNA probe	Electrochemical	0.34 fM	50 min	[133]
HIV-2 gene	13 nm silver coated sphere	DNA probe	DLS	10 fM	~1.5 h	[134]
Influenza A virus	16-30 nm citrate sphere	Antibody	DLS	100 TCID <sub>50</sub> /mL	30 min	[135]
Influenza A virus	13 nm citrate sphere	Antibody	Colorimetric UV-Vis	7.8 HU	30 min	[136]

Influenza A virus RNA	15 nm citrate sphere	RNA specific oligonucleotide	Scanometric detection of silver stain	1000 TCID <sub>50</sub> /mL	2.5 h	[137]
Influenza B virus surface hemagglutinin	20 nm sialic acid sphere	None	Colorimetric UV-Vis	0.156 vol% of 512 HU	12 min	[120]
HPV-16 L1 VLP	20 nm citrate sphere	None	Colorimetric UV-Vis; DLS	100 ng	20 min	[121]

International unit (IU), Cetyltrimethylammonium bromide (CTAB), hemagglutination units (HU)

Osmolytes can also aggregate the virus. Osmolytes are natural, organic compounds that are found in many organisms to maintain constant cell volume in a harsh environment, like extreme pH, high concentration of salt, and high pressure, by balancing the hydrostatic pressure between internal and external cellular spaces [138]. Osmolytes, based on their effects on protein stability, can be categorized into two groups, protecting and denaturing osmolytes. Protecting osmolytes, such as polyols, amino acids, sugars, and methylamines, can stabilize proteins by attaching to the water contents and rearranging the water molecules around the protein backbones [139]. Denaturing osmolytes, like urea, have the opposite effect: they can unfold the proteins by attaching to the protein backbones by hydrogen bonds [140]. Protecting osmolytes interact unfavorably with the protein backbone, resulting in preferential depletion from the protein surface [141]. Denaturing osmolytes interact favorably with the protein backbone and often unfold proteins [141].

It has been discovered that protecting osmolytes, including the amino acid (glycine) and sugar (mannitol), can flocculate both enveloped Sindbis virus (SINV) and non-enveloped PPV [142, 143], and resulted in 80% removal with a 0.2 µm filter. The proteins, BSA and lysozyme, were not flocculated and resulted in a less than 5% removal [142, 143]. This difference indicated that the osmolyte flocculation effect is specific to viruses, not tested proteins. The specificity is likely related to the high hydrophobicity of viruses as compared to the proteins [32].

Protecting osmolytes stabilize proteins due to unfavorable interaction with the protein backbone, causing an osmophobic effect [144, 145]. Osmolytes have a high affinity for water, thus can remove water molecules near hydrophobic residues on the protein surface [146]. To compensate for this change in free energy [141], the protein tends to fold, which results in a more compact shape to enhance protein stability [147]. Viruses tend to aggregate in this same dehydration by osmolytes due to two major differences between viruses and proteins: first, viral surfaces have more hydrophobic residues than proteins [32, 33], causing more water molecules to be removed from the viral surface. Second, viruses have a rigid shape and cannot collapse to account for the dehydrated surface. Viruses tend to attract each other and form aggregations. The osmolyte effect on virus and protein stability is shown in **Figure 2.14** [148]. Thus, protecting osmolytes can be used as virus flocculants [142, 143]. The flocculation can also be used for virus purification [148]. Osmolyte mannitol has been used as a flocculant for PPV and SINV and can purify the flocculated viruses from protein contaminants after



microfiltration. A 58-96% virus recovery and an 80% of contaminated protein removal could be achieved [148].

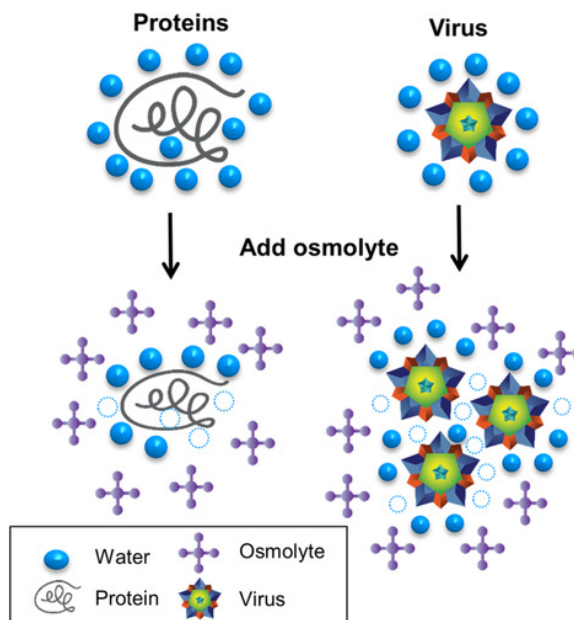


**Figure 2.14** Virus and protein stability with osmolyte. Reprinted from [148] with permission.

Osmolytes have shown preferential flocculation of both enveloped and non-enveloped viruses in virus removal and purification. We propose using the osmolytes as preferential viral flocculants in the ligand-free virus detection method. We want to use the preferential flocculation of osmolytes coupled with the AuNPs detection by measuring the aggregation (Chapter 5). The proposed method would be accomplished by coating the viral particles around AuNPs and then inducing the aggregation with osmolytes. Protein coated AuNPs that do not aggregate in osmolyte solutions would be used as a negative control for virus detection. This method would allow for the detection of viral particles without the need for expensive antibodies or oligonucleotides. It would also not be virus-specific. This method could be a potential quick, sensitive, inexpensive, and general method for detecting the presence of viral particles.

## 2.4 Virus thermal stability

### 2.4.1 Viral based vaccines

According to the WHO, vaccines are one of the most effective methods to prevent viral disease outbreaks. Since the first smallpox vaccine was created using a cowpox lesion fluid by Edward Jenner in 1796 [149], 81 vaccines have been licensed by the Food and Drug Administration (FDA) in the US to prevent against infectious diseases effectively [150]. Vaccines have been used to protect against more than 25 chronic or life-threatening diseases [151], such as measles, polio, hepatitis, influenza, smallpox, rabies, and cervical cancer. Currently, vaccines save about 3 million lives worldwide each year [152]. However, about 1.5 million people, primarily children, die due to vaccine-preventable diseases yearly [153], according to the Global Alliance for Vaccines and Immunizations (GAVI). A major portion of the problem results from the thermal instability of many currently used vaccines [154]. This triggered researchers to improve viral thermal stability.

There are three major types of viral-based vaccines licensed for human use, live attenuated, inactivated, and subunit vaccines [155, 156]. Live-attenuated vaccines are usually produced by extended passage of a disease-causing (wild) virus in non-human cell culture to weaken the wild virus [2, 157, 158]. The attenuated virus can still replicate and stimulate high immunity, but it loses the ability to cause disease. Live attenuated viral vaccines can cause strong and long-lasting immune response since the similarity to natural infection. Thus, this type of vaccine typically requires just one dose and can give people lifetime protection. Examples include MMR, smallpox, varicella (chickenpox), and yellow fever vaccines [157]. Inactivated vaccines are typically treated by chemical or heat inactivation to stop virus replication [2, 157, 158]. The inactivated virus cannot replicate, but can still produce immunogenicity, though not as strong as the live attenuated virus. This type of vaccine usually requires multiple doses and can protect people against the corresponding viral diseases for a limited time. It may require a booster shot to maintain ongoing immunity. Examples include hepatitis A, rabies, and polio vaccines [157]. Subunit vaccines use a component of the virus, such as a surface polysaccharide, capsid protein, or nucleic acid, to stimulate immune response [2, 157, 158]. Like the inactivated vaccine, this type of vaccine also require booster shots to obtain ongoing protection against diseases. Examples include hepatitis B, and HPV [157]. The immune response caused by these three types of vaccines from strong to weak in order as live attenuated > inactivated > subunit vaccines. However, the stability of these three types of vaccines is in reverse order.

### 2.4.2 Cold chain and cold storage problem

In order for viral vaccines to be effective, they must be transported and stored in a “cold chain” [159]. A cold chain is a system of transporting and storing vaccines at the recommended temperature, typically 2-8 °C, from the manufacturer until the point of use [159, 160]. **Figure 2.15A** [161] shows a typical cold chain from vaccine manufacturer

through different storage and transportation mechanisms until vaccine administration. If temperatures are not maintained during this supply chain, i.e., if a vaccine is exposed to excessive heat or cold, the vaccine may lose its potency and could no longer be effective in fighting disease. This is called the cold storage problem [161].

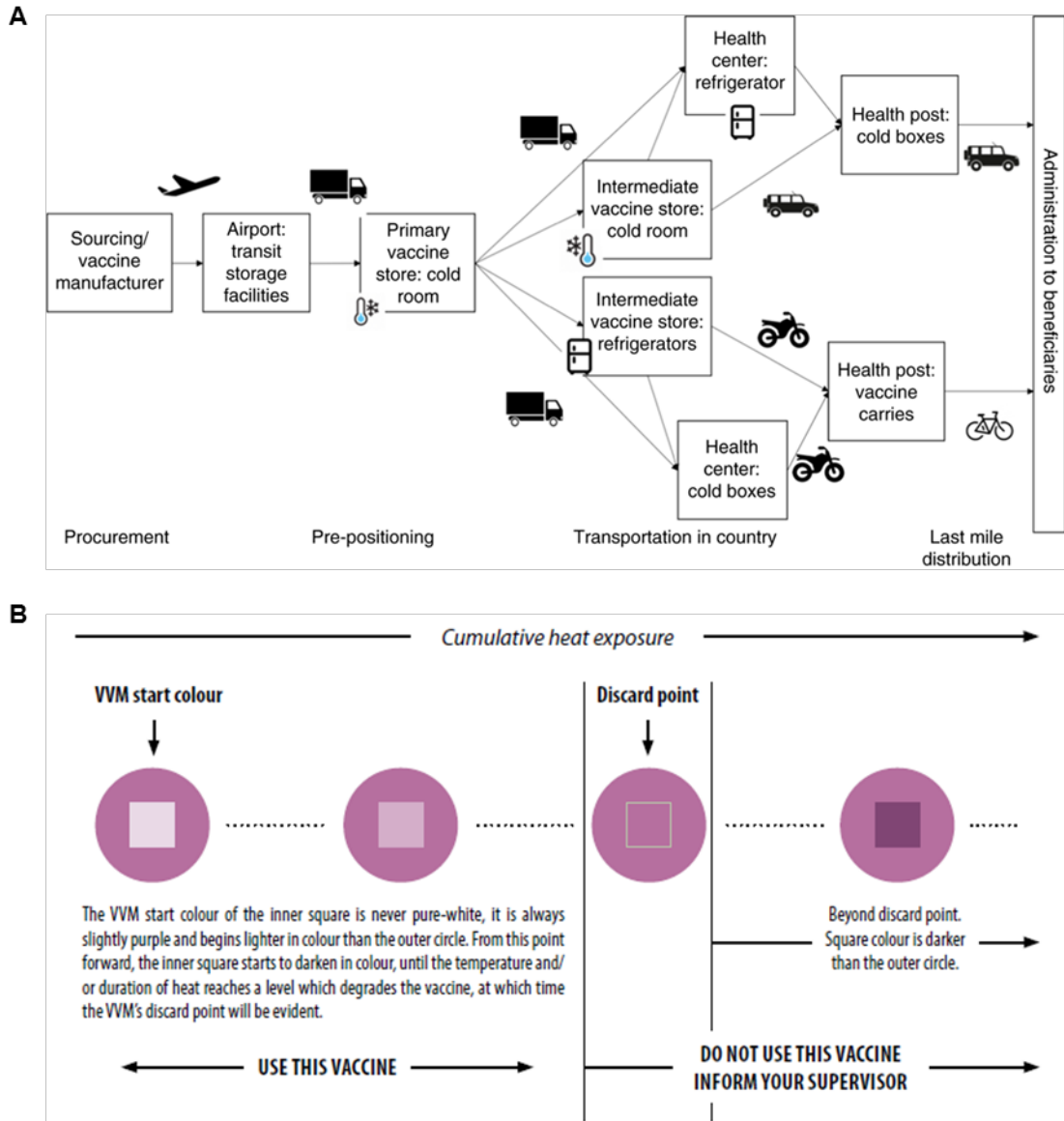


**Figure 2.15** Cold chain. (A) A typical flow of cold chain, reprinted from [161] with permission. (B) A vaccine vial monitor (VVM) to indicate the cumulative heat exposure of vaccine, reprinted from [162] with permission.

A vaccine vial monitor (VVM), which is a temperature monitoring device, typically accompanies vaccines throughout the transportation and storage of the vaccine. As shown in **Figure 2.15B** [162], a VVM is a chemical indicator label on the vaccine container and records its cumulative heat exposure by a gradual color change. The

vaccine needs to be discarded if the color or inner square is the same color or darker than the color of the outside circle, which indicates that the vaccine is exposed to excessive heat and, therefore, likely to be damaged. According to the WHO, about 50% of the vaccines produced are discarded due to poor thermal stability each year [163]. The unreliable cold chain system is one of the major causes of poor immunization coverage in developing countries [160, 161], which could increase the likelihood of a viral infectious disease outbreak. Key issues that limit the cold chain reliability in low resources countries are insufficient cold chain capacity, inadequate temperature monitoring and control, and lack of up-to-date cold chain equipment [160].

The unreliable cold chain can expose the vaccines to high temperatures. High temperatures can damage vaccines in a variety of ways, accelerating unwanted reactions, such as hydrolysis, deamination, and breakage of non-covalent bonds, causing proteins to denature or degrade, dissociating polysaccharides or reducing the infectivity of virus in the live attenuated vaccines [154, 164]. All vaccines will lose potency over time, and the rate of potency loss depends on temperature and exposure time. Heat damage is cumulative, so higher temperature and longer exposure time lead to faster vaccine thermal degradation [164]. Therefore, developing robust, thermostable viral vaccines that are less dependent on the cold chain is urgent and important for universal access to immunization.

### **2.4.3 Conventional vaccine formulation to stabilize viral vaccines**

Vaccines are formulated to generate a strong protective immune response to the targeted antigen and typically comprise three key components, antigen, adjuvant, and excipients [165, 166]. The antigenic component in a viral vaccine is the viral component that causes an immune response. The adjuvant is an agent that can be added to some vaccines to enhance the immunogenicity of the antigens *in vivo* and is typically used with less immunogenic antigens, like subunit and inactivated vaccines. Typically, aluminum hydroxide and aluminum phosphate are commonly used adjuvants in licensed vaccines [165]. Aluminum salts function by adsorption and slow release of antigen components at the injection site for the immune response. Excipients, the third component of a vaccine, are typically inert agents added to a vaccine for a specific purpose such as preservation, pH control, and stabilization; examples include preservatives, buffers, and stabilizers [166]. Preservatives prevent bacteria, and fungi growth; commonly used preservatives are 2-phenoxyethanol, phenol, and thiomersal [166]. Buffers are used to control the pH of the formulated vaccine within the physiological range. Stabilizers are used in the formulation to improve vaccine stability during transportation and storage. Examples include sugars such as sucrose, lactose, and trehalose, amino acids such as glycine or monosodium glutamate, and proteins such as human serum albumin or gelatin.

The mechanisms why stabilizer can improve antigen stability is still unclear. But major discussions on these bulk agents can create a crowding environment by either form a hydrogen bond between the sugar and the viral surface, non-specific interactions between the proteins and viral surface. The crowding environment has limited space for unfolded proteins and large aggregation. Thus, the crowding effect disfavors viral surface proteins unfolding and denaturation, facilitate heat-induced unfolded viral capsid proteins

refolding back to the native state [167], and inhibit viruses forming insoluble aggregates [168].

The formulation and thermal stability of commonly used FDA licensed viral vaccines are summarized in **Table 2.4** [164, 169, 170]. Inactivated and subunit vaccines typically require adjuvants to boost immune response but are rather stable when exposed to high temperatures. Live attenuated viral vaccines stimulate a stronger immune response than other types of vaccines and, therefore, do not contain adjuvants. However, they are more sensitive to temperature changes, and tight temperature control is required for them to remain immunogenic [168]. There is a need to develop versatile methods to thermally stabilize the live attenuated vaccines.

A conventional formulation strategy to improve the thermal stability of live-attenuated vaccines is to lyophilize the vaccines in excipients for long-term storage [170], as shown in **Table 2.4**. Lyophilization, or freeze-drying, involves controlled removal of bulk water and desorption of bound water, under decreased pressure and low temperature. The lyophilized vaccine product will typically have a low residual moisture content of <3% [171]. The lyophilized vaccine can be stored long-term and can be reconstituted immediately by mixing the dried vaccine powder with a buffer before use. The drying process typically requires cryoprotectants as well as stabilizers in the formulation to protect the vaccines from dehydration and ice-crystal formation. Sugars can form glass rather than crystals due to high glass-transition temperatures and can form hydrogen bonds to the dried virus surface as water substitutes [172]. Different excipients need to select for different live attenuated vaccine formulations and require a large number of screen experiments. The dried formulation has improved thermal stability, but most of the live-attenuated vaccine still need cold chain storage.

**Table 2.4** FDA-approved viral vaccines types, formulation, and thermal stability [164, 169, 170]

Vaccine type	Vaccine	Formulation	Stability at			
			2-8°C	25°	37°C	≥45°C
Live attenuated vaccine	MMR	Lyophilized, no adjuvant	2 years	>1 month	>1 week	unstable
	Yellow fever	Lyophilized, no adjuvant	2 years	>1 month	>2 weeks	unstable
	Varicella	Lyophilized, no adjuvant	2 years	6 h (27°C)	unstable	unstable
	Rotavirus	Liquid, no adjuvant	2 years	48 h	unstable	unstable
	Oral polio	Liquid, no adjuvant	6 months	>1 week	2 days	unstable
Inactivated vaccine	Inactivated polio	Liquid, no adjuvant	>18 months	N/A	3 months	N/A
	Rabies	Lyophilized, no adjuvant	3 years	N/A	3 months	N/A
	Hepatitis A	Liquid, aluminum adjuvant	3 years	3 months (28°C)	1-3 weeks	N/A
Subunit	Hepatitis B	Liquid, aluminum adjuvant	4 years	N/A	1 month	1 week
	HPV	Liquid, aluminum adjuvant	3 years	2 years	1.5 months	14 days

#### 2.4.4 Novel formulations to enhance the thermal stability of virus by complex coacervation

To develop robust, thermostable viral vaccines that are less dependent on the cold chain, a new formulation strategy for stabilizing viral vaccines thermally is proposed by using the complex coacervation to encapsulate the viral particles. Complex coacervation [173-175] is an associative liquid-liquid phase separation phenomena based on electrostatic interactions of two or more oppositely charged polymers, and entropy gains for releasing of small, bound, counter-ions from the polyelectrolyte salts into solution [168, 176, 177]. Oppositely charged polymers such as proteins, polypeptides, polynucleotides, and polysaccharides can be used to form complex coacervation. When oppositely charged polyelectrolytes interact in a solvent to reach net charge neutrality, two equilibrium phases can be formed. The polymer-rich dense phase is called the complex coacervate phase [173-175], and the polymer-poor dilute phase is called the supernatant, as shown in **Figure 2.16A** [178, 179]. Coacervates are formed by mixing clear, homogenous solutions of oppositely charged polymers until a turbid solution containing fine coacervate droplets is formed, causing a microphase separation [174, 175]. The droplets coalesce together over time or can be accelerated by centrifugation to form a dense bulk coacervate phase, causing a macrophase separation [174, 178]. Optical microscopic images of the coacervate droplets formed initially and in their coalesced form (after centrifugation) are shown in the insets circled images in **Figure 2.16A**.

The phase behavior of complex coacervation has been reported to be weakly affected by temperature [178, 180], showing the promise for application in high temperature. However, the phase behavior of complex coacervation is strongly dependent on the polyelectrolyte mixing ratio (stoichiometry), polyelectrolyte concentration, ionic strength (salt concentration), and solution pH. This phase behavior is depicted by the salt concentration vs. polymer concentration phase diagram, which separates the one-phase region from the two-phase region, as shown in **Figure 2.16B** [173]. At low salt and polymer concentrations, liquid-liquid phase separation as complex coacervation occurs underneath the binodal curves. The single-phase solution region is above the binodal curves. The different binodal curves represent how the immiscible region changes with different polymer chain lengths, and increasing polymer chain length can expand the two-phase region, as indicated by the arrow. Polymers with higher charge density can also increase the two-phase region [177, 181]. The critical point is the highest point of the binodal curve, which indicates that the existence of a limit of ionic strength when coacervation occurs for a given polymer system [173, 181]. The equilibrium concentration for a coexisting coacervate and supernatant phase is defined by the tie line, shown as the dashed line.

Complex coacervation has been used in a variety of areas, such as drug delivery [182, 183], gene therapy [184-186], and biomimic adhesives [187, 188]. One of the most important applications is as a method for encapsulation of biomolecules [45, 174, 186, 189-191], such as proteins, which can be achieved by using the proteins as a component of the complex coacervate matrix. Direct encapsulation of proteins by a binary protein-polyelectrolyte system [192] is sometimes limited by the polyampholyte nature of proteins, which bear both cationic and anionic groups. A two-component protein with oppositely charged polyelectrolyte can hardly form complex coacervates at physiological conditions due to the low charge density of the protein [193-195]. To overcome the limitations of the binary system, either the surface amino acids need to be modified to increase the protein charge density [193-195], or a tertiary system of complex coacervate is used to effectively encapsulate proteins [45, 190, 191, 196]. The advantage of using complex coacervation to encapsulate proteins is that the process allows for the encapsulation in aqueous physiological solution rather than harsh organic solvents. Precipitation [197] or emulsion [198] requires organic solvents to encapsulate proteins by poly (lactic-co-glycolic) acid (PLGA), and the process may denature the protein of interest [199]. Also, the complex coacervation in aqueous solution does not need extra separation steps for the removal of any toxic organic solvent [200].

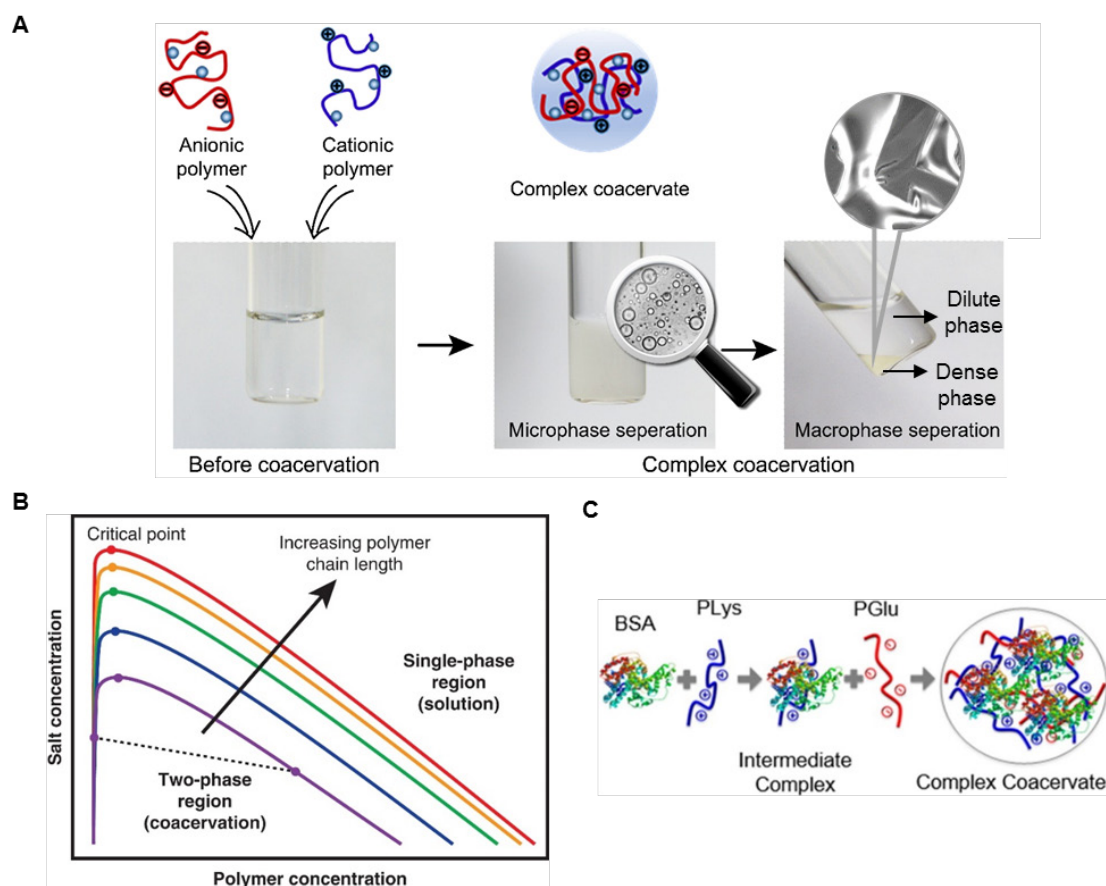


**Figure 2.16** Complex coacervation. (A) Scheme of complex coacervation of cationic polymer chitosan and anionic polymer hyaluronic acid (HA) in 0.1 M sodium acetate solution. Reprinted from [178] and [179] with permission. (B) Schematic representation of a typical phase diagram to define the phase boundaries as a function of salt concentration vs. polymer concentration for a given stoichiometry, pH, and temperature. Different colors represent different polymer chain lengths. Reprinted from [173] with permission. (C) BSA encapsulation via complex coacervation. Reprinted from [190] with permission.

A tertiary system of complex coacervate is typically used to encapsulate proteins effectively. Tertiary systems of coacervation will form an intermediate complex between the protein and oppositely charged polyelectrolyte. While some charges on the polyelectrolyte are neutralized by the charge on the protein, the overall charge of the intermediate complex is dominated by the polyelectrolyte. The coacervation is induced by adding a second, oppositely charged polyelectrolyte, which interacts directly with the intermediate complex by electrostatic attraction. The driving force for the coacervation is relying on the association of two opposite charged polyelectrolyte due to electrostatic attraction and the entropy gain from bound counterion release, which causes phase separation [168, 176, 177]. As shown in **Figure 2.16C** [190], a tertiary complex coacervate was formed to encapsulate BSA at neutral pH. BSA has a pI 4.5-5.0 [79], so it has a net negative surface charge at pH 7. The net negative BSA and polycation poly(L-lysine) (PLy) formed an intermediate complex first, and the intermediate further



interacted with a polyanion poly (D/L-glutamic acid) (PGlu) to form the final complex coacervate. This encapsulation of BSA with oppositely charged polypeptides showed better encapsulation efficiency near neutral pH compared with acidic pH, and it showed better stability at a higher degree of polymerization (the number of monomeric units in a polymer  $x=400$ ) compared with  $x=100$  [45, 190]. This system maintained the structural stability of the encapsulated BSA [190]. It showed promise for encapsulating our studied viruses since the pI of PPV and BVDV were similar to BSA, and encapsulation of viruses was desired at a neutral pH and in an organic-free aqueous solution. In all, the synthesized polypeptides are easily tunable for different degree of polymerization [177] and biocompatible with cells [190], and the coacervation did not affect the structural stability of the encapsulated proteins [168, 189-191, 201].

Complex coacervation not only maintained the structure stability of encapsulated proteins, but it also showed enhanced stability of proteins against harsh conditions [191], like denaturant urea environment, extreme pH, and high temperature. Encapsulated proteins (BSA, carbonic anhydrase, and  $\alpha$ -chymotrypsin) within poly(diallyldimethylammonium) and poly(acrylate) complex coacervates showed enhanced stability against urea-induced protein unfolding [167]. The coacervate droplets bound the protein conformers that were partially unfolded by urea and reduced the misfolding and aggregates [167]. An encapsulated BSA within poly(acrylic acid) (PAA) and poly(allylamine hydrochloride) (PAH) complex coacervates showed a reduced 10% protein unfolded fraction compared with 50% for free BSA, at the extreme pHs of 3 and 12 [191]. The reasons for why complex coacervates can protect proteins against extreme pH is likely due to extra hydrogen or hydroxide ions diffusing into the coacervate will first encounter polyelectrolytes and BSA molecules closest to the phase boundary between supernatant and coacervate. The polyelectrolytes on the phase boundary could shield the proteins further within the complex coacervate, and the small confined weak polyelectrolyte environment can act as a sort of buffer to maintain a stable pH environment within the coacervates. Moreover, the tertiary system of complex coacervates BSA-PAH-PAA showed protection of BSA against heat to a small degree, with a 45% unfolded fraction compared with 55% for free BSA at 70 °C [191]. The peak denaturation temperature of an encapsulated canola protein isolate (CPI) with chitosan (CS) complex coacervate was 92.3°C, higher than the 77°C for free CPI, indicating that the encapsulated CPI is more thermostable [202]. An encapsulated lysozyme by hyaluronic acid (HA) complex coacervates showed a high protein recovery at room temperature for 12-weeks' storage compared to free lysozyme compared at the same condition, indicated improved stability [168].

There are several possible mechanisms for a protein's enhanced thermal stability when encapsulated in a complex coacervate. The improved thermal stability of proteins in the coacervate phase could be attributed to the crowding environment, which disfavors proteins unfolding and denaturation, facilitate heat-induced unfolded proteins refolding back to the native state [167], and inhibit proteins forming insoluble aggregates [168]. The small, dense, compact, polymer-rich coacervate phase can provide entropic and enthalpic stabilization [168, 202]. The main driving force for protein unfolding is believed to be the high conformational entropy of the denatured state [203]. The flexible, unfolded state of a protein has a much greater conformational freedom than the compact,

folded state. The limited volume of the crowded environment would minimize the degrees of conformational freedom in the unfolded state, and hence improve the stabilization of the native state of protein due to an entropic stabilization [203, 204]. Also, unfolded proteins have larger hydration radii and occupy more volume compared to the folded state, and the excluded volume effect from the crowded environment lacks the space available for the extended denatured proteins, thus favoring any process like protein folding in which the volume decreases [203-205]. In addition, the denatured enthalpy of protein in polyelectrolyte complex has been shown to be much higher than free proteins [202], indicating that complex coacervation could impart thermal stability to proteins. Furthermore, complex coacervate microdroplets can be considered as a membrane-free, artificial cellular platform for proteins, thus serving as a type of protocell [206], which allows spatial compartmentalization for biomacromolecules without the use of membrane (vesicle) formation [207-209]. Thus, the coacervate stabilizes proteins by mimicking the proteins inside of a membrane-free cell, which is a highly crowded environment due to the presence of macromolecules, such as proteins, nucleic acids, ribosomes and carbohydrates [206]. In reality, protein folded inside cells, thus the intracellular environment mediated by the coacervates favors to fold protein in its compact native state and keep the stability of proteins. Besides, A water content of 68-83 wt% [178, 210] was reported for BSA- poly(diallyldimethylammonium chloride), PLys-PGlu, PLys-poly(L-aspartic acid), poly(L-histidine)-PGlu, poly (L-ornithine)-PGlu complex coacervates systems; the high amounts of water content trapped by coacervate dense phase can also protect the proteins against dehydration by heat evaporation.

The finding on encapsulated proteins by complex coacervation with improved thermal stability showed the promise for encapsulating viral particles and thermally stabilizing viruses via coacervation. We have developed a method to encapsulate viral particles in polymers that relies on the electrostatic interaction of viruses with polypeptides. Encapsulating viral particles via complex coacervation is a potential solution to the cold storage problem. The partitioning of viral particles into the dense phase and the effect of complex coacervates on the stability of viruses against high temperatures is described in Chapter 6.

## 2.5 References

1. Payne, S., *Viruses: from understanding to investigation*. 2017: Academic Press.
2. Flint, J., et al., *Principles of Virology*. 4th ed. 2015: ASM Press.
3. Moore, P.S. and Y.A. Chang, *Why do viruses cause cancer? Highlights of the first century of human tumour virology*. *Nature Reviews Cancer*, 2010. **10**(12): p. 878-889.
4. Ritchie, H. and M. Roser. *Causes of Death*. Our World in Data [cited 2019 September 30]; Available from: <https://ourworldindata.org/causes-of-death>.
5. Grubaugh, N.D., et al., *Tracking virus outbreaks in the twenty-first century*. *Nature microbiology*, 2019. **4**(1): p. 10-19.
6. WHO, *Situation report: Ebola virus disease, 10 June 2016*. World Health Organization, Geneva, 2016.
7. Dahl, B.A., *CDC's response to the 2014–2016 Ebola epidemic—Guinea, Liberia, and Sierra Leone*. *MMWR supplements*, 2016. **65**(3): p. 12-20.
8. WHO. *Ebola in the Democratic Republic of the Congo*. [cited 2019 September 30]; Available from: <https://www.who.int/emergencies/diseases/ebola/drc-2019>.
9. CDC. *Ebola (Ebola Virus Disease)*. [cited 2019 September 30]; Available from: <https://www.cdc.gov/vhf/ebola/index.html>.
10. WHO. *Ebola ring vaccination results 12 April 2019*. [cited 2019 April 12]; Available from: <https://www.who.int>.
11. Maxmen, A. *Two Ebola drugs show promise amid ongoing outbreak*. *Nature News*, 2019. DOI: 10.1038/d41586-019-02442-6.
12. Maes, P., et al., *Taxonomy of the order Mononegavirales: second update 2018*. *Archives of virology*, 2019. **164**(4): p. 1233-1244.
13. Bass III, P.F., *Measles makes a comeback: What to know, what to do*. *Contemporary Pediatrics*, 2019. **36**(7): p. 18-23.
14. CDC. *Measles (Rubeola)*. [cited 2019 September 26]; Available from: <https://www.cdc.gov/measles/cases-outbreaks.html>.
15. WHO. *Measles*. [cited 2019 May 9]; Available from: <https://www.who.int/news-room/fact-sheets/detail/measles>.
16. Dimitrov, D.S., *Virus entry: Molecular mechanisms and biomedical applications*. *Nature Reviews Microbiology*, 2004. **2**(2): p. 109-122.
17. Graham, B.S. and N.J. Sullivan, *Emerging viral diseases from a vaccinology perspective: preparing for the next pandemic*. *Nature Immunology*, 2018. **19**(1): p. 20-28.
18. ICTV, *ICTV Master Species List 2018b.v2*. 2018.
19. van Voorthuizen, E.M., N.J. Ashbolt, and A.I. Schafer, *Role of hydrophobic and electrostatic interactions for initial enteric virus retention by MF membranes*. *Journal of Membrane Science*, 2001. **194**(1): p. 69-79.
20. Dika, C., et al., *Isoelectric point is an inadequate descriptor of MS2, Phi X 174 and PRD1 phages adhesion on abiotic surfaces*. *Journal of Colloid and Interface Science*, 2015. **446**: p. 327-334.

21. Meder, F., et al., *The role of surface functionalization of colloidal alumina particles on their controlled interactions with viruses*. *Biomaterials*, 2013. **34**(17): p. 4203-4213.
22. Aronino, R., et al., *Removal of viruses from surface water and secondary effluents by sand filtration*. *Water Res*, 2009. **43**(1): p. 87-96.
23. Brown, M.R., et al., *Defining the Mechanistic Binding of Viral Particles to a Multi-modal Anion Exchange Resin*. *Biotechnology Progress*, 2018. **34**(4): p. 1019-1026.
24. Brown, M.R., et al., *A step-wise approach to define binding mechanisms of surrogate viral particles to multi-modal anion exchange resin in a single solute system*. *Biotechnology and Bioengineering*, 2017. **114**(7): p. 1487-1494.
25. Matsushita, T., et al., *Adsorptive virus removal with super-powdered activated carbon*. *Separation and Purification Technology*, 2013. **107**: p. 79-84.
26. Miesegaes, G.R., et al., *Monoclonal antibody capture and viral clearance by cation exchange chromatography*. *Biotechnology and Bioengineering*, 2012. **109**(8): p. 2048-2058.
27. Miesegaes, G., et al., *Viral clearance by flow-through mode ion exchange columns and membrane adsorbers*. *Biotechnology progress*, 2014. **30**(1): p. 124-131.
28. Strauss, D.M., et al., *Understanding the Mechanism of Virus Removal by Q Sepharose Fast Flow Chromatography During the Purification of CHO-Cell Derived Biotherapeutics*. *Biotechnology and Bioengineering*, 2009. **104**(2): p. 371-380.
29. Pan, C.W., et al., *Characterizing and enhancing virus removal by protein A chromatography*. *Biotechnology and Bioengineering*, 2019. **116**(4): p. 846-856.
30. Li, Z.J., et al., *Strong hydrophobicity enables efficient purification of HBc VLPs displaying various antigen epitopes through hydrophobic interaction chromatography*. *Biochemical Engineering Journal*, 2018. **140**: p. 157-167.
31. Brown, M.R., et al., *Evaluating the effect of in-process material on the binding mechanisms of surrogate viral particles to a multi-modal anion exchange resin*. *Journal of Biotechnology*, 2018. **267**: p. 29-35.
32. Heldt, C.L., et al., *Experimental and computational surface hydrophobicity analysis of a non-enveloped virus and proteins*. *Colloids and Surfaces B-Biointerfaces*, 2017. **153**: p. 77-84.
33. Johnson, S.A., et al., *The step-wise framework to design a chromatography-based hydrophobicity assay for viral particles*. *Journal of Chromatography B-Analytical Technologies in the Biomedical and Life Sciences*, 2017. **1061**: p. 430-437.
34. Voet, D., J.G. Voet, and C.W. Pratt, *Fundamentals of biochemistry: life at the molecular level*. 4th ed. 2013: John Wiley & Sons, Inc.
35. Balasubramanian, M.N., et al., *Enhanced detection of pathogenic enteric viruses in coastal marine environment by concentration using methacrylate monolithic chromatographic supports paired with quantitative PCR*. *Water Research*, 2016. **106**: p. 405-414.
36. Michen, B. and T. Graule, *Isoelectric points of viruses*. *Journal of applied microbiology*, 2010. **109**(2): p. 388-397.

37. Walker, G.C., *Net charge of trace proteins*. Nature Nanotechnology, 2016. **11**: p. 739.
38. Gerba, C.P. and W.Q. Betancourt, *Viral Aggregation: Impact on Virus Behavior in the Environment*. Environmental Science & Technology, 2017. **51**(13): p. 7318-7325.
39. Po, H.N. and N. Senozan, *The Henderson-Hasselbalch equation: its history and limitations*. Journal of Chemical Education, 2001. **78**(11): p. 1499.
40. Saeed, M., et al., *In Vitro Phosphorylation and Acetylation of the Murine Pocket Protein Rb2/p130*. Plos One, 2012. **7**(9).
41. Magarkar, A., et al., *Cholesterol level affects surface charge of lipid membranes in saline solution*. Scientific Reports, 2014. **4**.
42. Mi, X. and C.L. Heldt, *Adsorption of a non-enveloped mammalian virus to functionalized nanofibers*. Colloids and Surfaces B-Biointerfaces, 2014. **121**: p. 319-324.
43. Mi, X., K.S. Vijayaragavan, and C.L. Heldt, *Virus adsorption of water-stable quaternized chitosan nanofibers*. Carbohydrate Research, 2014. **387**: p. 24-29.
44. Leuchs, B., et al., *A novel scalable, robust downstream process for oncolytic rat parvovirus: isoelectric point-based elimination of empty particles*. Applied Microbiology and Biotechnology, 2017. **101**(8): p. 3143-3152.
45. McTigue, W.C.B. and S.L. Perry, *Design rules for encapsulating proteins into complex coacervates*. Soft Matter, 2019. **15**(15): p. 3089-3103.
46. Johnson, S., et al., *Characterization of Non-Infectious Virus-Like Particle Surrogates for Viral Clearance Applications*. Applied biochemistry and biotechnology, 2017. **183**(1): p. 318-331.
47. Shields, P.A. and S.R. Farrah, *Characterization of virus adsorption by using DEAE-sepharose and octyl-sepharose*. Applied and Environmental Microbiology, 2002. **68**(8): p. 3965-3968.
48. Xia, F., et al., *Evaluation of selectivity changes in HIC systems using a preferential interaction based analysis*. Biotechnology and Bioengineering, 2004. **87**(3): p. 354-363.
49. Walter, H., D.E. Brooks, and F. Derek, *Partitioning in aqueous two-phase system: theory, methods, uses, and applications to biotechnology*. 1985: Academic Press.
50. Miörner, H., P. Albertsson, and G. Kronvall, *Isoelectric points and surface hydrophobicity of Gram-positive cocci as determined by cross-partition and hydrophobic affinity partition in aqueous two-phase systems*. Infection and immunity, 1982. **36**(1): p. 227-234.
51. Joshi, P.U., et al., *Tie line framework to optimize non-enveloped virus recovery in aqueous two-phase systems*. Journal of Chromatography B, 2019. **1126**: p. 121744.
52. Vijayaragavan, K.S., et al., *Separation of porcine parvovirus from bovine serum albumin using PEG-salt aqueous two-phase system*. Journal of Chromatography B-Analytical Technologies in the Biomedical and Life Sciences, 2014. **967**: p. 118-126.

53. Wu, H.R., et al., *A resolution approach of racemic phenylalanine with aqueous two-phase systems of chiral tropine ionic liquids*. Journal of Chromatography A, 2015. **1418**: p. 150-157.
54. Zeng, C.X., et al., *Aqueous two-phase system based on natural quaternary ammonium compounds for the extraction of proteins*. Journal of Separation Science, 2016. **39**(4): p. 648-654.
55. Grilo, A.L., M.R. Aires-Barros, and A.M. Azevedo, *Partitioning in Aqueous Two-Phase Systems: Fundamentals, Applications and Trends*. Separation and Purification Reviews, 2016. **45**(1): p. 68-80.
56. Albertsson, P.-Å., S. SASAKAWA, and H. WALTER, *Cross partition and isoelectric points of proteins*. Nature, 1970. **228**(5278): p. 1329-1330.
57. Choi, H.J., et al., *Effect of Osmotic Pressure on the Stability of Whole Inactivated Influenza Vaccine for Coating on Microneedles*. Plos One, 2015. **10**(7).
58. Larryisgood. *Zeta Potential for a particle in dispersion medium*. 2011 [cited 2019 Dec. 15]; Available from: [https://en.wikipedia.org/wiki/File:Zeta\\_Potential\\_for\\_a\\_particle\\_in\\_dispersion\\_medium.png](https://en.wikipedia.org/wiki/File:Zeta_Potential_for_a_particle_in_dispersion_medium.png).
59. Wilson, W.W., et al., *Status of methods for assessing bacterial cell surface charge properties based on zeta potential measurements*. Journal of Microbiological Methods, 2001. **43**(3): p. 153-164.
60. Ayala-Torres, C., et al., *Zeta potential as a measure of the surface charge of mycobacterial cells*. Annals of Microbiology, 2014. **64**(3): p. 1189-1195.
61. Samandougou, I., I. Fliss, and J. Jean, *Zeta Potential and Aggregation of Virus-Like Particle of Human Norovirus and Feline Calicivirus Under Different Physicochemical Conditions*. Food and Environmental Virology, 2015. **7**(3): p. 249-260.
62. Hunter, R.J., *Zeta potential in colloid science: principles and applications*. Vol. 2. 2013: Academic press.
63. von Smoluchowski, M., *Handbuch der Electricität und des Magnetismus, volume II*. 1921, Graetz.
64. Shi, H. and V.V. Tarabara, *Charge, size distribution and hydrophobicity of viruses: Effect of propagation and purification methods*. Journal of Virological Methods, 2018. **256**: p. 123-132.
65. Dika, C., et al., *Impact of Internal RNA on Aggregation and Electrokinetics of Viruses: Comparison between MS2 Phage and Corresponding Virus-Like Particles*. Applied and Environmental Microbiology, 2011. **77**(14): p. 4939-4948.
66. Dika, C., et al., *Impact of the virus purification protocol on aggregation and electrokinetics of MS2 phages and corresponding virus-like particles*. Physical Chemistry Chemical Physics, 2013. **15**(15): p. 5691-5700.
67. Braun, M., et al., *A simple method to estimate the isoelectric point of modified Tomato bushy stunt virus (TBSV) particles*. Electrophoresis, 2017. **38**(21): p. 2771-2776.
68. Goodridge, L., et al., *Isoelectric point determination of norovirus virus-like particles by capillary Isoelectric focusing with whole column imaging detection*. Analytical Chemistry, 2004. **76**(1): p. 48-52.

69. Brorson, K., et al., *Characterization and purification of bacteriophages using chromatofocusing*. Journal of Chromatography A, 2008. **1207**(1-2): p. 110-121.
70. Pergande, M.R. and S.M. Cologna, *Isoelectric Point Separations of Peptides and Proteins*. Proteomes, 2017. **5**(1).
71. sharmin14, *Protein*. 2015.
72. Weichert, W.S., et al., *Assaying for structural variation in the parvovirus capsid and its role in infection*. Virology, 1998. **250**(1): p. 106-117.
73. Shen, H. and D.D. Frey, *Charge regulation in protein ion-exchange chromatography: Development and experimental evaluation of a theory based on hydrogen ion Donnan equilibrium*. Journal of Chromatography A, 2004. **1034**(1-2): p. 55-68.
74. Noy, A., D.V. Vezenov, and C.M. Lieber, *Chemical force microscopy*. Annual Review of Materials Science, 1997. **27**(1): p. 381-421.
75. Alsteens, D., et al., *Atomic force microscopy-based characterization and design of biointerfaces*. Nature Reviews Materials, 2017. **2**(5): p. 17008.
76. Barreto-Vieira, D.F. and O.M. Barth, *Negative and positive staining in transmission electron microscopy for virus diagnosis*. 2015: InTech.
77. Baro, A.M., et al., *DETERMINATION OF SURFACE-TOPOGRAPHY OF BIOLOGICAL SPECIMENS AT HIGH-RESOLUTION BY SCANNING TUNNELLING MICROSCOPY*. Nature, 1985. **315**(6016): p. 253-254.
78. Marchetti, M., G.J.L. Wuite, and W.H. Roos, *Atomic force microscopy observation and characterization of single virions and virus-like particles by nano-indentation*. Current Opinion in Virology, 2016. **18**: p. 82-88.
79. Guo, S.F., et al., *Measuring protein isoelectric points by AFM-based force spectroscopy using trace amounts of sample*. Nature Nanotechnology, 2016. **11**(9): p. 817-823.
80. Kuznetsov, Y.G. and A. McPherson, *Atomic Force Microscopy in Imaging of Viruses and Virus-Infected Cells*. Microbiology and Molecular Biology Reviews, 2011. **75**(2): p. 268-285.
81. Sullan, R.M.A., et al., *Atomic force microscopy with sub-picoNewton force stability for biological applications*. Methods, 2013. **60**(2): p. 131-141.
82. Alsteens, D., et al., *High-resolution imaging of chemical and biological sites on living cells using peak force tapping atomic force microscopy*. Langmuir, 2012. **28**(49): p. 16738-44.
83. Mateu, M.G., *Mechanical properties of viruses analyzed by atomic force microscopy: A virological perspective*. Virus Research, 2012. **168**(1-2): p. 1-22.
84. Baró, A.M. and R.G. Reifengerger, *Atomic Force Microscopy in Liquid*. 2012: Wiley-VCH.
85. Kuznetsov, Y.G., et al., *Imaging of viruses by atomic force microscopy*. Journal of General Virology, 2001. **82**(9): p. 2025-2034.
86. Moller, C., et al., *Tapping-mode atomic force microscopy produces faithful high-resolution images of protein surfaces*. Biophysical Journal, 1999. **77**(2): p. 1150-1158.

87. Pillet, F., et al., *Uncovering by Atomic Force Microscopy of an original circular structure at the yeast cell surface in response to heat shock*. *Bmc Biology*, 2014. **12**.
88. Ortega-Esteban, A., et al., *Monitoring dynamics of human adenovirus disassembly induced by mechanical fatigue*. *Scientific Reports*, 2013. **3**.
89. Leite, F., et al., *The atomic force spectroscopy as a tool to investigate surface forces: basic principles and applications*. *Modern Research and Educational Topics in Microscopy*, 2007.
90. Alessandrini, A. and P. Facci, *AFM: a versatile tool in biophysics*. *Measurement Science and Technology*, 2005. **16**(6): p. R65-R92.
91. Kámán, J., *Young's Modulus and Energy Dissipation Determination Methods by AFM, with Particular Reference to a Chalcogenide Thin Film*. *Periodica Polytechnica Electrical Engineering and Computer Science*, 2015. **59**(1): p. 18-25.
92. Ortega-Esteban, A., et al., *Structural and Mechanical Characterization of Viruses with AFM*, in *Atomic Force Microscopy*. 2019, Springer. p. 259-278.
93. de Pablo, P.J., *Atomic force microscopy of virus shells*. *Seminars in Cell & Developmental Biology*, 2018. **73**: p. 199-208.
94. de Pablo, P.J. and I.A.T. Schaap, *Atomic Force Microscopy of Viruses*, in *Physical Virology: Virus Structure and Mechanics*, U.F. Greber, Editor. 2019, Springer International Publishing: Cham. p. 159-179.
95. Ahimou, F., et al., *Probing microbial cell surface charges by atomic force microscopy*. *Langmuir*, 2002. **18**(25): p. 9937-9941.
96. El-Kirat-Chatel, S., et al., *Force Nanoscopy of Hydrophobic Interactions in the Fungal Pathogen *Candida glabrata**. *Acs Nano*, 2015. **9**(2): p. 1648-1655.
97. Williams, D.B. and C.B. Carter, *Transmission Electron Microscope*. Second ed. Part 1: Basics. 2009, New York: Springer.
98. Roingard, P., *Viral detection by electron microscopy: past, present and future*. *Biology of the Cell*, 2008. **100**(8): p. 491-501.
99. Horowitz, E.D., et al., *Biophysical and ultrastructural characterization of adeno-associated virus capsid uncoating and genome release*. *Journal of virology*, 2013. **87**(6): p. 2994-3002.
100. Roingard, P., et al., *Virus detection by transmission electron microscopy: Still useful for diagnosis and a plus for biosafety*. *Reviews in medical virology*, 2019. **29**(1): p. e2019.
101. Vashist, S.K. and J.H. Luong, *Handbook of immunoassay technologies: approaches, performances, and applications*. 2018: Academic Press.
102. Walsh, J.H., *RADIOIMMUNOASSAY OF AUSTRALIA ANTIGEN*. *Vox Sanguinis*, 1971. **20**(5): p. 460-&.
103. Cinquanta, L., D.E. Fontana, and N. Bizzaro, *Chemiluminescent immunoassay technology: what does it change in autoantibody detection?* *Autoimmunity Highlights*, 2017. **8**(1).
104. Chang, L., J.M. Li, and L.N. Wang, *Immuno-PCR: An ultrasensitive immunoassay for biomolecular detection*. *Analytica Chimica Acta*, 2016. **910**: p. 12-24.



105. Yu, S.T., et al., *Clinical evaluation of rapid fluorescent diagnostic immunochromatographic test for influenza A virus (H1N1)*. Scientific Reports, 2018. **8**.
106. Coleman, W.B. and G.J. Tsongalis, *Diagnostic Molecular Pathology: A Guide to Applied Molecular Testing*. 2016: Academic Press.
107. Enzoklop. *Polymerase chain reaction*. 2014 [cited 2020 Jan. 04]; Schematic drawing of the PCR cycle]. Available from: [https://commons.wikimedia.org/wiki/File:Polymerase\\_chain\\_reaction.svg](https://commons.wikimedia.org/wiki/File:Polymerase_chain_reaction.svg).
108. Mun, M.J., et al., *One-step multiplex real-time RT-PCR for detection and typing of dengue virus*. Molecular and Cellular Probes, 2019. **43**: p. 86-91.
109. Albertoni, G., M. Girao, and N. Schor, *Mini review: Current molecular methods for the detection and quantification of hepatitis B virus, hepatitis C virus, and human immunodeficiency virus type 1*. International Journal of Infectious Diseases, 2014. **25**: p. 145-149.
110. Blackburn, R.M., D. Frampton, and C.M.e.a.O.B.o.t.I.g. Smith, *Nosocomial transmission of influenza: A retrospective cross-sectional study using next generation sequencing at a hospital in England (2012-2014)*. Influenza and Other Respiratory Viruses, 2019(00).
111. Li, T., et al., *Metagenomic Next-Generation Sequencing of the 2014 Ebola Virus Disease Outbreak in the Democratic Republic of the Congo*. Journal of Clinical Microbiology, 2019. **57**(9): p. e00827-19.
112. Baer, A. and K. Kehn-Hall, *Viral Concentration Determination Through Plaque Assays: Using Traditional and Novel Overlay Systems*. Jove-Journal of Visualized Experiments, 2014(93).
113. Cromeans, T.L., et al., *Development of plaque assays for adenoviruses 40 and 41*. Journal of Virological Methods, 2008. **151**(1): p. 140-145.
114. Suchman, E. and C. Blair, *Cytopathic effects of viruses protocols*. 2007.
115. Smither, S.J., et al., *Comparison of the plaque assay and 50% tissue culture infectious dose assay as methods for measuring filovirus infectivity*. Journal of Virological Methods, 2013. **193**(2): p. 565-571.
116. Stockert, J.C., et al., *Tetrazolium salts and formazan products in Cell Biology: Viability assessment, fluorescence imaging, and labeling perspectives*. Acta Histochemica, 2018. **120**(3): p. 159-167.
117. Heldt, C.L., et al., *A colorimetric assay for viral agents that produce cytopathic effects*. J Virol Methods, 2006. **135**(1): p. 56-65.
118. Amendola, V., et al., *Surface plasmon resonance in gold nanoparticles: a review*. Journal of Physics-Condensed Matter, 2017. **29**(20).
119. Yeo, E.L.L., et al., *Understanding aggregation-based assays: nature of protein corona and number of epitopes on antigen matters*. Rsc Advances, 2015. **5**(20): p. 14982-14993.
120. Lee, C., et al., *Colorimetric viral detection based on sialic acid stabilized gold nanoparticles*. Biosensors & Bioelectronics, 2013. **42**: p. 236-241.
121. Palomino-Vizcaino, G., et al., *Effect of HPV16 L1 virus-like particles on the aggregation of non-functionalized gold nanoparticles*. Biosensors & Bioelectronics, 2018. **100**: p. 176-183.

122. Wang, X.H., et al., *Gold nanorod-based localized surface plasmon resonance biosensor for sensitive detection of hepatitis B virus in buffer, blood serum and plasma*. *Biosensors & Bioelectronics*, 2010. **26**(2): p. 404-410.
123. Wang, X.H., et al., *Detection of hepatitis B surface antigen by target-induced aggregation monitored by dynamic light scattering*. *Analytical Biochemistry*, 2012. **428**(2): p. 119-125.
124. Pylaev, T.E., et al., *Colorimetric and dynamic light scattering detection of DNA sequences by using positively charged gold nanospheres: a comparative study with gold nanorods*. *Nanotechnology*, 2011. **22**(28).
125. Chen, Y., et al., *Aggregation and antigenicity of virus like particle in salt solution-A case study with hepatitis B surface antigen*. *Vaccine*, 2015. **33**(35): p. 4300-4306.
126. Kaminska, A., et al., *Detection of Hepatitis B virus antigen from human blood: SERS immunoassay in a microfluidic system*. *Biosensors & Bioelectronics*, 2015. **66**: p. 461-467.
127. Lu, X.C., et al., *A gold nanorods-based fluorescent biosensor for the detection of hepatitis B virus DNA based on fluorescence resonance energy transfer*. *Analyst*, 2013. **138**(2): p. 642-650.
128. Wang, Y.F., et al., *Visual gene diagnosis of HBV and HCV based on nanoparticle probe amplification and silver staining enhancement*. *Journal of Medical Virology*, 2003. **70**(2): p. 205-211.
129. Wang, Y., et al., *Detection of Hepatitis B Virus Deoxyribonucleic Acid Based on Gold Nanoparticle Probe Chip*. *Chinese Journal of Analytical Chemistry*, 2010. **38**(8): p. 1133-1138.
130. Shawky, S.M., et al., *Gold aggregating gold: A novel nanoparticle biosensor approach for the direct quantification of hepatitis C virus RNA in clinical samples*. *Biosensors & Bioelectronics*, 2017. **92**: p. 349-356.
131. Li, W., et al., *Catalytic signal amplification of gold nanoparticles combining with conformation-switched hairpin DNA probe for hepatitis C virus quantification*. *Chemical Communications*, 2012. **48**(63): p. 7877-7879.
132. Shawky, S.M., D. Bald, and H.M.E. Azzazy, *Direct detection of unamplified hepatitis C virus RNA using unmodified gold nanoparticles*. *Clinical Biochemistry*, 2010. **43**(13-14): p. 1163-1168.
133. Hu, Y.W., et al., *Green-synthesized gold nanoparticles decorated graphene sheets for label-free electrochemical impedance DNA hybridization biosensing*. *Biosensors & Bioelectronics*, 2011. **26**(11): p. 4355-4361.
134. Xu, X.Y., et al., *Homogeneous detection of nucleic acids based upon the light scattering properties of silver-coated nanoparticle probes*. *Analytical Chemistry*, 2007. **79**(17): p. 6650-6654.
135. Driskell, J.D., et al., *One-step assay for detecting influenza virus using dynamic light scattering and gold nanoparticles*. *Analyst*, 2011. **136**(15): p. 3083-3090.
136. Liu, Y.J., et al., *Colorimetric detection of influenza A virus using antibody-functionalized gold nanoparticles*. *Analyst*, 2015. **140**(12): p. 3989-3995.
137. Zhao, J.Q., et al., *Multiplexed, rapid detection of H5N1 using a PCR-free nanoparticle-based genomic microarray assay*. *Bmc Biotechnology*, 2010. **10**.

138. Fonin, A., et al., *Protein folding and stability in the presence of osmolytes*. Biophysics, 2016. **61**(2): p. 185-192.
139. Timasheff, S.N., *Protein-solvent preferential interactions, protein hydration, and the modulation of biochemical reactions by solvent components*. Proceedings of the National Academy of Sciences of the United States of America, 2002. **99**(15): p. 9721-9726.
140. Auton, M., et al., *Osmolyte effects on protein stability and solubility: A balancing act between backbone and side-chains*. Biophysical Chemistry, 2011. **159**(1): p. 90-99.
141. Street, T.O., *A molecular mechanism for osmolyte-induced protein stability*. Biophysical Journal, 2007: p. 217A-217A.
142. Gencoglu, M.F., E. Pearson, and C.L. Heldt, *Porcine parvovirus flocculation and removal in the presence of osmolytes*. Journal of Biotechnology, 2014. **186**: p. 83-90.
143. Gencoglu, M. and C. Heldt, *Enveloped virus flocculation and removal in osmolyte solutions*. Journal of biotechnology, 2015. **206**: p. 8-11.
144. Hu, C.Y., B.M. Pettitt, and J. Roesgen, *Osmolyte solutions and protein folding*. F1000 biology reports, 2009. **1**(41): p. 1.
145. Bolen, D.W., *Effects of naturally occurring osmolytes on protein stability and solubility: issues important in protein crystallization*. Methods, 2004. **34**(3): p. 312-322.
146. Patel, A.J., et al., *Sitting at the edge: How biomolecules use hydrophobicity to tune their interactions and function*. The Journal of Physical Chemistry B, 2012. **116**(8): p. 2498-2503.
147. Godawat, R., S.N. Jamadagni, and S. Garde, *Characterizing hydrophobicity of interfaces by using cavity formation, solute binding, and water correlations*. Proceedings of the National Academy of Sciences of the United States of America, 2009. **106**(36): p. 15119-15124.
148. Heldt, C.L., et al., *A Generalized Purification Step for Viral Particles Using Mannitol Flocculation*. Biotechnology Progress, 2018. **34**(4): p. 1027-1035.
149. Willis, N., *Edward Jenner and the eradication of smallpox*. Scottish medical journal, 1997. **42**(4): p. 118-121.
150. FDA. *Vaccines Licensed for Use in the United States*. 2019 [cited 2019 July 20]; Available from: <https://www.fda.gov/vaccines-blood-biologics/vaccines/vaccines-licensed-use-united-states>.
151. WHO. *Vaccines*. 2019 [cited 2019 July 20]; Available from: <https://www.who.int/topics/vaccines/en/>.
152. WHO. *Immunization*. 2019 [cited 2019 July 20]; Available from: <https://www.who.int/news-room/facts-in-pictures/detail/immunization>.
153. GAVI. *Disease burden & equity*. 2019 [cited 2019 July 20]; Available from: <https://www.gavi.org/about/mission/facts-and-figures/>.
154. Brandau, D.T., et al., *Thermal stability of vaccines*. Journal of Pharmaceutical Sciences, 2003. **92**(2): p. 218-231.

155. Hamborsky, J., et al., *Epidemiology and prevention of vaccine-preventable diseases*. 2015: US Department of Health & Human Services, Centers for Disease Control and ....
156. Plotkin, S.A., *Vaccines: the fourth century*. Clin. Vaccine Immunol., 2009. **16**(12): p. 1709-1719.
157. HHS. *Vaccine Types*. 2019 [cited 2019 July 20]; Available from: <https://www.vaccines.gov/basics/types>.
158. NIH. *Vaccine Types*. 2019 [cited 2019 July 20]; Available from: <https://www.niaid.nih.gov/research/vaccine-types>.
159. Organization, W.H., W.H.O.D.o. Immunization, and Biologicals, *Immunization in practice: A practical guide for health staff*. 2015: World Health Organization.
160. Ashok, A., M. Brison, and Y. LeTallec, *Improving cold chain systems: Challenges and solutions*. Vaccine, 2017. **35**(17): p. 2217-2223.
161. Comes, T., K.B. Sandvik, and B. Van de Walle, *Cold chains, interrupted: The use of technology and information for decisions that keep humanitarian vaccines cool*. Journal of Humanitarian Logistics and Supply Chain Management, 2018. **8**(1): p. 49-69.
162. WHO, *Immunization in practice: A practical guide for health staff*. 2015: World Health Organization.
163. WHO, *Monitoring vaccine wastage at country level*. 2018.
164. Chen, D.X. and D. Kristensen, *Opportunities and challenges of developing thermostable vaccines*. Expert Review of Vaccines, 2009. **8**(5): p. 547-557.
165. HogenEsch, H., D.T. O'Hagan, and C.B. Fox, *Optimizing the utilization of aluminum adjuvants in vaccines: you might just get what you want*. Npj Vaccines, 2018. **3**.
166. Dangi, A.A., et al., *Formulation and development of vaccines and their selection for next generation*. Bull. Pharm. Res, 2011. **1**(3): p. 49-62.
167. Martin, N., M. Li, and S. Mann, *Selective Uptake and Refolding of Globular Proteins in Coacervate Microdroplets*. Langmuir, 2016. **32**(23): p. 5881-5889.
168. Water, J.J., et al., *Complex coacervates of hyaluronic acid and lysozyme: Effect on protein structure and physical stability*. European Journal of Pharmaceutics and Biopharmaceutics, 2014. **88**(2): p. 325-331.
169. Kristensen, D., *Summary of stability data for licensed vaccines*. PATH: Seattle, 2012.
170. Kumru, O.S., et al., *Vaccine instability in the cold chain: Mechanisms, analysis and formulation strategies*. Biologicals, 2014. **42**(5): p. 237-259.
171. Burke, C.J., T.A. Hsu, and D.B. Volkin, *Formulation, stability, and delivery of live attenuated vaccines for human use*. Critical Reviews in Therapeutic Drug Carrier Systems, 1999. **16**(1): p. 1-83.
172. Kaushik, J.K. and R. Bhat, *Why is trehalose an exceptional protein stabilizer? An analysis of the thermal stability of proteins in the presence of the compatible osmolyte trehalose*. Journal of Biological Chemistry, 2003. **278**(29): p. 26458-26465.

173. Blocher, W.C. and S.L. Perry, *Complex coacervate-based materials for biomedicine*. Wiley Interdisciplinary Reviews-Nanomedicine and Nanobiotechnology, 2017. **9**(4).
174. Timilsena, Y.P., et al., *Complex coacervation: Principles, mechanisms and applications in microencapsulation*. International Journal of Biological Macromolecules, 2019. **121**: p. 1276-1286.
175. Pathak, J., et al., *Complex coacervation in charge complementary biopolymers: Electrostatic versus surface patch binding*. Advances in Colloid and Interface Science, 2017. **250**: p. 40-53.
176. Perry, S.L., et al., *The Effect of Salt on the Complex Coacervation of Vinyl Polyelectrolytes*. Polymers, 2014. **6**(6): p. 1756-1772.
177. Chang, L.W., et al., *Sequence and entropy-based control of complex coacervates*. Nature Communications, 2017. **8**.
178. Priftis, D. and M. Tirrell, *Phase behaviour and complex coacervation of aqueous polypeptide solutions*. Soft Matter, 2012. **8**(36): p. 9396-9405.
179. Jho, Y., et al., *Molecular and structural basis of low interfacial energy of complex coacervates in water*. Advances in Colloid and Interface Science, 2017. **239**: p. 61-73.
180. Priftis, D., N. Laugel, and M. Tirrell, *Thermodynamic Characterization of Polypeptide Complex Coacervation*. Langmuir, 2012. **28**(45): p. 15947-15957.
181. Qin, J., et al., *Interfacial Tension of Polyelectrolyte Complex Coacervate Phases*. Acs Macro Letters, 2014. **3**(6): p. 565-568.
182. Sarmiento, B., et al., *Alginate/chitosan nanoparticles are effective for oral insulin delivery*. Pharmaceutical research, 2007. **24**(12): p. 2198-2206.
183. Johnson, N.R., T. Ambe, and Y.D. Wang, *Lysine-based polycation:heparin coacervate for controlled protein delivery*. Acta Biomaterialia, 2014. **10**(1): p. 40-46.
184. Liu, Z.H., et al., *Polysaccharides-based nanoparticles as drug delivery systems*. Advanced Drug Delivery Reviews, 2008. **60**(15): p. 1650-1662.
185. Leong, K.W., et al., *DNA-polycation nanospheres as non-viral gene delivery vehicles*. Journal of Controlled Release, 1998. **53**(1-3): p. 183-193.
186. Ozbas-Turan, S., et al., *Co-encapsulation of two plasmids in chitosan microspheres as a non-viral gene delivery vehicle*. Journal of Pharmacy and Pharmaceutical Sciences, 2003. **6**(1): p. 27-32.
187. Mann, L.K., et al., *Fetal membrane patch and biomimetic adhesive coacervates as a sealant for fetoscopic defects*. Acta Biomaterialia, 2012. **8**(6): p. 2160-2165.
188. Winslow, B.D., et al., *Biocompatibility of adhesive complex coacervates modeled after the sandcastle glue of *Phragmatopoma californica* for craniofacial reconstruction*. Biomaterials, 2010. **31**(36): p. 9373-9381.
189. Galan, A. and P. Ballester, *Stabilization of reactive species by supramolecular encapsulation*. Chemical Society Reviews, 2016. **45**(6): p. 1720-1737.
190. Black, K.A., et al., *Protein Encapsulation via Polypeptide Complex Coacervation*. Acs Macro Letters, 2014. **3**(10): p. 1088-1091.

191. Zhao, M.M. and N.S. Zacharia, *Protein encapsulation via polyelectrolyte complex coacervation: Protection against protein denaturation*. Journal of Chemical Physics, 2018. **149**(16).
192. de Kruijff, C.G., F. Weinbreck, and R. de Vries, *Complex coacervation of proteins and anionic polysaccharides*. Current Opinion in Colloid & Interface Science, 2004. **9**(5): p. 340-349.
193. Kapelner, R.A. and A.C. Obermeyer, *Ionic polypeptide tags for protein phase separation*. Chemical Science, 2019. **10**(9): p. 2700-2707.
194. Cummings, C.S. and A.C. Obermeyer, *Phase Separation Behavior of Supercharged Proteins and Polyelectrolytes*. Biochemistry, 2018. **57**(3): p. 314-323.
195. Obermeyer, A.C., et al., *Complex coacervation of supercharged proteins with polyelectrolytes*. Soft Matter, 2016. **12**(15): p. 3570-3581.
196. Lindhoud, S. and M. Claessens, *Accumulation of small protein molecules in a macroscopic complex coacervate*. Soft Matter, 2016. **12**(2): p. 408-413.
197. Giteau, A., et al., *Reversible protein precipitation to ensure stability during encapsulation within PLGA microspheres*. European Journal of Pharmaceutics and Biopharmaceutics, 2008. **70**(1): p. 127-136.
198. Kumar, P.S., et al., *Influence of microencapsulation method and peptide loading on formulation of poly(lactide-co-glycolide) insulin nanoparticles*. Pharmazie, 2006. **61**(7): p. 613-617.
199. Pisal, D.S., M.P. Kosloski, and S.V. Balu-Iyer, *Delivery of Therapeutic Proteins*. Journal of Pharmaceutical Sciences, 2010. **99**(6): p. 2557-2575.
200. Schmitt, C. and S.L. Turgeon, *Protein/polysaccharide complexes and coacervates in food systems*. Advances in colloid and interface science, 2011. **167**(1-2): p. 63-70.
201. Pippa, N., et al., *Complexation of cationic-neutral block polyelectrolyte with insulin and in vitro release studies*. International journal of pharmaceutics, 2015. **491**(1-2): p. 136-143.
202. Chang, P.G., et al., *Optimisation of the complex coacervation between canola protein isolate and chitosan*. Journal of food engineering, 2016. **191**: p. 58-66.
203. Kim, Y.H. and W.E. Stites, *Effects of excluded volume upon protein stability in covalently cross-linked proteins with variable linker lengths*. Biochemistry, 2008. **47**(33): p. 8804-8814.
204. Miklos, A.C., et al., *Volume Exclusion and Soft Interaction Effects on Protein Stability under Crowded Conditions*. Biochemistry, 2010. **49**(33): p. 6984-6991.
205. Aden, J. and P. Wittung-Stafshede, *Folding of an Unfolded Protein by Macromolecular Crowding in Vitro*. Biochemistry, 2014. **53**(14): p. 2271-2277.
206. Dzieciol, A.J. and S. Mann, *Designs for life: protocell models in the laboratory*. Chemical Society Reviews, 2012. **41**(1): p. 79-85.
207. Tang, T.Y.D., et al., *Fatty acid membrane assembly on coacervate microdroplets as a step towards a hybrid protocell model*. Nature Chemistry, 2014. **6**(6): p. 527-533.
208. Koga, S., et al., *Peptide-nucleotide microdroplets as a step towards a membrane-free protocell model*. Nature Chemistry, 2011. **3**(9): p. 720-724.

209. Tang, T.Y.D., et al., *Small-molecule uptake in membrane-free peptide/nucleotide protocells*. *Soft Matter*, 2013. **9**(31): p. 7647-7656.
210. Bohidar, H., et al., *Effects of protein-polyelectrolyte affinity and polyelectrolyte molecular weight on dynamic properties of bovine serum albumin-poly(diallyldimethylammonium chloride) coacervates*. *Biomacromolecules*, 2005. **6**(3): p. 1573-1585.

# **3 Virus surface chemistry characterization<sup>1</sup>**

---

<sup>1</sup> The material contained in this chapter is in preparation for submission.



### 3.1 Introduction

Virus surface chemistry, primarily the hydrophobicity and surface charge of the virus, determines its mobility and governs its colloidal behavior in virus adsorption processes. Both the hydrophobicity and surface charge of the virus can dominate virus removal performance in different solution environments [1-3]. Hydrophobic interaction chromatography (HIC) has been used to purify viral particles [4, 5] and as a measure of viral particle hydrophobicity [6, 7]. Viruses are well known to adhere to charged surfaces [2, 8] and charge-charge interaction is often used to remove viruses. However, each of these methods requires large amounts of virus for detection by infectivity assays or nucleic acid amplification by polymerase chain reaction. A method to develop virus purification and removal techniques is needed that requires less virus, therefore reducing time and resources. We propose that knowledge of virus surface chemistry measured in a small volume could fulfill this need.

There is limited information on the surface chemistry of virus [6, 9]. Current methods have been used to characterize the virus surface chemistry, including HIC [10], virus adsorption to known chemical surfaces [11, 12], zeta potential [13], and isoelectric focusing [14]. The disadvantages of these methods are that many require large amounts of virus, and they are bulk measurements. Bulk measurements can be affected by purification methods [15], solution conditions [16], and cannot account for heterogeneity in the virus population [17]. In addition, the cost of production and purification of a large quantity of virus is high. Hence, there is a need for methods that can accurately target single virus particles and simultaneously measure the surface chemistry of the virus with trace amounts of samples.

A novel surface characterization method, chemical force microscopy (CFM) [18], which uses chemical interactions between a functionalized atomic force microscopy (AFM) tip and a sample, is leading to a renewed look at single particle virus surface chemistry. CFM is a versatile method for monitoring the topography of the sample and measuring the interaction forces between a functionalized AFM tip and a sample [19]. The chemical interaction is measured by the deflection of the AFM cantilever during the AFM tip approach and withdrawal [20]. The deflection can be converted into the force needed to pull the functionalized AFM tip from the sample using the spring constant of the cantilever and Hooke's law [21]. The AFM probe pull-off force during withdrawal from the sample can be quantified as a measurement of adhesion force [18] and can be used to compare the surface chemistry of samples [22].

CFM is a sensitive and reliable tool to evaluate the surface chemistry of soft biological material. CFM has been reported to map the hydrophobic interactions of the microbial pathogen *Aspergillus fumigatus* with a hydrophobic (methyl-functionalized) AFM tip [23], and measure the hydrophobic forces between a fibronectin-modified AFM tip and a methyl acetate-modified substrate [24]. For surface charge measurements by CFM, it has been reported that carboxyl acid-modified AFM probes have been used to determine the surface charge of a single *S. cerevisiae* cell surface at various pH [25]. Protein surface charge at various pH has been explored by measuring the adhesion forces between four target proteins (bovine serum albumin, myoglobin, fibrinogen, and

ribonuclease A) that were covalently immobilized onto an AFM probe and a charged substrate [26].

CFM is suitable to probe the surface chemistry of nanometer-sized virus particles. One advantage of CFM is that the virus can be studied in a physiological environment without disturbing the natural state of the virus [27]. CFM can measure chemical interactions ranging from strong covalent bonds ( $\sim 100$  nN) to weak van der Waals forces ( $\sim 1$  pN) [18], making it a suitable tool for measurement of hydrophobic interactions and surface charge of virus particles.

To develop CFM as a way to measure virus surface chemistry, we first demonstrated that covalently binding virus to a surface could keep the natural size and shape of the virus without deformation or disassembly, as compared to a physical adsorption method. Then, AFM probe functionalization was explored and the optimal coating concentration and time for each interested chemistry were determined. Finally, the successfully functionalized AFM probes were used for virus surface chemistry study. CFM with a methyl-terminated probe was used to study the surface hydrophobicity of a virus. CFM with a charged probe was used to study the surface charge of a virus. With a thorough understanding of virus surface chemistry, future virus purification and removal techniques could be significantly improved to specifically absorb viral particles.

## 3.2 Experimental section

### 3.2.1 Materials

Potassium phosphate monobasic (molecular biology grade,  $\geq 99.0\%$ ), sodium phosphate monobasic monohydrate (ACS grade, 98.0-102.0%), and sodium chloride (ACS grade,  $\geq 99.0\%$ ) were a gift from Millipore Sigma (Burlington, MA). Sodium phosphate dibasic heptahydrate (ACS grade, 98.0-102.0%), 12-mercaptododecanoic acid ( $\text{HS}(\text{CH}_2)_{11}\text{COOH}$ , 96%), 1-dodecanethiol ( $\text{HS}(\text{CH}_2)_{11}\text{CH}_3$ ,  $\geq 98\%$ ), 11-mercaptoundecyl)-N,N,N-trimethylammonium bromide ( $\text{HS}(\text{CH}_2)_{11}\text{N}(\text{CH}_3)_3\text{Br}$ ), and primary amine ( $\text{NH}_2$ ) functionalized silica nanoparticles (nanoparticles  $< 30$  nm (DLS)) were purchased from Sigma-Aldrich (St. Louis, MO). N-hydroxysulfosuccinimide (NHS) and 1-ethyl-3-(3-dimethylaminopropyl) carbodiimide hydrochloride (EDC) were purchased from Thermo Fisher Scientific (Grand Island, NY). All aqueous solutions or buffers were prepared using purified water with a resistivity of  $\geq 18 \text{ M}\Omega \cdot \text{cm}$  from a Nanopure filtration system (Thermo Scientific, Waltham, MA) and filtered with a  $0.2 \mu\text{m}$  bottle top filter (VWR, Radnor, PA) or a  $0.2 \mu\text{m}$  syringe filter (VWR) prior to use. A standard phosphate buffered saline (PBS) (pH 7.2) was prepared by dissolving 0.21 g potassium phosphate monobasic, 0.726 g sodium phosphate dibasic heptahydrate, and 9 g sodium chloride into 1000 mL Nanopure water. A 20 mM phosphate buffer (PB) solution (pH 7.0) was prepared by dissolving 1.0763 g sodium phosphate monobasic monohydrate and 3.2705 g sodium phosphate dibasic heptahydrate into 1000 mL of Nanopure water.

### 3.2.2 Virus purification

Porcine parvovirus (PPV) strain NADL-2, was a gift from Dr. Ruben Carbonell (North Carolina State University, Raleigh, NC). Bovine viral diarrhea virus (BVDV) strain NADL was purchased from USDA APHIS. For purification of both PPV and BVDV, the virus was first dialyzed using a Biotech Cellulose Ester 1,000 kDa dialysis tubing (Rancho Dominguez, CA) at 4°C for two days with two buffer exchanges to remove small sized protein contaminants. The exchanged buffer was either PBS (for virus hydrophobicity study) or 20 mM PB (for virus surface charge study). The dialyzed virus was further purified with a Bio-Rad Econo-Pac 10DG desalting column (Hercules, CA). The concentrations of purified virus solutions were determined from titrations to be  $1 \times 10^8$  MTT<sub>50</sub>/mL for PPV and  $1 \times 10^7$  MTT<sub>50</sub>/mL for BVDV using an MTT assay [28, 29].

### 3.2.3 Virus samples and control surfaces preparation

A glass slide with an area of 2.54 cm<sup>2</sup> was coated with 5 nm of chromium with a Perkin-Elmer Randex Sputtering System (Model 2400, Waltham, MA). The chromium-coated slide was further coated with a 30 nm gold layer using the sputter. All of the deposition steps were performed under a  $5 \times 10^{-6}$  Torr vacuum. The bifunctional linkers were attached to the gold-coated slide by immersing the slide in 14 mL of a mixed solution containing a total of 2 mM of HS(CH<sub>2</sub>)<sub>11</sub>COOH and HS(CH<sub>2</sub>)<sub>11</sub>CH<sub>3</sub> in ethanol for 12 hours. Then the slide was rinsed with ethanol and air dried in a chemical hood. The ratio of carboxylic acid and methyl capped thiols was 1:1, unless stated otherwise. The functionalized surface was equilibrated with 14 mL Nanopure water for 15 minutes to remove any free bifunctional linkers from the surface. The surface was further treated with a total of 0.5 mL of an equal volume mixture of 0.1 M NHS and 0.4 M EDC in Nanopure water [30, 31] for 30 minutes and equilibrated with PBS (pH 7.2) for 2 minutes. This step was to activate the carboxylic acid groups to NHS esters. After activation, 0.5 mL of virus surrogate NH<sub>2</sub>-functionalized silica nanoparticles or purified PPV or BVDV was applied to the surface for 30 minutes. Finally, the surface was washed with Nanopure water three times to remove any unattached virus or silica particles. The virus or silica nanoparticles functionalized surfaces were stored in either a 14 mL of PBS or 14 mL of 20 mM PB (pH 7.0) at 4°C, depending on if hydrophobic or charge interactions were to be measured, respectively. The control surfaces were prepared in the same manner except one pure thiol compound was used.

### 3.2.4 AFM probe modification

For hydrophobicity measurements, gold-coated Bruker AC-40 AFM probes (spring constant ~0.1 N/m, tip radius ~10 nm) were immersed in a 14 mL ethanol containing 4 mM of HS(CH<sub>2</sub>)<sub>11</sub>CH<sub>3</sub> for 24 hours, rinsed with ethanol, and air-dried in a chemical hood. For surface charge measurement, negatively-charged AFM probes were prepared by immersing the AC-40 AFM probes in the same manner in HS(CH<sub>2</sub>)<sub>11</sub>COOH. Similarly, positively charged AFM probes were modified by incubating the NT-MDT GSG10/Au AFM probes (spring constant ~0.11 N/m, tip radius ~35 nm) in

a 14 mL ethanol-containing 10 mM solution of HS(CH<sub>2</sub>)<sub>11</sub>N(CH<sub>3</sub>)<sub>3</sub>Br for 48 hours, rinsed with ethanol, and air-dried in a chemical hood.

### 3.2.5 AFM imaging, force measurement and analysis

All AFM experiments were carried out at room temperature (~20°C), using a Bruker Dimension ICON Atomic Force Microscope with ScanAsyst (Santa Barbara, CA). The AFM topographic images were obtained using ScanAsyst in liquid (in imaging tapping mode) at a scanning rate of ~1 Hz and 512 × 512 pixels over scan areas of 500 × 500 nm, with a Bruker ScanAsyst-Fluid+ silicon nitride AFM probe (spring constant ~0.7 N/m, tip radius ~2 nm) or a NT-MDT GSG30 AFM probe (spring constant ~0.6 N/m, tip radius ~6 nm). All topographic images were obtained in PBS pH 7.2.

AFM force measurements were performed in PeakForce QNM (tapping mode) or contact mode in liquid. As the AFM probe spring constant can change during the chemical modification, it was calibrated before the force measurement experiment by measuring the thermal noise of the free cantilever in liquid [32]. We recorded five consecutive F-D curves for a single viral particle and then would move to another viral particle to record another set of curves. Over 500 F-D curves were recorded with at least three separate combinations of probe/virus samples. All F-D curve measurements between modified probes and viral particle surfaces were collected in liquid conditions with PBS (for hydrophobicity measurement) at pH 7.2 or in 20 mM PB at pH 7.0 (for surface charge measurement). The control experiments were carried out under the same conditions. Data analysis was performed with the Bruker Nanoscope Analysis software, and all the figures were drawn with Excel unless stated otherwise.

## 3.3 Results and discussion

To characterize virus surface chemistry by the single particle CFM method, the key steps were the functionalization of AFM probes with the chemical functional group of interest and immobilization of virus particles on a surface, as shown in **Figure 3.1**. We used standard methods to functionalize the gold-coated AFM tips. However, virus AFM experiments are commonly done by adsorption of the virus to a surface, and characterization is by nanoindentation [33-35]. The goal of nanoindentation is to measure the force needed to break open a virus capsid by pushing on it. However, in our work, we are pulling on the virus rather than pushing on it. By covalently bonding the virus to the surface, we would be assured that the AFM force experiment was measuring chemical interaction between the virus and the AFM probe, and not the virus and the solid surface.

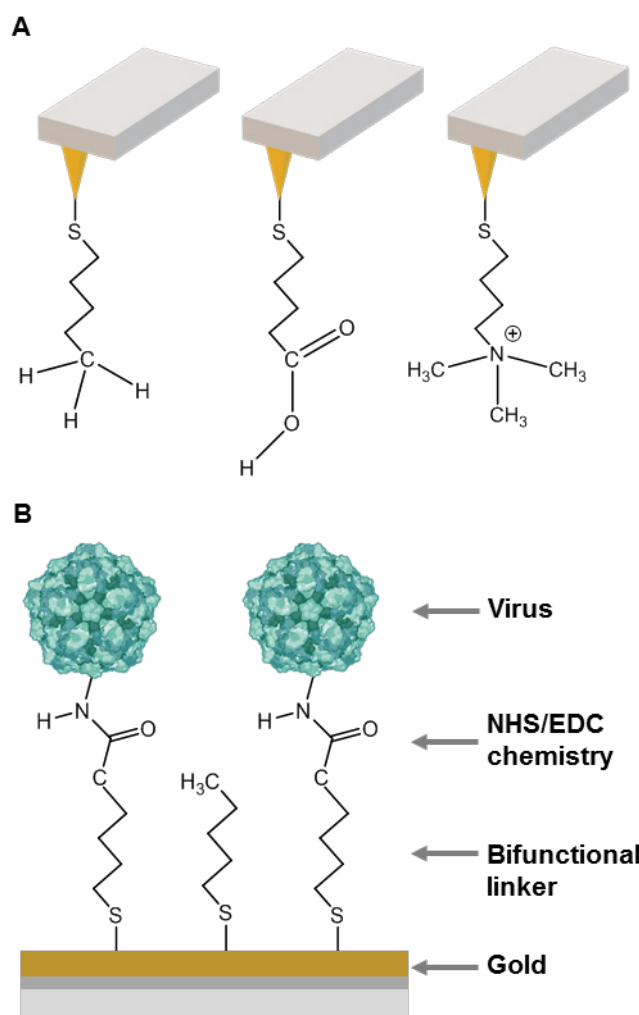


**Figure 3.1** Overview of AFM probe surface modification and virus attachment on a gold surface. (A) AFM probes were functionalized with either a hydrophobic methyl group, a negatively charged carboxyl acid group, or a positively charged quaternary amine group. (B) Virus particles were immobilized with NHS/EDC chemistry. (Virus image was created in BioRender)

### 3.3.1 Virus and virus surrogate immobilization

There are various methods to immobilize viruses on a surface, including physical adsorption [36], antibody capture [37, 38], and covalent attachment [39]. Physical adsorption by deposition of virus particles on a solid surface is simple, but the capsid proteins might deform during adsorption [36]. It is not clear if the deformation can change the exposed virus surface proteins and therefore change the virus surface properties. It was also a concern that the virus may have a stronger bond to the AFM probe than the surface. This would result in misleading results because we would not clearly know which bond rupture force we were measuring. The antibody capture and covalent binding methods provide strong bonds between the virus and the surface. The density of both the capture antibodies and covalent linkers will determine the number of

virus particles immobilized on a surface. The antibody binding method is virus-specific, but it is expensive and the antibodies could be denatured in some of the conditions explored during CFM. Thus, the method of covalently binding the virus to the surface was chosen.

To covalently bond the virus to the surface, a bifunctional linker that contained a thiol functional group was chemisorbed onto the gold surface [40]. The linker contained a carbon chain that self-assembled onto the gold-coated slide (**Figure 3.1B**). The functional group was always a carboxylic acid (COOH) was chosen because it covalently attaches to lysines on the virus surface using EDC and NHS chemistry [30, 31]. The surface was a mixture of COOH-capped and CH<sub>3</sub>-capped compounds to control the density of the COOH bifunctional linker.

To test the covalent immobilization chemistry, NH<sub>2</sub>-functionalized silica nanoparticles were used as a virus surrogate and attached to the COOH functional the surface. The natural particle size of 10-15 nm was detected for NH<sub>2</sub>-functionalized silica nanoparticle topographic images, as shown in **Figure 3.2A-C**, confirming the utility of the immobilization chemistry. To determine the optimal density of particles attached to the surface, various ratios of COOH-capped and CH<sub>3</sub>-capped thiol linkers at 9:1, 1:1, and 1:9 were tested. A ratio of 9:1 COOH/CH<sub>3</sub> caused a high density of nanoparticles and resulted in aggregated nanoparticles that could not be individually distinguished, as shown in **Figure 3.2A**. The best concentration was 50 w/w% COOH-capped and 50 w/w% of CH<sub>3</sub>-capped compounds, shown in **Figure 3.2B**, and this condition was used for further experiments. At a ratio of 1:9, too few nanoparticles attached to the surface, as shown in **Figure 3.2C**, making locating the virus difficult. Control surfaces were measured to determine the roughness of the surface at different stages of functionalization. **Figure 3.2D** shows that the hydrophobic functional group SAM-CH<sub>3</sub> modified surface had a surface roughness of ~1 nm. This is the same roughness as was found for the bare gold surface control in **Figure 3.2E** and the NHS-EDC modified surface in **Figure 3.2F**.

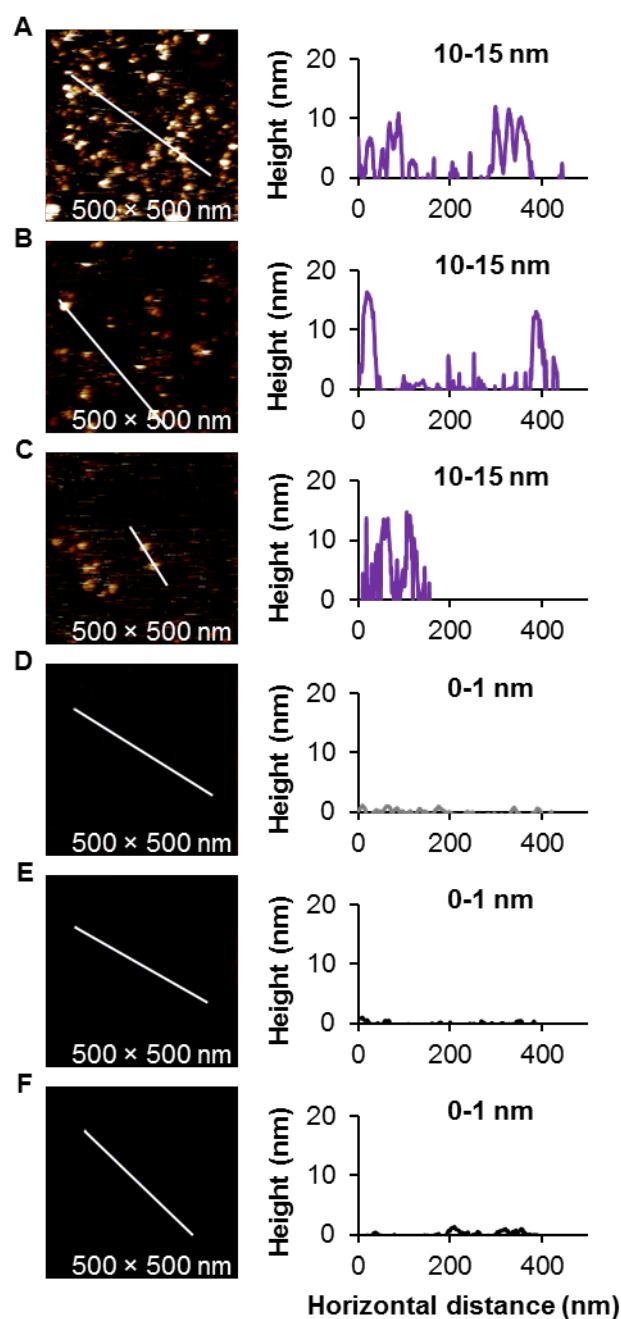


**Figure 3.2** Topographic images and corresponding height analysis of virus surrogate  $\text{NH}_2$ -functionalized silica NPs with different ratios of  $\text{COOH}$  and  $\text{CH}_3$ -capped thiol linkers and controls. Silica NPs were imaged after immobilization with (A) 9:1, (B) 1:1, and (C) 1:9  $\text{COOH}$  to  $\text{CH}_3$  ratios. Control surfaces were (D) methyl-modified surface, (E) bare gold surface, and (F) NHS-EDC surface.

The successful immobilization of virus particles was demonstrated using PPV and BVDV through topographic images and corresponding height analysis, as shown in **Figure 3.3A** and **3.3B**. The PPV had a measured size of 24 nm, which falls into the

reported size range of PPV of 18 - 26 nm [41]. PPV immobilized with an antibody capture method had a height of  $\sim 18$  nm [42] in AFM topographic images, smaller than the size of PPV measured in our method. In addition, **Figure 3.3B** shows that BVDV has a size of 40-60 nm, which is consistent with the reported size of BVDV reported [43]. The height analysis results also indicate that our covalent virus immobilizing method can keep a natural form of the virus without deformation or disassembly. We also used physical adsorption to immobilize virus particles by depositing the virus particles onto the gold surface without covalently binding, as shown in **Figure 3.3C** and **3.3D**. The measured sizes for both PPV and BVDV were smaller than the literature reported sizes, indicating that deformation of the virus particles occurred, and further confirmed the advantage of covalent immobilization of virus.

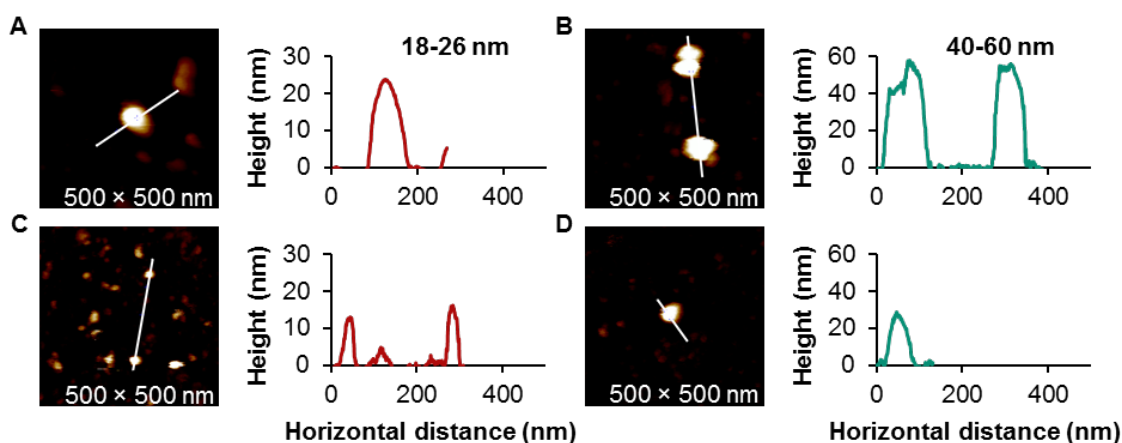


**Figure 3.3** Topographic images and corresponding height analysis of virus. (A) PPV covalently bound to gold, (B) BVDV covalently bound to gold, (C) PPV deposited on gold, and (D) BVDV deposited on gold.

### 3.3.2 AFM probe modification

There are many ways to modify an AFM probe with a chemical functional group, including silanization [44, 45], esterification [46, 47] and thiol attachment [23, 25]. The chemical groups of interest that functionalize the AFM probes determines what viral surface chemistry can be explored. Commercially available AFM tips are typically made of silicon nitride, which can form a silanol (Si-OH) surface layer on the AFM tip in air. Common methods for functionalization of AFM tips are silanization between the silanol groups on the AFM probe and a silane coupling agent such as  $R-(CH_2)_n-Si-(OC_2H_5)_3$  [44, 45] (R represents any interested chemical group), and esterification between the silanol groups on the AFM probe and a hydroxyl terminated agent  $R-(CH_2)_n-OH$  [46]. AFM tip silanization typically occurred in the vapor phase and required heat treatment of the silanized tip at  $\sim 110^\circ C$  for  $\sim 10$  min [44, 45]. Direct AFM tip esterification typically required a heating treatment over  $100^\circ C$  for several hours to functionalize the AFM probe [46, 47]. Another option is to coat the AFM tip with gold and adsorb an alkanethiol agent  $R-(CH_2)_n-SH$  onto the AFM tip [23, 25]. One key advantage of thiol attachment chemistry over the previous mentioned covalent binding chemistry for AFM probe



functionalization is that the tip modification can be performed at room temperature with a low concentration (~1 mM) of alkanethiol agent [23, 25]. Another advantage is that commercially available alkanethiol agents are terminated in a variety of chemistries. The disadvantage of the thiol method is that the adsorption takes longer than the higher temperature methods. We chose to use the thiol attachment method, for the AFM probe modification in our study, shown in **Figure 3.1A**.

**Table 3.1** Adhesion force at different AFM probe functionalization conditions.

Concentration	Chemistry			
	HS(CH <sub>2</sub> ) <sub>11</sub> CH <sub>3</sub>		HS(CH <sub>2</sub> ) <sub>11</sub> N(CH <sub>3</sub> ) <sub>3</sub> Br	
	Time			
	12 hours	24 hours	24 hours	48 hours
1 mM	0 pN	N/A	N/A	
2 mM	0 pN			N/A
4 mM		1734 pN	0 pN	
10 mM	N/A	N/A	N/A	165 pN

N/A: condition not tested.

All mean forces >0 were calculated based on the adhesion forces from 500 recorded F-D curves with at least three separate combinations of probe/control samples. Null adhesion force was based on 50 F-D curves with one combination of probe/control sample.

To measure small molecular binding interactions, a very soft, gold-coated Bruker AC-40 AFM probe (spring constant ~0.1 N/m, tip radius ~ 10 nm) was used. To functionalize the tip with a methyl functional group (CH<sub>3</sub>), a coating condition of 1 mM of HS(CH<sub>2</sub>)<sub>11</sub>CH<sub>3</sub> in ethanol for 12 hours[23] was used. To confirm the probe functionalization, the force between the coated probe and a CH<sub>3</sub> modified control surface in PBS at pH 7.2 was measured. However, no adhesion force could be detected, as shown in **Table 3.1**. The coating concentration was increased to 2 mM for 12 hours, and still, no adhesion force was measured. Next, the coating concentration was increased to 4 mM and coating time to 24 hours. These changes resulted in strong adhesion forces with a mean value of 1734 pN, shown in **Table 3.1** and **Figure 3.4A**. Over 500 force-distance curves were collected to create the histogram in **Figure 3.4A** showing the range of interactions with multiple virus particles. The possible reason why the literature reported coating condition did not work in our experiment might be due to the tiny AFM tips used in our experiment as compared to the larger tip area used in the previous work [23]. The small available area for coating limited the efficiency of methyl group binding.

To confirm the probe modification for the viral surface charge study, the negatively charged carboxyl (COO<sup>-</sup>)-terminated probe at coating condition with 4 mM of

HS(CH<sub>2</sub>)<sub>11</sub>COOH in ethanol for 24 hours was tested with positively charged silica nanoparticles in PB at pH 7.0. Strong adhesion forces with a mean value of 210 pN were measured, as shown in **Figure 3.4B**. No adhesion forces could be detected on the negatively charged COO<sup>-</sup> modified control surface at pH 7.0 (data not shown). This was the only coating condition tested for this condition.

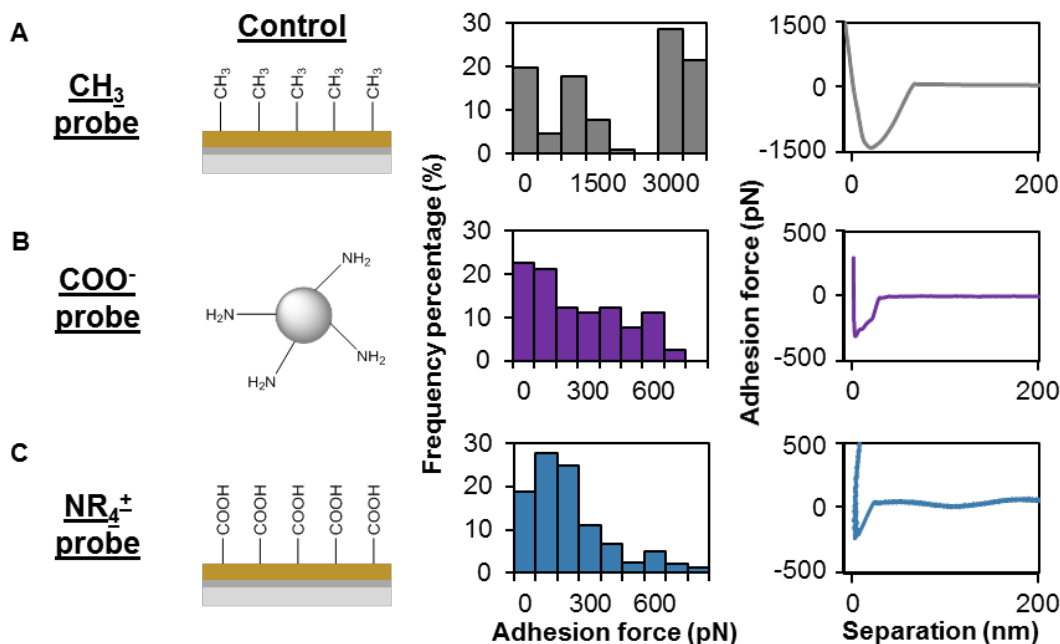


**Figure 3.4** Probe functionalization confirmation. Adhesion histograms and representative force-distance curves (retraction only) of positive control surface with a CH<sub>3</sub>-terminated, COOH-terminated, or a NR<sub>4</sub><sup>+</sup>-terminated probe. (A) CH<sub>3</sub>-terminated probe with a CH<sub>3</sub>-modified surface, (B) COO<sup>-</sup>-terminated probe with a primary amine-modified silica NPs, and (C) NR<sub>4</sub><sup>+</sup>-terminated probe with a COOH-modified surface. (A) Measured in PBS buffer at pH 7.2, and (B&C) measured in 20 mM phosphate buffers at pH 7.0. Multiple (n= 500) F-D curves were recorded over 500 nm × 500 nm areas.

The positively charged quaternary amine (NR<sub>4</sub><sup>+</sup>)-terminated probe was with a negatively charged COO<sup>-</sup> modified control surface in PB at pH 7.0. To functionalize with the positively charged NR<sub>4</sub><sup>+</sup>, the same coating condition with 4 mM for 24 hours were used with the gold-coated Bruker AC-40 AFM probe. No adhesion forces could be detected, as seen in **Table 3.1**. The probe coating might have been hindered by the small available areas of AC-40 probe, so another soft NT-MDT GSG10/Au AFM probe (spring constant ~0.11 N/m, tip radius ~ 35 nm) was coated following the same coating concentration with an HS(CH<sub>2</sub>)<sub>11</sub>N(CH<sub>3</sub>)<sub>3</sub>Br in ethanol. On average, 1 out of 10 probes tested were successfully coated with the quaternary amine. To improve the binding efficiency, a coating condition of 10 mM for 48 hours was tested to coat the GSG10/Au probe. Strong adhesion forces could also be seen in **Figure 3.4C**, with a mean force of 165 pN. No adhesion forces could be detected on the positively charged silica nanoparticles control surface (data not shown). It is likely that a high coating

concentration and long coating time were needed due to the repulsion of the positively charged quaternary amine.

### 3.3.3 Virus surface probing by CFM

A virus surface is heterogeneous, containing hydrophobic and charged patches. On the virus surface, the ratio of aliphatic amino acids such as valine, leucine, isoleucine, and methionine to aromatic amino acids such as phenylalanine, tyrosine, and tryptophan determine the net hydrophobicity of the virus [48]. Also, the ratio of protonated positively charged groups contributed by lysine, arginine, and histidine to deprotonated negatively charged groups contributed by aspartic acid (or aspartate) and glutamic acid (or glutamate) determine the net surface charge of the virus [49]. Though several methods have been established to evaluate the surface charge virus such as zeta potential [13], chromatofocusing [50], chromatography [6, 51], and isoelectric focusing [14], there seems to be no universal hydrophobicity measurement for the virus, making it difficult to compare among published results. The CFM is capable of detecting the surface chemistry of viral capsids at a single particle level with a trace amount of samples  $\sim 1500 \mu\text{L}$ , and could be established as a baseline comparison of the surface chemistry between different types of viruses.

Viruses have a higher hydrophobicity as compared to many proteins [6, 51]. Viral surface hydrophobicity plays a crucial role in virus removal [1, 52] and purification [53, 54]. CFM was able to quantify hydrophobic interactions between a  $\text{CH}_3$ -modified AFM probe and an immobilized viral particle. This enabled the direct comparison of hydrophobicity between different viruses. For the hydrophobicity study, CFM force measurements were performed in PBS buffer at pH 7.2.

**Table 3.2** Model virus properties.

Virus	Capsid	Family	Nucleic acid	Size (nm)	pI	Related human viruses	References
<b>Porcine parvovirus (PPV)</b>	Non-enveloped	Parvoviridae	ssDNA	18-26	$\sim 5.0$	B-19 human parvovirus	[41, 55]
<b>Bovine viral diarrhea virus (BVDV)</b>	Enveloped	Flaviviridae	ssRNA	40-60	–	Hepatitis C	[41, 43]

Non-enveloped PPV and enveloped BVDV were selected to explore virus surface chemistry with CFM. Some of their properties can be found in **Table 3.2**. The adhesion of PPV and BVDV to a hydrophobic probe are shown in the top graphs of **Figure 3.5**. In **Figure 3.5**, all the histograms were summarized and the mean forces were calculated based on the adhesion forces from 500 recorded F-D curves with at least three separate

combinations of probe/virus samples. The results are found in **Table 3.3**. PPV showed a higher adhesion force than BVDV, indicating that PPV is more hydrophobic than BVDV. One possible reason may be that the enveloped BVDV contains glycolipids with hydrophilic heads [56]. Thus, PPV might prefer to adsorb to more hydrophobic surfaces than BVDV. If PPV and BVDV are model viruses used in virus clearance studies, with an understanding of the viral surface hydrophobicity, we can better design a process that will retain multiple viruses in different pools than the protein product.

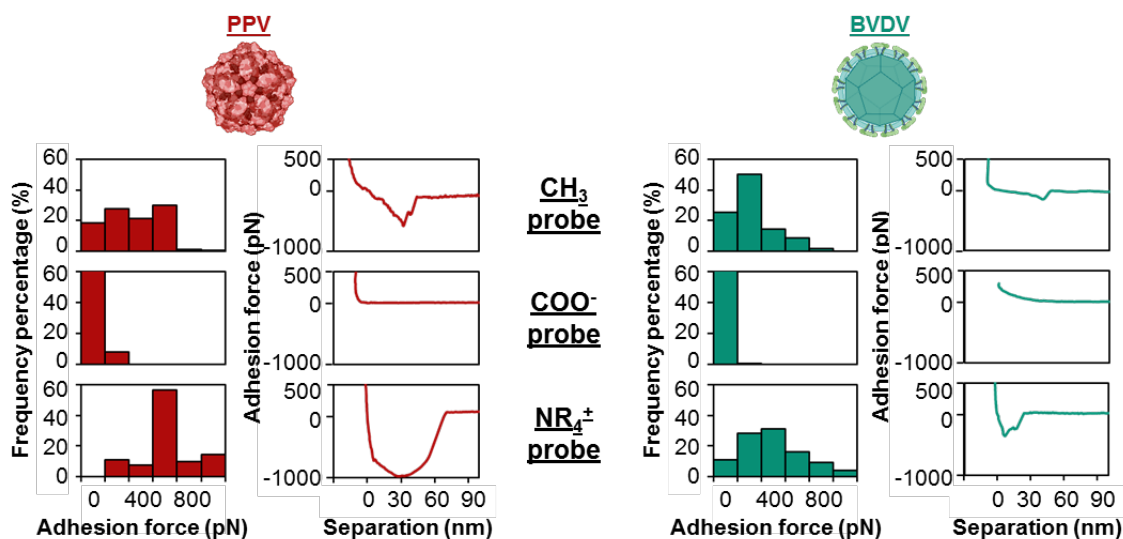


**Figure 3.5** Adhesion histograms and representative force-distance curves (retraction only) of virus with a CH<sub>3</sub>-terminated, COO<sup>-</sup>-terminated, or a NR<sub>4</sub><sup>+</sup>-terminated probe, recorded in PBS at pH 7.2 (for hydrophobicity measurement) or 20 mM phosphate buffers at pH 7.0 (for surface charge measurement). Multiple (n= 500) F-D curves were recorded over 500 nm × 500 nm areas. (Virus images were created in BioRender)

**Table 3.3** Mean force measured during CFM at a pH of 7.2 for the methyl probe and 7.0 for the charged probes.

Chemistry	Virus	
	PPV	BVDV
CH <sub>3</sub>	272 pN	118 pN
COO <sup>-</sup>	0 pN	0 pN
NR <sub>4</sub> <sup>+</sup>	570 pN	304 pN

Most viruses carry a negative charge under physiological conditions due to the viral isoelectric point (pI) typically being below pH 7 [9]. Viral surface charge plays a key role in controlling virus adsorption and aggregation. AFM probes terminated with negatively charged COO<sup>-</sup> groups and positively charged NR<sub>4</sub><sup>+</sup> groups were used to

measure the surface charge of PPV and BVDV. To explore the electrostatic interactions of viral surface, viruses were studied in a low ionic strength buffer since high salt concentration will shield electrostatic interactions. The electrostatic attractions between the surface of viruses and charged chemical modified AFM probes were measured at pH 7.0.

The middle graphs in **Figure 3.5** show PPV adhesion to a negatively charged  $\text{COO}^-$  probe. Almost no adhesion was observed at pH 7.0. In the complementary experiment with the positively charged  $\text{NR}_4^+$  modified AFM probe, strong adhesion was observed for PPV at pH 7.0 (the bottom of **Figure 3.5** and **Table 3.3**). Similar force measurements were performed for the enveloped virus BVDV, as shown in **Figure 3.5**. Similar adhesion phenomena were observed for probing the surface charge of BVDV. However, the mean electrostatic force collected for BVDV was smaller than PPV. More study is needed of the viral proteins to understand this charge difference.

### 3.4 Conclusions

Our covalent virus immobilization method can retain a natural form of the virus without deformation or disassembly. Our AFM probe functionalizing method of thiol attachment to gold-coated probes can be achieved at room temperature and allows the attachment of many chemical functional groups of interest. With the immobilized virus and functionalized AFM tips, we have studied viral surface chemistry with trace amounts of sample using CFM. We determined that PPV is more hydrophobic than BVDV using a methyl-terminated AFM probe. When charged groups were put on the AFM probes, the surface charge of the virus could be measured. Both PPV and BVDV carry a negative charge at neutral pH.

The CFM can detect the surface chemistry of viral capsids at a single particle level and enable the comparison of the surface chemistry between different types of viruses. Another appealing advantage of CFM to determine the virus surface chemistry over other methods is the amount of virus used in this study is very low, reducing the high cost of producing biological samples. With a thorough understanding of virus surface chemistry, future virus purification and removal techniques could be significantly improved to specifically target viral particles.

### 3.5 References

1. Chung, J.W., et al., *Simultaneous removal of rotavirus and adenovirus from artificial ground water using hydrochar derived from swine feces*. Journal of Water and Health, 2016. **14**(5): p. 754-767.
2. Mi, X., K.S. Vijayaragavan, and C.L. Heldt, *Virus adsorption of water-stable quaternized chitosan nanofibers*. Carbohydrate Research, 2014. **387**: p. 24-29.
3. Mi, X. and C.L. Heldt, *Adsorption of a non-enveloped mammalian virus to functionalized nanofibers*. Colloids and Surfaces B-Biointerfaces, 2014. **121**: p. 319-324.
4. Wolff, M.W., et al., *Purification of Cell Culture-Derived Modified Vaccinia Ankara Virus by Pseudo-Affinity Membrane Adsorbers and Hydrophobic Interaction Chromatography*. Biotechnology and Bioengineering, 2010. **107**(2): p. 312-320.
5. Jin, J., et al., *Evaluation of the impact of lipid fouling during the chromatographic purification of virus-like particles from Saccharomyces cerevisiae*. Journal of Chemical Technology and Biotechnology, 2010. **85**(2): p. 209-215.
6. Heldt, C.L., et al., *Experimental and computational surface hydrophobicity analysis of a non-enveloped virus and proteins*. Colloids and Surfaces B-Biointerfaces, 2017. **153**: p. 77-84.
7. Johnson, S., et al., *Characterization of Non-Infectious Virus-Like Particle Surrogates for Viral Clearance Applications*. Applied biochemistry and biotechnology, 2017. **183**(1): p. 318-331.
8. Gentile, G.J., et al., *Electrostatic interactions in virus removal by ultrafiltration membranes*. Journal of Environmental Chemical Engineering, 2018. **6**(1): p. 1314-1321.
9. Michen, B. and T. Graule, *Isoelectric points of viruses*. Journal of applied microbiology, 2010. **109**(2): p. 388-397.
10. Li, Z.J., et al., *Strong hydrophobicity enables efficient purification of HBc VLPs displaying various antigen epitopes through hydrophobic interaction chromatography*. Biochemical Engineering Journal, 2018. **140**: p. 157-167.
11. Farkas, K., A. Varsani, and L. Pang, *Adsorption of Rotavirus, MS2 Bacteriophage and Surface-Modified Silica Nanoparticles to Hydrophobic Matter*. Food and Environmental Virology, 2015. **7**(3): p. 261-268.
12. Aronino, R., et al., *Removal of viruses from surface water and secondary effluents by sand filtration*. Water Res, 2009. **43**(1): p. 87-96.
13. Samandougou, I., I. Fliss, and J. Jean, *Zeta Potential and Aggregation of Virus-Like Particle of Human Norovirus and Feline Calicivirus Under Different Physicochemical Conditions*. Food and Environmental Virology, 2015. **7**(3): p. 249-260.
14. Braun, M., et al., *A simple method to estimate the isoelectric point of modified Tomato bushy stunt virus (TBSV) particles*. Electrophoresis, 2017. **38**(21): p. 2771-2776.

15. Dika, C., et al., *Impact of the virus purification protocol on aggregation and electrokinetics of MS2 phages and corresponding virus-like particles*. Phys Chem Chem Phys, 2013. **15**(15): p. 5691-700.
16. Dika, C., et al., *Isoelectric point is an inadequate descriptor of MS2, Phi X 174 and PRD1 phages adhesion on abiotic surfaces*. Journal Of Colloid And Interface Science, 2015. **446**: p. 327-34.
17. Leuchs, B., et al., *A novel scalable, robust downstream process for oncolytic rat parvovirus: isoelectric point-based elimination of empty particles*. Applied Microbiology And Biotechnology, 2017. **101**: p. 3143-3152.
18. Noy, A., D.V. Vezenov, and C.M. Lieber, *Chemical force microscopy*. Annual Review of Materials Science, 1997. **27**(1): p. 381-421.
19. Alessandrini, A. and P. Facci, *AFM: a versatile tool in biophysics*. Measurement Science and Technology, 2005. **16**(6): p. R65-R92.
20. Leite, F., et al., *The atomic force spectroscopy as a tool to investigate surface forces: basic principles and applications*. Modern Research and Educational Topics in Microscopy, 2007.
21. Cappella, B. and G. Dietler, *Force-distance curves by atomic force microscopy*. Surface science reports, 1999. **34**(1-3): p. 1-104.
22. Kim, H., et al., *Characterization of mixed self-assembled monolayers for immobilization of streptavidin using chemical force microscopy*. Ultramicroscopy, 2008. **108**(10): p. 1140-1143.
23. Alsteens, D., et al., *High-resolution imaging of chemical and biological sites on living cells using peak force tapping atomic force microscopy*. Langmuir, 2012. **28**(49): p. 16738-44.
24. Gelmi, A., et al., *Optical switching of protein interactions on photosensitive-electroactive polymers measured by atomic force microscopy*. Journal of Materials Chemistry B, 2013. **1**(16): p. 2162-2168.
25. Ahimou, F., et al., *Probing microbial cell surface charges by atomic force microscopy*. Langmuir, 2002. **18**(25): p. 9937-9941.
26. Guo, S.F., et al., *Measuring protein isoelectric points by AFM-based force spectroscopy using trace amounts of sample*. Nature Nanotechnology, 2016. **11**(9): p. 817-823.
27. Alsteens, D., et al., *Atomic force microscopy-based characterization and design of biointerfaces*. Nature Reviews Materials, 2017. **2**(5): p. 17008.
28. Tafur, M.F., K.S. Vijayaragavan, and C.L. Heldt, *Reduction of porcine parvovirus infectivity in the presence of protecting osmolytes*. Antiviral Research, 2013. **99**(1): p. 27-33.
29. Meng, H., et al., *Biomimetic recyclable microgels for on-demand generation of hydrogen peroxide and antipathogenic application*. Acta biomaterialia, 2019. **83**: p. 109-118.
30. Grabarek, Z. and J. Gergely, *ZERO-LENGTH CROSSLINKING PROCEDURE WITH THE USE OF ACTIVE ESTERS*. Analytical Biochemistry, 1990. **185**(1): p. 131-135.

31. Lahiri, J., et al., *A strategy for the generation of surfaces presenting ligands for studies of binding based on an active ester as a common reactive intermediate: A surface plasmon resonance study*. Analytical Chemistry, 1999. **71**(4): p. 777-790.
32. Hutter, J.L. and J. Bechhoefer, *CALIBRATION OF ATOMIC-FORCE MICROSCOPE TIPS (VOL 64, PG 1868, 1993)*. Review of Scientific Instruments, 1993. **64**(11): p. 3342-3342.
33. Ortega-Esteban, Á., et al., *Structural and Mechanical Characterization of Viruses with AFM*, in *Atomic Force Microscopy*. 2019, Springer. p. 259-278.
34. Marchetti, M., G.J.L. Wuite, and W.H. Roos, *Atomic force microscopy observation and characterization of single virions and virus-like particles by nano-indentation*. Current Opinion in Virology, 2016. **18**: p. 82-88.
35. de Pablo, P.J., *Atomic force microscopy of virus shells*. Seminars in Cell & Developmental Biology, 2018. **73**: p. 199-208.
36. Zeng, C., et al., *Probing the link among genomic cargo, contact mechanics, and nanoindentation in recombinant adeno-associated virus 2*. The Journal of Physical Chemistry B, 2017. **121**(8): p. 1843-1853.
37. Moloney, M., L. McDonnell, and H. O'Shea, *Immobilisation of Semliki Forest virus for atomic force microscopy*. Ultramicroscopy, 2002. **91**(1-4): p. 275-279.
38. Hodges, J.A. and S. Saffarian, *Sample preparation for single virion atomic force microscopy and super-resolution fluorescence imaging*. JoVE (Journal of Visualized Experiments), 2014(83): p. e51366.
39. Meillan, M., et al., *Self-assembled monolayer for AFM measurements of Tobacco Mosaic Virus (TMV) at the atomic level*. RSC Advances, 2014. **4**(23): p. 11927-11930.
40. Pensa, E., et al., *The chemistry of the sulfur–gold interface: in search of a unified model*. Accounts of chemical research, 2012. **45**(8): p. 1183-1192.
41. Norkin, L.C., *Virology: Molecular Biology and Pathogenesis*. 2010: ASM Press.
42. Driskell, J.D., et al., *Control of antigen mass transfer via capture substrate rotation: An absolute method for the determination of viral pathogen concentration and reduction of heterogeneous immunoassay incubation times*. Journal of Virological Methods, 2006. **138**(1-2): p. 160-169.
43. KIM, I.S., Y.W. CHOI, and S.R. LEE, *Optimization and validation of a virus filtration process for efficient removal of viruses from urokinase solution prepared from human urine*. Journal of microbiology and biotechnology, 2004. **14**(1): p. 140-147.
44. Ratto, T.V., et al., *Force spectroscopy of the double-tethered concanavalin-A mannose bond*. Biophysical Journal, 2004. **86**(4): p. 2430-2437.
45. Ratto, T.V., et al., *Nonlinearly additive forces in multivalent ligand binding to a single protein revealed with force spectroscopy*. Langmuir, 2006. **22**(4): p. 1749-1757.
46. Riener, C.K., et al., *Simple test system for single molecule recognition force microscopy*. Analytica Chimica Acta, 2003. **479**(1): p. 59-75.
47. Blanchette, C.D., A. Loui, and T.V. Ratto, *Tip functionalization: Applications to chemical force spectroscopy*, in *Handbook of Molecular Force Spectroscopy*. 2008, Springer. p. 185-203.



48. Chen, M., et al., *Hydrophobicity of reactive site loop of SCCA1 affects its binding to hepatitis B virus*. World Journal of Gastroenterology, 2005. **11**(19): p. 2864-2868.
49. Nap, R.J., et al., *The Role of Solution Conditions in the Bacteriophage PP7 Capsid Charge Regulation*. Biophysical Journal, 2014. **107**(8): p. 1970-1979.
50. Leuchs, B., et al., *A novel scalable, robust downstream process for oncolytic rat parvovirus: isoelectric point-based elimination of empty particles*. Applied Microbiology and Biotechnology, 2017. **101**(8): p. 3143-3152.
51. Johnson, S.A., et al., *The step-wise framework to design a chromatography-based hydrophobicity assay for viral particles*. Journal of Chromatography B-Analytical Technologies in the Biomedical and Life Sciences, 2017. **1061**: p. 430-437.
52. van Voorthuizen, E.M., N.J. Ashbolt, and A.I. Schafer, *Role of hydrophobic and electrostatic interactions for initial enteric virus retention by MF membranes*. Journal of Membrane Science, 2001. **194**(1): p. 69-79.
53. Vijayaragavan, K.S., et al., *Separation of porcine parvovirus from bovine serum albumin using PEG-salt aqueous two-phase system*. Journal of Chromatography B-Analytical Technologies in the Biomedical and Life Sciences, 2014. **967**: p. 118-126.
54. Joshi, P.U., Weiss, M., Corbin-Escalante, G., Schroeder, M., and Heldt, C.L, *Tie Line Framework to Optimize Non-Enveloped Virus Recovery in Aqueous Two-Phase Systems*. In review.
55. Weichert, W.S., et al., *Assaying for structural variation in the parvovirus capsid and its role in infection*. Virology, 1998. **250**(1): p. 106-117.
56. Lorizate, M. and H.G. Krausslich, *Role of Lipids in Virus Replication*. Cold Spring Harbor Perspectives in Biology, 2011. **3**(10).

# 4 Virus isoelectric point determination<sup>2</sup>

---

<sup>2</sup> The material contained in this chapter has been accepted by Langmuir. Citation: *Mi, X., Bromley, E., Joshi, P. U., Long, F., Heldt, C. L. Virus isoelectric point determination using single-particle chemical force microscopy. Langmuir 2019.*

## 4.1 Introduction

The characterization of virus particles traditionally takes place at the molecular level using genetic manipulation of viral capsid proteins to understand individual amino acid interaction [1, 2] or in bulk by characterization of viral solutions [3, 4]. However, there is an intermediate scale at the single-particle level [5, 6] that is missing. Measuring the variability in a viral population at the single-particle level could help explain or more accurately measure infectious to noninfectious particle ratios [7], thus improving our understanding of the virus infection cycle. Single-particle methods could also provide insight into the ratio of empty to full capsids in gene therapy manufacturing [8], thus providing a quick quantitation of the quality of a gene therapy preparation for human use. In addition, the virus surface charge can be used to evaluate the adhesion forces between the virus and a target substrate to predict the likelihood of virus attachment to a charged surface [9]. The surface charge can be used to design virus removal filters based on electrostatic adsorption [10, 11] and to eliminate empty virus capsids that lack nucleic acids during packaging from full virus particles by anion exchange chromatography for gene therapy purification [12].

One important surface characteristic is the virus surface charge, most often characterized by the isoelectric point (pI). The pI corresponds to the pH where the net charge on the virus particle is zero [13]. Although the net surface charge is zero, due to the large size of viruses, there are many charged patches distributed on the viral surface at the pI. The excess of protonated or deprotonated functional groups of the charged amino acids highly contributes to the net surface charge of viruses. The surface charges of viral capsid proteins at a certain pH based on the dissociation constants of charged residues can be used for calculation of the virus pI using the Henderson-Hasselbalch equation [14]. Like any other charged particle, when a charged virus particle is in liquid, an electrical double layer will form around the virus particle comprising of a Stern layer, which is a rigid layer of counter-ions first attached to the charged particle, and a diffuse layer, which is a loose outer layer of free ions in liquid attracted to the Stern layer [15]. The surface charge of the virus particle measured here is the charge at the slipping plane, which is the outer edge of the diffuse layer of the virus particle. Thus, the surface charge of the virus particle is a function of pH and ionic strength of the fluid.

Various characterization methods have been employed to determine the pI of virus particles. Zeta potential, as a measure of surface charges of virus particles at the slipping plane, requires a high concentration of purified virus particles and is affected by the ionic strength of solutions and different virus purification methods [4, 16]. Isoelectric focusing is an electrophoretic technique based on the separation of virus particles, according to their pI [17]. Isoelectric focusing typically requires long and complicated experimental steps, and it is limited by the low solubility of virus particles [17, 18]. Cross-partitioning can be measured using an aqueous two-phase system (ATPS) [19, 20]. An ATPS cross-partitioning method containing charged poly(ethylene glycol) (PEG) was used to measure the pI of various groups of Streptococci and Staphylococci bacteria [19], and it has the potential to measure the pI of virus particles. However, zeta potential, isoelectric focusing, and cross-partitioning methods are limited by the purity of virus

samples [21] and solution conditions [4, 16, 19]. Both zeta potential and cross-partitioning methods require a large number of purified virus samples. An inexpensive, robust, and reliable single-particle method to characterize the virus surface charge is needed.

A novel surface characterization method known as chemical force microscopy (CFM) [22], which uses an atomic force microscope (AFM), has the potential to measure single virus particle surface chemistry. CFM measures the chemical interactions between a functionalized AFM tip and a sample. CFM has been reported to explore the surface charge of a single *Saccharomyces cerevisiae* cell [23] and to measure the pI values of various proteins: bovine serum albumin, myoglobin, fibrinogen, and ribonuclease with trace amounts of protein samples [24]. CFM has also become popular to measure the interactions between biomolecules, such as specific antibody-antigen interaction [25], protein-protein interaction [26], and ligand-receptor interaction [27]. One significant advantage of CFM over other microscopy methods for virus surface characterization is that the measurement can be performed in physiological aqueous solutions without disturbing the natural state of the virus [28]. In addition, CFM uses a small amount of biological samples [24], which can overcome the disadvantage of bulk characterization methods that can consume a large number of purified virus samples. CFM is therefore less expensive and is not reliant on the purification method since contaminant proteins will not interfere with the measurement.

In this research, we used modified AFM probes functionalized with either a positive or negative charge to determine the viral pI using CFM. We validated the CFM by comparing the pI of non-enveloped porcine parvovirus (PPV) with its known pI value. CFM also determined the pI of enveloped bovine viral diarrhea virus (BVDV), which does not have a literature-reported pI value. The bulk measurements of zeta potential and ATPS were used as a comparison of the virus pI. Most of the bulk measurements were in good agreement with the pI values determined by CFM, but it required significantly more viral samples to complete. We also compared our experimental data to computationally calculated virus electrostatic surface property data. The CFM can detect the surface charge of viral capsids at a single-particle level, and it can enable the comparison of the surface charge between different types of viruses or subpopulations of different virus samples. With a thorough understanding of the virus surface charge, the understanding of virus interaction with surfaces and other biological materials can be better understood.

## 4.2 Experimental section

### 4.2.1 Materials.

Sodium phosphate monobasic monohydrate (ACS grade, 98.0-102.0%), poly(ethylene glycol) (PEG, average MW: 12 kDa), and sodium chloride (ACS grade,  $\geq 99.0\%$ ) were a gift from MilliporeSigma (Burlington, MA). Sodium phosphate dibasic heptahydrate (ACS grade, 98.0-102.0%), citric acid monohydrate (ACS grade,  $\geq 99.0\%$ ), sodium citrate tribasic dihydrate (ACS grade,  $\geq 99.0\%$ ), 12-mercaptododecanoic acid ( $\text{HS}(\text{CH}_2)_{11}\text{COOH}$ , 96%), 1-dodecanethiol ( $\text{HS}(\text{CH}_2)_{11}\text{CH}_3$ ,  $\geq 98\%$ ), 11-mercaptoundecyl-N,N,N-trimethylammonium bromide ( $\text{HS}(\text{CH}_2)_{11}\text{N}(\text{CH}_3)_3\text{Br}$ ), primary amine ( $\text{NH}_2$ )-functionalized silica nanoparticles (nanoparticles  $<30$  nm (DLS)), and sodium hydroxide (NaOH, ACS grade,  $\geq 97.0\%$ ) were purchased from Sigma-Aldrich (St. Louis, MO). N-hydroxysulfosuccinimide (NHS) and 1-ethyl-3-(3-dimethylaminopropyl) carbodiimide hydrochloride (EDC) were purchased from Thermo Fisher Scientific (Waltham, MA). Phosphate-buffered saline (PBS) (pH 7.2) was purchased from Life Technologies (Grand Island, NY). Thiazolyl blue tetrazolium bromide (MTT) (98%) was purchased from Alfa Aesar (Haverhill, MA). Sodium dodecyl sulfate (SDS) was purchased from VWR (Radnor, PA). Hydrochloric acid (HCl, ACS grade, 36.5-38.0%) was purchased from Fisher Scientific (Pittsburgh, PA). All aqueous solutions or buffers were prepared using purified water with a resistivity of  $\geq 18 \text{ M}\Omega\cdot\text{cm}$  from a Nanopure filtration system (Thermo Scientific) and filtered with a  $0.2 \mu\text{m}$  bottle top filter or a  $0.2 \mu\text{m}$  syringe filter (VWR) prior to use.

### 4.2.2 Buffers.

Citrate buffer (CB) solutions with different pH (3.0–6.0) were prepared by mixing different volume percentages of 20 mM stock solution of citric acid and sodium citrate tribasic. Phosphate buffer (PB) solution at pH 7.0 was prepared by mixing 20 mM stock solution of sodium phosphate monobasic and sodium phosphate dibasic. The final pH was adjusted with 1 M NaOH or HCl, as needed, and it was measured with a Fisherbrand Accumet AE150 benchtop pH meter (Hampton, NH) with a 3-in-1 single-junction gel pH/ATC probe (cat. 13-620-AE6) calibrated using the manufacturer's instructions.

### 4.2.3 Virus production, purification, and titration.

Porcine kidney cells (PK-13, CRL-6489) were purchased from ATCC. Porcine parvovirus (PPV) strain NADL-2 was a gift from Dr. Ruben Carbonell (North Carolina State University, Raleigh, NC). PPV was propagated in PK-13 cells, as described previously [29], and stored at  $-80^\circ\text{C}$ . Bovine turbinate cells (BT-1, CRL-1390) were purchased from ATCC, and bovine viral diarrhea virus (BVDV) strain NADL was purchased from USDA APHIS. BVDV was propagated by infecting 80% confluent flasks of BT-1 cells with  $10^5 \text{ MTT}_{50}/\text{mL}$  of the virus in PBS and collecting the virus released

into the media after 72 h. The BVDV had 10 v/v% glycerol added before storing it at  $-80^{\circ}\text{C}$ .

For purification of PPV or BVDV [30], the virus was first dialyzed using a Biotech Cellulose Ester 1,000 kDa dialysis tubing (Rancho Dominguez, CA) at  $4^{\circ}\text{C}$  for 2 days with two buffer exchanges of 20 mM PB. The dialyzed virus was further purified with a BioRad Econo-Pac 10DG desalting column (Hercules, CA).

Both types of viruses were titrated with a cell viable MTT assay [29]. Briefly, either  $8 \times 10^4$  cells/mL PK-13 cells (to titrate PPV) [31] or  $2.5 \times 10^5$  cells/mL BT-1 cells (to titrate BVDV) [32] were seeded into a 96-well plate in a volume of 100  $\mu\text{L}$ /well. After a 24 h incubation, 25  $\mu\text{L}$ /well of the virus sample was added to the corresponding host cells in quadruplicate, and it was serially diluted across the plate. After 6 days, 10  $\mu\text{L}$ /well of 5 mg/mL MTT salt in PBS (pH 7.2) was added to the plate. After 4 h, this was followed by the addition of 100  $\mu\text{L}$ /well of the solubilizing agent, consisting of 10 w/v% SDS in 0.01 M HCl (pH 2.5). Plates were read for absorbance at 550 nm on a Synergy Mx monochromator-based multimode microplate reader (Winooski, VT) 12-20 h after the solubilizing agent addition. The virus dilution that killed 50% of the cells is stated as the virus titer  $\text{MTT}_{50}$ . The concentrations of purified virus solutions were determined by the MTT assay to be  $1 \times 10^8$   $\text{MTT}_{50}/\text{mL}$  for PPV and  $1 \times 10^7$   $\text{MTT}_{50}/\text{mL}$  for BVDV.

#### 4.2.4 Virus samples and control surfaces preparation.

A diced glass slide (1 in.  $\times$  1 in.  $\times$  1 mm) was coated with a 5 nm thick chromium layer followed by a 30 nm gold layer using a Perkin-Elmer Randex sputtering system (Model 2400, Waltham, MA). The gold-coated slide was soaked in a glass Petri dish containing 14 mL of a 1:1 solution of 2 mM solution of  $\text{HS}(\text{CH}_2)_{11}\text{COOH}$  and  $\text{HS}(\text{CH}_2)_{11}\text{CH}_3$  in ethanol for 12 h, rinsed with ethanol, and then air-dried in a chemical hood. The surface was then equilibrated with 14 mL of Nanopure water for 15 min. A total of 0.5 mL of an equal volume mixture of 0.1 M NHS and 0.4 M EDC was added to the surface for 30 min, and it was then washed and incubated with PBS (pH 7.2) for 2 min. A 0.5 mL of purified PPV or BVDV or positively charged control  $\text{NH}_2$ -functionalized silica nanoparticles was applied to the surface for 30 min. Finally, the surface was rinsed three times with Nanopure water and soaked in 14 mL of 20 mM CB (pH 3.0-6.0) or PB (pH 7.0) at the desired pH and stored at  $4^{\circ}\text{C}$ . The negatively charged control carboxyl acid-modified surface was prepared in the same manner except the solution contained pure  $\text{HS}(\text{CH}_2)_{11}\text{COOH}$ . The controls were used for testing the chemistry of virus immobilization and probe functionalization.

#### 4.2.5 AFM probe functionalization.

Negatively charged AFM probes were prepared by incubating the gold-coated Bruker AC-40 AFM probe ( $\sim 0.1$  N/m) in a 4 mM solution of  $\text{HS}(\text{CH}_2)_{11}\text{COOH}$  in ethanol for 24 h, rinsed with ethanol, and air-dried in a chemical hood. Similarly, the positively charged AFM probe was prepared by immersing the NT-MDT GSG10/Au AFM probe ( $\sim 0.1$  N/m) in a 10 mM solution of  $\text{HS}(\text{CH}_2)_{11}\text{N}(\text{CH}_3)_3\text{Br}$  in ethanol for 48 h,

rinsed with ethanol, and air-dried in a chemical hood. Functionalized probes were used immediately after they were prepared.

#### 4.2.6 AFM imaging, force measurement, and analysis.

All AFM experiments were performed at room temperature on a Bruker Dimension ICON AFM with the ScanAsyst system (Santa Barbara, CA). AFM topographic images were obtained using tapping mode in PBS with a Bruker ScanAsyst Fluid+ silicon nitride AFM probe or a NT-MDT GSG30 AFM probe. AFM force measurements were made in peak force tapping mode or contact mode. The spring constant of the modified AFM probe was calibrated before the force measurement by using the thermal noise method [33]. More than 500 force-distance ( $F$ - $D$ ) curves were collected with at least three separate combinations of probe/virus samples. All  $F$ - $D$  curve measurements between modified probes and viral surfaces were performed in either 20 mM CB solutions at the desired pH or in a 20 mM PB at pH 7.0. The control experiments were carried out in 20 mM PB at pH 7.0. Data analysis was performed with the Bruker Nanoscope Analysis software. To determine the pI of the virus, the mean adhesion force from 500  $F$ - $D$  curves was plotted as a function of pH and fit to a sigmoidal curve [34] described by Eq. 4.1,

$$Y = \frac{y_f}{1 + e^{-\frac{x-x_0}{\tau}}} \quad (4.1)$$

where  $Y$  is the adhesion force,  $x$  is the pH, and  $x_0$  is the pI.  $y_f$  is the maximum adhesion force, and the rate constant for the change of the mean adhesion force is given by  $1/\tau$ .

#### 4.2.7 Zeta potential measurement.

Purified PPV or BVDV was diluted 1:10 in either 20 mM CB at the desired pH or 20 mM PB solutions at pH 7.0. The zeta potential was measured with a Malvern Zetasizer Nano ZS (Worcestershire, U.K.). Measurements were performed at 25°C using a capillary zeta cell (750  $\mu$ L) with an equilibration time of 2 min. Three measurements of 10-100 runs were carried out using the automatic option.

#### 4.2.8 ATPS measurement.

A stock solution of 33 w/w% PEG 12 kDa and 30 w/w% citrate at pH 4.5-6.5 was used to prepare the ATPS. The total system size was 1 g, at a final concentration of 15 w/w% PEG, 14 w/w% citrate, and 0.1 g of purified PPV, at various pH values [35]. The systems were mixed with a vortex and subjected to 12,300  $\times$ g for phase separation in an ST16R centrifuge (Thermo Scientific) at 21°C for 5 min. The top (PEG-rich) and bottom (citrate-rich) phases were collected for further virus titration. The partition coefficient ( $K$ ) was calculated as,

$$K = \frac{V_P * T_P}{V_C * T_C} \quad (4.2)$$

where  $V$  is the volume of the PEG-rich phase (P) or citrate-rich phase (C) and  $T$  is the titer of PPV in either phase expressed as MTT<sub>50</sub>/mL.

#### 4.2.9 Theoretical calculation of virus surface potential and pI.

The pI of the virus by an amino acid sequence was calculated by an online protein isoelectric point calculator (<http://isoelectric.ovh.org>) [36], using the theoretical average value from 16 methods. The amino acid sequence was from the UniProt Knowledgebase (UniProtKB) [37].

The surface potential of the virus was calculated from the protein crystal structure using the protein contact potential in PyMOL [38]. Each protein crystal structure was from the Protein Data Bank (PDB) based on its corresponding ID. The electrostatic potential map of the virus surface based on its overall surface charge distribution was also created in PyMOL, and it was applied on the protein surface by calculating the electrostatic potential in a vacuum and using the protein contact potential [38].

### 4.3 Results and discussion

#### 4.3.1 Surface and probe preparations.

The first step was to prepare the surface and AFM probes needed for CFM measurements. Probe modifications using gold-coated AFM tips are common [23, 39], and the modifications used are shown in **Figure 4.1A**. However, a new method to attach the virus was needed. One of the common characterizations of the virus with an AFM is nanoindentation [5, 40, 41]. Nanoindentation is typically conducted by depositing the virus on a gold surface and pushing on the virus. We were concerned that if we deposited the virus on gold and then pulled on it, we would not be confident if the bond that broke during the measurement was the tip-virus interaction or the gold-virus interaction. Therefore, we decided to covalently bond the virus to the surface, as shown in **Figure 4.1B**. We created a mixed surface with terminated carboxylic acid and methyl groups, and we used NHS/EDC chemistry to covalently bond the virus to the carboxylic acid groups [42, 43]. The mixed surface was designed to increase the spacing of the viral particles. There was no need to orient the virus on the surface because the viruses tested are symmetric.



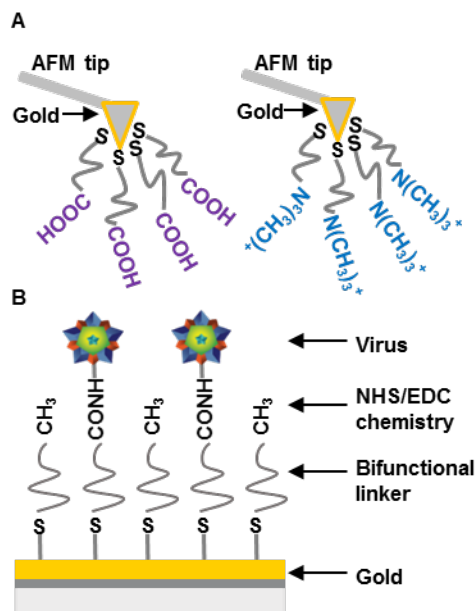


**Figure 4.1** Overview of AFM probe functionalization and virus immobilization on a gold surface. (A) AFM probes were functionalized with either a negatively charged carboxyl acid group or a positively charged quaternary amine group and (B) virus particles were immobilized with NHS/EDC chemistry.

Non-enveloped PPV and enveloped BVDV were successfully immobilized to the surface. Topographic images and corresponding height analysis, as shown in **Figure 4.2**, confirmed that the virus immobilization method retained a natural form of the virus without deformation or disassembly. It is common to use height as a confirmation of no modification or deformation of the viral particles [44, 45]. A total of 18 viral particles from three purified batches for PPV and BVDV were measured with topographic images. PPV had an average height of  $23 \pm 3$  nm, and BVDV had an average height of  $46 \pm 8$  nm. Confirmation of the viral envelope prior to attachment and zeta potential measurements was confirmed by the ability of BVDV to infect cell culture and by transmission electron microscopy (TEM) images (SI **Figure A.1.1**).

The quality of the topographic images was limited. It is possible that the length of the bifunctional linker used to immobilize the virus particles created a soft surface that resulted in the blurred edges in the virus particle images. To obtain higher-quality topographic images for PPV and BVDV in liquid, the virus particles were deposited onto a gold surface without covalent bonding, as shown in SI **Figure A.1.2A&B**. The blurred fringes of virus particles were greatly reduced in these improved conditions. A total of nine viral particles from two purified batches for PPV and BVDV were measured. PPV had an average height of  $18 \pm 3$  nm, and BVDV had an average height of  $30 \pm 2$  nm. Viruses on gold had a smaller size than those covalently attached to the surface. This could be due to the virus spreading out on the gold surface [46].

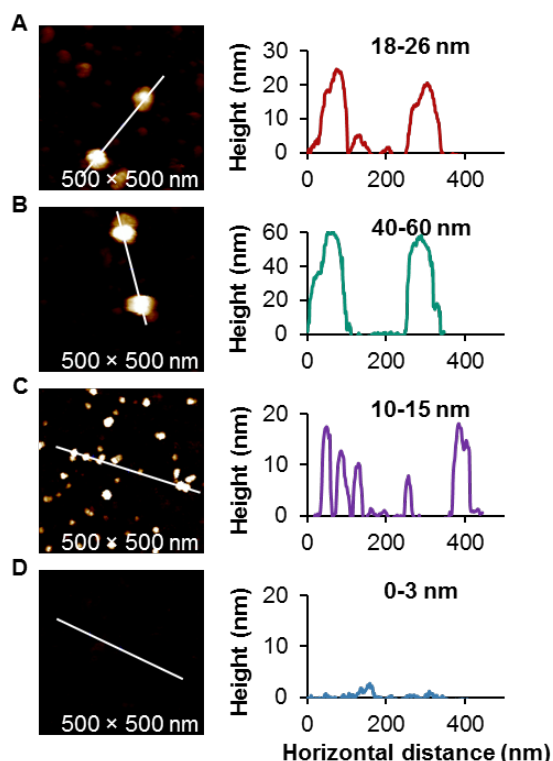


**Figure 4.2** Topographic image and corresponding height analysis of viruses and controls. (A) PPV, (B) BVDV, (C)  $\text{NH}_2$ -functionalized silica NPs, and (D) carboxylic acid-modified surface.

Controls were conducted to confirm that the virus immobilization method was required. **Figure 4.2C** shows that positively charged primary amine-functionalized silica nanoparticles were successfully immobilized with the NHS/EDC method, and the size of  $15 \pm 4$  nm was measured with the AFM for 18 particles from three different immobilization trials. The size was the same as given by the manufacturer. In addition, we found that the negatively charged SAM-COOH-modified surface had a surface roughness of 3 nm, as shown in **Figure 4.2D**. This is the same roughness as was found for the bare gold surface with the NHS/EDC control (SI **Figure A.1.2C**). The need for the NHS/EDC addition is shown in SI **Figures A.1.2D&E**, where very little PPV and no BVDV could be found when the NHS/EDC step was removed from the protocol.

Probe functionalization was confirmed by verifying the charge on the probe. The negatively charged carboxyl-terminated probe ( $\text{COO}^-$ ) interacted with the positively charged silica nanoparticles at pH 7.0 (SI **Figure A.1.3A**). No adhesion forces could be detected on the negatively charged  $\text{COO}^-$ -modified control surface at pH 7.0 (data not shown). For the positively charged quaternary amine-terminated probe ( $\text{NR}_4^+$ ), strong adhesion was found when interacting with the negatively charged  $\text{COO}^-$  control surface at pH 7.0 (SI **Figure A.1.3B**). No adhesion forces could be detected between the positively charged silica nanoparticles and the positively functionalized tip (data not shown).

### 4.3.2 Virus pI using CFM.

Most viruses carry a negative charge under physiological pH due to the pI of the virus typically being below 7 [13]. As a proof of concept that CFM can measure the pI of viral capsids, the non-enveloped virus, PPV, and the enveloped virus, BVDV, were selected to explore the virus surface charge. Some of their physical properties can be found in **Table 4.1**. PPV has a literature-reported pI of 5.0, measured by isoelectric focusing [18]. No pI information could be found for BVDV.

**Table 4.1** Model virus properties.

Virus	Capsid	Family	Nucleic acid	Size (nm)	pI	Related human viruses	References
Porcine parvovirus (PPV)	Non-enveloped	Parvoviridae	ssDNA	18-26	~5.0	B-19 human parvovirus	[18, 47]
Bovine viral diarrhea virus (BVDV)	Enveloped	Flaviviridae	ssRNA	40-60	–	Hepatitis C	[47, 48]

AFM probes terminated with either  $\text{COO}^-$  or  $\text{NR}_4^+$  were used to measure the surface charge of each virus. To provide maximum electrostatic interactions while still maintaining pH control, low ionic strength buffers at 20 mM concentration were used. **Figure 4.3A** shows the adhesion of PPV to the negatively charged  $\text{COO}^-$ -modified AFM probe as a function of pH. One representative *F-D* curve (retraction only) is shown for each pH, and they changed shape across different pHs. The overall histogram shape also changed as a function of pH. The strongest adhesion forces were observed at pH 3.0, compared with almost no adhesion being observed at pH 6.0.

In a similar experiment with the positively charged  $\text{NR}_4^+$ -modified AFM probe, the opposite adhesion trend was observed (**Figure 4.3B**). The strongest adhesion force was present at pH 6.0, and the adhesion force decreased with a decrease in pH. The adhesion forces had a significant increase when the pH was increased to pH 5.0 and above.

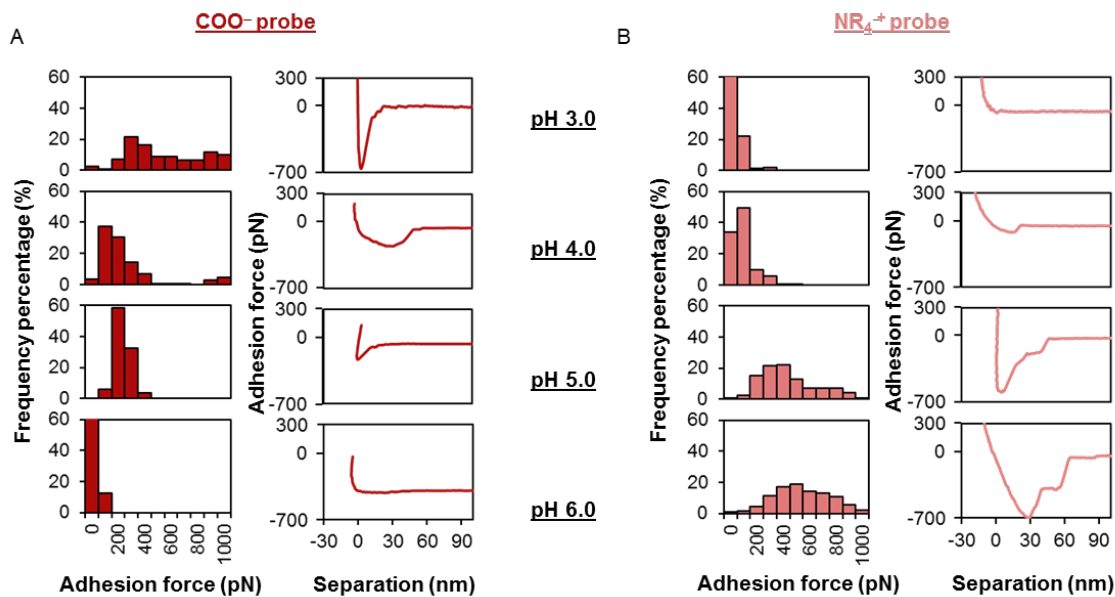


**Figure 4.3** Adhesion histograms and representative  $F$ - $D$  curves (retraction part) of PPV with a COO<sup>-</sup>-terminated probe (A) or a NR<sub>4</sub><sup>+</sup>-terminated probe (B), recorded in 20 mM citrate or phosphate buffers of varying pH. Multiple ( $n=500$ )  $F$ - $D$  curves were recorded over 500 nm  $\times$  500 nm areas.

The adhesion force data for PPV as a function of pH are summarized in **Figure 4.4A** and **4.4B**. All of the adhesion forces are the mean values, which were calculated from 500 recorded  $F$ - $D$  curves with at least three separate combinations of probe/virus samples at each pH. To determine the pI of PPV, the experimental data were fitted to a sigmoidal curve described by **Eq. 4.1**, and the pI was determined to be the inflection point of the fitted curve. The inflection point was chosen because other measurements of pI for biological molecules, with respect to pH, often show an inflection point at the pI. This includes zeta potential curves [4, 49], ATPS [20], and CFM for proteins [24]. The inflection point for PPV was found at 5.1 for the COO<sup>-</sup> probe. Similarly, the inflection point for the NR<sub>4</sub><sup>+</sup>-modified probe was 4.8. Therefore, the pI of PPV is 4.8-5.1, as determined by CFM. This is similar to the literature-reported pI of 5.0 for PPV [18].

Bulk methods were also used as a comparison to the CFM results. The zeta potential for PPV shifted from negative to positive at pH 4.0, as shown in **Figure 4.4C**, thus giving a pI of 4.0. The pI value of PPV was also estimated by a nontraditional bulk method, ATPS cross-partitioning [20]. The partitioning of PPV in a PEG-citrate system was measured at different pH values. The virus particles remained in the citrate-rich phase, comprising of negatively charged citrate ions when the virus had a positive charge. Moreover, the virus particles repelled the negatively charged citrate ions when the virus became negatively charged, and therefore partitioned to the PEG-rich phase. The pI of PPV was estimated as 5.4 by ATPS cross-partitioning. **Figure 4.4D** shows that the viral particles mostly partitioned to the citrate-rich phase at a pH < 5.4. At a pH > 5.4, the majority of the virus could be found in the PEG-rich phase. However, the cross-partitioning of the virus particles is not purely dependent on the charge repulsion from the

citrate-rich phase. The net partitioning in either phase is driven by a synergistic effect of charge repulsion from the citrate-rich phase and hydrophobic interaction from the PEG-rich phase [35, 50].

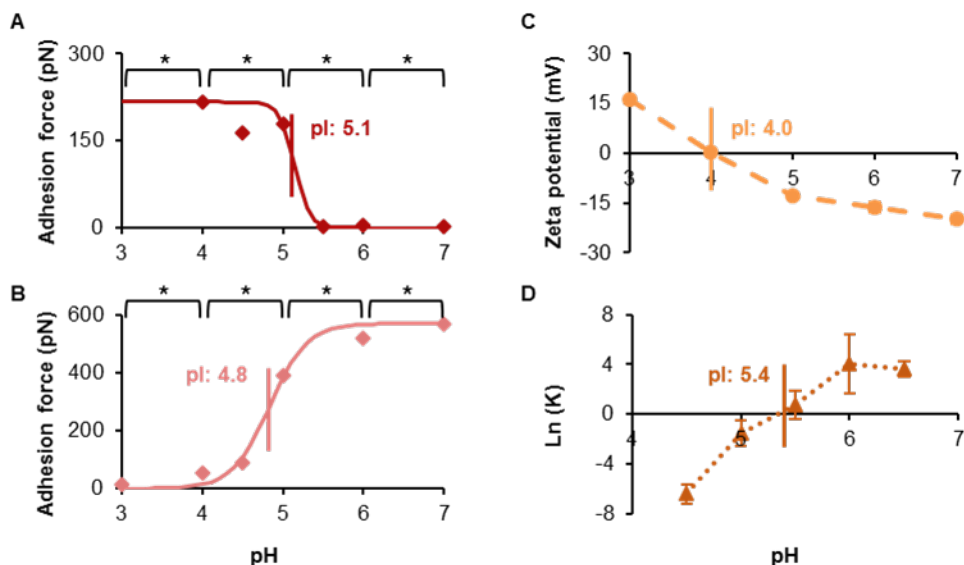


**Figure 4.4** PPV pI determination using a variety of methods. (A) CFM with the COO<sup>-</sup> probe, (B) CFM with the NR<sub>4</sub><sup>+</sup> probe, (C) zeta potential, and (D) ATPS. The CFM data were fit to a sigmoidal curve. Error bars are the standard deviation of three separate experiments. \* $p < 0.01$  using Student's  $t$ -test.

The pI values estimated by the two bulk methods for PPV both have a larger shift from the literature-reported pI value 5.0 by isoelectric focusing [18], as compared to CFM. Zeta potential and cross-partitioning methods are bulk measurements. Zeta potential has been shown to be limited by the purity of virus samples [21]. Contaminating proteins present in the virus solutions can affect the measured pI result. For cross-partitioning measurements, there are several driving forces that dictate the partitioning of biomolecules [35, 51, 52]. The measurement is not purely a measurement of charge. However, the single-particle CFM precisely targets individual virus particles, and it is not affected by contaminant proteins. In addition, the amount of the virus used in CFM is as low as that used in isoelectric focusing. However, isoelectric focusing is limited by the low solubility of virus particles [17, 18], making it difficult to obtain measurements for a variety of viral species. Herein, we have demonstrated that the CFM method is a reliable method to measure the pI of PPV since the pI determined by CFM is correlated with the pI values of PPV by other characterization measurements.

Similar force measurement experiments were performed for the enveloped BVDV. The BVDV data can be found in SI **Figure A.1.4**. Similar adhesion trends were observed for BVDV as was found for PPV. The pI value of BVDV is estimated to be 4.3-4.5 by CFM, and it is shown in **Figure 4.5A&B**. The pI by CFM was in good agreement with the pI value determined by zeta potential at pH 4.2 (**Figure 4.5**). The zeta potential correlated better to the CFM results for BVDV than PPV might be due to less

contaminated proteins existed in purified BVDV samples, but we did not test the contaminated protein levels in either virus preparation. The infectivity of both viruses was confirmed prior to zeta potential measurements, confirming the structural integrity of each virus and the presence of an envelope for BVDV.

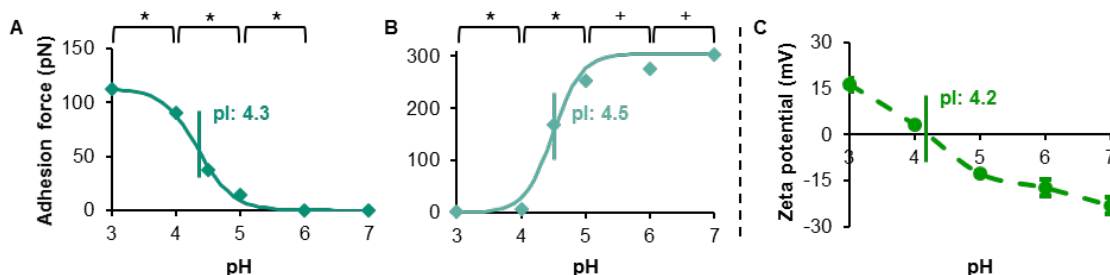


**Figure 4.5** BVDV pI determination using two methods. (A) CFM with the COO<sup>-</sup> probe, (B) CFM with the NR<sub>4</sub><sup>+</sup> probe, and (C) zeta potential. The CFM data were fit to a sigmoidal curve. Error bars are the standard deviation of three separate experiments. \* $p < 0.01$  and + $p < 0.05$  using Student's  $t$ -test.

The ATPS cross-partitioning method was unable to evaluate the pI value of BVDV. ATPS contains high concentrations of salt and polymer, likely producing a high osmotic shock to the viral particles that could cause structural deformations of the BVDV envelope [53]. This was measured by a large reduction in the BVDV viral infectivity after contact with the ATPS solutions. Enveloped viruses are more susceptible to structural damage by osmotic stress as compared to non-enveloped viruses. Hence, the ATPS cross-partitioning method is not applicable to all types of viruses.

### 4.3.3 Comparison to theoretically calculated virus pI and surface potential.

Two methods were used to calculate the electrostatic surface properties of model viruses. The first method used the entire amino acid sequence to predict the pI of the virus by the Henderson-Hasselbalch equation [14]. This is a common method to calculate protein pI [36, 54, 55]. However, it does not take into account protein folding. Only the surface amino acids actually contribute to the experimental pI, whereas all amino acids, even ones that are buried, contribute to the calculated pI. For the second method used, only the surface amino acids for one viral surface protein were calculated to determine the electrostatic surface property of the virus [38]. A similar method was used to determine the hydrophobicity of a virus, as compared to proteins [56]. The electrostatic surface potentials of the viruses tested here are based on the surface maps shown in SI **Figure A.1.5**. The electrostatic surface property did not directly report a pI, but it can be used to compare the general trends of the experimental pI by CFM, the calculated pI based on the entire amino acid sequence, and the surface potential of only the surface amino acids, using single protein crystal structures.

**Table 4.2** Computational electrostatic surface properties of the model virus vs. CFM-determined pI.

Virus	Protein	PDB ID	UniPlotKB ID	Calculated pI <sup>^</sup>	Electrostatic surface potential (mV) <sup>+</sup>	CFM determined pI <sup>*</sup>
Porcine parvovirus (PPV)	Capsid protein VP2	1K3V [262]	U5YT56	5.78	-9	4.8-5.1
Bovine viral diarrhea virus (BVDV)	Glycoprotein E2	4ILD [263]	Q5G8Z1	6.91	2	4.3-4.5
		4JNT [263]			6	

<sup>^</sup>Calculations based on entire amino acid sequence [256]

<sup>+</sup>Calculations based on surface amino acids [258]

<sup>\*</sup>This work

The sequence of the VP2 capsid protein in PPV was used to calculate the theoretical pI and the electrostatic potential, and the results are shown in **Table 4.2**. PPV has an icosahedral capsid containing viral proteins (VP) 1, 2, and 3 [57]. VP2 is the major coat protein, and composes 80% of the viral capsid [57]. Virus-like particles spontaneously form when only VP2 is expressed. Therefore, the crystal structure of VP2 was used in this work.

For enveloped viruses, the pI is affected by both the lipid and glycoprotein content in the envelope. In our current calculations, we are disregarding the contribution of the lipid bilayer. Three structural glycoproteins are embedded into the BVDV envelope, E<sup>ms</sup>, E1, and E2 [59]. E2 is the major envelope protein located on the outer surface of the BVDV, and it plays a key role in virus attachment and entry to host cells [60]. Thus, E2 was used for the BVDV computational electrostatic surface property calculations.

In the case of PPV and BVDV, the calculation of the pI for both viruses shifted to a higher pH as compared to the experimental CFM values, as shown in **Table 4.2**. It is possible that the nucleic acids inside the virus capsid could reduce the pI [49, 61]. However, the general trends are not the same for the experimental and calculated pIs, as BVDV has a higher calculated pI than PPV. When the surface charge is calculated by the electrostatic surface potential, the trend holds the same as the calculated pI, where BVDV has a higher pI than PPV. However, this simple calculation does not take into account chemical modifications (e.g., amino acids phosphorylated or acetylated) that are often observed [62]. For the enveloped virus, the level of cholesterol affects the surface charge. It has been shown that increasing the level of cholesterol in a lipid bilayer reduces Na<sup>+</sup> binding to lipid head groups, thus reducing the surface charge of the membrane [63]. This may explain why enveloped BVDV, which is cholesterol-rich [59], has lower adhesion forces measured by CFM than that of non-enveloped PPV at pH 3 by the COO<sup>-</sup> probe and at pH 7 by the NR<sub>4</sub><sup>+</sup> probe (comparing **Figures 4.4 & 4.5**). The pI values calculated by theoretical methods do not correlate well with the pI values determined experimentally, which is mainly due to that the electrostatic surface properties of viruses are not purely

determined by the surface capsid proteins. Virus particles are much more complex systems, and the theoretical calculations do not take into account the effects of the amino acids and the virus envelope. For these reasons, we need to determine the pI values of viruses by the experimental CFM method.

CFM can detect the electrostatic surface properties of viral capsids at a single-particle level. Another benefit of using CFM to determine the virus pI is the amount of the virus used in this study is as low as  $\sim 150 \mu\text{L}$  at a titer of  $10^8 \text{ MTT}_{50}/\text{mL}$ . As is known, virus samples can be expensive. CFM allows the study of virus surface charge with small amounts of samples, as has been demonstrated as an advantage of CFM for proteins [24]. This single-particle technique could improve our understanding of the virus infection cycle, quantify the quality of a gene therapy preparation for human use, and improve future technologies in areas of bioseparations and biosensing.

## 4.4 Conclusions

We have used functionalized AFM tips to study viral electrostatic surface properties with small amounts of sample. We chose to covalently attach the virus to a gold surface to guarantee that the bond that is broken during CFM is the virus-tip interaction and not the virus-surface interaction. This attachment method maintained a natural virus state without deformation or disassembly. The adhesion force as a function of pH was a good fit for a sigmoidal curve, which allowed the determination of the inflection point as the pI of the virus. CFM determined the pI of PPV to be 4.8-5.1 and BVDV to be 4.3-4.5. PPV had a literature-reported pI of 5.0, and BVDV did not have a literature-reported pI. The pI values determined by CFM are in good agreement with most of the pI values determined by the bulk measurements of zeta potential and ATPS.

CFM can detect the surface charge of viral capsids at a single-particle level, and it can enable the comparison of the surface charge between different types of viruses. Virus particles are much more complex systems than surface capsid proteins, and the theoretical calculations done here did not provide an accurate measure of the virus surface pI due to effects not taken into account, like amino acid modifications and the viral envelope. Therefore, we need to determine the pI of viruses experimentally. With a thorough understanding of virus surface chemistry, future technologies in areas of biosensing, vaccines, gene therapy, and targeted drug delivery could be significantly improved by using CFM to characterize the viral particle surface charge.



## 4.5 References

1. Cuevas-Romero, S., et al., *Molecular characterisation of Porcine rubulavirus (PorPV) isolates from different outbreaks in Mexico*. *Virus Genes*, 2016. **52**(1): p. 81-90.
2. Khamina, K., et al., *Characterization of host proteins interacting with the lymphocytic choriomeningitis virus L protein*. *Plos Pathogens*, 2017. **13**(12).
3. Dika, C., et al., *Isoelectric point is an inadequate descriptor of MS2, Phi X 174 and PRD1 phages adhesion on abiotic surfaces*. *Journal of Colloid and Interface Science*, 2015. **446**: p. 327-334.
4. Samandoulgou, I., I. Fliss, and J. Jean, *Zeta Potential and Aggregation of Virus-Like Particle of Human Norovirus and Feline Calicivirus Under Different Physicochemical Conditions*. *Food and Environmental Virology*, 2015. **7**(3): p. 249-260.
5. Marchetti, M., G.J.L. Wuite, and W.H. Roos, *Atomic force microscopy observation and characterization of single virions and virus-like particles by nano-indentation*. *Current Opinion in Virology*, 2016. **18**: p. 82-88.
6. Bernaud, J., et al., *Characterization of AAV vector particle stability at the single-capsid level*. *Journal of Biological Physics*, 2018. **44**(2): p. 181-194.
7. Fonville, J.M., et al., *Influenza Virus Reassortment Is Enhanced by Semi-infectious Particles but Can Be Suppressed by Defective Interfering Particles*. *Plos Pathogens*, 2015. **11**(10).
8. Adamson-Small, L., et al., *A scalable method for the production of high-titer and high-quality adeno-associated type 9 vectors using the HSV platform*. *Molecular Therapy-Methods & Clinical Development*, 2016. **3**.
9. Brown, M.R., et al., *Defining the Mechanistic Binding of Viral Particles to a Multimodal Anion Exchange Resin*. *Biotechnology Progress*, 2018. **34**(4): p. 1019-1026.
10. Mi, X., K.S. Vijayaragavan, and C.L. Heldt, *Virus adsorption of water-stable quaternized chitosan nanofibers*. *Carbohydrate Research*, 2014. **387**: p. 24-29.
11. Mi, X. and C.L. Heldt, *Adsorption of a non-enveloped mammalian virus to functionalized nanofibers*. *Colloids and Surfaces B-Biointerfaces*, 2014. **121**: p. 319-324.
12. Leuchs, B., et al., *A novel scalable, robust downstream process for oncolytic rat parvovirus: isoelectric point-based elimination of empty particles*. *Applied Microbiology and Biotechnology*, 2017. **101**(8): p. 3143-3152.
13. Michen, B. and T. Graule, *Isoelectric points of viruses*. *Journal of applied microbiology*, 2010. **109**(2): p. 388-397.
14. Po, H.N. and N. Senozan, *The Henderson-Hasselbalch equation: its history and limitations*. *Journal of Chemical Education*, 2001. **78**(11): p. 1499.
15. Harrison, R.G., et al., *Bioseparations Science and Engineering*. *Topics in Chemical Engineering*. 2001: Oxford University Press.
16. Aronino, R., et al., *Removal of viruses from surface water and secondary effluents by sand filtration*. *Water Res*, 2009. **43**(1): p. 87-96.

17. Braun, M., et al., *A simple method to estimate the isoelectric point of modified Tomato bushy stunt virus (TBSV) particles*. Electrophoresis, 2017. **38**(21): p. 2771-2776.
18. Weichert, W.S., et al., *Assaying for structural variation in the parvovirus capsid and its role in infection*. Virology, 1998. **250**(1): p. 106-117.
19. Miörner, H., P. Albertsson, and G. Kronvall, *Isoelectric points and surface hydrophobicity of Gram-positive cocci as determined by cross-partition and hydrophobic affinity partition in aqueous two-phase systems*. Infection and immunity, 1982. **36**(1): p. 227-234.
20. Walter, H., D.E. Brooks, and F. Derek, *Partitioning in aqueous two-phase system: theory, methods, uses, and applications to biotechnology*. 1985: Academic Press.
21. Dika, C., et al., *Impact of the virus purification protocol on aggregation and electrokinetics of MS2 phages and corresponding virus-like particles*. Physical Chemistry Chemical Physics, 2013. **15**(15): p. 5691-5700.
22. Noy, A., D.V. Vezenov, and C.M. Lieber, *Chemical force microscopy*. Annual Review of Materials Science, 1997. **27**(1): p. 381-421.
23. Ahimou, F., et al., *Probing microbial cell surface charges by atomic force microscopy*. Langmuir, 2002. **18**(25): p. 9937-9941.
24. Guo, S.F., et al., *Measuring protein isoelectric points by AFM-based force spectroscopy using trace amounts of sample*. Nature Nanotechnology, 2016. **11**(9): p. 817-823.
25. Kaur, J., et al., *Atomic force spectroscopy-based study of antibody pesticide interactions for characterization of immunosensor surface*. Biosensors & Bioelectronics, 2004. **20**(2): p. 284-293.
26. Bonazza, K., et al., *Visualization of a protein-protein interaction at a single-molecule level by atomic force microscopy*. Analytical and Bioanalytical Chemistry, 2014. **406**(5): p. 1411-1421.
27. Tsai, H., et al., *Estimation of Molecular Interaction Force Using Atomic Force Microscopy for Bioapplication*. Journal of Physical Chemistry B, 2016. **120**(42): p. 10932-10935.
28. Alsteens, D., et al., *Atomic force microscopy-based characterization and design of biointerfaces*. Nature Reviews Materials, 2017. **2**(5): p. 17008.
29. Heldt, C.L., et al., *A colorimetric assay for viral agents that produce cytopathic effects*. J Virol Methods, 2006. **135**(1): p. 56-65.
30. Mi, X., et al., *Mannitol-induced gold nanoparticle aggregation for the ligand-free detection of viral particles*. Analyst, 2019. **144**(18): p. 5486-5496.
31. Tafur, M.F., K.S. Vijayaragavan, and C.L. Heldt, *Reduction of porcine parvovirus infectivity in the presence of protecting osmolytes*. Antiviral Research, 2013. **99**(1): p. 27-33.
32. Meng, H., et al., *Biomimetic recyclable microgels for on-demand generation of hydrogen peroxide and antipathogenic application*. Acta Biomaterialia, 2019. **83**: p. 109-118.
33. Hutter, J.L. and J. Bechhoefer, *CALIBRATION OF ATOMIC-FORCE MICROSCOPE TIPS (VOL 64, PG 1868, 1993)*. Review of Scientific Instruments, 1993. **64**(11): p. 3342-3342.

34. Nielsen, L., et al., *Effect of environmental factors on the kinetics of insulin fibril formation: elucidation of the molecular mechanism*. *Biochemistry*, 2001. **40**(20): p. 6036-6046.
35. Joshi, P.U., et al., *Tie line framework to optimize non-enveloped virus recovery in aqueous two-phase systems*. *Journal of Chromatography B*, 2019. **1126**: p. 121744.
36. Kozlowski, L.P., *Proteome-pI: proteome isoelectric point database*. *Nucleic acids research*, 2016. **45**(D1): p. D1112-D1116.
37. Bateman, A., et al., *UniProt: a worldwide hub of protein knowledge*. *Nucleic Acids Research*, 2019. **47**(D1): p. D506-D515.
38. Hagemans, D., et al., *A script to highlight hydrophobicity and charge on protein surfaces*. *Frontiers in molecular biosciences*, 2015. **2**: p. 56.
39. Alsteens, D., et al., *High-resolution imaging of chemical and biological sites on living cells using peak force tapping atomic force microscopy*. *Langmuir*, 2012. **28**(49): p. 16738-44.
40. Ortega-Esteban, Á., et al., *Structural and Mechanical Characterization of Viruses with AFM*, in *Atomic Force Microscopy*. 2019, Springer. p. 259-278.
41. de Pablo, P.J., *Atomic force microscopy of virus shells*. *Seminars in Cell & Developmental Biology*, 2018. **73**: p. 199-208.
42. Grabarek, Z. and J. Gergely, *ZERO-LENGTH CROSSLINKING PROCEDURE WITH THE USE OF ACTIVE ESTERS*. *Analytical Biochemistry*, 1990. **185**(1): p. 131-135.
43. Lahiri, J., et al., *A strategy for the generation of surfaces presenting ligands for studies of binding based on an active ester as a common reactive intermediate: A surface plasmon resonance study*. *Analytical Chemistry*, 1999. **71**(4): p. 777-790.
44. Zeng, C., et al., *Probing the link among genomic cargo, contact mechanics, and nanoindentation in recombinant adeno-associated virus 2*. *The Journal of Physical Chemistry B*, 2017. **121**(8): p. 1843-1853.
45. Driskell, J.D., et al., *Control of antigen mass transfer via capture substrate rotation: An absolute method for the determination of viral pathogen concentration and reduction of heterogeneous immunoassay incubation times*. *Journal of Virological Methods*, 2006. **138**(1-2): p. 160-169.
46. Eleta-Lopez, A. and A. Calò, *Key factors of scanning a plant virus with AFM in air and aqueous solution*. *Microscopy research and technique*, 2017. **80**(1): p. 18-29.
47. Norkin, L.C., *Virology: Molecular Biology and Pathogenesis*. 2010: ASM Press.
48. Kim, I.S., Y.W. Choi, and S.R. Lee, *Optimization and validation of a virus filtration process for efficient removal of viruses from urokinase solution prepared from human urine*. *Journal of Microbiology and Biotechnology*, 2004. **14**(1): p. 140-147.
49. Dika, C., et al., *Impact of Internal RNA on Aggregation and Electrokinetics of Viruses: Comparison between MS2 Phage and Corresponding Virus-Like Particles*. *Applied and Environmental Microbiology*, 2011. **77**(14): p. 4939-4948.
50. Vijayaragavan, K.S., et al., *Separation of porcine parvovirus from bovine serum albumin using PEG-salt aqueous two-phase system*. *Journal of Chromatography B-Analytical Technologies in the Biomedical and Life Sciences*, 2014. **967**: p. 118-126.

51. Andrews, B.A. and J.A. Asenjo, *Theoretical and Experimental Evaluation of Hydrophobicity of Proteins to Predict their Partitioning Behavior in Aqueous Two Phase Systems: A Review*. Separation Science and Technology, 2010. **45**(15): p. 2165-2170.
52. Grilo, A.L., M.R. Aires-Barros, and A.M. Azevedo, *Partitioning in Aqueous Two-Phase Systems: Fundamentals, Applications and Trends*. Separation and Purification Reviews, 2016. **45**(1): p. 68-80.
53. Choi, H.J., et al., *Effect of Osmotic Pressure on the Stability of Whole Inactivated Influenza Vaccine for Coating on Microneedles*. Plos One, 2015. **10**(7).
54. Audain, E., et al., *Accurate estimation of isoelectric point of protein and peptide based on amino acid sequences*. Bioinformatics, 2016. **32**(6): p. 821-827.
55. Venkatakrishnan, B., et al., *Structure and Dynamics of Adeno-Associated Virus Serotype 1 VP1-Unique N-Terminal Domain and Its Role in Capsid Trafficking*. Journal of Virology, 2013. **87**(9): p. 4974-4984.
56. Heldt, C.L., et al., *Experimental and computational surface hydrophobicity analysis of a non-enveloped virus and proteins*. Colloids and Surfaces B-Biointerfaces, 2017. **153**: p. 77-84.
57. Simpson, A.A., et al., *The structure of porcine parvovirus: Comparison with related viruses*. Journal of Molecular Biology, 2002. **315**(5): p. 1189-1198.
58. Li, Y., et al., *Crystal structure of glycoprotein E2 from bovine viral diarrhea virus*. Proceedings of the National Academy of Sciences of the United States of America, 2013. **110**(17): p. 6805-6810.
59. Callens, N., et al., *Morphology and Molecular Composition of Purified Bovine Viral Diarrhea Virus Envelope*. Plos Pathogens, 2016. **12**(3): p. e1005476.
60. El Omari, K., et al., *Structure of a Pestivirus Envelope Glycoprotein E2 Clarifies Its Role in Cell Entry*. Cell Reports, 2013. **3**(1): p. 30-35.
61. Langlet, J., et al., *Impact of chemical and structural anisotropy on the electrophoretic mobility of spherical soft multilayer particles: the case of bacteriophage MS2*. Biophys J, 2008. **94**(8): p. 3293-312.
62. Saeed, M., et al., *In Vitro Phosphorylation and Acetylation of the Murine Pocket Protein Rb2/p130*. Plos One, 2012. **7**(9).
63. Magarkar, A., et al., *Cholesterol level affects surface charge of lipid membranes in saline solution*. Scientific Reports, 2014. **4**.

# 5 Virus detection by mannitol-induced gold nanoparticle aggregation<sup>3</sup>

---

<sup>3</sup> The material contained in this chapter has been published in *Analyst*. Full citation: *Mi, X., Lucier, E. M., Turpeinen, D. G., Yeo, E. L. L., Kah, J. C. Y., Heldt, C. L. Mannitol-induced gold nanoparticle aggregation for the ligand-free detection of viral particles. Analyst 2019, 144, 5486-5496.*

## 5.1 Introduction

The novel properties of gold nanoparticles (AuNPs) can be harnessed to create specialized sensors for biomolecules.<sup>1-3</sup> One class of biomolecule that has shown great promise for AuNPs detection are viral particles.<sup>4-6</sup> Viruses are unique colloids that consist of a protein capsid shell that encapsulate nucleic acids and may be surrounded by a lipid bilayer. Most commonly, the capsid proteins or nucleic acids are the biochemical targets for direct virus detection.<sup>7-10</sup> Virus can be detected with lateral flow assays, in which the AuNPs function as direct coloring,<sup>11-12</sup> or through the aggregation of the AuNPs.<sup>3, 10, 13-14</sup> While these are promising methods for disease detection of specific viral infections, there is a need to detect the presence of infectious virus particles without being virus specific. In one case, blood transfusions in Africa are commonly tested for only three different viruses, HIV, hepatitis B and hepatitis C,<sup>15</sup> whereas in the US, blood donations are tested for at least seven different viruses.<sup>16</sup> A general virus detection method could alleviate the need for low resource countries to test for specific viruses in blood donations. The goal is not a disease diagnosis, but the general safety of the blood supply.

Another application could be the evaluation of the cleanliness of a surface. One example would be the elimination of norovirus after a cruise ship outbreak. According to the Centers for Disease Control and Prevention (CDC), norovirus causes about 20 million people in the US to have acute gastroenteritis each year<sup>17</sup> and the virus can be transmitted through contact with contaminated food, water or surfaces. A rapid and inexpensive virus detection method could alleviate many of these transmissions through the testing of surface cleanliness.

AuNPs are widely used as a colorimetric detection mechanism due to their unique surface plasmon resonance (SPR) property. A strong optical absorbance peak of AuNPs is dependent on the size of AuNPs and also highly sensitive to inter-particle separations. Aggregation of AuNPs results in a red-shift and peak broadening of the ultraviolet-visible (UV-Vis) absorption spectrum and an obvious color change from red to dark blue or gray.<sup>18-19</sup> However, this type of detection is not sensitive to lower degrees of aggregation and not suitable for the analysis of colored samples. To overcome the limitations of colorimetric assays by UV-Vis detection,<sup>20-21</sup> the light scattering properties of AuNPs have been used for biomolecule detections.<sup>6, 14, 22</sup> Light scattering-based assays have a lower limit of detection, up to four orders of magnitude, as compared to UV-Vis spectrophotometric-based AuNPs aggregation detection.<sup>23</sup> Light scattering methods may be required to detect pathogens, which can be infectious at very low concentrations.

There have been assays developed for the detection of proteins using AuNP aggregation. Proteins non-specifically adsorb to AuNPs, creating a protein corona<sup>24-25</sup> through a combination of hydrophobic interactions,<sup>26</sup> electrostatic interactions,<sup>27</sup> and coordinate binding between the thiol or amino groups of proteins and the AuNPs.<sup>28-29</sup> A protein concentration assay has been developed by determining the amount of protein needed to create a protein corona around an AuNP that will protect the nanoparticle from salt-induced aggregation.<sup>30</sup> This demonstrates the application of a non-specific biomolecule concentration assay using AuNPs aggregation.

AuNPs can be easily conjugated with biomolecules, making them a good candidate for specific virus detection using antibodies or oligonucleotides. AuNPs conjugated with an antibody can sensitively detect the presence of the H3N2 influenza A virus with a detection limit of 7.8 hemagglutination units.<sup>13</sup> Hepatitis C virus (HCV) specific oligonucleotide-functionalized AuNPs were used to quantify HCV RNA in clinical samples by AuNPs aggregation with a limit of detection of 4.57 international units (IU)/ $\mu\text{L}$ .<sup>10</sup> However, these systems require an antibody or oligonucleotide that is specific to the virus of interest for detection. But what if we need to know if any virus is present? To develop a non-specific viral particle assay based on AuNPs aggregation, methods to aggregate generic viral particles need to be explored.

Virus particles can aggregate in a variety of solution conditions through manipulation of pH, salt concentration, and osmolyte concentration. Viruses tend to form aggregates close to their isoelectric point (pI), where the net charge of the virus surface is neutral and the repulsive electrostatic forces on the virus surfaces are the lowest.<sup>31</sup> MS2,  $\Phi\text{X174}$ , and PRD1 bacteriophage particles formed aggregates when the pH was lowered from 7 to near their pI of 4.<sup>32</sup> Viruses show different degrees of aggregation depending on salt types and concentration. A sodium chloride solution ranging from 0.5-4 M reversibly aggregated the hepatitis B surface antigen (HBsAg) virus-like particles (VLPs) into oligomeric particles, while 1-2 M ammonium sulfate irreversibly aggregated the VLPs.<sup>33</sup>

Osmolytes have been shown to preferentially aggregate both the non-enveloped porcine parvovirus (PPV) and enveloped Sindbis virus (SINV) while not aggregating bovine serum albumin (BSA) or lysozyme.<sup>34-36</sup> The hypothesis of why this aggregation occurs is based on the differences between virus and protein surface chemistry. Most osmolytes protect proteins from high osmotic stress, resulting in enhanced protein stability.<sup>37</sup> Osmolytes have a high affinity for water and a low affinity for the protein backbone.<sup>38-39</sup> Therefore, osmolytes are able to remove water molecules near hydrophobic residues on the protein surface.<sup>40</sup> To compensate for this change in free energy, the protein rearranges into a more compact structure.<sup>37</sup> Viruses tend to aggregate in this same situation due to two major differences between viruses and proteins: viruses have been shown to be more hydrophobic than proteins,<sup>41-42</sup> allowing more surface area to be dehydrated, and viruses are more rigid than proteins and cannot collapse to compensate for the free energy change. In response to the change in free energy, viruses aggregate.

In this study, PPV and bovine viral diarrhea virus (BVDV) were detected by comparing the aggregation of virus-coated AuNPs in mannitol solutions and sodium chloride solutions to BSA and thyroglobulin-coated AuNPs. PPV and BVDV were chosen to demonstrate the robustness of this general virus particle detection assay, as PPV is a small non-enveloped virus while BVDV is a larger, enveloped virus. Results indicate that virus and protein-coated nanoparticles can be distinguished by a difference in aggregate size measured by dynamic light scattering (DLS). Two proof-of-concept tests were conducted to determine if PPV could be detected in simulated applications. PPV was dried on a surface and then recovered by rubbing the area with a wet cotton swab. The reconstituted PPV was quantitatively measured with the developed AuNPs aggregation assay. PPV could also be quantitatively detected in different concentrations of BSA solution matrix, demonstrating the possible application in testing blood

donations. These results indicate that ligand-free AuNPs aggregation may be a promising detection method for the presence of viral particles. This nonspecific virus detection method is promising for determining the presence of viruses in a blood transfusion sample or on a contaminated surface.

## 5.2 Experimental section

### 5.2.1 Materials

Bovine serum albumin (BSA) ( $\geq 98\%$ ) and thyroglobulin from porcine thyroid gland were purchased from Sigma-Aldrich (St. Louis, MO). For synthesis of AuNPs, gold (III) chloride trihydrate ( $\text{HAuCl}_4 \cdot 3\text{H}_2\text{O}$ ) ( $\geq 99.9\%$ ) and trisodium citrate (ACS grade,  $\geq 99.0\%$ ) were purchased from Sigma-Aldrich. Potassium phosphate monobasic (molecular biology grade,  $\geq 99.0\%$ ), sodium phosphate monobasic monohydrate (ACS grade, 98.0-102.0%), and sodium chloride (ACS grade,  $\geq 99.0\%$ ) were a gift from Millipore Sigma (Burlington, MA). Sodium phosphate dibasic heptahydrate (ACS grade, 98.0-102.0%), D-mannitol ( $\geq 98\%$ ), and glutaraldehyde solution (Grade I, 70% in  $\text{H}_2\text{O}$ ) were purchased from Sigma-Aldrich. Phosphate buffered saline (PBS) (pH = 7.2) was purchased from Life Technologies (Grand Island, NY). Thiazolyl blue tetrazolium bromide (MTT) (98%) was purchased from Alfa Aesar (Haverhill, MA). All aqueous solutions or buffers were prepared using purified water with a resistivity of  $\geq 18 \text{ M}\Omega \cdot \text{cm}$  from a Nanopure filtration system (Thermo Scientific, Waltham, MA) and filtered with a 0.2  $\mu\text{m}$  bottle top filter (VWR, Radnor, PA) or a 0.2  $\mu\text{m}$  syringe filter (VWR) prior to use.

### 5.2.2 Virus titration and purification

Porcine kidney cells (PK-13, CRL-6489) and bovine turbinate cells (BT-1, CRL-1390) were purchased from ATCC. Porcine parvovirus (PPV) strain NADL-2 was a gift from Dr. Ruben Carbonell (North Carolina State University, Raleigh, NC). Bovine viral diarrhea virus (BVDV) strain NADL was purchased from USDA APHIS. PPV was propagated in PK-13 cells and BVDV was propagated in BT-1 cells. Both PPV and BVDV were titrated with an MTT assay, as described previously.<sup>43-44</sup> The MTT assay is a cell viability assay that can be correlated with viral infectivity. For purification of virus, PPV or BVDV was first dialyzed using a Biotech Cellulose Ester 1000 kDa dialysis tubing (Rancho Dominguez, CA) at 4°C for two days with two buffer exchanges in 4 mM phosphate buffer (pH 7.2). The dialyzed virus was then polished with an Econo-Pac 10DG desalting column (Hercules, CA).

### 5.2.3 Synthesis and characterization of AuNPs

The citrate-capped AuNPs were synthesized using the previously established citrate reduction method.<sup>30</sup> Briefly, a trisodium citrate solution was added to boiling



hydrochloroauric acid (HAuCl<sub>4</sub>) solution and kept boiling for 15 minutes. The boiling solution color was observed to turn from pale yellow to purple, followed by the formation of deep red AuNPs colloids. The AuNP colloidal solution was cooled to room temperature for further characterization.

The synthesized AuNPs were characterized by UV-Vis absorption spectroscopy, dynamic light scattering (DLS), and transmission electron microscopy (TEM). The AuNPs solution was transferred into one well of a 96-well plate and the UV-Vis absorption spectrum was measured from 400 – 900 nm wavelength with a Synergy Mx microplate reader (Winooski, VT). The hydrodynamic diameter and zeta potential of AuNPs were measured with a Malvern Zetasizer Nano ZS (Worcestershire, United Kingdom). The morphology of the AuNPs was characterized with a JEOL JEM-2010 TEM (Peabody, MA) at 200 kV. The concentration of the AuNPs was determined by the molar extinction coefficient, which is related to the particle diameter, using a previously established method.<sup>45</sup> The synthesized AuNPs were prepared fresh and kept at room temperature until use. The AuNPs were washed once by re-suspending the AuNPs pellet into nanopure water after pelleting with an ST16R Centrifuge (Thermo Scientific, Asheville, NC) at  $7,000 \times g$  for 20 minutes and diluted to a final concentration of 3.5 nM for subsequent experiments.

#### 5.2.4 Coating and characterization of virus-AuNPs complexes

Different concentrations of purified PPV, BVDV, BSA, or thyroglobulin were added to the 3.5 nM AuNPs for a final concentration of 1.75 nM AuNPs. The coated AuNPs were vortexed and rotated end-over-end for 20 hours on a Roto-shake Genie rocker (Bohemia, NY) at the maximum rotation speed and then centrifuged at  $6,000 \times g$  for 20 minutes. The coated AuNPs were characterized by UV-Vis spectroscopy and DLS. The coated AuNPs were resuspended in a 1 M mannitol or 1 M sodium chloride solution and characterized.

Prior to detection of coated AuNPs with the Malvern Zetasizer, the virus was inactivated according to university biosafety protocols. A quantity 7.14  $\mu$ L of 70% glutaraldehyde solution was added to 1 mL of coated AuNPs before and after osmolyte or salt treatment to make the final solution concentration of 0.5% glutaraldehyde. Each tube was incubated at room temperature for 2 hours and was measured with the Malvern Zetasizer.

To quantify the aggregation of AuNPs, the mean hydrodynamic diameter ( $D_H$ ), was measured by DLS. The change in the hydrodynamic diameter after treatment ( $\Delta D_H$ ) was calculated by Eq. 5.1.

$$\Delta D_H = D_{H \text{ coated AuNPs after treatment}} - D_{H \text{ coated AuNPs before treatment}} \quad (5.1)$$

A high  $\Delta D_H$  represents a high degree of aggregation of coated AuNPs by either osmolyte or salt treatment.

For TEM characterization, 8 log PPV, 8 log PPV-coated AuNPs, and 8 log PPV-coated AuNPs after 1 M mannitol aggregation were adsorbed to a plasma etched TEM copper grids (Carbon Type-B, 300 mesh) for 2 minutes and were negatively stained with

2% uranyl acetate (Fisher Scientific) for 2 minutes. The morphology of the virus samples was imaged with a JEOL JEM-2010 TEM at 80 kV.

### **5.2.5 Proof-of-concept tests**

To determine the effect of protein interference on the virus detection, 500  $\mu\text{L}$  of PPV was spiked into the same volume of solution containing different concentrations of BSA in PBS. The diameter was measured by DLS before and after addition of 1 M mannitol.

To simulate testing a surface for virus contamination, a swab test was developed.<sup>46-47</sup> Five 20  $\mu\text{L}$  droplets of purified PPV in PBS buffer were placed on a sterile petri dish and dried in the biosafety cabinet for 1 hour. After the droplets evaporated, 100  $\mu\text{L}$  of PBS buffer was pipetted onto the surface. The surface was then swabbed with a sterile cotton swab in a horizontal, vertical and diagonal direction, five times for each direction. The cotton swab was placed in a tube containing 800  $\mu\text{L}$  PBS buffer, incubated for 10 minutes, vortexed for 10 seconds and incubated for an additional 10 minutes. Liquid retained in the swab was removed by pressing of the cotton against the tube wall. The diameter was measured by DLS before and after addition of 1 M mannitol.

### **5.2.6 Statistical analysis**

Statistical analysis was performed using R statistical software. A two sample t-test assuming equal variances (estimate pooled variance) was employed for comparison of virus-coated AuNPs with protein-coated AuNPs to determine an analytical limit of detection. Statistically significant differences are indicated by an asterisk (\*).

## 5.3 Results and discussion

### 5.3.1 Rationale of virus detection method

Traditional virus detection methods require the specific detection of either capsid proteins by antiviral antibodies<sup>13-14</sup> or viral nucleic acids by complementary oligonucleotides.<sup>3, 10</sup> While this is a reliable method to detect known viral contaminants, it will not detect unknown viral particles. This work is a proof-of-concept study demonstrating that the behavior of virus and AuNPs in osmolyte and salt solutions can be used for virus detection of general viral contamination, without targeting a specific virus.

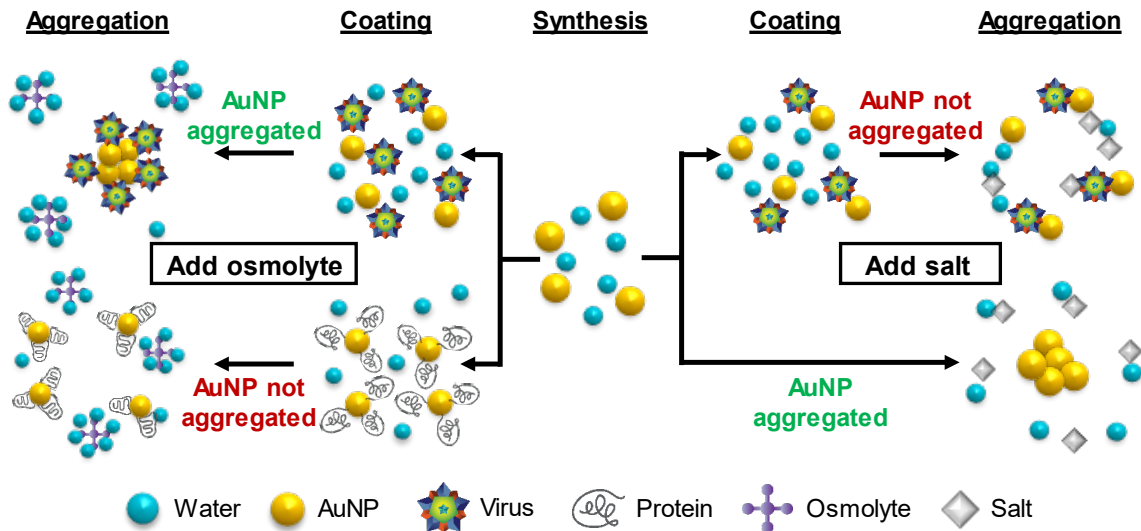


**Figure 5.1** The outcome of AuNPs aggregation detection of virus.

Earlier work demonstrated that viral particles preferentially flocculate in the presence of osmolytes.<sup>34-35</sup> As described in the introduction, this is due to the hydrophobicity and rigidity of virus particles. Osmolytes dehydrate protein and virus surfaces. However, since viruses are more hydrophobic than proteins,<sup>41-42</sup> they aggregate when there is a loss of their hydrating layer. Thus, viruses aggregate when in the presence of high osmolyte concentrations, while proteins do not. This study will apply this knowledge to induce the aggregation of virus and detect that aggregation with AuNPs as a beacon. A cartoon of AuNPs aggregation to probe the presence of viral particles is shown in **Figure 5.1**. In the presence of osmolytes, virus-coated AuNPs aggregate and a measurable size increase is observed. However, the aggregation is not detected when protein-coated AuNPs are in the presence of osmolyte solutions. Salts are known to induce the aggregation of AuNPs,<sup>48-50</sup> since electrolytes can neutralize repulsive forces arising from the surface charge of citrate-coated AuNPs, causing the AuNPs to

aggregate.<sup>51</sup> Minimal aggregation was shown when the osmolytes mannitol and glycine contacted uncoated AuNPs (see SI A.2). Viruses on the surface of AuNPs can stabilize the nanoparticles from salt-induced aggregation, likely with a similar mechanism that protein-coated AuNPs are stabilized from salt-induced aggregation.<sup>30</sup> The reaction of the coated AuNPs to salt-induced and osmolyte-induced aggregation allowed the virus-containing samples to be identified from the protein-only samples.

### 5.3.2 Synthesis and characterization of AuNPs

The characterization of synthesized and coated AuNPs can be found in **Figure 5.2**. Synthesized AuNPs formed a red colloidal solution and were monodisperse and uniform, as shown in **Figure 5.2A**. The AuNPs showed a mean zeta potential of  $-36 \pm 3$  mV, indicating the synthesized citrate-capped AuNPs were stable and negatively charged (**Figure 5.2B**). The isolated AuNPs had an absorbance peak at 519 nm in the UV-Vis absorbance spectrum (**Figure 5.2C**). The PPV-coated AuNPs and the BSA-coated AuNPs had a red-shift of 6 nm in the peak wavelength, as compared to bare AuNPs. This demonstrated that the AuNPs were coated successfully.<sup>52</sup> Coating of AuNPs with PPV or BSA also increased the hydrodynamic diameter of the AuNPs, as shown in **Figure 5.2D**. The bare AuNPs had a mean hydrodynamic diameter of  $15 \pm 0.4$  nm. When the AuNPs were coated with PPV or BSA, the hydrodynamic diameter increased according to the size of the coating molecule, PPV is 18-26 nm<sup>53</sup> and BSA is  $\sim 6.8$  nm<sup>54</sup>. Both the red-shift in the UV-Vis spectrum and the increase in the size indicated the formation of a monolayer<sup>25</sup> on the AuNPs surface for either protein or virus.

For biosafety reasons, the PPV had to be inactivated before testing with DLS. It was confirmed that the size did not change for the BSA-coated AuNPs before and after crosslinking. It was also observed that the size of the coated nanoparticles prior to aggregating agent addition was as expected in **Figure 5.2D**, providing evidence that the crosslinking did not induce AuNPs aggregation.

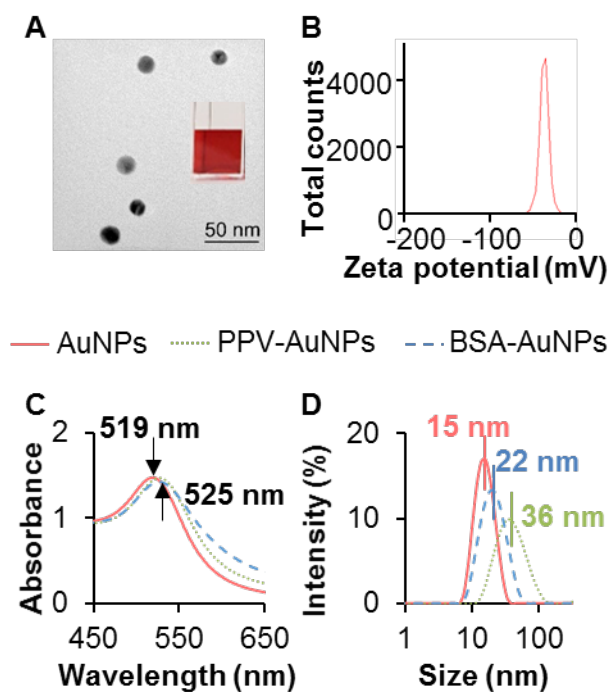


**Figure 5.2** Characterization of synthesized and coated AuNPs. (A) TEM image of the AuNPs, the inset image showing the color of synthesized AuNPs, (B) zeta potential, (C) UV-Vis absorption spectrum, (D) hydrodynamic diameter.

### 5.3.3 Concentration dependence

It was difficult to compare the concentration of PPV and BSA. It was determined that the best way to compare the virus and protein would be to find a concentration of each that covered the same area on the AuNP assuming similar binding affinities. It was calculated that 1 nM BSA covered the same area on the AuNPs as  $10^8$  MTT<sub>50</sub>/mL of PPV (see SI A.2), which is the highest concentration of PPV that can be obtained from our virus propagation method. The calculation assumed that the structure of the virus or BSA did not change from the crystal structure size<sup>53-54</sup> and that there was a 1:1,000,000 ratio of infectious to non-infectious virus particles for the PPV.<sup>55</sup> A higher concentration range of BSA was also tested because it has been shown that 1 nM BSA is too low a concentration to form a protein monolayer on AuNPs<sup>56-57</sup> that can halt salt-induced aggregation.<sup>51</sup>

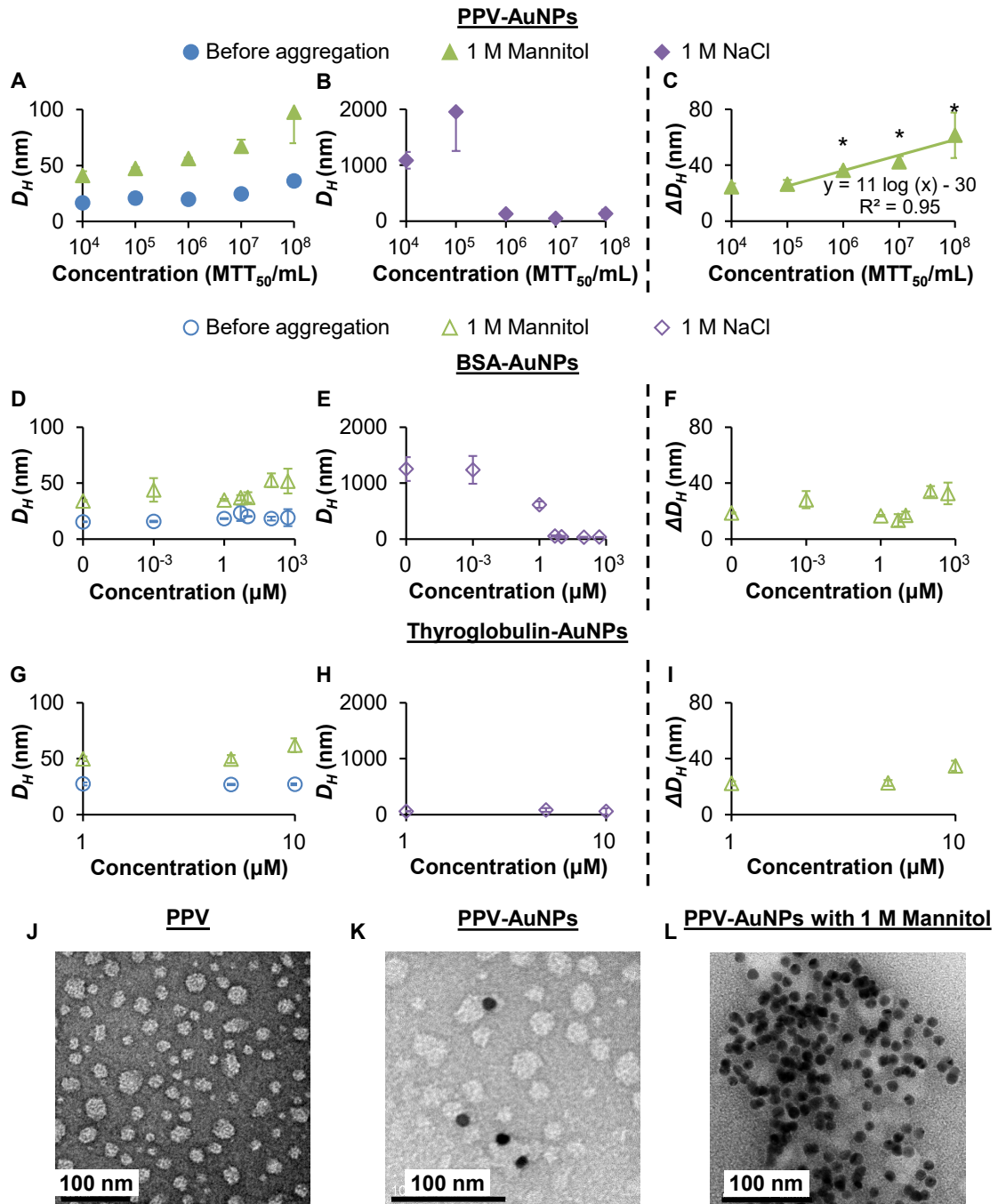


**Figure 5.3** Concentration dependence for detection of PPV versus control BSA & thyroglobulin. (A&D&G) Size profile of PPV, BSA or thyroglobulin coated AuNPs as a function of concentrations before and after 1 M mannitol addition as measured by DLS. (B&E&H) Size profile of PPV, BSA or thyroglobulin coated AuNPs as a function of concentrations after 1 M NaCl addition as measured by DLS. (C&F&I) Change in AuNPs aggregation size for PPV, BSA or thyroglobulin after 1 M mannitol addition. Solid markers represent PPV, open markers represent BSA and thyroglobulin. All data points are the average of three separate tests and error bars represent the standard deviation. Concentrations are plotted as a log scale. TEM images of (J) 8 log PPV, (K) 8 log PPV-coated AuNPs and (L) 8 log PPV-coated AuNPs with 1 M mannitol. \* $p < 0.05$  for virus compared to BSA and thyroglobulin controls.

The mean hydrodynamic diameter ( $D_H$ ) measured by DLS was used to quantify the size of AuNPs before coating, after coating, and after inducing aggregation with either mannitol or salt.  $\Delta D_H$  designates the change in the size of coated AuNPs after induction of aggregation with either osmolyte or salt (**Eq. 5.1**). **Figure 5.3A** shows that PPV-coated AuNPs increase in size after 1 M mannitol aggregation. The aggregation of PPV-coated AuNPs in mannitol is likely due to the flocculation of PPV caused by mannitol.<sup>34, 36</sup> Higher concentrations of PPV, starting at  $10^6$  MTT<sub>50</sub>/mL, reduced aggregation in NaCl due to the virus protecting the AuNPs from salt-induced aggregation, shown in **Figure 5.3B**. The calculated  $\Delta D_H$  for PPV shows a linear trend when plotted against the log of PPV titer when PPV has a concentration greater than  $10^5$  MTT<sub>50</sub>/mL (**Figure 5.3C**). The change in  $D_H$  due to the mannitol-induced aggregation of PPV increased from  $25 \pm 2$  nm to  $61 \pm 16$  nm between  $10^4$  MTT<sub>50</sub>/mL and  $10^8$  MTT<sub>50</sub>/mL. The lowest concentration of PPV that could be detected was estimated to be  $10^6$  MTT<sub>50</sub>/mL, which is  $\sim 1$  pM. This lowest detectable concentration is lower than standard antibody binding assays that detect virus,<sup>58-60</sup> which typically have a nanomolar detection limit.<sup>61-62</sup>

The size of BSA-coated AuNPs in mannitol was much smaller than PPV-coated AuNPs, as shown in **Figure 5.3**. This demonstrates that there is a clear difference between AuNPs aggregation with mannitol in the presence of PPV versus BSA, demonstrating mannitol aggregation as a potential method to detect the virus. BSA-coated AuNPs showed the same trend as PPV-coated AuNPs, in the presence of salt. However, BSA-coated AuNPs is less protected than PPV from 0-1 nM, if we assume  $10^8$  PPV is equal to 1 nM of BSA, as calculated based on the same coverage area in the SI **A.2**. This is likely due to a difference in binding affinity for BSA and PPV. The size difference,  $\Delta D_H$ , in BSA-coated AuNPs induced by mannitol as a function of protein concentration can be seen in **Figure 5.3F**. The size increase of BSA-coated AuNPs in 1 M mannitol had a  $\Delta D_H$  value in the range of  $19 \pm 1$  nm to  $33 \pm 8$  nm for all protein concentrations studied. For PPV, the  $\Delta D_H$  reached  $61 \pm 16$  nm for the highest concentration studied. This difference is the main basis for determining the detection of virus versus proteins.

Thyroglobulin-coated AuNPs (see SI **A.2** for UV-Vis and DLS confirmation of coating) were also tested for their ability to aggregate in mannitol and salt. Thyroglobulin is a major protein involved with iodine metabolism and is 12 nm<sup>63</sup> in size. The reference range for thyroglobulin concentration in serum is about 20 to 25 ng/mL<sup>64</sup> (equivalent to 30-38 nM). All tested concentrations of thyroglobulin-coated AuNPs protected the AuNPs from aggregation by NaCl, shown in **Figure 5.3H**. The size increase of thyroglobulin-coated AuNPs in 1 M mannitol had a  $\Delta D_H$  value in the range of  $22 \pm 1$  nm to  $35 \pm 4$  nm for all protein concentrations studied (**Figure 5.3I**). This  $\Delta D_H$  is smaller than PPV-coated AuNPs in mannitol. This further demonstrated that there is a clear difference between AuNPs aggregation with mannitol when in the presence of PPV versus protein controls.

The aggregation profile of PPV-coated AuNPs compared with protein-coated AuNPs by 1 M NaCl is similar to the aggregation profile of human papillomaviruses (HPV) type 16 L1 VLPs-coated AuNPs compared with BSA-coated AuNPs induced by 70 mM NaCl.<sup>65</sup> Aggregation of AuNPs-coated VLPs was sharply decreased as VLPs

concentration was increased, while BSA-coated AuNPs showed a flat trend for AuNPs aggregation by salt.<sup>65</sup> While changes in NaCl aggregation of virus-coated AuNPs may detect viral particles compared with BSA near 1  $\mu\text{M}$ , our data suggests that mannitol aggregation is more quantitative and less susceptible to contaminating proteins in solution.

TEM images of PPV, PPV-coated AuNPs and PPV-coated AuNPs with 1 M mannitol are shown in **Figure 5.3J-L**, respectively. The size of PPV detected in the images falls into the reported size range for PPV of 18 - 26 nm.<sup>53</sup> **Figure 5.3K** confirmed the successful interaction of PPV with the AuNPs. **Figure 5.3L** showed aggregation of PPV-coated AuNPs in mannitol. This demonstrates that PPV-coated AuNPs aggregate in the presence of mannitol.

UV-Vis absorption spectrum was used as a secondary detection method for AuNPs aggregation, however, no significant difference between the red-shift for mannitol-induced aggregation for PPV and the red-shift for mannitol-induced aggregation for control BSA could be found (see **SI**). This is possibly due to the lack of sensitivity of the UV-Vis absorption spectrum that is needed to identify the small differences in aggregation between mannitol-induced aggregates of PPV and AuNPs.

#### **5.3.4 Application: virus detection in protein solution matrix**

To determine the interference of proteins on virus detection using the AuNPs aggregation method, PPV was spiked into an equal volume of BSA solution with different concentrations to keep a constant final virus concentration of  $10^{8.3} \pm 10^{0.2}$   $\text{MTT}_{50}/\text{mL}$ . **Figure 5.4A** shows the average size of PPV-coated AuNPs in different concentrations of BSA before and after mannitol-induced aggregation. PPV-coated AuNPs placed in BSA solutions had a significantly larger size than BSA-coated AuNPs alone (**Figure 5.4B**). The highest BSA concentration of 500  $\mu\text{M}$  was chosen because it is the physiological concentration of albumin in serum.<sup>66-67</sup> The calculated average concentration from the AuNPs standard detection curve for PPV was  $10^{8.5} \pm 10^{0.7}$   $\text{MTT}_{50}/\text{mL}$ , which is within  $\pm 10^{0.5}$  ( $\text{MTT}_{50}/\text{mL}$ ) (the known MTT error) from the PPV titer determined with the MTT assay. This reproducibility across different BSA concentrations indicates that AuNP aggregation in mannitol could be a promising diagnostic for virus in a protein solution.



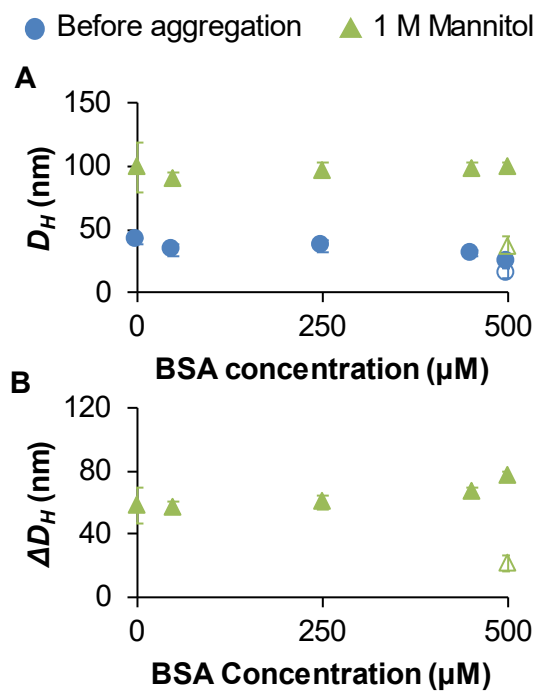


**Figure 5.4** Detection of virus in a protein solution matrix. (A) The average size of PPV-coated AuNPs in different concentrations of BSA before and after 1 M mannitol addition and measured by DLS. (B) The change in the size of PPV-coated AuNPs in different concentrations of BSA after 1 M mannitol addition. Solid symbols represent PPV and open symbols represent BSA only. All data points are the average of three separate tests and error bars represent the standard deviation.

### 5.3.5 Application: evaluation of surface contamination

AuNPs aggregation in mannitol was used as a proof-of-concept test to detect viral contamination on a surface. PPV was allowed to dry on a petri dish and was then collected with a cotton swab, as shown in **Figure 5.5A**. PPV at a concentration of  $10^{6.9} \pm 10^{0.2}$  MTT<sub>50</sub>/mL was collected with this swab sampling method, achieving a  $60 \pm 23\%$  virus recovery. **Figure 5.5B** shows the  $\Delta D_H$  after induction with mannitol. Swabbed PPV had a significantly larger aggregation of AuNPs caused by mannitol as compared to BSA. To determine the concentration of swabbed PPV using the AuNPs aggregation method, the PPV titer was determined from the AuNPs standard curve in **Figure 5.3E**. The calculated titer was within the error of the MTT assay. This reproducibility indicates that the comparison of AuNPs aggregation in mannitol can be a promising test for the cleanliness of a surface for viral contamination.

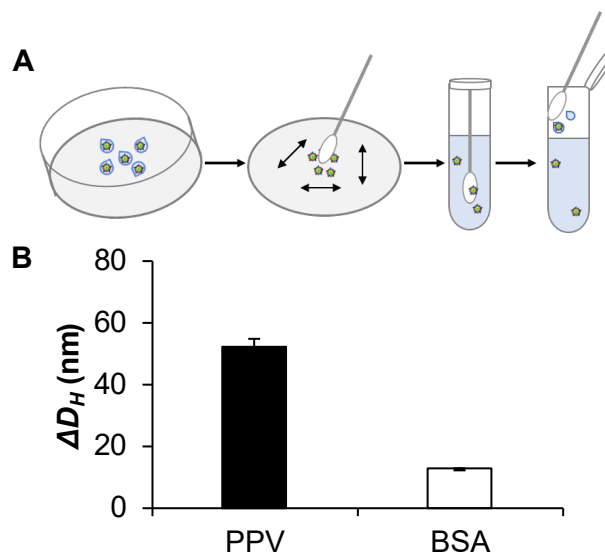


**Figure 5.5** Swab sampling to detect contamination of PPV on a surface. (A) The process of swab sampling, (B) Size aggregation measured by DLS for swabbed PPV versus control swabbed BSA. Swabbed PPV is  $106.9 \pm 100.2$  MTT<sub>50</sub>/mL as measured by the MTT assay and  $10^{7.4}$  MTT<sub>50</sub>/mL as measured by the PPV-AuNPs aggregation assay in 1 M mannitol. All data points are the average of three separate tests and error bars represent the standard deviation.

### 5.3.6 Nonspecific virus detection

To test the non-specificity of the AuNPs aggregation assay, an enveloped virus BVDV with a size of 40-60 nm<sup>68</sup> was detected by mannitol-induced AuNP aggregation. The confirmation of BVDV-coated AuNPs is in the SI. Using the same procedure as PPV and the control proteins, the mean  $D_H$  was used to quantify the size of AuNPs before coating, after coating, and after inducing aggregation with either mannitol or salt. **Figure 5.6A** shows that BVDV-coated AuNPs increase in size after 1 M mannitol addition. At a concentration of  $10^5$  BVDV MTT<sub>50</sub>/mL or higher, the AuNPs were protected from salt-induced aggregation, as shown in **Figure 5.6B**. The  $\Delta D_H$  due to the mannitol-induced aggregation of BVDV increased from  $51 \pm 13$  nm to  $165 \pm 31$  nm between  $10^4$  MTT<sub>50</sub>/mL and  $10^7$  MTT<sub>50</sub>/mL, as shown in **Figure 5.6C**. The lowest detectable concentration was estimated to be  $10^4$  MTT<sub>50</sub>/mL for BVDV. BVDV was detectable at a lower concentration than PPV. This could be due to the BVDV being an enveloped virus, potentially increasing its affinity for AuNPs. Or the size ratio between the virus and the AuNP could be important. In this study, only 15 nm AuNPs were used with viruses that were ~20 nm (PPV) and between 40-60 nm for BVDV. Future work will explore a larger range of virus to AuNP size ratios.

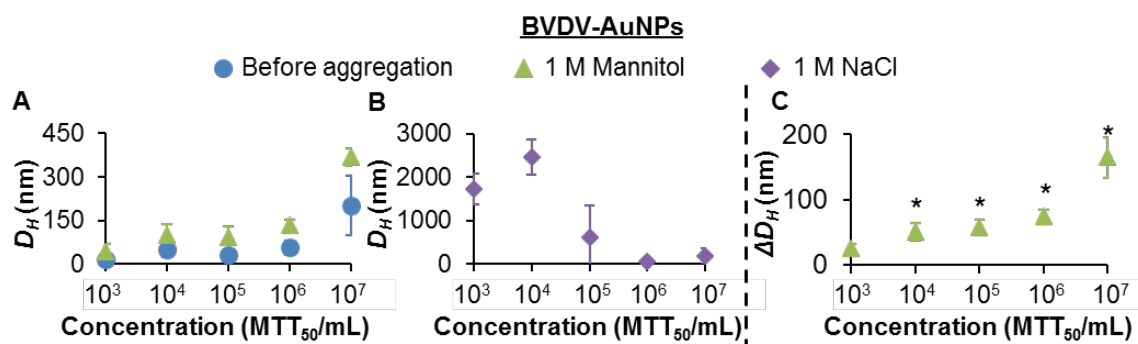


**Figure 5.6** Concentration dependence for detection of BVDV. (A) Size profile of BVDV coated AuNPs as a function of concentrations before and after 1 M mannitol addition as measured by DLS. (B) Size profile of BVDV coated AuNPs as a function of concentrations after 1 M NaCl addition as measured by DLS. (C) Change in AuNPs aggregation size for BVDV after 1 M mannitol addition. All data points are the average of three separate tests and error bars represent the standard deviation. \* $p < 0.05$  for virus compared to BSA and thyroglobulin controls in **Figure 5.3**.

## 5.4 Conclusions

The aggregation of virus-coated AuNPs in mannitol can be detected by DLS and there is a linear increase in aggregate size with an increase in PPV concentration on a semi-log plot. This indicates the potential of quantitative detection of virus with this described AuNPs aggregation method. The lowest detectable concentration of virus was estimated to be  $10^6$  MTT<sub>50</sub>/mL, which is lower than standard antibody assays. The non-specific nature of this assay was tested by detecting the aggregation of BVDV-coated AuNPs in mannitol. The lowest detection concentration for BVDV was estimated to be  $10^4$  MTT<sub>50</sub>/mL.

The AuNPs aggregation assay has the ability to determine the presence of virus in up to 500  $\mu$ M of BSA quantitatively, used as a model contaminant in a protein-rich biological fluid. Also, PPV was detected quantitatively after it was swabbed from a dried sample on a petri dish. The developed ligand-free AuNPs aggregation method can determine the presence of virus within 24 hours, which is comparable or faster than current virus detection methods. This general virus detection method could be a quick, sensitive, inexpensive and portable method for detecting the presence of viral particles in low resource countries. Future work includes exploring additional viruses, reducing the time for the assay, and determining the ideal AuNP size and shape. The goal is to develop this assay into an early screening step for a viral infection in blood samples or cleanliness of a surface, which could help to control a viral disease outbreak.

## 5.5 References

1. Chang, T.J., et al., *Duplex Identification of Staphylococcus aureus by Aptamer and Gold Nanoparticles*. Journal of Nanoscience and Nanotechnology, 2016. **16**(6): p. 5513-5519.
2. Xiong, L.H., et al., *Highly Sensitive Naked-Eye Assay for Enterovirus 71 Detection Based on Catalytic Nanoparticle Aggregation and Immunomagnetic Amplification*. ACS Applied Materials & Interfaces, 2017. **9**(17): p. 14691-14699.
3. Dharanivasan, G., et al., *DNA templated self-assembly of gold nanoparticle clusters in the colorimetric detection of plant viral DNA using a gold nanoparticle conjugated bifunctional oligonucleotide probe*. RSC Advances, 2016. **6**(14): p. 11773-11785.
4. Kumvongpin, R., et al., *High sensitivity, loop-mediated isothermal amplification combined with colorimetric gold-nanoparticle probes for visual detection of high risk human papillomavirus genotypes 16 and 18*. Journal of Virological Methods, 2016. **234**: p. 90-95.
5. Lee, C., et al., *Colorimetric viral detection based on sialic acid stabilized gold nanoparticles*. Biosensors & Bioelectronics, 2013. **42**: p. 236-241.
6. Driskell, J.D., et al., *One-step assay for detecting influenza virus using dynamic light scattering and gold nanoparticles*. Analyst, 2011. **136**(15): p. 3083-3090.
7. Heidari, Z., S.E. Rezafofighi, and S. Rastegarzadeh, *A Novel Unmodified Gold Nanoparticles-Based Assay for Direct Detection of Unamplified Bovine Viral Diarrhea Virus-RNA*. Journal of Nanoscience and Nanotechnology, 2016. **16**(12): p. 12344-12350.
8. Wang, L., et al., *Visual detection of Maize chlorotic mottle virus by asymmetric polymerase chain reaction with unmodified gold nanoparticles as the colorimetric probe*. Analytical Methods, 2016. **8**(38): p. 6959-6964.
9. Poonthiyil, V., et al., *Gold Nanoparticles Decorated with Sialic Acid Terminated Bi-antennary N-Glycans for the Detection of Influenza Virus at Nanomolar Concentrations*. Chemistryopen, 2015. **4**(6): p. 708-716.
10. Shawky, S.M., et al., *Gold aggregating gold: A novel nanoparticle biosensor approach for the direct quantification of hepatitis C virus RNA in clinical samples*. Biosensors & Bioelectronics, 2017. **92**: p. 349-356.
11. Hwang, S.G., et al., *Rapid and simple detection of Tamiflu-resistant influenza virus: Development of oseltamivir derivative-based lateral flow biosensor for point-of-care (POC) diagnostics*. Scientific Reports, 2018. **8**.
12. Wu, J.C., et al., *Electrophoresis-Enhanced Detection of Deoxyribonucleic Acids on a Membrane-Based Lateral Flow Strip Using Avian Influenza H5 Genetic Sequence as the Model*. Sensors, 2014. **14**(3): p. 4399-4415.
13. Liu, Y.J., et al., *Colorimetric detection of influenza A virus using antibody-functionalized gold nanoparticles*. Analyst, 2015. **140**(12): p. 3989-3995.
14. Lai, Y.H., et al., *Rapid screening of antibody-antigen binding using dynamic light scattering (DLS) and gold nanoparticles*. Analytical Methods, 2015. **7**(17): p. 7249-7255.

15. Prugger, C., et al., *Screening for transfusion transmissible infections using rapid diagnostic tests in Africa: a potential hazard to blood safety?* Vox sanguinis, 2016. **110**(2): p. 196-198.
16. FDA. *Complete List of Donor Screening Assays for Infectious Agents and HIV Diagnostic Assays*. 2018; Available from: <https://www.fda.gov/BiologicsBloodVaccines/BloodBloodProducts/ApprovedProducts/LicensedProductsBLAs/BloodDonorScreening/InfectiousDisease/ucm080466.htm>.
17. CDC. *Prevent the Spread of Norovirus*. 2017; Available from: <https://www.cdc.gov/features/norovirus/index.html>.
18. Park, J.-E., et al., *Metal Nanoparticles for Virus Detection*. ChemNanoMat, 2016. **2**(10): p. 927-936.
19. Radwan, S. and H.M.E. Azzazy, *Gold nanoparticles for molecular diagnostics*. Expert review of molecular diagnostics, 2009. **9**(5): p. 511-524.
20. Jans, H., et al., *Dynamic Light Scattering as a Powerful Tool for Gold Nanoparticle Bioconjugation and Biomolecular Binding Studies*. Analytical Chemistry, 2009. **81**(22): p. 9425-9432.
21. Ling, J., et al., *Light-scattering signals from nanoparticles in biochemical assay, pharmaceutical analysis and biological imaging*. Trac-Trends in Analytical Chemistry, 2009. **28**(4): p. 447-453.
22. Wang, X.H., et al., *Detection of hepatitis B surface antigen by target-induced aggregation monitored by dynamic light scattering*. Analytical Biochemistry, 2012. **428**(2): p. 119-125.
23. Storhoff, J.J., et al., *Homogeneous detection of unamplified genomic DNA sequences based on colorimetric scatter of gold nanoparticle probes*. Nature Biotechnology, 2004. **22**: p. 883.
24. Sanchez-Pomales, G., et al., *A lectin-based gold nanoparticle assay for probing glycosylation of glycoproteins*. Biotechnology and Bioengineering, 2012. **109**(9): p. 2240-2249.
25. Ho, Y.T., et al., *An instantaneous colorimetric protein assay based on spontaneous formation of a protein corona on gold nanoparticles*. Analyst, 2015. **140**(4): p. 1026-1036.
26. Dominguez-Medina, S., et al., *Adsorption of a Protein Mono layer via Hydrophobic Interactions Prevents Nanoparticle Aggregation under Harsh Environmental Conditions*. Acs Sustainable Chemistry & Engineering, 2013. **1**(7): p. 833-842.
27. Wang, A.L., et al., *Electrostatic Interactions and Protein Competition Reveal a Dynamic Surface in Gold Nanoparticle-Protein Adsorption*. Journal of Physical Chemistry C, 2016. **120**(42): p. 24231-24239.
28. Johnston, B.D., et al., *Colloidal Stability and Surface Chemistry Are Key Factors for the Composition of the Protein Corona of Inorganic Gold Nanoparticles*. Advanced Functional Materials, 2017. **27**(42): p. 9.
29. Burt, J.L., et al., *Noble-metal nanoparticles directly conjugated to globular proteins*. Langmuir, 2004. **20**(26): p. 11778-11783.

30. Yeo, E.L.L., et al., *Understanding aggregation-based assays: nature of protein corona and number of epitopes on antigen matters*. RSC Advances, 2015. **5**(20): p. 14982-14993.
31. Michen, B. and T. Graule, *Isoelectric points of viruses*. Journal of applied microbiology, 2010. **109**(2): p. 388-397.
32. Dika, C., et al., *Isoelectric point is an inadequate descriptor of MS2, Phi X 174 and PRD1 phages adhesion on abiotic surfaces*. Journal of Colloid and Interface Science, 2015. **446**: p. 327-334.
33. Chen, Y., et al., *Aggregation and antigenicity of virus like particle in salt solution-A case study with hepatitis B surface antigen*. Vaccine, 2015. **33**(35): p. 4300-4306.
34. Gencoglu, M.F., E. Pearson, and C.L. Heldt, *Porcine parvovirus flocculation and removal in the presence of osmolytes*. Journal of Biotechnology, 2014. **186**: p. 83-90.
35. Gencoglu, M. and C. Heldt, *Enveloped virus flocculation and removal in osmolyte solutions*. Journal of biotechnology, 2015. **206**: p. 8-11.
36. Heldt, C.L., et al., *A Generalized Purification Step for Viral Particles Using Mannitol Flocculation*. Biotechnology Progress, 2018. **34**(4): p. 1027-1035.
37. Godawat, R., S.N. Jamadagni, and S. Garde, *Characterizing hydrophobicity of interfaces by using cavity formation, solute binding, and water correlations*. Proceedings of the National Academy of Sciences of the United States of America, 2009. **106**(36): p. 15119-15124.
38. Hu, C.Y., B.M. Pettitt, and J. Roesgen, *Osmolyte solutions and protein folding*. F1000 biology reports, 2009. **1**(41): p. 1.
39. Bolen, D.W., *Effects of naturally occurring osmolytes on protein stability and solubility: issues important in protein crystallization*. Methods, 2004. **34**(3): p. 312-322.
40. Patel, A.J., et al., *Sitting at the edge: How biomolecules use hydrophobicity to tune their interactions and function*. The Journal of Physical Chemistry B, 2012. **116**(8): p. 2498-2503.
41. Heldt, C.L., et al., *Experimental and computational surface hydrophobicity analysis of a non-enveloped virus and proteins*. Colloids and Surfaces B-Biointerfaces, 2017. **153**: p. 77-84.
42. Johnson, S.A., et al., *The step-wise framework to design a chromatography-based hydrophobicity assay for viral particles*. Journal of Chromatography B-Analytical Technologies in the Biomedical and Life Sciences, 2017. **1061**: p. 430-437.
43. Tafur, M.F., K.S. Vijayaragavan, and C.L. Heldt, *Reduction of porcine parvovirus infectivity in the presence of protecting osmolytes*. Antiviral Research, 2013. **99**(1): p. 27-33.
44. Meng, H., et al., *Biomimetic recyclable microgels for on-demand generation of hydrogen peroxide and antipathogenic application*. Acta biomaterialia, 2019. **83**: p. 109-118.
45. Haiss, W., et al., *Determination of size and concentration of gold nanoparticles from UV-vis spectra*. Analytical chemistry, 2007. **79**(11): p. 4215-4221.

46. Scherer, K., et al., *Application of a Swab Sampling Method for the Detection of Norovirus and Rotavirus on Artificially Contaminated Food and Environmental Surfaces*. Food and Environmental Virology, 2009. **1**(1): p. 42-49.
47. Park, G.W., P. Chhabra, and J. Vinje, *Swab Sampling Method for the Detection of Human Norovirus on Surfaces*. Jove-Journal of Visualized Experiments, 2017(120).
48. Christau, S., et al., *Salt-Induced Aggregation of Negatively Charged Gold Nanoparticles Confined in a Polymer Brush Matrix*. Macromolecules, 2017. **50**(18): p. 7333-7343.
49. Sun, M.M., et al., *Salt-induced aggregation of gold nanoparticles for photoacoustic imaging and photothermal therapy of cancer*. Nanoscale, 2016. **8**(8): p. 4452-4457.
50. Han, X.G., et al., *Role of Salt in the Spontaneous Assembly of Charged Gold Nanoparticles in Ethanol*. Langmuir, 2011. **27**(9): p. 5282-5289.
51. Pamies, R., et al., *Aggregation behaviour of gold nanoparticles in saline aqueous media*. Journal of Nanoparticle Research, 2014. **16**(4).
52. Kah, J.C.Y., et al., *Early diagnosis of oral cancer based on the surface plasmon resonance of gold nanoparticles*. International Journal of Nanomedicine, 2007. **2**(4): p. 785-798.
53. Norkin, L.C., *Virology: Molecular Biology and Pathogenesis*. 2010: ASM Press.
54. Flecha, F.L.G. and V. Levi, *Determination of the molecular size of BSA by fluorescence anisotropy*. Biochemistry and Molecular Biology Education, 2003. **31**(5): p. 319-322.
55. Muzyczka, N. and K.I. Berns, *Parvoviridae: The Viruses and Their Replication*, in *Field's Virology*, D.M. Knipe and P.M. Howely, Editors. 2001, Lippincott Williams & Wilkins. p. 2327-59.
56. Davidson, A.M., et al., *Sensitive analysis of protein adsorption to colloidal gold by differential centrifugal sedimentation*. Analytical chemistry, 2017. **89**(12): p. 6807-6814.
57. Lacerda, S.H.D.P., et al., *Interaction of gold nanoparticles with common human blood proteins*. ACS nano, 2009. **4**(1): p. 365-379.
58. Rivera, E., L. Sjoland, and K.A. Karlsson, *A solid-phase fluorescent immunoassay for the rapid detection of virus-antigen or antibodies in fetuses infected with porcine parvovirus*. Archives of Virology, 1986. **88**(1-2): p. 19-26.
59. Csagola, A., et al., *Detection of Porcine Parvovirus 2 (Ungulate Tetraparvovirus 3) Specific Antibodies and Examination of the Serological Profile of an Infected Swine Herd*. Plos One, 2016. **11**(3).
60. Westenbrink, F., M.A. Veldhuis, and J.M.A. Brinkhof, *an enzyme-linked immunosorbent-assay for detection of antibodies to porcine parvovirus*. Journal of Virological Methods, 1989. **23**(2): p. 169-178.
61. Brinker, C.J. and G. Cao, *Annual review of nano research*. Vol. 1. 2006: World Scientific.
62. Chen, L. and S. Neethirajan, *A homogenous fluorescence quenching based assay for specific and sensitive detection of influenza virus A hemagglutinin antigen*. Sensors, 2015. **15**(4): p. 8852-8865.

63. Schön, P., et al., *Charge propagation in "ion channel sensors" based on protein-modified electrodes and redox marker ions*. Journal of the American Chemical Society, 2005. **127**(32): p. 11486-11496.
64. Indrasena, B.S.H., *Use of thyroglobulin as a tumour marker*. World journal of biological chemistry, 2017. **8**(1): p. 81.
65. Palomino-Vizcaino, G., et al., *Effect of HPV16 L1 virus-like particles on the aggregation of non-functionalized gold nanoparticles*. Biosensors & Bioelectronics, 2018. **100**: p. 176-183.
66. Peters Jr, T., *All about albumin: biochemistry, genetics, and medical applications*. 1995: Academic press.
67. Choi, S., et al., *A rapid, simple measurement of human albumin in whole blood using a fluorescence immunoassay (I)*. Clinica Chimica Acta, 2004. **339**(1-2): p. 147-156.
68. Kim, I.S., Y.W. Choi, and S.R. Lee, *Optimization and validation of a virus filtration process for efficient removal of viruses from urokinase solution prepared from human urine*. Journal of microbiology and biotechnology, 2004. **14**(1): p. 140-147.



# **6 Stabilization of viruses through complex coacervation<sup>4</sup>**

---

<sup>4</sup> The material contained in this chapter is in preparation for submission.

## 6.1 Introduction

According to the World Health Organization (WHO), millions of people die from viral infectious disease each year [1]. One of the most effective methods to prevent viral infection is with vaccines. In order for viral vaccines to be effective, they must be transported and stored in a “cold chain” [2]. A cold chain is a system of transporting and storing vaccines at the recommended temperature, typically 2-8 °C, from the manufacturer until the point of use [2, 3]. If temperatures are not maintained, the vaccine may lose its potency and could no longer be effective in fighting disease [4]. Approximately half of the vaccines produced are discarded due to poor thermal stability each year [5]. The unreliable cold chain system is one of the major causes of poor immunization coverage in developing countries [4]. Therefore, developing robust, thermostable viral vaccines that are less dependent on the cold chain is urgent and crucial for universal access to immunizations.

There are three major types of viral-based vaccines licensed for human use, live attenuated, inactivated, and subunit vaccines [6, 7]. Live-attenuated vaccines are usually produced by extended passage of a disease-causing (wild) virus in non-human cell culture to weaken the wild virus [8-10]. The attenuated virus can still replicate and stimulate high immunity, but it loses the ability to cause disease. Inactivated vaccines are typically treated by chemical or heat inactivation to stop virus replication [8-10]. The inactivated virus cannot replicate, but can still produce immunogenicity. Subunit vaccines use a component of the virus, such as a surface polysaccharide, capsid protein, or nucleic acid, to stimulate immune response [8-10]. The immune response caused by these three types of vaccines from strong to weak in order as live attenuated > inactivated > subunit vaccines. However, the stability of these three types of vaccines is in reverse order. Live attenuated viral vaccines are the most sensitive to temperature changes, and tight temperature control is required for them to remain immunogenic [6]. There is a need to develop versatile methods to thermally stabilize the live attenuated vaccines.

Various methods have been developed to create thermostable viral vaccines. One method to stabilize viral vaccines is to engineer the vaccines to withstand degradation. Genetic modification of the fusion protein of a respiratory syncytial virus showed greater immunogenicity and enhanced thermal stability than the wild virus at 37°C [11]. Foot-and-mouth disease virus mutants were engineered to slow the rate of dissociation of the virus, thus stabilizing the viral vaccine [12]. However, the method of modifying each viral vaccine is labor-intensive and virus-specific. A more standard method to stabilize vaccine formulations is to add stabilizing excipients [13-15]. At 37°C for 10 days, an adenovirus serotype 5 in the presence of a molar concentration of sucrose solution maintained high infectivity, and its vaccine strain in sucrose kept the immunogenicity *in vivo* for viruses [13]. In order to further improve the thermal stability of viruses, vaccines are often dried by lyophilization, spray drying, or foam drying [15, 16]. Drying aims to slow down the physical and chemical degradation of the vaccine. Lyophilized rotavirus vaccines formulated in optimized HEPES buffer, bulking agent polyvinyl pyrrolidone, cryoprotectant sucrose, and amino acids L-arginine and glycine, can retain its potency for 20 months at 37°C and 7 months at 45°C [17]. Two enveloped viruses showed enhanced

thermal stability in trehalose, while one non-enveloped virus had improved thermal stability in mannitol by spray drying [14]. Small-sized monosaccharide mannitol can tightly bind the non-enveloped viral capsid proteins, while polysaccharide trehalose can behave as a glassy stabilizing matrix by forming strong hydrogen bonds with the viral envelope to maintain the fluidity of the lipid bilayer membrane and prevent crystalline formation [14, 18]. The viruses remained hydrated due to water molecules around the viruses that were confined by the formation of hydrogen bonds with the excipients [14]. Although these methods showed promise for creating thermostable vaccines, their applicability is limited by complicated treatment procedures and expensive specialized equipment for drying samples. In addition, most vaccine formulations required large amounts of trial and error experiments for selections of excipients, since the thermodynamic reason for the stabilization is unknown. Therefore, a simple, inexpensive, and versatile approach for stabilizing viruses against heat is needed to be explored.

Our proposed formulation strategy for thermally stabilizing viral vaccines is to encapsulate the virus. Virus encapsulation by hydrated silica provided a protective layer that slowed the infectivity loss of the human-enterovirus type 71 by six-fold at 37°C for 20 days, or at 40 °C for 36 hours [19]. Our approach has been to use biocompatible polypeptides to create a complex coacervate to encapsulate the viral particles. Complex coacervation [20-22] is an associative liquid-liquid phase separation phenomena based on electrostatic interactions of two or more oppositely charged polymers. Entropic gains for releasing of small, bound, counter-ions from the polyelectrolyte salts into solution [23-25] can also drive the phase separation. When oppositely charged polymers interact in a solvent to reach net charge neutrality, two equilibrium phases can be formed: a polymer-rich dense phase known as a complex coacervate [20-22], and a polymer-poor dilute phase known as the supernatant. The phase behavior of complex coacervation has been reported strongly dependent on polyelectrolyte mixing ratio (stoichiometry), polyelectrolyte concentration, ionic strength (salt concentration), and solution pH, but weakly affected by temperature [26, 27].

Complex coacervation has been used in a variety of areas, such as drug delivery [28, 29], gene therapy [30-32], and biomimic adhesives [33, 34]. One of the most important application is as a method for encapsulation of proteins [35-38]. A tertiary system of two polyelectrolytes and a protein have created complex coacervates that successfully encapsulated the protein [35-37, 39]. The encapsulated proteins maintained either structure [24, 35, 36, 38, 40] and were also able to enhance the stability of the proteins against high temperatures [36]. Protein unfolding occurs when heat increases the kinetic energy of the protein and causes the molecules to vibrate until the non-covalent bonds holding the structure together are disrupted [41]. A variety of protein systems have shown thermal protection against denaturation, including bovine serum albumin (BSA) in a poly(allylamine hydrochloride)/poly(acrylic acid) system [36], canola protein isolate (CPI) in chitosan (CS) [42] and lysozyme in hyaluronic acid (HA) [24]. The finding on encapsulated proteins by complex coacervation with improved thermal stability showed the promise for encapsulating viral particles and stabilizing the viruses thermally via complex coacervation.

In this study, two viruses, non-enveloped porcine parvovirus (PPV) and enveloped bovine viral diarrhea virus (BVDV) were explored to form virus complex coacervates. The viruses were encapsulated by a positively charged poly(L-lysine) (PLys) and negatively charged poly(D,L-glutamic acid) (PGlu). The formation of virus coacervates was explored as a function of charge fractions, which is the ratio of the polycation, PLys to the polyanion PGlu, qualitatively and quantitatively. Virus thermal stability studies were performed as a proof-of-concept for thermostable vaccines. The polypeptide complex coacervates demonstrated effective protection for the non-enveloped PPV against high temperature, but not for the enveloped BVDV. This method showed its promise for formulating thermostable non-enveloped live attenuated vaccines.

## 6.2 Materials and Methods

### 6.2.1 Materials

Potassium phosphate monobasic (molecular biology grade,  $\geq 99.0\%$ ) and sodium chloride (NaCl, ACS grade,  $\geq 99.0\%$ ) were a gift from Millipore Sigma (Burlington, MA). Sodium phosphate dibasic heptahydrate (ACS grade, 98.0-102.0%), sodium hydroxide (NaOH, ACS grade,  $\geq 97.0\%$ ), sodium dodecyl sulfate (SDS) and dimethyl sulfoxide (DMSO, BioReagent,  $>99.7\%$ ) were purchased from Sigma-Aldrich (St. Louis, MO). Hydrochloric acid (HCl, ACS grade, 36.5-38.0%) and (4-(2-hydroxyethyl)-1-piperazineethanesulfonic acid) (HEPES) ( $\geq 99.0\%$ ) were purchased from Fisher Scientific (Pittsburgh, PA). Homopolypeptides poly(D,L-glutamic acid) (PGlu) and poly(L-lysine) (PLys) with a degree of polymerization of 400 were purchased from Alamanda Polymers (Huntsville, AL). The polypeptides were used as received without further purification. Pierce fluorescent dye 5-(and 6)-carboxy-tetramethyl-rhodamine succinimidyl ester (NHS-Rhodamine) was purchased from Thermo Fisher Scientific (Waltham, MA). Thiazolyl blue tetrazolium bromide (MTT) (98%) was purchased from Alfa Aesar (Haverhill, MA). All aqueous solutions and buffers were prepared using purified water with a resistivity of  $\geq 18 \text{ M}\Omega \cdot \text{cm}$  from a Nanopure filtration system (Thermo Scientific, Waltham, MA) and filtered with a 0.2  $\mu\text{m}$  bottle top filter (VWR, Radnor, PA) or a 0.2  $\mu\text{m}$  syringe filter (VWR) prior to use. Phosphate buffered saline (PBS) ( $\text{pH } 7.20 \pm 0.03$ ) was prepared by dissolving 0.21 g potassium phosphate monobasic, 0.726 g sodium phosphate dibasic heptahydrate, and 9 g NaCl into 1000 mL Nanopure water. Stock solutions of 10 mM polypeptide solutions were prepared on a charged monomer basis and adjusted with 1 M HCl and NaOH to the desired  $\text{pH } 8.00 \pm 0.03$  pH units. Zwitterionic buffer solution of 0.4 M HEPES was also adjusted with 1 M HCl and NaOH to the desired  $\text{pH } 8.00 \pm 0.03$  pH units.

## 6.2.2 Virus production, purification and titration

Porcine kidney cells (PK-13, CRL-6489) and bovine turbinate cells (BT-1, CRL-1390) were purchased from ATCC. Porcine parvovirus (PPV) strain NADL-2, was a gift from Dr. Ruben Carbonell (North Carolina State University, Raleigh, NC). Bovine viral diarrhea virus (BVDV) strain NADL was purchased from USDA APHIS. PPV was propagated in PK-13 cells, and BVDV was propagated in BT-1 cells, as described previously [43, 44], and stored at  $-80^{\circ}\text{C}$  until further use. PPV or BVDV were further purified with a Biotech Cellulose Ester 1,000 kDa dialysis tubing (Rancho Dominguez, CA) and a BioRad Econo-Pac 10DG desalting column (Hercules, CA) in PBS buffer, as previously described [45], and stored at  $4^{\circ}\text{C}$  until further use.

To determine the concentration of the infectious virus, an MTT assay was used. Briefly, either  $8 \times 10^4$  cells/mL PK-13 cells (to titrate PPV) [46] or  $2.5 \times 10^5$  cells/mL BT-1 cells (to titrate BVDV) [47] were seeded in a 96-well plate in a volume of 100  $\mu\text{L}$ /well. After one day incubation, 25  $\mu\text{L}$ /well of virus sample was added to the corresponding host cells in quadruplicate and serially diluted across the plate. After 6 days post-inoculation, 10  $\mu\text{L}$ /well of 5 mg/mL MTT salt in PBS (pH 7.2) was added to the plate. After 4 hours, 100  $\mu\text{L}$ /well of solubilizing agent, 10% SDS in 0.01 M HCl (pH 2.5), was added to the plate. After 12 to 24 hours, plates were read at 550 nm in a Synergy Mx monochromator-based multimode microplate reader (Winooski, VT). The virus dilution that killed 50% of the cells is stated as virus titer  $\text{MTT}_{50}$  [44].

## 6.2.3 Formation of virus complex coacervates

Complex coacervates with encapsulated virus samples were formed by first pipetting water, and then HEPES buffer into a 1.7 mL microcentrifuge tube, followed by the virus (PPV or BVDV), PLys, and PGlu. The samples were vortexed for 5 seconds after the addition of one component to ensure fast and complete mixing. A typical experiment varied the ratio of Plys to PGlu but maintained a constant total polymer concentration of 7 mM and a constant virus concentration. The final virus concentrations were 4-6  $\log_{10}$  ( $\text{MTT}_{50}/\text{mL}$ ) for PPV and 4-5  $\log_{10}$  ( $\text{MTT}_{50}/\text{mL}$ ) for BVDV. All the virus complex coacervates were prepared immediately before use and studied at room temperature. Each sample contained a total volume of 240  $\mu\text{L}$ . All experiments were performed in triplicate.

## 6.2.4 Virus complex coacervates characterization and quantification

To qualitatively measure the formation of the virus complex coacervate, turbidity was measured by placing 100  $\mu\text{L}$  into a 96-well plate and measuring the absorbance at 562 nm [37, 48] on the microplate reader. The measured signal was referenced against a control well containing only Nanopure water and HEPES buffer. Samples were then examined using an Olympus IX51 microscope with a DP72 camera (Center Valley, PA) to confirm the presence or absence of coacervation.

Viruses were also labeled with a fluorescent dye NHS-Rhodamine that absorbs visible green light at a wavelength of 552 nm and emits orange-red visible light at 575nm

to confirm the presence of the virus in the coacervate phase. 1 mL of purified virus solutions (8 log PPV or 7 log BVDV) were incubated with 10 mg/mL NHS-Rhodamine in DMSO solution (2.15  $\mu$ L for PPV and 6.5  $\mu$ L for BVDV) for 1 hour at room temperature, and excess non-tagged fluorescent dye was removed with a desalting column. The fluorescently labeled virus was used immediately to form the virus coacervates, as described in **Section 2.3**. An aliquot of 100  $\mu$ L of tagged virus coacervates was transferred to one well of a 96-well plate and examined with an Olympus IX51 microscope. The coacervates droplets were imaged using both brightfield and fluorescence modes and analyzed with ImageJ.

To determine the virus complex coacervate quantitatively, each phase was measured with the MTT virus infectivity assay [44]. A total of 240  $\mu$ L of the complex coacervate sample containing the virus in the micro-centrifuge tube was centrifuged using an ST16R Centrifuge (Thermo Scientific, Asheville, NC) at 14000 rpm for 20 min at 15°C to phase separate the supernatant and dense coacervate phase. Following centrifugation, 220  $\mu$ L of the supernatant was carefully transferred into a new micro-centrifuge tube, and the volume of the remaining supernatant was measured via pipetting. A volume of 220  $\mu$ L of 2 M NaCl solution was added to the dense coacervate phase (transparent gel) to dismantle the coalesced virus coacervate, followed by vortexing. Both the supernatant and dismantled coacervate were further titrated by the MTT assay.

The partitioning of the virus into the complex coacervate phase was also determined. The partition coefficient ( $K$ ) was calculated by **Eq.6.1** [36, 37].

$$K = \frac{C_c}{C_s} \quad (6.1)$$

where  $C_c$  is the virus concentration in the coacervate phase, and  $C_s$  is the virus concentration in the supernatant phase.

### 6.2.5 Virus thermal stability study

A microcentrifuge tube containing either the PPV dense coacervate phase or purified PPV was capped and wrapped in paraffin film and put in a digital dry bath (USA Scientific, Ocala, FL) at 60°C. The BVDV complex coacervate and purified BVDV were put in the dry bath at 40°C. At each time point, a 1~2  $\mu$ L dense virus coacervate sample was removed from the heating block and dismantled in 220  $\mu$ L of 2 M NaCl solution. One purified virus sample was also removed from the heat at the same time. Both the dismantled virus coacervate and purified virus sample were evaluated with the MTT assay to determine the remaining infectious virus concentrations.

A log reduction value (LRV) of the virus was calculated by **Eq. 6.2**.

$$LRV = -\log_{10}\left(\frac{C_f}{C_i}\right) \quad (6.2)$$

where  $C_f$  is the final virus concentration after heat treatment, and the  $C_i$  is the initial virus concentration.

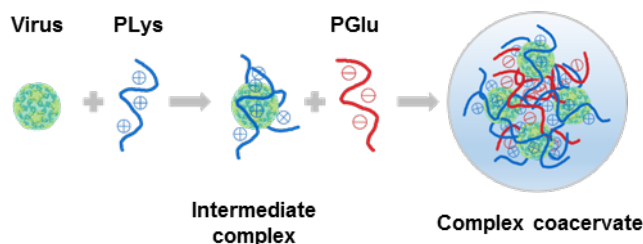
## 6.3 Results and Discussion

### 6.3.1 Virus coacervates characterization

We examined the complex coacervation of two viruses, non-enveloped PPV and enveloped BVDV. Some of the physical properties of the studied viruses are shown in **Table 6.1**. PPV has an isoelectric point (pI) of 4.8-5.1, and BVDV has a pI of 4.3-4.5 [43]. The pI corresponded to the pH where the net surface charge of the viral particle is zero [49]. The virus carries a net negative charge if the solution pH is higher than the viral pI, and a net positive charge if the solution pH is lower than the viral pI [49]. Thus, both the viruses carried a net negative charge at the solution condition (HEPES, pH 8.0) we studied. We used oppositely charged polypeptides PLys and PGlu to encapsulate viruses to form a tertiary system of complex coacervate. Previous work showed that BSA encapsulated within these two oppositely charged polypeptides achieved the highest encapsulation efficiency and the optimum partition of BSA into the coacervate phase at pH 8.0 at 0 mM NaCl concentration [35, 37]. In addition, the complex coacervation did not affect the structural stability of the encapsulated proteins [35, 37]. Thus, these two polypeptides in salt-free HEPES buffer at pH 8.0 were chosen for forming virus complex coacervates. Charged viruses can be encapsulated via the electrostatic interaction of charged polypeptides, as shown in **Scheme 6.1**. The negatively charged virus and the polycation, PLys, were mixed first to form an intermediate complex. The polyanion, PGlu, was then added to form a stable virus complex coacervate system.

**Table 6.1** Model virus properties.

Virus	Capsid	Family	Nucleic acid	Size (nm)	pI	Related human viruses	References
Porcine parvovirus (PPV)	Non-enveloped	Parvoviridae	ssDNA	18-26	4.8-5.1	B-19 human parvovirus	[43, 50, 51]
Bovine viral diarrhea virus (BVDV)	Enveloped	Flaviviridae	ssRNA	40-60	4.3-4.5	Hepatitis C	[43, 50, 52]



**Scheme 6.1** Encapsulate virus via electrostatic association of charged polypeptides.

To characterize the encapsulation of viruses, optical micrographs of virus encapsulation within coacervate droplets were taken and are shown in **Figure 6.1**. PPV and BVDV were both fluorescently labeled and used to form the complex coacervates. The co-localization of the orange-red fluorescence from the viruses within the coacervates droplets indicated the successful formation of PPV and BVDV complex coacervates.

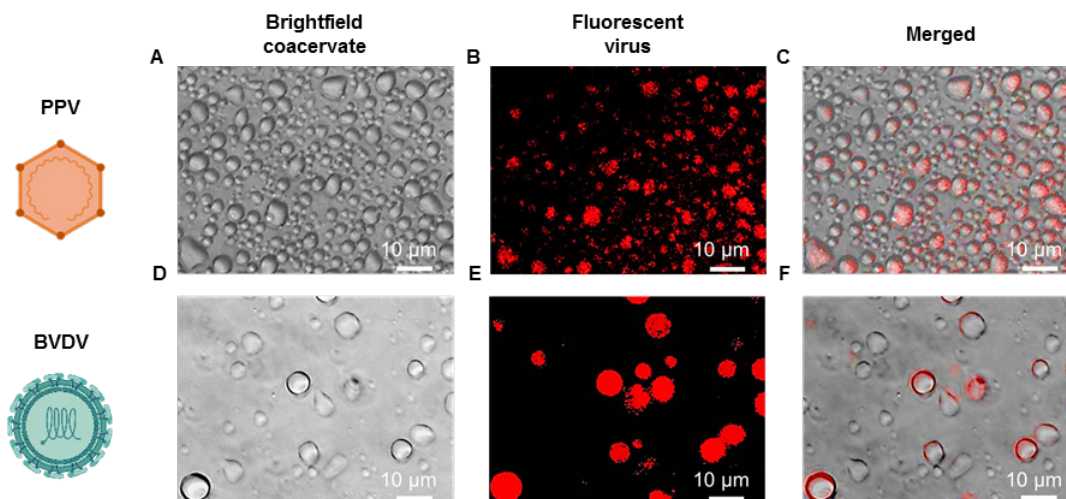


**Figure 6.1** Optical micrographs of virus encapsulation within coacervate droplets. (A&B&C) PPV coacervates, and (D&E&F) BVDV coacervates. (A&D) Brightfield micrograph of virus coacervate droplets, (B&E) fluorescent image of NHS-Rhodamine tagged virus, and (C&F) overlay of the brightfield and fluorescent images.

### 6.3.2 Encapsulation of virus as a function of coacervate charge stoichiometry

To determine the encapsulation of the virus at different charge ratios, turbidity was used for the measurement of total complex formation. The turbidity of three different concentrations of encapsulated PPV as a function of charge fraction, which is the ratio of the polycation, PLys to the polyanion PGlu, is shown in **Figure 6.2A**. Bimodal curves were obtained for 4 and 6  $\log_{10}$  (MTT<sub>50</sub>/mL) of PPV coacervates. The peaks of the turbidity indicated the complex coacervate formation. The second peak of turbidity was near the charge fraction of 0.5 for 4 and 6  $\log_{10}$  (MTT<sub>50</sub>/mL) PPV. The turbidity reading increased with an increase of PPV concentration, indicating more complex coacervates were formed when increasing the virus concentration. Bimodal curves were observed for BVDV coacervates, as shown in **Figure 6.2B**. Only two concentrations of BVDV coacervates were studied due to the initial concentration of enveloped BVDV propagated being lower than PPV. Similar turbidity curve shapes were obtained for both viruses, but the second peaks of turbidity were shifted to a higher charge fraction 0.6 for 4 and 5  $\log_{10}$  (MTT<sub>50</sub>/mL) BVDV. This shift means that more cationic PLys was needed to achieve a neutral charge complex coacervate. It indicated the electrostatic nature of complex coacervation, and the preference for the system to reach charge neutrality.



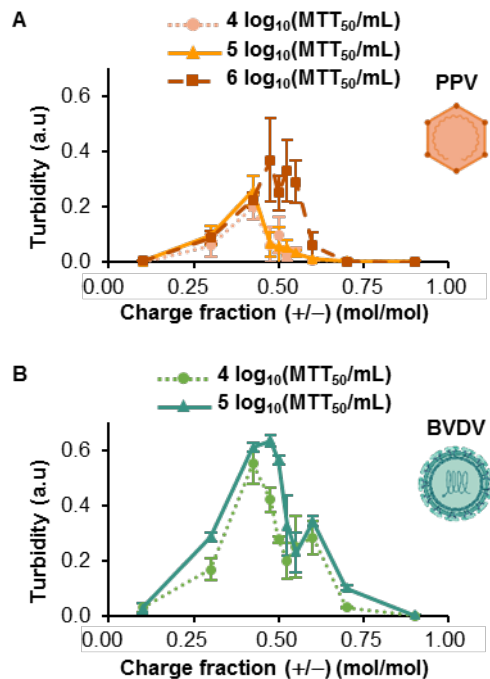


**Figure 6.2** Turbidity of encapsulated virus. (A) PPV coacervates, and (B) BVDV coacervates. All data points are the average of three separate tests and error bars represent the standard deviation.

While optical microscopic images and turbidity confirmed the successful formation of virus coacervates, it did not provide any quantitative information on how much virus was taken up into the coacervates. Therefore, the MTT cell viability assay was used to quantify the concentration of infectious virus in each phase. The virus titer as a function of coacervate charge stoichiometry is shown in **Figure 6.3**. When the cationic charge fraction increased, PPV and BVDV were extracted into the dense coacervate phase, resulting in an obvious increase in the virus titer in the coacervate phase and a corresponding decrease of virus titer in the supernatant phase. The maximum amount of virus in the coacervate phase corresponded to the second peak in the turbidity measurements. At higher cationic charge fractions, the virus particles were excluded from the coacervate phase but were back to the initial levels in the supernatant. The viruses showed the same trend as BSA, human hemoglobin, and hen egg white lysozyme concentrations titration as a function of coacervate charge stoichiometry [37].

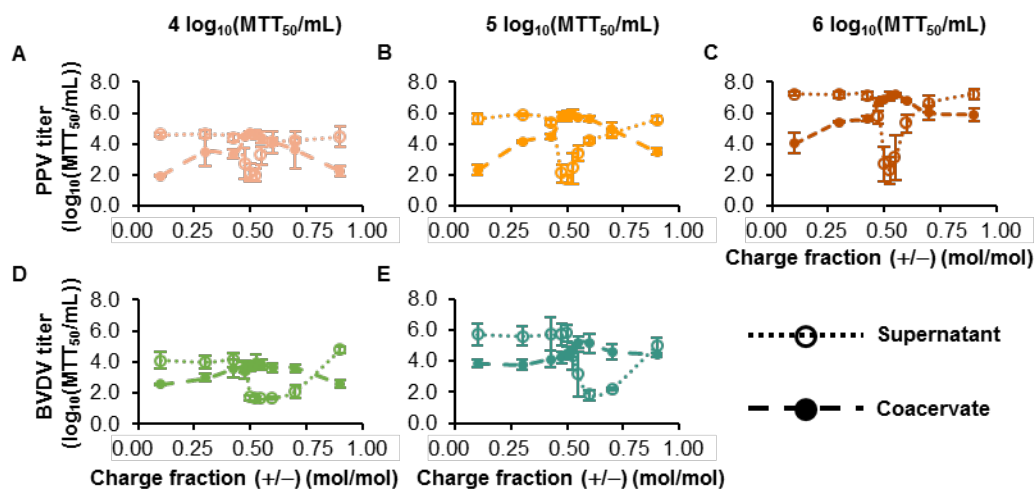


**Figure 6.3** Live virus titration. (A&B&C) Encapsulated PPV, and (D&E) encapsulated BVDV. (A&D)  $4 \log_{10}(\text{MTT}_{50}/\text{mL})$ , (B&E)  $5 \log_{10}(\text{MTT}_{50}/\text{mL})$ , and (C)  $6 \log_{10}(\text{MTT}_{50}/\text{mL})$ . All data points are the average of three separate tests and error bars represent the standard deviation.

From **Figure 6.3A-C**, the majority of the PPV particles were taken into the coacervate phase occurred near the charge ratio 0.5. It is consistent with the second peak of PPV coacervates turbidity occurring near the charge fraction of 0.5 in **Figure 6.2A**. Similar to PPV, the MTT results of BVDV also match with the turbidity data. The highest level of BVDV encapsulated in the dense phase occurred near the charge ratio of 0.6, as shown in **Figure 6.3D and E**, which is also consistent with the second peak of BVDV coacervates turbidity occurring near the charge fraction of 0.6 in **Figure 6.2B**.

In addition, the partition of viruses into the coacervate phase as a function of coacervate charge stoichiometry is calculated and shown in **Figure 6.4**. A positive  $\ln(K)$  value means the partitioning of viral particles favored the coacervate phase, while a negative value means the viral particles stayed in the supernatant phase. When the cationic charges fractions increased, PPV and BVDV were partitioned into the dense coacervate phase, achieving a maximum point of partitioning. Afterward, the viral particles were excluded from the coacervate phase back into the supernatant when the charge fractions continue to increase. The maximum partition of the virus into the coacervate phase happened at the charge fraction when the second peak in the turbidity measurements appeared, which is also consistent with **Figure 6.3**.

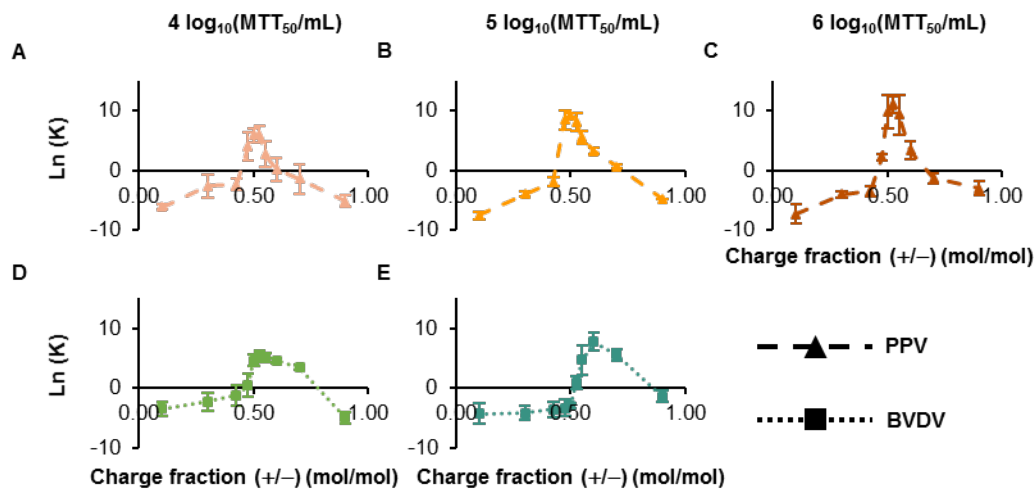


**Figure 6.4** Partition coefficient. (A&B&C) Encapsulated PPV, and (D&E) encapsulated BVDV. (A&D) 4  $\log_{10}(\text{MTT}_{50}/\text{mL})$ , (B&E) 5  $\log_{10}(\text{MTT}_{50}/\text{mL})$ , and (C) 6  $\log_{10}(\text{MTT}_{50}/\text{mL})$ . All data points are the average of three separate tests and error bars represent the standard deviation.

The coacervates have the maximum capacity to extract PPV from solution near the charge ratio 0.5, and to extract BVDV near the charge ratio 0.6. In all cases, the highest level of virus encapsulation and partition in the dense coacervate phase occurred around the point where the system was net neutral. The shift to higher charge fraction for BVDV extraction is likely due to the BVDV having a lower pI than PPV [43]. The pI of BVDV is further away from the buffer solution pH of 8.0 than PPV, as shown in **Table 6.1**. Therefore, BVDV carries a more net negative charge than PPV, thus needing more positively charged polypeptide to form the neutrally charged complex coacervate.

Virus recovery in the dense coacervate phase was also calculated and shown in **SI Figure A.3.1**. At each peak of the virus titer in the coacervate phase, and each maximum virus partition point (**Figure 6.3&4**), the maximum virus recovery was observed (**SI Figure A.3.1**). PPV coacervates could achieve a 100% encapsulation and recovery from the dense phase, whereas BVDV only recovered 50% of the infectious virus. This is likely due to enveloped BVDV is less stable than non-enveloped PPV in a high concentration of salt solution since the high osmotic pressure by high concentrations of salt can cause leakage in the viral envelope membrane [53].

### 6.3.3 Thermal stability of encapsulated virus vs. free virus

To demonstrate the effect of complex coacervates on the stability of viruses against high temperatures, free purified PPV or BVDV were first explored to find a critical starting temperature point where the virus could be completely inactivated. A temperature of 60°C was selected for the non-enveloped PPV for up to one week due to PPV started to lose 1 log of infectivity at 60°C for 1 hour [54]. A temperature of 40°C was selected for the enveloped BVDV for up to two days since BVDV lost 50% of infectivity at 37°C for 6 hours [55].

Free PPV in aqueous solution and encapsulated PPV were incubated at 60°C, followed by releasing the encapsulated PPV back to the solution with 2 M NaCl. The high salt solution has been shown to disassemble coalesced coacervate [25, 26, 37] due to salt interrupting the electrostatic interactions that hold the coacervate together. The stability of encapsulated PPV compared with free PPV against heat is shown in **Figure 6.5A**. After 1 day at 60°C, encapsulated PPV effectively maintained its viral titer, only losing  $1.0 \pm 0.1 \log_{10}$  (MTT<sub>50</sub>/mL). In comparison, free PPV showed a LRV of  $2.9 \pm 0.3 \log_{10}$  (MTT<sub>50</sub>/mL). Moreover, free PPV was found to be completely inactivated after 7 days under 60°C, with an LRV of  $5.9 \pm 0.5 \log_{10}$ (MTT<sub>50</sub>/mL). In comparison, encapsulated PPV only had a titer loss of  $2.7 \pm 0.1 \log_{10}$ (MTT<sub>50</sub>/mL) after 7 days. These results demonstrated that complex coacervates offer effective protection for non-enveloped PPV against thermal degradation.

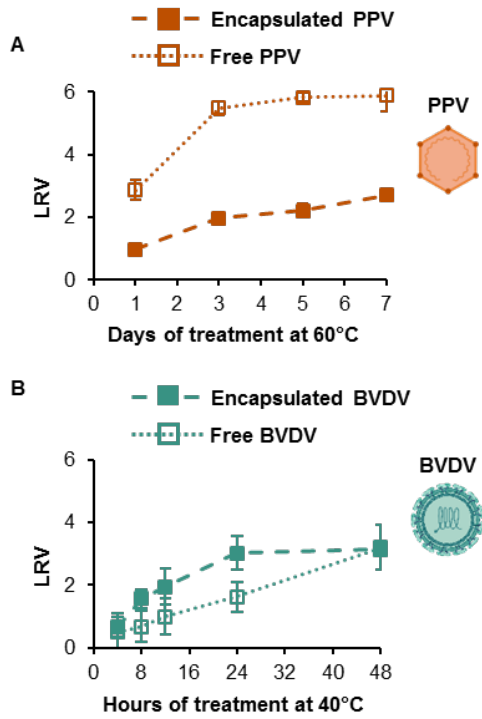


**Figure 6.5** Thermal stability of free and encapsulated virus. (A) PPV, and (B) BVDV. All data points are the average of three separate tests and error bars represent the standard deviation.

In addition, the lifetime of infectious PPV particles was determined using the simplest model for infectivity loss  $n(t) = n(0)e^{-t/\tau}$ [13], where  $t$  is the length of thermal treatment,  $n(t)$  is virus titer at  $t$ ,  $n(0)$  is the initial virus titer,  $\tau$  is the inverse decay rate, corresponding to the mean lifetime of an infectious viral particle. This model assumes the infectious viral particles degrade from alive to disrupted state at a constant rate, and the corresponding fitted data curves of encapsulated and free PPV are shown in SI **Figure**

**A.3.2.** The lifetime of encapsulated PPV is determined to be 14 days at 60°C, much longer than the lifetime of free PPV to be 4 days at 60°C.

The enhanced thermal stability of encapsulated PPV compared to the free PPV could be attributed to the crowding environment, which disfavors viral surface capsid proteins unfolding and denaturation, facilitate heat-induced unfolded viral proteins refolding back to the native state [56], and inhibit viruses forming insoluble aggregates [24]. The small, dense, compact, polymer-rich coacervate phase can provide entropy and enthalpy stabilization [24, 42]. The main driving force for viral capsid protein unfolding is believed to be the high conformational entropy of the denatured state [57], and the flexible unfolded state has a much greater conformational freedom than the compact folded state of a viral protein. The limited volume of the crowding environment would minimize the degrees of conformational freedom in the unfolded state, and hence improves the stabilization of the native state of viral protein due to an entropic stabilization [57, 58]. Also, unfolded viral proteins have larger hydration radii and occupy more volume compared to the folded state, and the excluded volume effect from the crowding environment lacks the space available for the extended denatured proteins, thus favors any process like protein folding in which the volume decreases [57-59]. In addition, the denaturation enthalpy of protein in polyelectrolyte complex has been shown much higher than free proteins [42], indicating that complex coacervation could impart thermal stability to viral capsid proteins.

Furthermore, complex coacervate microdroplet can be considered as a membrane-free artificial cellular platform for the viruses, served as a type of protocell [60], which is spatial compartmentalization rich in biomacromolecules independent of membrane (vesicle) formation [61-63]. Thus, the coacervate stabilizes viruses by mimicking the viruses inside of a membrane-free cell, which is a highly crowded environment due to the presence of macromolecules, such as proteins, nucleic acids, ribosomes and carbohydrates [60]. In reality, viruses replicated and folded their capsid proteins inside cells; thus, the intracellular environment mediated by the coacervates favors to fold viral capsid proteins in their compact native states and keep the structural stability of viral particles. Besides, A water content of 68-83 wt% [26, 64] was reported for BSA-poly(diallyldimethylammonium chloride), PLys-PGlu, PLys-poly(L-aspartic acid), poly(L-histidine)-PGlu, poly(L-ornithine)-PGlu complex coacervates systems; the high amounts of water content trapped by coacervate dense phase can also protect the viral particles against dehydration by heat evaporation. Such stabilization has also been shown to improve the thermal stability of proteins [24, 36, 42].

Furthermore, the stability of an enveloped virus BVDV against heat was also explored, and the result of encapsulated BVDV vs. free BVDV is shown in **Figure 6.5B**. Free BVDV in aqueous solution and encapsulated BVDV were incubated at 40°C, also followed by disassembling the encapsulated BVDV back to the solution with salt. However, complex coacervates offered no protection for enveloped BVDV against high temperature. The data demonstrated that encapsulated BVDV inactivated faster than free BVDV. It might be due to BVDV having a lipid bilayer envelope surrounding its viral capsid protein. PLys has been shown to penetrate negatively charged lipid bilayers [65], and it might interfere with the BVDV envelope, thus decreasing the thermal stability of the enveloped BVDV. This might also be the reason for the 50% BVDV recovery in SI

**Figure A.3.1.** In addition, PLys alone showed slight toxicity, as shown in SI **Figure A.3.3**, possibly due to its interaction with the negatively charged cell membrane, which resulted in membrane disruption and cell deaths.

Herein, we have demonstrated that the complex coacervation can be used to stabilize a non-enveloped virus PPV thermally, and the encapsulated PPV can keep its lifetime at 60°C for up to two weeks. This method could provide a promising platform for creating thermally stable non-enveloped live attenuated vaccines. Other positively charged polypeptides might need to be screened for the enveloped virus.

## 6.4 Conclusions

Two viruses, non-enveloped PPV and enveloped BVDV, were explored for their ability to be encapsulated into complex coacervates. At a charge ratio close to 0.5 (50% positively charged PLys to 50% negatively charged PGlu), all of the PPV particles were extracted from the solution and were encapsulated in the coacervate. The majority of the BVDV particles were taken into the coacervate phase near a charge ratio of 0.6. The shift to higher charge fraction for BVDV extraction is likely due to the BVDV having a lower pI than PPV. The pI of BVDV is further away from the buffer solution pH 8.0 than PPV, BVDV carried more net negative charges than PPV, thus need more positively charged polypeptide PLys to form the neutral charged complex coacervates system. An encapsulated non-enveloped PPV was thermally stabilized and retained its lifetime at 60°C for up to two weeks. Coacervates could help prevent the cold storage problem seen not only in developing countries but is also a very real problem here in rural parts of America.

## 6.5 References

1. Ritchie, H. and M. Roser. *Causes of Death*. Our World in Data [cited 2019 September 30]; Available from: <https://ourworldindata.org/causes-of-death>.
2. Organization, W.H., W.H.O.D.o. Immunization, and Biologicals, *Immunization in practice: A practical guide for health staff*. 2015: World Health Organization.
3. Ashok, A., M. Brison, and Y. LeTallec, *Improving cold chain systems: Challenges and solutions*. *Vaccine*, 2017. **35**(17): p. 2217-2223.
4. Comes, T., K.B. Sandvik, and B. Van de Walle, *Cold chains, interrupted: The use of technology and information for decisions that keep humanitarian vaccines cool*. *Journal of Humanitarian Logistics and Supply Chain Management*, 2018. **8**(1): p. 49-69.
5. WHO, *Monitoring vaccine wastage at country level*. 2018.
6. Hamborsky, J., et al., *Epidemiology and prevention of vaccine-preventable diseases*. 2015: US Department of Health & Human Services, Centers for Disease Control and ....
7. Plotkin, S.A., *Vaccines: the fourth century*. *Clin. Vaccine Immunol.*, 2009. **16**(12): p. 1709-1719.
8. Flint, J., et al., *Principles of Virology*. 4th ed. 2015: ASM Press.
9. HHS. *Vaccine Types*. 2019 [cited 2019 July 20]; Available from: <https://www.vaccines.gov/basics/types>.
10. NIH. *Vaccine Types*. 2019 [cited 2019 July 20]; Available from: <https://www.niaid.nih.gov/research/vaccine-types>.
11. Stobart, C.C., et al., *A live RSV vaccine with engineered thermostability is immunogenic in cotton rats despite high attenuation*. *Nature Communications*, 2016. **7**.
12. Mateo, R., et al., *Engineering Viable Foot-and-Mouth Disease Viruses with Increased Thermostability as a Step in the Development of Improved Vaccines*. *Journal of Virology*, 2008. **82**(24): p. 12232-12240.
13. Pelliccia, M., et al., *Additives for vaccine storage to improve thermal stability of adenoviruses from hours to months*. *Nature Communications*, 2016. **7**.
14. Toniolo, S.P., et al., *Excipient selection for thermally stable enveloped and non-enveloped viral vaccine platforms in dry powders*. *International Journal of Pharmaceutics*, 2019. **561**: p. 66-73.
15. Kumru, O.S., et al., *Vaccine instability in the cold chain: Mechanisms, analysis and formulation strategies*. *Biologicals*, 2014. **42**(5): p. 237-259.
16. Burke, C.J., T.A. Hsu, and D.B. Volkin, *Formulation, stability, and delivery of live attenuated vaccines for human use*. *Critical Reviews in Therapeutic Drug Carrier Systems*, 1999. **16**(1): p. 1-83.
17. Madan, M., et al., *Rational design of heat stable lyophilized rotavirus vaccine formulations*. *Human Vaccines & Immunotherapeutics*, 2018. **14**(9): p. 2132-2141.
18. Kaushik, J.K. and R. Bhat, *Why is trehalose an exceptional protein stabilizer? An analysis of the thermal stability of proteins in the presence of the compatible*

- osmolyte trehalose*. Journal of Biological Chemistry, 2003. **278**(29): p. 26458-26465.
19. Wang, G.C., et al., *Hydrated Silica Exterior Produced by Biomimetic Silicification Confers Viral Vaccine Heat-Resistance*. *Acs Nano*, 2015. **9**(1): p. 799-808.
  20. Blocher, W.C. and S.L. Perry, *Complex coacervate-based materials for biomedicine*. Wiley Interdisciplinary Reviews-Nanomedicine and Nanobiotechnology, 2017. **9**(4).
  21. Timilsena, Y.P., et al., *Complex coacervation: Principles, mechanisms and applications in microencapsulation*. *International Journal of Biological Macromolecules*, 2019. **121**: p. 1276-1286.
  22. Pathak, J., et al., *Complex coacervation in charge complementary biopolymers: Electrostatic versus surface patch binding*. *Advances in Colloid and Interface Science*, 2017. **250**: p. 40-53.
  23. Perry, S.L., et al., *The Effect of Salt on the Complex Coacervation of Vinyl Polyelectrolytes*. *Polymers*, 2014. **6**(6): p. 1756-1772.
  24. Water, J.J., et al., *Complex coacervates of hyaluronic acid and lysozyme: Effect on protein structure and physical stability*. *European Journal of Pharmaceutics and Biopharmaceutics*, 2014. **88**(2): p. 325-331.
  25. Chang, L.W., et al., *Sequence and entropy-based control of complex coacervates*. *Nature Communications*, 2017. **8**.
  26. Priftis, D. and M. Tirrell, *Phase behaviour and complex coacervation of aqueous polypeptide solutions*. *Soft Matter*, 2012. **8**(36): p. 9396-9405.
  27. Priftis, D., N. Laugel, and M. Tirrell, *Thermodynamic Characterization of Polypeptide Complex Coacervation*. *Langmuir*, 2012. **28**(45): p. 15947-15957.
  28. Sarmiento, B., et al., *Alginate/chitosan nanoparticles are effective for oral insulin delivery*. *Pharmaceutical research*, 2007. **24**(12): p. 2198-2206.
  29. Johnson, N.R., T. Ambe, and Y.D. Wang, *Lysine-based polycation:heparin coacervate for controlled protein delivery*. *Acta Biomaterialia*, 2014. **10**(1): p. 40-46.
  30. Liu, Z.H., et al., *Polysaccharides-based nanoparticles as drug delivery systems*. *Advanced Drug Delivery Reviews*, 2008. **60**(15): p. 1650-1662.
  31. Leong, K.W., et al., *DNA-polycation nanospheres as non-viral gene delivery vehicles*. *Journal of Controlled Release*, 1998. **53**(1-3): p. 183-193.
  32. Ozbas-Turan, S., et al., *Co-encapsulation of two plasmids in chitosan microspheres as a non-viral gene delivery vehicle*. *Journal of Pharmacy and Pharmaceutical Sciences*, 2003. **6**(1): p. 27-32.
  33. Mann, L.K., et al., *Fetal membrane patch and biomimetic adhesive coacervates as a sealant for fetoscopic defects*. *Acta Biomaterialia*, 2012. **8**(6): p. 2160-2165.
  34. Winslow, B.D., et al., *Biocompatibility of adhesive complex coacervates modeled after the sandcastle glue of *Phragmatopoma californica* for craniofacial reconstruction*. *Biomaterials*, 2010. **31**(36): p. 9373-9381.
  35. Black, K.A., et al., *Protein Encapsulation via Polypeptide Complex Coacervation*. *Acs Macro Letters*, 2014. **3**(10): p. 1088-1091.



36. Zhao, M.M. and N.S. Zacharia, *Protein encapsulation via polyelectrolyte complex coacervation: Protection against protein denaturation*. Journal of Chemical Physics, 2018. **149**(16).
37. McTigue, W.C.B. and S.L. Perry, *Design rules for encapsulating proteins into complex coacervates*. Soft Matter, 2019. **15**(15): p. 3089-3103.
38. Galan, A. and P. Ballester, *Stabilization of reactive species by supramolecular encapsulation*. Chemical Society Reviews, 2016. **45**(6): p. 1720-1737.
39. Lindhoud, S. and M. Claessens, *Accumulation of small protein molecules in a macroscopic complex coacervate*. Soft Matter, 2016. **12**(2): p. 408-413.
40. Pippa, N., et al., *Complexation of cationic-neutral block polyelectrolyte with insulin and in vitro release studies*. International journal of pharmaceutics, 2015. **491**(1-2): p. 136-143.
41. Chi, E.Y., et al., *Physical stability of proteins in aqueous solution: Mechanism and driving forces in nonnative protein aggregation*. Pharmaceutical Research, 2003. **20**(9): p. 1325-1336.
42. Chang, P.G., et al., *Optimisation of the complex coacervation between canola protein isolate and chitosan*. Journal of food engineering, 2016. **191**: p. 58-66.
43. Mi, X., et al., *Virus isoelectric point determination using single-particle chemical force microscopy*. Langmuir, 2019.
44. Heldt, C.L., et al., *A colorimetric assay for viral agents that produce cytopathic effects*. J Virol Methods, 2006. **135**(1): p. 56-65.
45. Mi, X., et al., *Mannitol-induced gold nanoparticle aggregation for the ligand-free detection of viral particles*. Analyst, 2019. **144**(18): p. 5486-5496.
46. Tafur, M.F., K.S. Vijayaragavan, and C.L. Heldt, *Reduction of porcine parvovirus infectivity in the presence of protecting osmolytes*. Antiviral Research, 2013. **99**(1): p. 27-33.
47. Meng, H., et al., *Biomimetic recyclable microgels for on-demand generation of hydrogen peroxide and antipathogenic application*. Acta Biomaterialia, 2019. **83**: p. 109-118.
48. Kitchener, B.B., J. Wainwright, and A.J. Parsons, *A review of the principles of turbidity measurement*. Progress in Physical Geography, 2017. **41**(5): p. 620-642.
49. Michen, B. and T. Graule, *Isoelectric points of viruses*. Journal of applied microbiology, 2010. **109**(2): p. 388-397.
50. Norkin, L.C., *Virology: Molecular Biology and Pathogenesis*. 2010: ASM Press.
51. Weichert, W.S., et al., *Assaying for structural variation in the parvovirus capsid and its role in infection*. Virology, 1998. **250**(1): p. 106-117.
52. Kim, I.S., Y.W. Choi, and S.R. Lee, *Optimization and validation of a virus filtration process for efficient removal of viruses from urokinase solution prepared from human urine*. Journal of Microbiology and Biotechnology, 2004. **14**(1): p. 140-147.
53. Choi, H.J., et al., *Effect of Osmotic Pressure on the Stability of Whole Inactivated Influenza Vaccine for Coating on Microneedles*. Plos One, 2015. **10**(7).
54. Blumel, J., et al., *Inactivation of parvovirus B19 during pasteurization of human serum albumin*. Transfusion, 2002. **42**(8): p. 1011-1018.

55. Depner, K., T. Bauer, and B. Liess, *Thermal and pH stability of pestiviruses*. REVUE SCIENTIFIQUE ET TECHNIQUE-OFFICE INTERNATIONAL DES EPIZOOTIES, 1992. **11**: p. 885-885.
56. Martin, N., M. Li, and S. Mann, *Selective Uptake and Refolding of Globular Proteins in Coacervate Microdroplets*. Langmuir, 2016. **32**(23): p. 5881-5889.
57. Kim, Y.H. and W.E. Stites, *Effects of excluded volume upon protein stability in covalently cross-linked proteins with variable linker lengths*. Biochemistry, 2008. **47**(33): p. 8804-8814.
58. Miklos, A.C., et al., *Volume Exclusion and Soft Interaction Effects on Protein Stability under Crowded Conditions*. Biochemistry, 2010. **49**(33): p. 6984-6991.
59. Aden, J. and P. Wittung-Stafshede, *Folding of an Unfolded Protein by Macromolecular Crowding in Vitro*. Biochemistry, 2014. **53**(14): p. 2271-2277.
60. Dzieciol, A.J. and S. Mann, *Designs for life: protocell models in the laboratory*. Chemical Society Reviews, 2012. **41**(1): p. 79-85.
61. Tang, T.Y.D., et al., *Fatty acid membrane assembly on coacervate microdroplets as a step towards a hybrid protocell model*. Nature Chemistry, 2014. **6**(6): p. 527-533.
62. Koga, S., et al., *Peptide-nucleotide microdroplets as a step towards a membrane-free protocell model*. Nature Chemistry, 2011. **3**(9): p. 720-724.
63. Tang, T.Y.D., et al., *Small-molecule uptake in membrane-free peptide/nucleotide protocells*. Soft Matter, 2013. **9**(31): p. 7647-7656.
64. Bohidar, H., et al., *Effects of protein-polyelectrolyte affinity and polyelectrolyte molecular weight on dynamic properties of bovine serum albumin-poly(diallyldimethylammonium chloride) coacervates*. Biomacromolecules, 2005. **6**(3): p. 1573-1585.
65. Takechi, Y., et al., *Comparative study on the interaction of cell-penetrating polycationic polymers with lipid membranes*. Chemistry and Physics of Lipids, 2012. **165**(1): p. 51-58.

# 7 Conclusion and future work

## 7.1 Conclusions

In this dissertation, we demonstrated how we developed a single-particle chemical force microscopy (CFM) method to characterize the chemical surface of virus, focusing on hydrophobicity and surface charge. CFM can detect the surface chemistry of viral capsids at a single-particle level and enable the comparison of the surface chemistry between different types of viruses. Our covalent virus immobilization method can retain a natural virus state without deformation or disassembly. We chose to covalently attach the virus to a gold surface to guarantee that the bond that is broken during CFM measurements is the virus-tip interaction and not the virus-surface interaction. Our atomic force microscope (AFM) probe functionalizing method of thiol attachment to gold-coated probes can be achieved at room temperature and allows the attachment of many chemical functional groups of interest. With the immobilized virus and functionalized AFM tips, we have studied viral surface chemistry with small amounts of samples using CFM. We determined that porcine parvovirus (PPV) is more hydrophobic than bovine viral diarrhea virus (BVDV) using a methyl-terminated AFM probe. When charged groups were put on the AFM probes, the surface charge of the virus could be measured. Both PPV and BVDV carry a negative charge at neutral pH.

We have used oppositely charged groups modified AFM tips to study viral electrostatic surface properties at various pH solutions. The adhesion force as a function of pH was a good fit for a sigmoidal curve, which allowed the determination of the inflection point as the isoelectric point (pI) of the virus. CFM determined the pI of PPV to be 4.8-5.1 and BVDV to be 4.3-4.5. PPV had literature reported pI of 5.0, and BVDV did not have literature reported pI. The pI values determined by CFM are in good agreement with most of the pI values determined by the bulk measurements of zeta potential and aqueous two-phase system (ATPS). Virus particles are much more complex systems than surface capsid proteins, and the theoretical calculations did not provide an accurate measure of virus surface pI due to effects not taken into accounts, such as amino acid modifications and the viral envelope. Therefore, we need to determine the pI of viruses experimentally. With a thorough understanding of virus surface chemistry, future technologies in areas of bio-sensing, vaccines, gene therapy, and targeted drug delivery could be significantly improved by using CFM to characterize the particle surface chemistry.

The biochemical surface properties of viruses were further exploited for ligand-free, nonspecific virus detection. The detection depends on the interaction of the virus with the osmolyte mannitol. The aggregation of virus-coated gold nanoparticles (AuNPs) in mannitol can be detected by dynamic light scattering (DLS), and there is a linear increase in aggregate size with an increase in PPV concentration on a semi-log plot. This indicates the potential of quantitative detection of the virus with this described AuNPs aggregation method. The lowest detectable concentration of the virus was analyzed statistically to be  $10^6$  MTT<sub>50</sub>/mL, which is lower than standard antibody assays. The non-specific nature of this assay was tested by detecting the aggregation of BVDV-coated AuNPs in mannitol. The lowest detection concentration for BVDV was determined to be  $10^4$  MTT<sub>50</sub>/mL. The AuNPs aggregation assay has the ability to determine the presence

of a virus in up to 500  $\mu\text{M}$  of bovine serum albumin (BSA) quantitatively, used as a model contaminant in a protein-rich biological fluid. Also, PPV was detected quantitatively after it was swabbed from a dried sample on a petri dish. The developed ligand-free AuNPs aggregation method can determine the presence of virus within 24 hours, which is comparable or faster than current virus detection methods. This general virus detection method could be a quick, sensitive, inexpensive, and portable method for detecting the presence of viral particles in low resource countries.

PPV and BVDV were also explored for their ability to be encapsulated into complex coacervates. At a charge ratio close to 0.5 (50% positively charged poly (L-lysine) (PLys) to 50% negatively charged poly (D, L-glutamic acid) (PGlu)), all of the PPV particles were extracted from the solution and were encapsulated in the coacervate. The majority of the BVDV particles were taken into the coacervate phase near a charge ratio of 0.6. The shift to higher charge fraction for BVDV extraction is likely due to the BVDV having a lower pI than PPV, measured by the CFM. The pI of BVDV is further away from the buffer solution pH 8.0 than PPV, BVDV carried more net negative charges than PPV, thus need more positively charged polypeptide PLys to form the neutral charged complex coacervates system. An encapsulated non-enveloped PPV was thermally stabilized and retained its lifetime at 60°C for up to two weeks. Coacervates could help prevent the cold storage problem seen not only in developing countries but is also a very real problem here in rural parts of America.

## 7.2 Future work

For virus surface chemistry characterization by CFM, we would like to explore more on viral surface hydrophobicity, PPV, BVDV, and symmetric less hydrophobic protein control thyroglobulin will be performed in standard PBS buffer, with a hydrophobic methyl and a hydrophilic hydroxyl group functionalized AFM probe. To perturb the system, the surfactant Triton X-100 will be added to the solution to disrupt hydrophobic interaction between the viral surface and SAM-CH<sub>3</sub> modified AFM probe. In the opposite regard, lysine will be added to the buffer solution to increase the hydrophobic interaction [1]. It has been shown that the charging of the lysine side-chain amino groups enhanced the hydrophobic interactions between the non-polar domain of GA-Lys and the AFM tip [1]. Other hydrophobic interactions modifiers, such as ethanol, poly (ethylene glycol) (PEG), and osmolytes, were also interested in adding to the solutions.

Comparisons of the adhesion of hydrophobic or electrostatic interactions by CFM work to the adhesion to corresponding chromatography columns will be explored. A space linker, e.g., PEG, is highly suggested to be used rather than the current ten carbon lengths to modify the AFM probe, avoiding any non-specific interactions confusing the interested specific interactions at zero separations in the force-distance curves [2]. In addition, a quaternary amine and sulphonic acid-functionalized AFM probe will be used to explore the surface chemistry difference between full and empty adeno-associated virus (AAV) capsids in different buffers conditions used in industry chromatography, to better understand the separation of empty capsids from full capsids in gene therapy.

Furthermore, the interparticle interactions of viral particles are also interesting to explore, AFM tips will be functionalized with carboxyl terminated bifunctional linker, covalently binding with the same virus that will be probed, allowing measurement of the self-interaction forces in different solution conditions. To confirm the virus attached to the AFM tip, the functionalized tip will be characterized by confocal microscopy of the fluorescently labeled virus [3]. Similar experiments will be conducted as done in the virus surface study by changing the buffer conditions. The self-interaction will also be varied by changing pH, ionic strength, and surfactant to measure changes in the ionic, hydrophobic, and hydrogen bonding of the virus with itself. Reducing water molecules environments (i.e., high concentrations of salt, 20%-40% ethanol, 4% PEG, and high concentrations of osmolytes) will enhance virus self-interaction due to high hydrophobicity of the viral surface.

For virus detection by AuNPs aggregation, we would like to explore additional viruses, reducing the time for the assay, and determining the ideal AuNP size and shape. Gold nanospheres in 10, 20, and 40 nm for PPV (~20 nm), and gold nanospheres in 25, 50, and 100 nm for BVDV (~50 nm) will be explored. Additionally, 40×10 nm gold nanorods, and 100 nm gold nanostars will also be used to detect the viruses. The goal is to develop this assay into an early screening step for a viral infection in blood samples or cleanliness of a surface, which could help to control a viral disease outbreak.

For stabilization of virus by polyelectrolytes dense phase, other combinations of synthesized polypeptides, e.g., PLY-PGlu, PLY-poly(L-aspartic acid), poly(L-histidine)-

PGlu, poly (L-ornithine)-PGlu (different charge patterns, degree of polymerization) will be likely to explore. Except for polyelectrolyte mixing ratio (stoichiometry), the effects of polyelectrolyte concentrations, solution pH, and different ionic strengths of solutions on the phase behavior of virus complex coacervates are also interested in studying. Sugars such as trehalose are planned to add into the formulation of enveloped BVDV complex coacervates to improve the thermal stability. Other enveloped viruses like HSV, hepatitis A virus, are likely to be explored.

### 7.3 References

1. Ma, C.D., et al., *Modulation of hydrophobic interactions by proximally immobilized ions*. Nature, 2015. **517**(7534): p. 347-350.
2. Blanchette, C.D., A. Loui, and T.V. Ratto, *Tip functionalization: Applications to chemical force spectroscopy*, in *Handbook of Molecular Force Spectroscopy*. 2008, Springer. p. 185-203.
3. Alsteens, D., et al., *Nanomechanical mapping of first binding steps of a virus to animal cells*. Nature Nanotechnology, 2017. **12**(2): p. 177-183.



## A Supplementary information

### A.1 Virus isoelectric point determination

#### Additional Methods

#### Preparation of 20 mM citrate buffer solutions at pH 3.0-6.0

A total of 2.101 g citric acid monohydrate was dissolved in 500 mL Nanopure water at room temperature with gentle stirring for 10 min to make a 0.02 M homogeneous citric acid solution. Then a total of 2.941 g sodium citrate tribasic dihydrate was added into 500 mL Nanopure water at room temperature with gentle stirring for 10 min to make a 0.02 M homogeneous trisodium citrate solution. To prepare 20 mM citrate buffer solutions at pH 3.0-6.0, the volume of 0.02 M citric acid solution and 0.02 M trisodium citrate solution was mixed as follows in **Table S1**. The final pH was adjusted with 1 M NaOH or HCl, as needed, and measured with a calibrated pH meter.

**Table A.1** the citrate buffer at pH 3.0-6.0 recipe

pH of citrate buffer	Volume (mL) 0.02 M citric acid	Volume (mL) 0.02 M trisodium citrate
3.0	41.0	9.0
4.0	29.5	20.5
4.5	23.4	26.5
5.0	17.5	32.5
5.5	11.6	38.3
6.0	5.7	44.2

#### Preparation of 20 mM phosphate buffer solution at pH 7.0

A total of 5.361 g sodium phosphate dibasic heptahydrate was dissolved in 1000 mL Nanopure water at room temperature with gentle stirring for 10 min to make a 0.02 M homogeneous solution. Then, a total of 2.7598 g sodium phosphate monobasic monohydrate was added into 1000 mL Nanopure water at room temperature with gentle stirring for 10 min to make a 0.02 M homogeneous solution. To prepare 20 mM phosphate buffer solutions at pH 7.0, 610 ml 0.02 M sodium phosphate dibasic solution, and 390 ml 0.02 M sodium phosphate monobasic solution was mixed. The final pH was adjusted with 1 M NaOH or HCl, as needed, and measured with a calibrated pH meter.

## Characterization of BVDV

For TEM characterization,  $7 \log_{10}$  MTT<sub>50</sub>/ml purified BVDV was adsorbed to a plasma etched TEM copper grid (Carbon Type-B, 300 mesh) for 2 minutes and then negatively stained with 2% uranyl acetate (Fisher Scientific) for 2 minutes. The morphology of the virus samples was imaged with a FEI Titan Themis Scanning Transmission Electron Microscope at 80 kV.

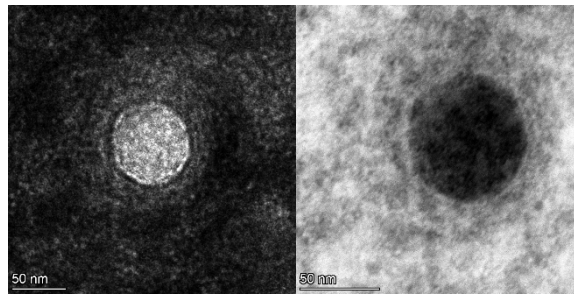


**Figure A.1.1** TEM images of enveloped BVDV showing the viral envelope. (A) Bright field image, and (B) dark field image.

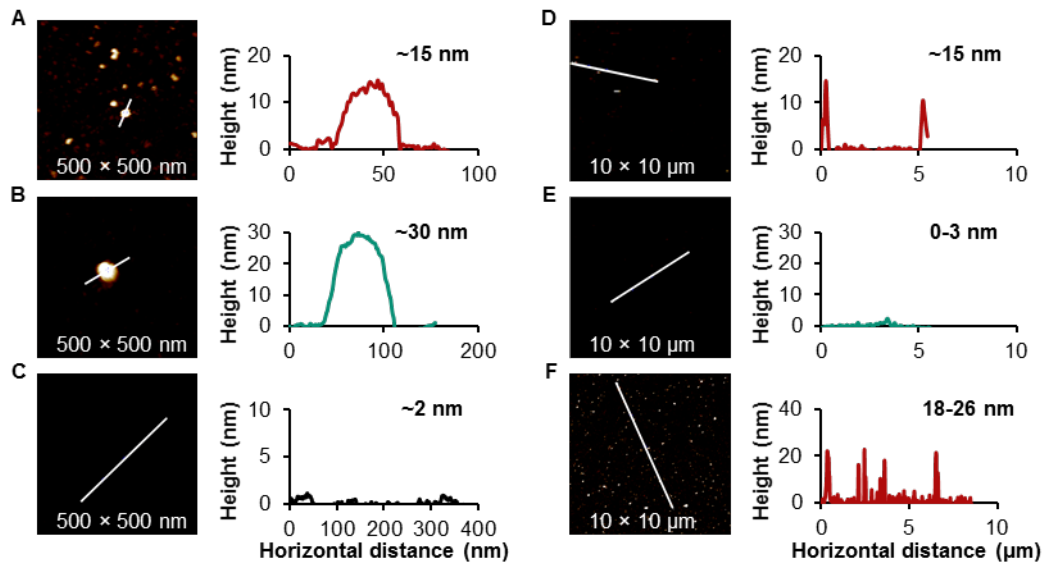


**Figure A.1.2** Topographic image and corresponding height analysis of virus and controls in liquid. (A&B) Viruses deposited on gold. (A) PPV and (B) BVDV. (C) NHS-EDC background. (D&E) Viruses deposited on SAM-COOH and direct addition of virus without addition of NHS/EDC. (D) PPV, (E) BVDV. (F) PPV covalently immobilized on SAM-COOH with addition of NHS/EDC as a comparison to (D) without NHS/EDC.

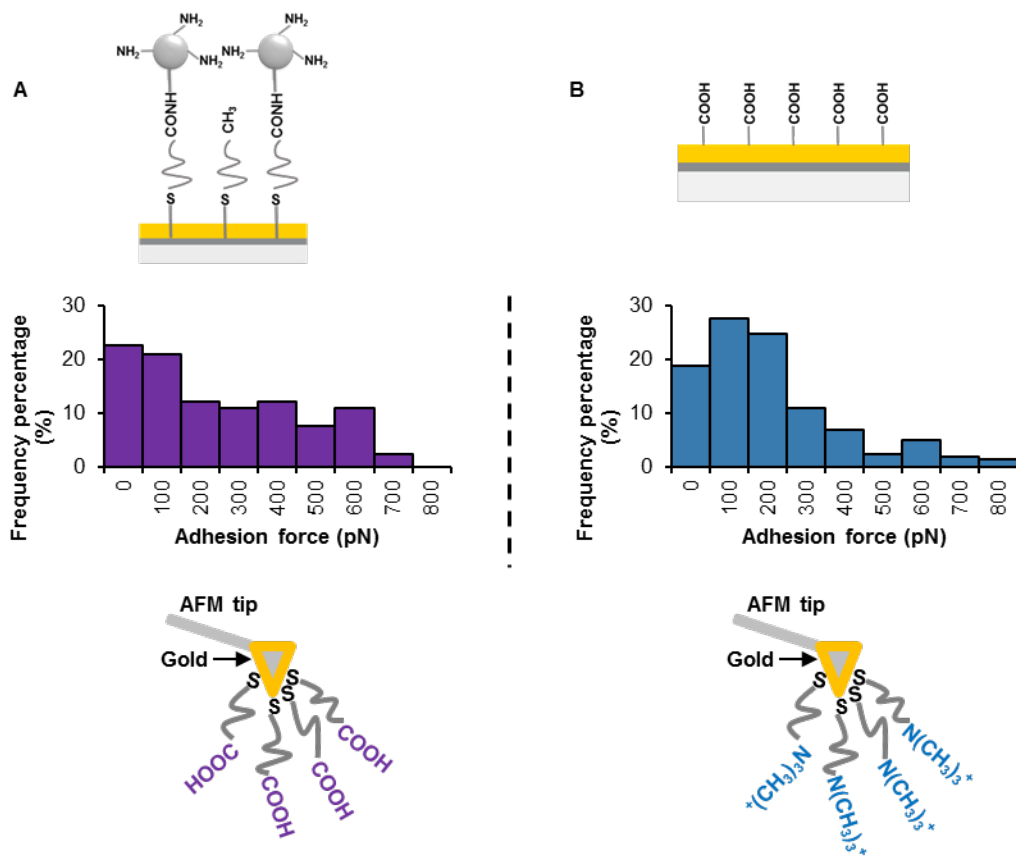


**Figure A.1.3** Confirm probe functionalization. (A) Primary amine modified silica NPs with a COOH-terminated probe, (B) COOH modified surface with a NR<sub>4</sub><sup>+</sup>-terminated probe. Adhesion histograms of positive control with a COOH-terminated probe or a NR<sub>4</sub><sup>+</sup>-terminated probe, recorded in 20 mM phosphate buffers at pH 7.0. Multiple (n= 500) F-D curves were recorded over 500 nm × 500 nm areas.

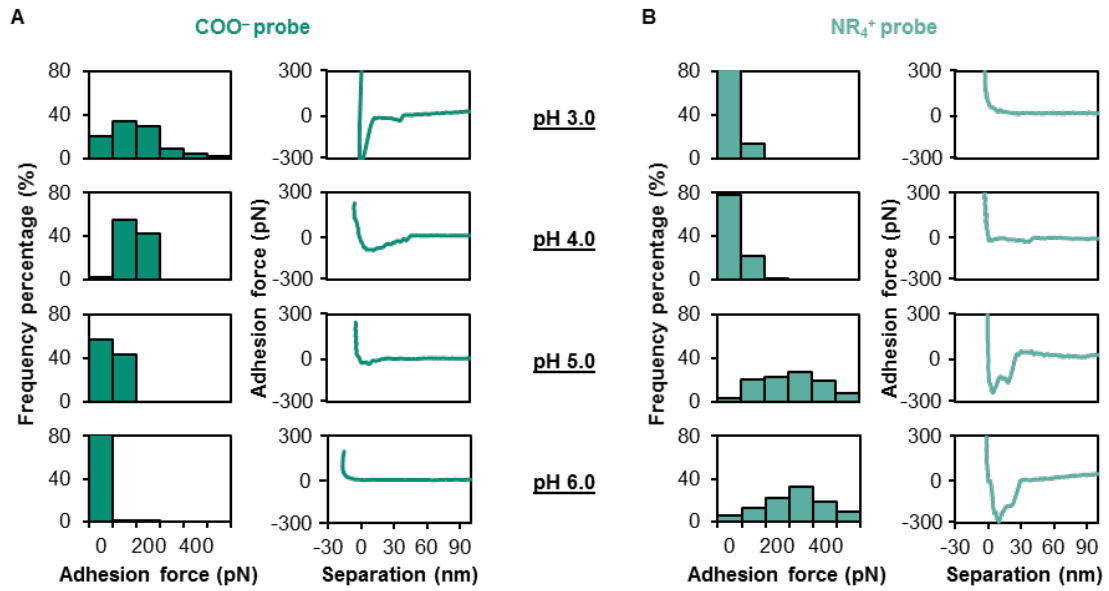


**Figure A.1.4** Adhesion histograms and representative force-distance curves (retraction part) of BVDV with a COOH-terminated probe (A) or a NR<sub>4</sub><sup>+</sup>-terminated probe (B), recorded in 20 mM citrate or phosphate buffers of varying pH. Multiple (n= 500) F-D curves were recorded over 500 nm × 500 nm areas.

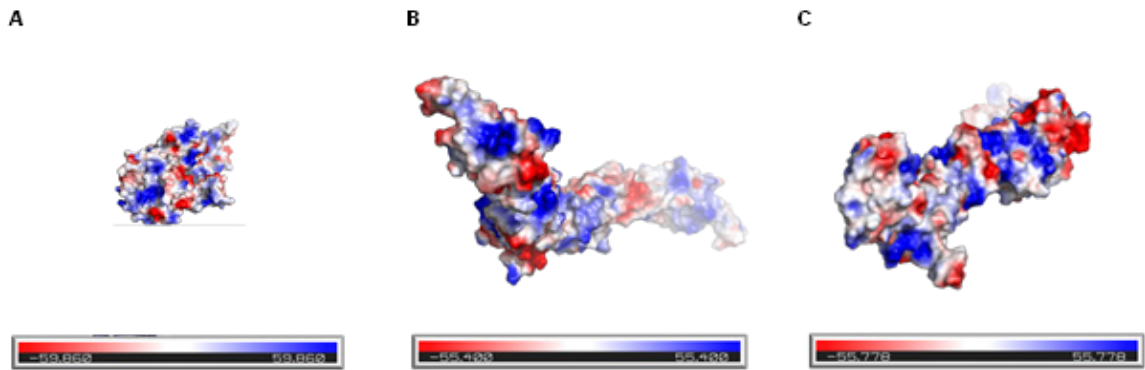


**Figure A.1.5** The electrostatic potential map of virus surface. (A) PPV capsid protein VP2, (B) BVDV glycoprotein E2, and (C) BVDV glycoprotein E2. (Created in PyMOL)

## A.2 Virus detection by mannitol-induced gold nanoparticle aggregation

The calculation for concentration of control BSA of  $10^{-3}$   $\mu\text{M}$  based on the same area coverage of  $10^8$   $\text{MTT}_{50}/\text{mL}$  virus PPV on AuNPs is shown as follows:

Step 1, unit conversion from PPV titer to number of PPV particles:

$$10^8 \frac{\text{MTT}_{50}}{\text{mL}} = 8 \log_{10} \left( \frac{\text{MTT}_{50}}{\text{mL}} \right) \times \frac{10^7 \frac{\text{pfu}}{\text{mL}}}{7.8 \log_{10} \left( \frac{\text{MTT}_{50}}{\text{mL}} \right)} \times \frac{1 \times 10^6 \text{ particles}^{**}}{1 \text{ pfu}}$$

$$= 1.0 \times 10^{13} \frac{\text{particles}}{\text{mL}}$$

$$* 7 \log_{10} \left( \frac{\text{pfu}}{\text{mL}} \right) = 7.8 \log_{10} \left( \frac{\text{MTT}_{50}}{\text{mL}} \right),^1 \text{ thus } 10^7 \frac{\text{pfu}}{\text{mL}} = 7.8 \log_{10} \left( \frac{\text{MTT}_{50}}{\text{mL}} \right)$$

$$** \text{ Infectivity ratio} = \frac{\text{infectious particles}}{\text{total particles}} = 1,000,000,^2$$

$$\text{thus } 1 \text{ pfu} = 1,000,000 \text{ particles}$$

$$\text{Step 2, coverage area of PPV} = A_{\text{PPV}} = \pi r_{\text{PPV}}^2 = \pi \left( \frac{d_{\text{PPV}}}{2} \right)^2 = \pi \left( \frac{25 \text{ nm}}{2} \right)^2 = 156\pi \text{ nm}^2$$

$$\text{Coverage area of BSA} = A_{\text{BSA}} = \pi r_{\text{BSA}}^2 = \pi \left( \frac{d_{\text{BSA}}}{2} \right)^2 = \pi \left( \frac{6.78 \text{ nm}}{2} \right)^2 = 11.5\pi \text{ nm}^2$$

$$\text{Ratio of coverage area PPV/BSA} = \frac{156\pi \text{ nm}^2}{11.5\pi \text{ nm}^2} = 14$$

Therefore, concentration of control

$$\text{BSA} = \frac{1.0 \times 10^{13} \frac{\text{particles}}{\text{mL}} \times 14}{6 \times 10^{23} \text{ particles/mol}^{***}} \approx 10^{-9} \frac{\text{mol}}{\text{mL}} = 1 \text{ nM} = 10^{-3} \mu\text{M}$$

$$*** \text{ Avogadro's constant} = 6 \times 10^{23} \text{ mol}^{-1},^3 \text{ thus } 1 \text{ mol} = 6 \times 10^{23} \text{ particles}$$

## REFERENCES

- (1) Heldt, C. L.; Hernandez, R.; Mudiganti, U.; Gurgel, P. V.; Brown, D. T.; Carbonell, R. G. A Colorimetric Assay for Viral Agents That Produce Cytopathic Effects. *J. Virol. Methods* **2006**, *135* (1), 56-65.
- (2) Muzyczka, N.; Berns, K. I. Parvoviridae: The Viruses and Their Replication. In *Field's Virology*; Knipe, D. M.; Howely, P. M., Eds.; Lippincott Williams & Wilkins: 2001; pp 2327-59.
- (3) Prausnitz, J. M. P.; Lichtenthaler, R. N.; Azevedo, E. G. *Molecular Thermodynamics of Fluid-Phase Equilibria*, Third Edition ed.; Prentice Hall PTR: 1999.

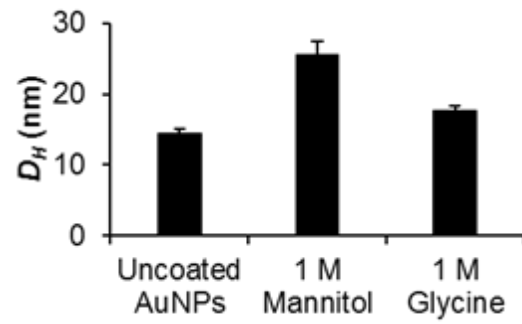


**Figure A.2.1** Uncoated AuNPs before and after 1 M osmolyte. All data points are the average of three separate tests and error bars represent the standard deviation.



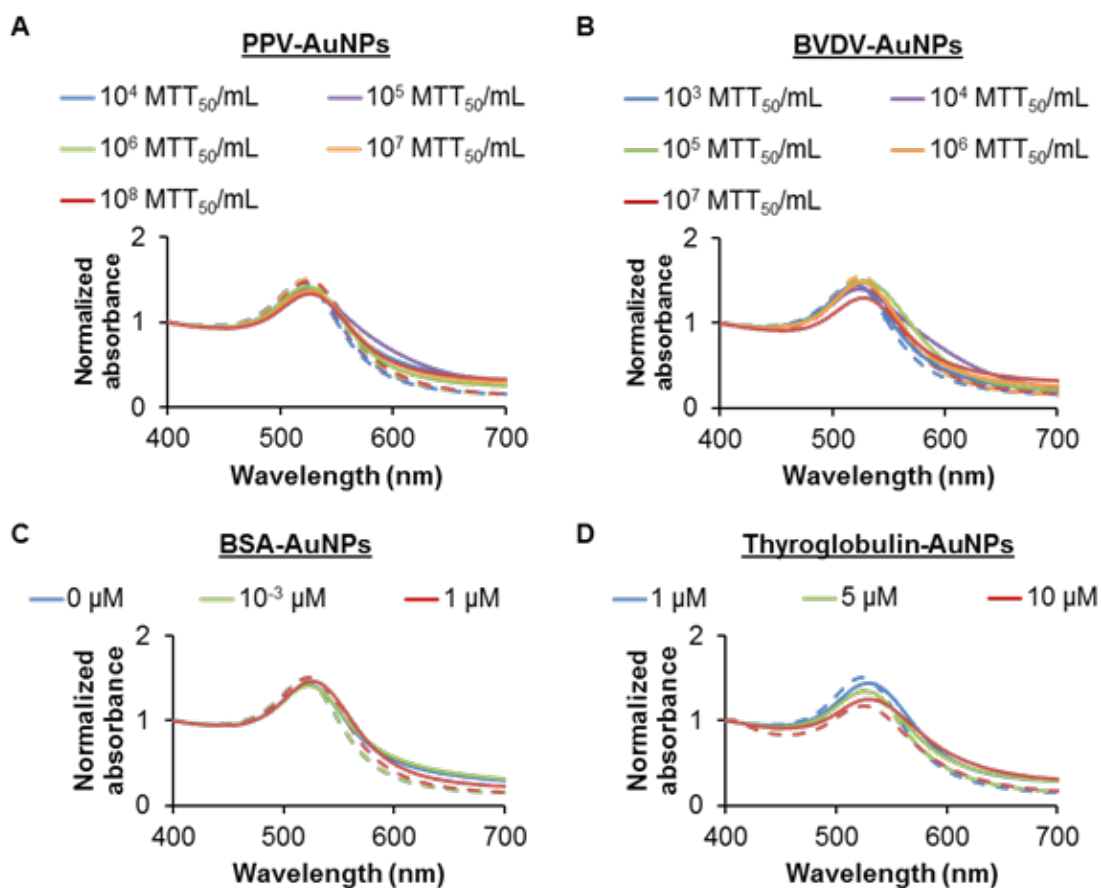


**Figure A.2.2** UV-Vis absorbance spectra of coated AuNPs before and after 1 M osmolyte. Dashed lines represent coated AuNPs before 1 M mannitol and solid lines represent coated AuNPs after 1 M mannitol.

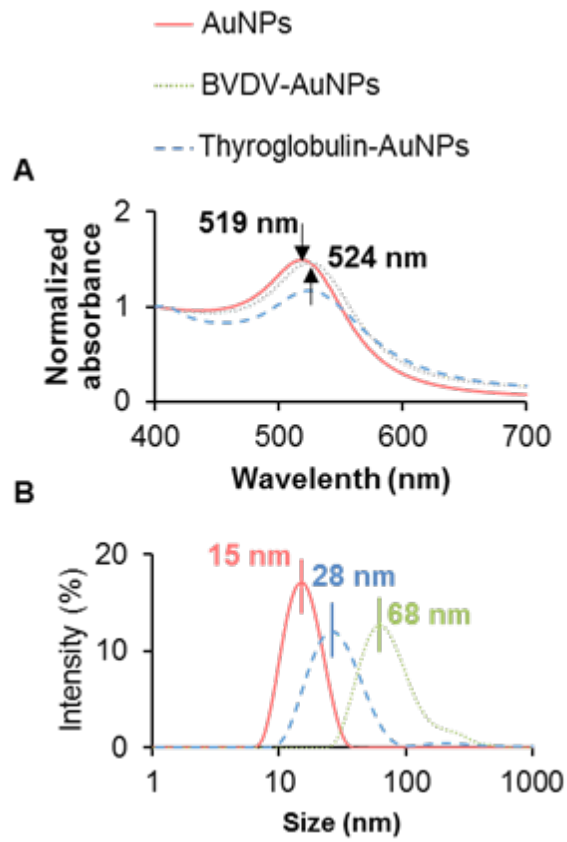


**Figure A.2.3** Characterization of synthesized and BVDV or thyroglobulin coated AuNPs. (A) UV-Vis absorption spectrum, (B) hydrodynamic diameter

### A.3 Stabilization of viruses through complex coacervation

The recovery of the virus was calculated by **Eq.A.3.1**.

$$Recovery (\%) = \frac{C_c \times V_c}{C_i \times V_i} \times 100 \quad (\text{A.3.1})$$

where,  $C_c$  is the virus concentration in the coacervate phase,  $V_c$  is the virus volume in the coacervate phase,  $C_i$  is the initial virus concentration, and  $V_i$  is the initial virus volume in the overall system.

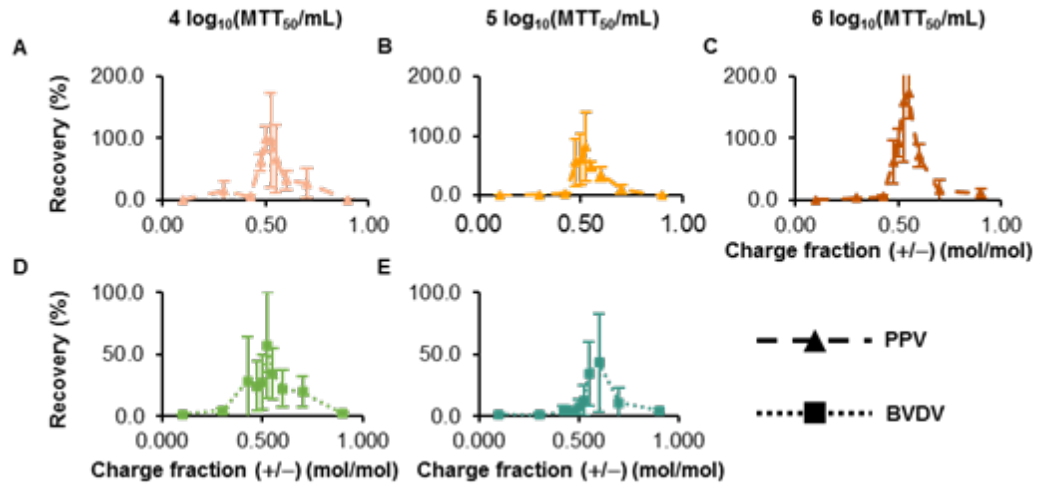


**Figure A.3.1** Live virus recovery in coacervate. (A&B&C) Encapsulated PPV, and (D&E) Encapsulated BVDV. (A&D)  $4 \log_{10}(\text{MTT}_{50}/\text{mL})$ , (B&E)  $5 \log_{10}(\text{MTT}_{50}/\text{mL})$ , and (C)  $6 \log_{10}(\text{MTT}_{50}/\text{mL})$ . All data points are the average of three separate tests and error bars represent the standard deviation.

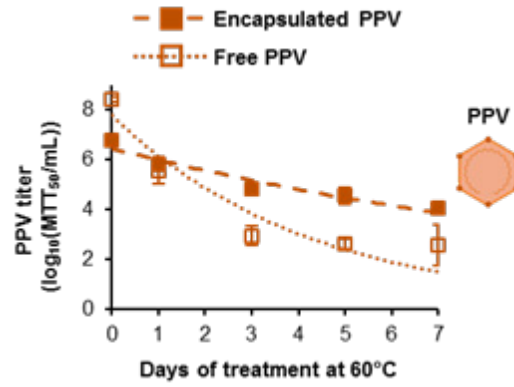


**Figure A.3.2** The infectivity loss of free and encapsulated virus. All data points are the average of three separate tests and error bars represent the standard deviation.

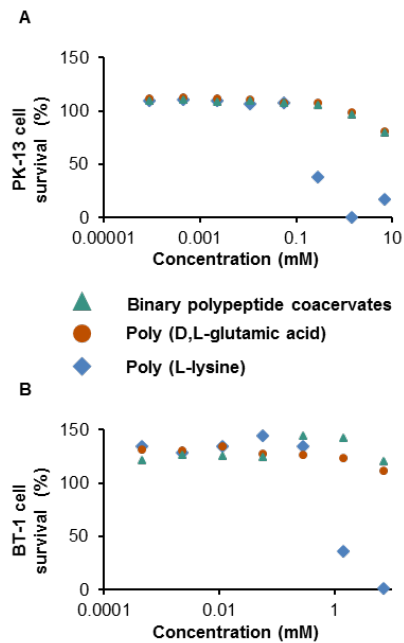


**Figure A.3.3** Cytotoxicity of polypeptides. (A) PK-13 cells, and (B) BT-1 cells.

## B Copyright permission documentation

### B.1 Figure 2.1 permission



Home

Help

Live Chat

Sign in

Create Account



#### Experimental and computational surface hydrophobicity analysis of a non-enveloped virus and proteins

Author: Caryn L. Heldt, Amna Zahid, K. Saagar Vijayaragavan, Xue Mi

Publication: Colloids and Surfaces B: Biointerfaces

Publisher: Elsevier

Date: 1 May 2017

© 2017 Elsevier B.V. All rights reserved.

Please note that, as the author of this Elsevier article, you retain the right to include it in a thesis or dissertation, provided it is not published commercially. Permission is not required, but please ensure that you reference the journal as the original source. For more information on this and on your other retained rights, please visit: <https://www.elsevier.com/about/our-business/policies/copyright#Author-rights>

BACK

CLOSE WINDOW

## B.2 Figure 2.2 permission

### SPRINGER NATURE LICENSE TERMS AND CONDITIONS

Nov 25, 2019

---

---

This Agreement between Michigan Technological University ("You") and Springer Nature ("Springer Nature") consists of your license details and the terms and conditions provided by Springer Nature and Copyright Clearance Center.

License Number	4715830046266
License date	Nov 25, 2019
Licensed Content Publisher	Springer Nature
Licensed Content Publication	Nature Nanotechnology
Licensed Content Title	Net charge of trace proteins
Licensed Content Author	Gilbert C. Walker
Licensed Content Date	Jul 25, 2016
Type of Use	Thesis/Dissertation
Requestor type	non-commercial (non-profit)
Format	electronic
Portion	figures/tables/illustrations
Number of figures/tables/illustrations	1



High-res required	no
Will you be translating?	no
Circulation/distribution	1 - 29
Author of this Springer Nature content	no
Title	Detection and thermal stabilization of virus based on surface properties
Institution name	Michigan Technological University
Expected presentation date	Dec 2019
Order reference number	37
Portions	Figure 2.2
Requestor Location	Michigan Technological University 1803 Woodmar Dr  HOUGHTON, MI 49931 United States Attn: Michigan Technological University
Total	0.00 USD

### B.3 Figure 2.4 permission

Figure 2.4 is licensed under the [Creative Commons Attribution-Share Alike 3.0 Unported](#)

## B.4 Figure 2.5 permission

### ELSEVIER LICENSE TERMS AND CONDITIONS

Nov 25, 2019

---

---

This Agreement between Michigan Technological University ("You") and Elsevier ("Elsevier") consists of your license details and the terms and conditions provided by Elsevier and Copyright Clearance Center.

License Number 4715860867494

License date Nov 25, 2019

Licensed Content Publisher Elsevier

Licensed Content Publication Virus Research

Licensed Content Title Mechanical properties of viruses analyzed by atomic force microscopy: A virological perspective

Licensed Content Author Mauricio G. Mateu

Licensed Content Date Sep 1, 2012

Licensed Content Volume 168

Licensed Content Issue 1-2

Licensed Content Pages 22

Start Page 1

End Page 22

Type of Use	reuse in a thesis/dissertation
Portion	figures/tables/illustrations
Number of figures/tables/illustrations	1
Format	electronic
Are you the author of this Elsevier article?	No
Will you be translating?	No
Title	Detection and thermal stabilization of virus based on surface properties
Institution name	Michigan Technological University
Expected presentation date	Dec 2019
Order reference number	83
Portions	Figure 2.5
Requestor Location	Michigan Technological University 1803 Woodmar Dr HOUGHTON, MI 49931 United States Attn: Michigan Technological University
Publisher Tax ID	98-0397604
Total	0.00 USD

## B.5 Figure 2.6 permission

**SPRINGER NATURE**

Monitoring dynamics of human adenovirus disassembly induced by mechanical fatigue

Author: A. Ortega-Esteban et al

Publication: Scientific Reports

Publisher: Springer Nature

Date: Mar 13, 2013

*Copyright © 2013, Springer Nature*

### Creative Commons

This is an open access article distributed under the terms of the [Creative Commons CC BY](#) license, which permits unrestricted use, distribution, and reproduction in any medium, provided the original work is properly cited.

You are not required to obtain permission to reuse this article.

To request permission for a type of use not listed, please contact [Springer Nature](#)

© 2019 Copyright - All Rights Reserved | [Copyright Clearance Center, Inc.](#) | [Privacy statement](#) | [Terms and Conditions](#)  
Comments? We would like to hear from you. E-mail us at [customercare@copyright.com](mailto:customercare@copyright.com)

## B.6 Figure 2.7 permission



### IOP Publishing, Ltd - License Terms and Conditions

Order Date	05-Jan-2020
Order license ID	1011845-1
ISSN	0957-0233
Type of Use	Republish in a thesis/dissertation
Publisher	IOP Publishing
Portion	Chart/graph/table/figure

#### LICENSED CONTENT

Publication Title	Measurement Science and Technology	Country	United Kingdom of Great Britain and Northern Ireland
Author/Editor	Institute of Physics (Great Britain), American Institute of Physics.	Rightsholder	IOP Publishing, Ltd
Date	01/01/1990	Publication Type	Journal
Language	English		

#### REQUEST DETAILS

Portion Type	Chart/graph/table/figure	Distribution	Worldwide
Number of charts / graphs / tables / figures requested	2	Translation	Original language of publication
Format (select all that apply)	Electronic	Copies for the disabled?	No
Who will republish the content?	Academic institution	Minor editing privileges?	Yes
Duration of Use	Life of current edition	Incidental promotional use?	No
Lifetime Unit Quantity	Up to 499	Currency	USD
Rights Requested	Main product		

#### NEW WORK DETAILS

Title	Detection and thermal stabilization of virus based on surface properties	Institution name	Michigan Technological University
Instructor name	Dr. Caryn Heldt	Expected presentation date	2020-01-08

#### ADDITIONAL DETAILS

Order reference number	N/A	The requesting person / organization to appear on the license	Xue Mi
------------------------	-----	---	--------

#### REUSE CONTENT DETAILS

<b>Title, description or numeric reference of the portion(s)</b>	AFM: a versatile tool in biophysics	<b>Title of the article/chapter the portion is from</b>	AFM: a versatile tool in biophysics
<b>Editor of portion(s)</b>	Andrea Alessandrini and Paolo Facci	<b>Author of portion(s)</b>	Institute of Physics (Great Britain); American Institute of Physics.
<b>Volume of serial or monograph</b>	N/A	<b>Issue, if republishing an article from a serial</b>	N/A
<b>Page or page range of portion</b>	R76	<b>Publication date of portion</b>	2005-04-28

## PUBLISHER TERMS AND CONDITIONS

These special terms and conditions are in addition to the standard terms and conditions for CCC's Republication Service and, together with those standard terms and conditions, govern the use of the Works. As the User you will make all reasonable efforts to contact the author(s) of the article which the Work is to be reused from, to seek consent for your intended use. Contacting one author who is acting expressly as authorised agent for their co-author(s) is acceptable. User will reproduce the following wording prominently alongside the Work: the source of the Work, including author, article title, title of journal, volume number, issue number (if relevant), page range (or first page if this is the only information available) and date of first publication. This information can be contained in a footnote or reference note; and a link back to the article (via DOI); and if practicable, and IN ALL CASES for new works published under any of the Creative Commons licences, the words "© IOP Publishing. Reproduced with permission. All rights reserved" Without the express permission of the author(s) and the Rightsholder of the article from which the Work is to be reused, User shall not use it in any way which, in the opinion of the Rightsholder, could: (i) distort or alter the author(s)' original intention(s) and meaning; (ii) be prejudicial to the honour or reputation of the author(s); and/or (iii) imply endorsement by the author(s) and/or the Rightsholder. This licence does not apply to any article which is credited to another source and which does not have the copyright line "© IOP Publishing Ltd". User must check the copyright line of the article from which the Work is to be reused to check that IOP Publishing Ltd has all the necessary rights to be able to grant permission. User is solely responsible for identifying and obtaining separate licences and permissions from the copyright owner for reuse of any such third party material/figures which the Rightsholder is not the copyright owner of. The Rightsholder shall not reimburse any fees which User pays for a republication licence for such third party content. This licence does not apply to any material/figure which is credited to another source in the Rightsholder's publication or has been obtained from a third party. User must check the Version of Record of the article from which the Work is to be reused, to check whether any of the material in the Work is third party material. Third party citations and/or copyright notices and/or permissions statements may not be included in any other version of the article from which the Work is to be reused and so cannot be relied upon by the User. User is solely responsible for identifying and obtaining separate licences and permissions from the copyright owner for reuse of any such third party material/figures where the Rightsholder is not the copyright owner. The Rightsholder shall not reimburse any fees which User pays for a republication licence for such third party content. User and CCC acknowledge that the Rightsholder may, from time to time, make changes or additions to these special terms and conditions without express notification, provided that these shall not apply to permissions already secured and paid for by User prior to such change or addition. User acknowledges that the Rightsholder (which includes companies within its group and third parties for whom it publishes its titles) may make use of personal data collected through the service in the course of their business. If User is the author of the Work, User may automatically have the right to reuse it under the rights granted back when User transferred the copyright in the article to the Rightsholder. User should check the copyright form and the relevant author rights policy to check whether permission is required. If User is the author of the Work and does require permission for proposed reuse of the Work, User should select 'Author of requested content' as the Requestor Type. The Rightsholder shall not reimburse any fees which User pays for a republication licence. If User is the author of the article which User wishes to reuse in User's thesis or dissertation, the republication licence covers the right to include the Accepted Manuscript version (not the Version of Record) of the article. User must include citation details and, for online use, a link to the Version of Record of the article on the Rightsholder's website. User may need to obtain separate permission for any third party content included within the article. User must check this with the copyright owner of such third party content. User may not include the article in a thesis or dissertation which is published by ProQuest. Any other commercial use of User's thesis or dissertation containing the article would also need to be expressly notified in writing to the Rightsholder at the time of request and would require separate written permission from the Rightsholder. User does not need to request permission for Work which has been published under a CC BY licence. User must check the Version of Record of the CC BY article from which the Work is to be reused, to check whether any of the material in the Work is third party material and so not published under the CC BY licence. User is solely responsible for identifying and obtaining separate licences and permissions from the copyright owner for reuse of any such third party

## B.7 Figure 2.8 permission

 **ACS Publications**  
Most Trusted. Most Cited. Most Read.

**Probing Microbial Cell Surface Charges by Atomic Force Microscopy**  
Author: François Ahimou, Frédéric A. Denis, Ahmed Touhami, et al  
Publication: Langmuir  
Publisher: American Chemical Society  
Date: Dec 1, 2002  
Copyright © 2002, American Chemical Society

### PERMISSION/LICENSE IS GRANTED FOR YOUR ORDER AT NO CHARGE

This type of permission/license, instead of the standard Terms & Conditions, is sent to you because no fee is being charged for your order. Please note the following:

- Permission is granted for your request in both print and electronic formats, and translations.
  - If figures and/or tables were requested, they may be adapted or used in part.
  - Please print this page for your records and send a copy of it to your publisher/graduate school.
  - Appropriate credit for the requested material should be given as follows: "Reprinted (adapted) with permission from (COMPLETE REFERENCE CITATION). Copyright (YEAR) American Chemical Society." Insert appropriate information in place of the capitalized words.
  - One-time permission is granted only for the use specified in your request. No additional uses are granted (such as derivative works or other editions). For any other uses, please submit a new request.
- If credit is given to another source for the material you requested, permission must be obtained from that source.

[BACK](#)

[CLOSE WINDOW](#)

© 2019 Copyright - All Rights Reserved | [Copyright Clearance Center, Inc.](#) | [Privacy statement](#) | [Terms and Conditions](#)  
Comments? We would like to hear from you. E-mail us at [customer-care@copyright.com](mailto:customer-care@copyright.com)

 **ACS Publications**  
Most Trusted. Most Cited. Most Read.

**High-Resolution Imaging of Chemical and Biological Sites on Living Cells Using Peak Force Tapping Atomic Force Microscopy**  
Author: David Alsteens, Vincent Dupres, Sami Yunus, et al  
Publication: Langmuir  
Publisher: American Chemical Society  
Date: Dec 1, 2012  
Copyright © 2012, American Chemical Society

### PERMISSION/LICENSE IS GRANTED FOR YOUR ORDER AT NO CHARGE

This type of permission/license, instead of the standard Terms & Conditions, is sent to you because no fee is being charged for your order. Please note the following:

- Permission is granted for your request in both print and electronic formats, and translations.
  - If figures and/or tables were requested, they may be adapted or used in part.
  - Please print this page for your records and send a copy of it to your publisher/graduate school.
  - Appropriate credit for the requested material should be given as follows: "Reprinted (adapted) with permission from (COMPLETE REFERENCE CITATION). Copyright (YEAR) American Chemical Society." Insert appropriate information in place of the capitalized words.
  - One-time permission is granted only for the use specified in your request. No additional uses are granted (such as derivative works or other editions). For any other uses, please submit a new request.
- If credit is given to another source for the material you requested, permission must be obtained from that source.

[BACK](#)

[CLOSE WINDOW](#)

© 2019 Copyright - All Rights Reserved | [Copyright Clearance Center, Inc.](#) | [Privacy statement](#) | [Terms and Conditions](#)  
Comments? We would like to hear from you. E-mail us at [customer-care@copyright.com](mailto:customer-care@copyright.com)

## B.8 Figure 2.9 permission



**AMERICAN SOCIETY FOR MICROBIOLOGY**

**Biophysical and Ultrastructural Characterization of Adeno-Associated Virus Capsid Uncoating and Genome Release**

**Author:**  
Eric D. Horowitz, K. Shefaet Rahman, Brian D. Bower, David J. Dismuke, Michael R. Falvo, Jack D. Griffith, Stephen C. Harvey, Aravind Asokan

**Publication:** Journal of Virology

**Publisher:** American Society for Microbiology

**Date:** Feb 22, 2013

*Copyright © 2013, American Society for Microbiology*

### Permissions Request


ASM authorizes an advanced degree candidate to republish the requested material in his/her doctoral thesis or dissertation. If your thesis, or dissertation, is to be published commercially, then you must reapply for permission.

[BACK](#)

[CLOSE WINDOW](#)

© 2019 Copyright - All Rights Reserved | [Copyright Clearance Center, Inc.](#) | [Privacy statement](#) | [Terms and Conditions](#)  
Comments? We would like to hear from you. E-mail us at [customer-care@copyright.com](mailto:customer-care@copyright.com)

## B.9 Figure 2.10 permission



**SPRINGER NATURE**

**Clinical evaluation of rapid fluorescent diagnostic immunochromatographic test for influenza A virus (H1N1)**

**Author:** Seung-Taek Yu et al

**Publication:** Scientific Reports

**Publisher:** Springer Nature

**Date:** Sep 7, 2018

*Copyright © 2018, Springer Nature*

### Creative Commons

This is an open access article distributed under the terms of the [Creative Commons CC BY](#) license, which permits unrestricted use, distribution, and reproduction in any medium, provided the original work is properly cited.

You are not required to obtain permission to reuse this article.

To request permission for a type of use not listed, please contact [Springer Nature](#)

© 2019 Copyright - All Rights Reserved | [Copyright Clearance Center, Inc.](#) | [Privacy statement](#) | [Terms and Conditions](#)  
Comments? We would like to hear from you. E-mail us at [customer-care@copyright.com](mailto:customer-care@copyright.com)

## B.10 Figure 2.11 permission

Figure 2.11 is licensed under the [Creative Commons Attribution-Share Alike 3.0 Unported](#)



## B.11 Figure 2.12 permission

Portion	figures/tables/illustrations
Number of figures/tables/illustrations	1
Format	electronic
Are you the author of this Elsevier article?	No
Will you be translating?	No
Title	Detection and thermal stabilization of virus based on surface properties
Institution name	Michigan Technological University
Expected presentation date	Dec 2019
Order reference number	113
Portions	Figure 2.12
Requestor Location	Michigan Technological University 1803 Woodmar Dr HOUGHTON, MI 49931 United States Attn: Michigan Technological University
Publisher Tax ID	98-0397604
Total	0.00 USD
Terms and Conditions	

ELSEVIER LICENSE  
TERMS AND CONDITIONS

Nov 25, 2019

---

This Agreement between Michigan Technological University ("You") and Elsevier ("Elsevier") consists of your license details and the terms and conditions provided by Elsevier and Copyright Clearance Center.

License Number 4715901254004

License date Nov 25, 2019

Licensed Content Publisher Elsevier

Licensed Content Publication Journal of Virological Methods

Licensed Content Title Development of plaque assays for adenoviruses 40 and 41

Licensed Content Author Theresa L. Cromeans, Xiaoyan Lu, Dean D. Erdman, Charles D. Humphrey, Vincent R. Hill

Licensed Content Date Jul 1, 2008

Licensed Content Volume 151

Licensed Content Issue 1

Licensed Content Pages 6

Start Page 140

End Page 145

Type of Use reuse in a thesis/dissertation

## B.12 Figure 2.13 permission

[Attribution-Non Commercial 3.0 Unported Licence](#)



[View PDF Version](#)

[Previous Article](#)

[Next Article](#)

Open Access Article

This Open Access Article is licensed under a [Creative Commons Attribution-Non Commercial 3.0 Unported Licence](#)

DOI: [10.1039/C4RA12089B](https://doi.org/10.1039/C4RA12089B) (Paper) *RSC Adv.*, 2015, 5, 14982-14993

### Understanding aggregation-based assays: nature of protein corona and number of epitopes on antigen matters†

Eugenia Li Ling Yeo <sup>a</sup>, Anthony Jin Shun Chua <sup>bc</sup>, Krupakar Parthasarathy <sup>bc</sup>, Hui Yu Yeo <sup>b</sup>, Mah Lee Ng <sup>bc</sup> and James Chen Yong Kah <sup>\*a</sup>

<sup>a</sup>Nanomedicine & Nanorobotics Laboratory, Department of Biomedical Engineering, National University of Singapore, 9 Engineering Drive 1, EA-03-12, Singapore 117575. E-mail: [biekaj@nus.edu.sg](mailto:biekaj@nus.edu.sg)

<sup>b</sup>Flavivirology Laboratory, Department of Microbiology, Yong Loo Lin School of Medicine, National University Health System, National University of Singapore, 5 Science Drive 2, MD4 Level 3, Singapore 117545

<sup>c</sup>NUS Graduate School for Integrative Sciences and Engineering, National University of Singapore, Centre for Life Sciences (CeLS), 28 Medical Drive, #05-01, Singapore 117456

<sup>d</sup>Centre for Drug Discovery and Development, Sathyabama University, Jeppiaar Nagar, Rajiv Gandhi Road, Chennai-600 119, Tamilnadu, India

Received 10th October 2014, Accepted 12th January 2015

First published on 12th January 2015

## B.13 Figure 2.14 permission

### JOHN WILEY AND SONS LICENSE TERMS AND CONDITIONS

Nov 25, 2019

---

This Agreement between Michigan Technological University ("You") and John Wiley and Sons ("John Wiley and Sons") consists of your license details and the terms and conditions provided by John Wiley and Sons and Copyright Clearance Center.

License Number	4715920083085
License date	Nov 25, 2019
Licensed Content Publisher	John Wiley and Sons
Licensed Content Publication	Biotechnology Progress
Licensed Content Title	A generalized purification step for viral particles using mannitol flocculation
Licensed Content Author	Majid Ghafarian, Pratik U. Joshi, Ashish Saksule, et al
Licensed Content Date	Jul 5, 2018
Licensed Content Volume	34
Licensed Content Issue	4
Licensed Content Pages	9
Type of use	Dissertation/Thesis
Requestor type	University/Academic
Format	Electronic

Portion	Figure/table
Number of figures/tables	1
Original Wiley figure/table number(s)	Figure 2.14
Will you be translating?	No
Order reference number	148
Title of your thesis / dissertation	Detection and thermal stabilization of virus based on surface properties
Expected completion date	Dec 2019
Expected size (number of pages)	1
Requestor Location	Michigan Technological University 1803 Woodmar Dr  HOUGHTON, MI 49931 United States Attn: Michigan Technological University
Publisher Tax ID	EU826007151
Total	0.00 USD
Terms and Conditions	

## B.14 Figure 2.15 permission

License: Published by Emerald Publishing Limited. This article is published under the Creative Commons Attribution (CC BY 4.0) licence. Anyone may reproduce, distribute, translate and create derivative works of this article (for both commercial and non-commercial purposes), subject to full attribution to the original publication and authors. The full terms of this licence may be seen at <http://creativecommons.org/licences/by/4.0/legalcode>.

License:WHO CC BY-NC-SA 3.0 IGO”

## B.15 Figure 2.16 permission

### ELSEVIER LICENSE TERMS AND CONDITIONS

Nov 25, 2019

---

This Agreement between Michigan Technological University ("You") and Elsevier ("Elsevier") consists of your license details and the terms and conditions provided by Elsevier and Copyright Clearance Center.

License Number 4715930723093

License date Nov 25, 2019

Licensed Content Publisher Elsevier

Licensed Content Publication Advances in Colloid and Interface Science

Licensed Content Title Molecular and structural basis of low interfacial energy of complex coacervates in water

Licensed Content Author YongSeok Jho, Hee Young Yoo, Yanxian Lin, Songi Han, Dong Soo Hwang

Licensed Content Date Jan 1, 2017

Licensed Content Volume 239

Licensed Content Issue n/a

Licensed Content Pages 13

Start Page 61

End Page 73

Type of Use	reuse in a thesis/dissertation
Portion	figures/tables/illustrations
Number of figures/tables/illustrations	1
Format	electronic
Are you the author of this Elsevier article?	No
Will you be translating?	No
Title	Detection and thermal stabilization of virus based on surface properties
Institution name	Michigan Technological University
Expected presentation date	Dec 2019
Order reference number	179
Portions	Figure 2.16
Requestor Location	Michigan Technological University 1803 Woodmar Dr
	HOUGHTON, MI 49931 United States Attn: Michigan Technological University
Publisher Tax ID	98-0397604
Total	0.00 USD

## Royal Society of Chemistry - License Terms and Conditions

Order Date	05-Jan-2020
Order license ID	1011843-1
ISSN	1744-6848
Type of Use	Republish in a thesis/dissertation
Publisher	ROYAL SOCIETY OF CHEMISTRY
Portion	Chart/graph/table/figure

### LICENSED CONTENT

Publication Title	Soft matter	Country	United Kingdom of Great Britain and Northern Ireland
Author/Editor	Royal Society of Chemistry (Great Britain)		
Date	06/01/2005	Rightholder	Royal Society of Chemistry
Language	English	Publication Type	e-Journal
		URL	<a href="http://www.rsc.org/Publishing/Journals/sm/index.asp">http://www.rsc.org/Publishing/Journals/sm/index.asp</a>

### REQUEST DETAILS

Portion Type	Chart/graph/table/figure	Distribution	Worldwide
Number of charts / graphs / tables / figures requested	1	Translation	Original language of publication
Format (select all that apply)	Electronic	Copies for the disabled?	No
Who will republish the content?	Academic institution	Minor editing privileges?	Yes
Duration of Use	Life of current edition	Incidental promotional use?	Yes
Lifetime Unit Quantity	Up to 499	Currency	USD
Rights Requested	Main product		

### NEW WORK DETAILS

Title	Detection and thermal stabilization of virus based on surface properties	Institution name	Michigan Technological University
Instructor name	Dr. Caryn Heldt	Expected presentation date	2020-01-08

### ADDITIONAL DETAILS

Order reference number	N/A	The requesting person / organization to appear on the license	Xue Mi
------------------------	-----	---	--------

### REUSE CONTENT DETAILS



Title, description or numeric reference of the portion(s)	Phase behaviour and complex coacervation of aqueous polypeptide solutions	Title of the article/chapter the portion is from	Phase behaviour and complex coacervation of aqueous polypeptide solutions
Editor of portion(s)	Dimitrios Priftis and Matthew Tirrell	Author of portion(s)	Royal Society of Chemistry (Great Britain)
Volume of serial or monograph	8	Issue, if republishing an article from a serial	N/A
Page or page range of portion	9398	Publication date of portion	2012-04-25

## CCC Republication Terms and Conditions

1. Description of Service; Defined Terms. This Republication License enables the User to obtain licenses for republication of one or more copyrighted works as described in detail on the relevant Order Confirmation (the "Work(s)"). Copyright Clearance Center, Inc. ("CCC") grants licenses through the Service on behalf of the rightsholder identified on the Order Confirmation (the "Rightsholder"). "Republishing", as used herein, generally means the inclusion of a Work, in whole or in part, in a new work or works, also as described on the Order Confirmation. "User", as used herein, means the person or entity making such republication.
2. The terms set forth in the relevant Order Confirmation, and any terms set by the Rightsholder with respect to a particular Work, govern the terms of use of Works in connection with the Service. By using the Service, the person transacting for a republication license on behalf of the User represents and warrants that he/she/it (a) has been duly authorized by the User to accept, and hereby does accept, all such terms and conditions on behalf of User, and (b) shall inform User of all such terms and conditions. In the event such person is a "freelancer" or other third party independent of User and CCC, such party shall be deemed jointly a "User" for purposes of these terms and conditions. In any event, User shall be deemed to have accepted and agreed to all such terms and conditions if User republishes the Work in any fashion.
3. Scope of License; Limitations and Obligations.
  - 3.1. All Works and all rights therein, including copyright rights, remain the sole and exclusive property of the Rightsholder. The license created by the exchange of an Order Confirmation (and/or any invoice) and payment by User of the full amount set forth on that document includes only those rights expressly set forth in the Order Confirmation and in these terms and conditions, and conveys no other rights in the Work(s) to User. All rights not expressly granted are hereby reserved.
  - 3.2. General Payment Terms: You may pay by credit card or through an account with us payable at the end of the month. If you and we agree that you may establish a standing account with CCC, then the following terms apply: Remit Payment to: Copyright Clearance Center, 29118 Network Place, Chicago, IL 60673-1291. Payments Due: Invoices are payable upon their delivery to you (or upon our notice to you that they are available to you for downloading). After 30 days, outstanding amounts will be subject to a service charge of 1-1/2% per month or, if less, the maximum rate allowed by applicable law. Unless otherwise specifically set forth in the Order Confirmation or in a separate written agreement signed by CCC, invoices are due and payable on "net 30" terms. While User may exercise the rights licensed immediately upon issuance of the Order Confirmation, the license is automatically revoked and is null and void, as if it had never been issued, if complete payment for the license is not received on a timely basis either from User directly or through a payment agent, such as a credit card company.
  - 3.3. Unless otherwise provided in the Order Confirmation, any grant of rights to User (i) is "one-time" (including the editions and product family specified in the license), (ii) is non-exclusive and non-transferable and (iii) is subject to any and all limitations and restrictions (such as, but not limited to, limitations on duration of use or circulation) included in the Order Confirmation or invoice and/or in these terms and conditions. Upon completion of the licensed use, User shall either secure a new permission for further use of the Work(s) or immediately cease any new use of the Work(s) and shall render inaccessible (such as by

JOHN WILEY AND SONS LICENSE  
TERMS AND CONDITIONS

Nov 25, 2019

---

This Agreement between Michigan Technological University ("You") and John Wiley and Sons ("John Wiley and Sons") consists of your license details and the terms and conditions provided by John Wiley and Sons and Copyright Clearance Center.

License Number	4715931031047
License date	Nov 25, 2019
Licensed Content Publisher	John Wiley and Sons
Licensed Content Publication	Wiley Interdisciplinary Reviews - Nanomedicine and Nanobiotechnology
Licensed Content Title	Complex coacervate-based materials for biomedicine
Licensed Content Author	Whitney C. Blocher, Sarah L. Perry
Licensed Content Date	Nov 4, 2016
Licensed Content Volume	9
Licensed Content Issue	4
Licensed Content Pages	28
Type of use	Dissertation/Thesis
Requestor type	University/Academic
Format	Electronic

Portion	Figure/table
Number of figures/tables	1
Original Wiley figure/table number(s)	Figure 2.16
Will you be translating?	No
Order reference number	173
Title of your thesis / dissertation	Detection and thermal stabilization of virus based on surface properties
Expected completion date	Dec 2019
Expected size (number of pages)	1
Requestor Location	Michigan Technological University 1803 Woodmar Dr  HOUGHTON, MI 49931 United States Attn: Michigan Technological University
Publisher Tax ID	EU826007151
Total	0.00 USD
Terms and Conditions	



## Protein Encapsulation via Polypeptide Complex Coacervation

Author: Katie A. Black, Dimitrios Priftis, Sarah L. Perry, et al

Publication: ACS Macro Letters

Publisher: American Chemical Society

Date: Oct 1, 2014

Copyright © 2014, American Chemical Society

### PERMISSION/LICENSE IS GRANTED FOR YOUR ORDER AT NO CHARGE

This type of permission/license, instead of the standard Terms & Conditions, is sent to you because no fee is being charged for your order. Please note the following:

- Permission is granted for your request in both print and electronic formats, and translations.
  - If figures and/or tables were requested, they may be adapted or used in part.
  - Please print this page for your records and send a copy of it to your publisher/graduate school.
  - Appropriate credit for the requested material should be given as follows: "Reprinted (adapted) with permission from (COMPLETE REFERENCE CITATION). Copyright (YEAR) American Chemical Society." Insert appropriate information in place of the capitalized words.
  - One-time permission is granted only for the use specified in your request. No additional uses are granted (such as derivative works or other editions). For any other uses, please submit a new request.
- If credit is given to another source for the material you requested, permission must be obtained from that source.

[BACK](#)

[CLOSE WINDOW](#)